

Tensegrity Structures: Form-finding, Modelling, Structural Analysis, Design and Control

MUSA ABDULKAREEM BEng, MSc(Eng)



The
University
Of
Sheffield.

Thesis submitted as a requirement for the degree of
Doctor of Philosophy
in the Department of Automatic Control and Systems Engineering
University of Sheffield, UK

March 2013

ABSTRACT

Tensegrity structures are a type of structural systems that consist of a given set of cables connected to a configuration of rigid bodies and stabilized by internal forces of the cables in the absence of external forces. Such structures provide an important platform for exploring advanced active control technologies. This thesis is, thus, a research on tensegrity structures' related problems across a wide range of engineering disciplines and from a control system's viewpoint. It proposes a new algorithm for the form-finding of tensegrity structures. This is a process that involves using the mathematical properties of these structures to search and/or define a configuration that makes the structures to satisfy the conditions of static equilibrium while being pre-stressed.

The dynamic model of tensegrity structures is derived using the Finite Element Method (FEM), and the static and dynamic analyses of tensegrity structures are carried-out. Furthermore, the effect of including additional structural members (than strictly necessary) on the dynamics of n-stage tensegrity structures is also investigated and how the resulting change in their geometric properties can be explored for self-diagnosis and self-repair in the event of structural failure is examined. Also, the procedures for model reduction and optimal placement of actuators and sensors for tensegrity structures to facilitate further analysis and design of control systems are described.

A new design approach towards the physical realization of these structures using novel concepts that have not been hitherto investigated in the available literature on this subject is proposed. In particular, the proposed realization approach makes it possible to combine the control of the cable and bar lengths simultaneously, thereby combining together the advantages of both bar control and cable control techniques for the active control of tensegrity structural systems. The active control of tensegrity structures in a multivariable and centralized control context is presented for the design of collocated and non-collocated control systems. A new method is presented for the determination of the feedback gain for collocated controllers to reduce the control effort as much as possible while the closed-loop stability of the system is unconditionally guaranteed. In addition, the LQG (Linear system, Quadratic cost, Gaussian noise) controllers which are suitable for both collocated and non-collocated control systems is applied to actively control tensegrity structural systems for vibration suppression and precision control.

To my dear parents

ACKNOWLEDGEMENTS

All praises and thanks are to Almighty Allah who alone created the universe.

It is a great pleasure for me to acknowledge those many people who have played a major role through their support and help during the course of my PhD studies, in particular, and in my career and life, in general. I have worked with many colleagues, friends and other researchers and it is not possible for me to mention each one and the extent of their support. However, I do gratefully acknowledge and appreciate every help I receive from everyone at various stages of my research. Of these, I would like to specifically mention and thank a number of people whose assistance and support have been invaluable.

It is with immense gratitude that I acknowledge the support and help of my supervisor, Professor Mahdi Mahfouf, for giving me the opportunity to study for a PhD degree under his supervision, and with whom I consider it an honour to work with. I am also indebted to the University of Sheffield for their sponsorship and aid through the Overseas Research Student (ORS) Award to pursue my degree.

I would like to thank Professor Didier Theilliol of the University of Lorraine (France), for many discussions that helped me in understanding many areas of this work and for inviting me over to spend few weeks in his research lab, and Professor René Motro of the University of Montpellier (France), a prominent researcher on tensegrity structures, for accepting my request to visit him to discuss my research work despite being on his retirement. Many thanks also go to the staff and my fellow students at our Intelligent Systems and IMPETUS research groups for their friendship, particularly, Osman Ishaque, Shen Wang, Guangrui Zhang, Alicia Adriana Rodriguez, Ali Zughrat and Drs. Mouloud Denaï, Sid-Ahmed Gaffour and Qian Zhang.

I would also like to extend my gratitude to the academic, technical and support staffs of the Department of Automatic Control and Systems Engineering at the University of Sheffield who have given me unlimitedly help and guidance during my studies. The

help of the technical staff, Craig Bacon, Ian Hammond and Anthony Whelpton, in assembling the structural system I designed in this project are gratefully appreciated. I have also come to know many residents of Sheffield, in at least hundreds, due to many community projects that I was involved in and I wholeheartedly thank them for the kindness, patience and opportunity that they gave me to be part of them. I will forever be indebted for this honour.

I wish to thank my wife, Rasheedah, and my son, Abdullah, for their patience, understanding, support and encouragement during the period of conducting this research.

Importantly, I am deeply indebted to all my brothers and sisters who have been a great source of cooperation throughout my life. I thank them for their unwavering support and understanding that has made it possible for me to pay full attention on my studies and I hope that my achievement is well-worth their sacrifices during the period that I have been away from Nigeria.

Last, but not least, I would like to express my utmost and deepest gratitude to my parents for their unequivocal support; indeed, this is a very small acknowledgement of their unfailing love and affection.

All praises and thanks are to Almighty Allah at the end as at the beginning.

MUSA ABDULKAREEM

Sheffield, March 2013

PUBLICATIONS

Conference Papers:

- **Abdulkareem, M.**, Mahfouf, M. and Didier, T, ‘*Dynamic Modelling of Tensegrity Structures with Expanding Properties*’, Vibration Problems ICOVP2011: The 10th International Conference on Vibration Problems, 5-8 September, 2011, Prague, Czech Republic (*In Springer Proceedings in Physics, 2011*).
- **Abdulkareem, M.**, Mahfouf, M. and Didier, T, ‘*Design of Tensegrity Structures: the kinematic method with forces in structural members*’, Proc. of the 13th International Conference on Civil, Structural and Environmental Engineering Computing, 6-9 September, 2011, Crete, Greece.
- **Abdulkareem, M.**, Mahfouf, M. and Didier, T, ‘*A Constrained Optimization Approach for Form-Finding of Tensegrity Structures and their Static-load Deflection Properties*’, Proc. of the 13th International Conference on Civil, Structural and Environmental Engineering Computing, 6-9 September, 2011, Crete, Greece.

Contributions in Colloquia:

- **Abdulkareem, M.**, Mahfouf, M. and Didier, T, ‘*Tensegrity Structure: From theory to design and implementation*’, IMPPETUS Colloquium, 3-4 April, 2012, University of Sheffield, UK.
- **Abdulkareem, M.**, Mahfouf, M. and Didier, T, ‘*Dynamic Modelling of Tensegrity Structures*’, IMPPETUS Colloquium, 19-20 April, 2011, University of Sheffield, UK.
- **Abdulkareem, M.**, Mahfouf, M. and Didier, T, ‘*Tensegrity Structures: Background, Analysis, Current and Future Industrial Applications*’, IMPPETUS Colloquium, 30-31 March, 2010, University of Sheffield, UK.

Contributions in Seminars:

- **Abdulkareem, M.**, Mahfouf, M. and Didier, T, ‘*Tensegrity Structures: An overview and current challenges*’, Centre de Recherche en Automatique de Nancy (CRAN), Faculté des Sciences et Technique, 7th February, 2012, Nancy Université, FRANCE.

AWARDS

- **The Royal Academy of Engineering (RAE) Travel Award** Grant of £300 towards attendance of the International Course on Modal Analysis: Theory and Practice (ISMA36), Division of Production Engineering, Machine Design and Automation, Department of Mechanical Engineering, Katholieke Universiteit Leuven, Belgium (20-21 September, 2011).
- **IMMPETUS Mike Frolish Prize** Best Oral Presentation at the 13th Annual Colloquium of the Institute for Microstructural and Mechanical Process Engineering: The University of Sheffield (IMMPETUS), 19-20 April, 2011.
- **Overseas Research Student (ORS) Award of the University of Sheffield, United Kingdom** October, 2009.
- **Engineering and Physical Sciences Research Council (EPSRC) Case Award** October, 2009.

CONTENTS

Abstract	iii
Dedication	v
Acknowledgments	vii
Publications	ix
Awards	xi
Contents	xiii
List of Figures	xvii
List of Tables	xxv
List of Main Symbols and Abbreviations	xxvii
1 INTRODUCTION.....	1
1.1 Definition of Tensegrity Structures	1
1.2 Origin of Tensegrity Structures	4
1.3 Research and Application of Tensegrity Structures and Concept	5
1.4 Project Motivation and Description.....	8
1.5 Thesis Outline	11
2 FORM-FINDING OF TENSEGRITY STRUCTURES	15
2.1 Introduction.....	15
2.2 Form-finding Method for Tensegrity Structures: The Constrained Optimization Approach.....	16
2.2.1 Matrix Analysis of Tensegrity Structures	16
2.2.1.1 Definitions and Notations	17
2.2.1.2 Matrix Decompositions related to Equations of Equilibrium	21
2.2.2 Penalty Function Method of Constrained Optimization	28
2.2.2.1 Obtaining Tension Coefficients from the Equilibrium Matrix	33
2.2.2.2 Obtaining Nodal Coordinates from the Force Density Matrix	35
2.2.2.3 Obtaining Nodal Coordinates from Geometric Consideration	36
2.2.3 A Constrained Optimization Approach for the Form-finding of Tensegrity Structures.....	42

2.2.4 Examples of Applications of the Constrained Optimization Form-finding Algorithm	46
2.2.5 Discussions	50
2.3 Other Form-finding Methods	51
2.4 Summary	53
3 STATIC AND DYNAMIC ANALYSES OF TENSEGRITY STRUCTURES	54
3.1 Introduction	54
3.2 Static and Dynamic Analyses of Tensegrity Structures Using the Finite Element Method	55
3.2.1 Derivation and Assembly of the Element Matrices	55
3.2.1.1 The Stiffness Matrix	55
3.2.1.2 The Relationship between the Geometric and Elastic Stiffness Matrices and the Stiffness Matrix of the Conventional Finite Element Method	60
3.2.1.3 The Mass Matrix	62
3.2.2 Basic Equations and Solution Procedure	63
3.2.2.1 Equations of Motion of a Discretized System	63
3.2.2.2 Eigenvalue Problem and Uncoupled Equations of Motion	64
3.2.2.3 Rigid Body Modes and Static Model Reduction	67
3.2.2.4 Pseudo-Static Deflection Properties of a 2-stage Tensegrity Structure	68
3.2.3 State-Space Model Representation	73
3.2.4 Dynamic Model Simulation of n-stage Tensegrity Structures	81
3.3 Discussions	92
3.4 Summary	97
4 MODEL REDUCTION AND OPTIMAL ACTUATOR AND SENSOR PLACEMENT	98
4.1 Introduction	98
4.2 Definitions and Notations	100
4.2.1 Controllability, Observability and Grammians	101
4.2.2 The \mathbf{H}_2 , \mathbf{H}_∞ and Hankel Norms	104
4.3 Model Reduction	107
4.3.1 Truncation Method	107
4.3.2 Residualization Method	108
4.3.3 Model Reduction Error	108
4.4 Optimal Actuator and Sensor Placement	109
4.4.1 State, Actuator and Sensor Norms	111
4.4.2 Placement Indices and Matrices	112

4.5 Numerical Applications	116
4.5.1 Minimal Multistage Tensegrity Structures	116
4.5.2 Non-minimal Multistage Tensegrity Structures	118
4.6 Discussions	119
4.7 Summary	137
5 PHYSICAL REALIZATION OF TENSEGRITY STRUCTURAL SYSTEMS	
PART I: PHYSICAL STRUCTURE DESIGN	138
5.1 Introduction.....	138
5.2 Tensegrity Prisms and their Regularity, Minimality and Design Approaches	141
5.3 Designs of Compressive and Tensile Structural Members.....	143
5.3.1 Selection of Extensible Bars	146
5.3.2 Design of Cables	153
5.3.3 Design of Active Cables.....	158
5.4 Collision avoidance, detection and related issues.....	165
5.5 Motion of Tensegrity Structures	172
5.5.1 Translation of the Tensegrity Prisms	174
5.5.2 Rotation of the Tensegrity Prisms	178
5.6 Discussions	181
5.7 Summary.....	183
6 PHYSICAL REALIZATION OF TENSEGRITY STRUCTURAL SYSTEMS	
PART II: HARDWARE ARCHITECTURE AND A DECENTRALIZED	
CONTROL SCHEME.....	185
6.1 Introduction.....	185
6.2 Hardware Architecture and Components and the Serial Communication Protocol using the USB interface	186
6.2.1 The Interface Board.....	187
6.2.2 Configuration of the Interface Board	191
6.2.3 The Serial Port Interface and the ‘Pololu’ Communication Protocol	192
6.2.4 Control Parameters and Algorithm of the Interface Board	198
6.3 Control Strategy, Design Characteristics and Setbacks.....	206
6.4 Modelling and Simulation of the 3-bar Tensegrity Structural System	218
6.5 Discussions	222
6.6 Summary.....	224

7 CONTROL SYSTEM DESIGN FOR TENSEGRITY STRUCTURES	225
7.1 Introduction.....	225
7.2 Collocated Control of Tensegrity Structures	226
7.3 Linear Optimal Control of Tensegrity Structures	245
7.3.1 Collocated Control with Linear Optimal State-feedback Regulator	246
7.3.2 Non-collocated Control with Linear Optimal Output-feedback Controller	247
7.3.3 Robust Tracking System for Active Tensegrity Structures.....	250
7.4 Discussions	255
7.5 Summary.....	261
8 CONCLUSIONS AND FUTURE WORK	263
8.1 Conclusions.....	263
8.2 Future Work.....	265
REFERENCES.....	267
Appendix: LINEAR OPTIMAL CONTROL SYSTEMS	286
A.1 Linear Optimal State-feedback Regulator	286
A.2 Linear Optimal Observer	288
A.3 Linear Optimal Output-feedback Controller.....	292
A.4 Linear Optimal Tracking System and Integral Control	294

LIST OF FIGURES

Figure 1.1: A simple tensegrity structure with 3 bars (thick black lines) and 9 cables (thin blue lines). ...	2
Figure 1.2: A simple example of class 3 tensegrity structures.	3
Figure 1.3: A simple structural system that cannot be stabilized in the absence of external forces.	4
Figure 1.4: Ioganson’s Sculpture, Snelson’s X-piece and Snelson’s simplex.	5
Figure 2.1: A view of an unconstrained node i connected to nodes j and h through members l and m , respectively.....	18
Figure 2.2: A class 3 tensegrity structure (thick and thin lines represent bars and cables, respectively) ...	19
Figure 2.3: Singular value decomposition of the equilibrium matrix illustrating the relationships between m , r , s and \mathbb{U} , \mathbb{V} , \mathbb{W}	23
Figure 2.4: An illustrating on obtaining tension coefficients from the right orthonormal matrix.	24
Figure 2.5: Tensegrity structures associated with nodal coordinates defined in Table 2.2.	27
Figure 2.6: An illustrative example of the implementation of algorithm in Method 1.....	29
Figure 2.7: Tension coefficients obtained from the equilibrium matrix using a constrained optimization approach.	34
Figure 2.8: Nodal coordinates obtained from the force density matrix of valid set of tension coefficients using an optimization approach.	39
Figure 2.9: Tensegrity structure to be determined from geometric consideration.....	40
Figure 2.10: Tensegrity structures obtained using form-finding methods A, B and C.....	45
Figure 2.11: A class 2 tensegrity configuration.....	46
Figure 2.12: Tensegrity structure obtained from a class 2 tensegrity configuration using constrained optimization form-finding approach.....	47
Figure 2.13: A truss-like class 2 tensegrity configuration and structure	49
Figure 3.1: A 2-stage tensegrity structure with three bars per stage.....	70
Figure 3.2: (a) Displacements in the x-,y- and z-axis of node 12 as tension coefficients scaling factor c_q varies on loads 1N, 10N, 50N, 100N and 200N. (b) Vertical displacements of nodes 10, 11, and 12 as tension coefficients scaling factor c_q is varied on vertical loads 1N, 10N, 50N, 100N and 200N.....	71
Figure 3.3: Vertical displacements of nodes 10, 11, and 12 as static loads on these nodes are varied for various tension coefficients scaling factor c_q	72

Figure 3.4: Vertical displacements of nodes 10, 11, and 12 for the tension coefficients scaling factor of $c_q = 10$ as the nodal coordinates scaling factor varies on loads 10N, 50N, 100N, 150N and 200N.	72
Figure 3.5: Vertical displacements of nodes 10, 11, and 12 for loads 1KN placed vertically on these nodes as the nodal coordinates scaling factor varies for the tension coefficient scaling factor c_q of values 50, 100, 150, 200 and 250.	73
Figure 3.6: Dynamic response of the 2-stage tensegrity structure to three vertically downward loads of 300N on nodes 10, 11, and 12 suddenly applied at time $t = 0$ (sec): Nodal Displacements (meter) Vs time (sec) for the x and y axes.	77
Figure 3.7: Dynamic response of the 2-stage tensegrity structure to three vertically downward loads of 300N on nodes 10, 11, and 12 suddenly applied at time $t = 0$ (sec): Nodal Displacements (meter) Vs time (sec) for the z axis.	78
Figure 3.8: Dynamic response of the 2-stage tensegrity structure to three vertically downward loads of 300N on nodes 10, 11, and 12 suddenly applied at time $t = 0$ (sec): Nodal Velocities (meter/sec) Vs time (sec) for the x and y axes.	79
Figure 3.9: Dynamic response of the 2-stage tensegrity structure to three vertically downward loads of 300N on nodes 10, 11, and 12 suddenly applied at time $t = 0$ (sec): Nodal Velocities (meter/sec) Vs time (sec) for the z axis.	80
Figure 3.10: (a) A minimal 2-stage 3-order tensegrity structure; (b) A 2-stage 3-order tensegrity structure with additional structural members (shown in red).	82
Figure 3.11: (a) A minimal 3-stage 3-order tensegrity structure; (b) A 3-stage 3-order tensegrity structure with additional structural members (shown in red).	82
Figure 3.12: (a) and (b) show the nomenclature adopted for numbering the structural members of figures 3.10 (b) and 3.11 (b), respectively; in both cases, the numberings of structural members and nodes are in blue and black, respectively. [Scale of Plots: meter in all axes]. .	83
Figure 3.13: (a) and (b) are the dynamic response (nodal displacements (meter) Vs time (sec) along the x-axis) of the 2-stage 3-order tensegrity structures of Figure 3.10 (a) and (b), respectively, to three vertically downward loads of 300N on nodes 10, 11, and 12 suddenly applied at time $t = 0$ (sec).....	86
Figure 3.14: (a) and (b) are the dynamic response (nodal displacements (meter) Vs time (sec) along the y-axis) of the 2-stage 3-order tensegrity structures of Figure 3.10 (a) and (b), respectively, to three vertically downward loads of 300N on nodes 10, 11, and 12 suddenly applied at time $t = 0$ (sec).....	87
Figure 3.15: (a) and (b) are the dynamic response (nodal displacements (meter) Vs time (sec) along the z-axis) of the 2-stage 3-order tensegrity structures of Figure 3.10 (a) and (b), respectively, to three vertically downward loads of 300N on nodes 10, 11, and 12 suddenly applied at time $t = 0$ (sec).....	88
Figure 3.16: (a) and (b) are the dynamic response (nodal displacements (meter) Vs time (sec) along the x-axis) of the 3-stage 3-order tensegrity structures of Figure 3.11 (a) and (b), respectively, to three vertically downward loads of 300N on nodes 16, 17, and 18 suddenly applied at time $t = 0$ (sec).....	89
Figure 3.17: (a) and (b) are the dynamic response (nodal displacements (meter) Vs time (sec) along the y-axis) of the 3-stage 3-order tensegrity structures of Figure 3.11 (a) and (b), respectively, to three vertically downward loads of 300N on nodes 16, 17, and 18 suddenly applied at time $t = 0$ (sec).....	90

Figure 3.18: (a) and (b) are the dynamic response (nodal displacements (meter) Vs time (sec) along the z-axis) of the 3-stage 3-order tensegrity structures of Figure 3.11 (a) and (b), respectively, to three vertically downward loads of 300N on nodes 16, 17, and 18 suddenly applied at time $t = 0$ (sec).....	91
Figure 3.19: An example of non-minimal 3-stage 3-order tensegrity structure (additional structural members are shown in red).....	94
Figure 4.1: A block diagram of the model reduction procedure.....	110
Figure 4.2: A block diagram of the optimal actuator and sensor placement procedure using the H^∞ norm	115
Figure 4.3: (a) A 1-stage 3-order tensegrity structure; (b) a plot of the Hankel singular values of the structure; and (c) a plot of the frequency response of the structure.	121
Figure 4.4: (a) A 2-stage 3-order tensegrity structure; (b) a plot of the Hankel singular values of the structure (only the largest 30 out of a total of 54 are shown); and (c) a plot of the frequency response of the structure.	122
Figure 4.5: (a) A 3-stage 3-order tensegrity structure; (b) a plot of the Hankel singular values of the structure (only the largest 30 out of a total of 90 are shown); and (c) a plot of the frequency response of the structure.	123
Figure 4.6: (a) A 4-stage 3-order tensegrity structure; (b) a plot of the Hankel singular values of the structure (only the largest 30 out of a total of 126 are shown); and (c) a plot of the frequency response of the structure.	124
Figure 4.7: (a) A 5-stage 3-order tensegrity structure; (b) a plot of the Hankel singular values of the structure (only the largest 35 out of a total of 162 are shown); and (c) a plot of the frequency response of the structure.	125
Figure 4.8: (a) A 3-stage 5-order tensegrity structure; (b) a plot of the Hankel singular values of the structure (only the largest 40 out of a total of 150 are shown); and (c) a plot of the frequency response of the structure.	126
Figure 4.9: (a) A 3-stage 6-order tensegrity structure; (b) a plot of the Hankel singular values of the structure (only the largest 50 out of a total of 180 are shown); and (c) a plot of the frequency response of the structure.	127
Figure 4.10: (a) A 6-stage 3-order tensegrity structure; (b) a plot of the Hankel singular values of the structure (only the largest 50 out of a total of 198 are shown; 2 of these are unstable); and (c) a plot of the frequency response of the structure.....	128
Figure 4.11: (a) A 7-stage 3-order tensegrity structure; (b) a plot of the Hankel singular values of the structure (only the largest 50 out of a total of 234 are shown; 2 of these are unstable); and (c) a plot of the frequency response of the structure.....	129
Figure 4.12: (a) A plot of the frequency response of the 2-stage 3-order tensegrity structure; and (b) a plot of the frequency response of the structure.....	130
Figure 4.13: (a) Frequency response plots of minimal and non-minimal 2-stage 3-order tensegrity structure; and (b) frequency response plots of minimal and non-minimal 3-stage 3-order tensegrity structure.	132
Figure 4.14 (a): (i) and (ii) are the plots of the actuator placement indices for the states 1, 3, and 5 of the 2-stage 3-order minimal and non-minimal tensegrity structures, respectively.	133

Figure 4.14 (b): (i) and (ii) are the plots of the actuator placement indices over all states (T_a'), the Hankel singular values ($\eta_1, \eta_2, \dots, \eta_n$ – only the largest 30 out of a total of 54 are shown), and the state importance indices (M_a) of the 2-stage 3-order minimal and non-minimal tensegrity structures, respectively.....	134
Figure 4.15 (a): (i) and (ii) are the plots of the actuator placement indices for the states 1, 3, and 5 of the 3-stage 3-order minimal and non-minimal tensegrity structures, respectively.	135
Figure 4.15 (b): (i) and (ii) are the plots of the actuator placement indices over all states (T_a'), the Hankel singular values ($\eta_1, \eta_2, \dots, \eta_n$ – only the largest 30 out of a total of 90 are shown), and the state importance indices (M_a) of the 3-stage 3-order minimal and non-minimal tensegrity structures, respectively.....	136
Figure 5.1: Examples of 3-bar minimal tensegrity prisms: (a) A regular minimal tensegrity prism with $r_t = r_b$; (b) A regular minimal tensegrity prism with $r_t < r_b$; and (c) An irregular minimal tensegrity prism with $r_t = r_b$	142
Figure 5.2: Top view of a 4-bar regular minimal tensegrity prism with $r = r_t = r_b$	143
Figure 5.3: The initial 3-bar tensegrity prism (the length of each bar equals to 60 cm and $r_t = r_b$)	145
Figure 5.4: A picture of the 12” stroke linear actuator with feedback (LD series actuator) manufactured by Concentric International	148
Figure 5.5: Plots of the degree of stability (measured by the norm of the nodal residual forces) versus the bar lengths of the 3-bar minimal tensegrity prism in two-dimension	151
Figure 5.6: A depiction of the stability region of the 3-bar minimal tensegrity prism in three-dimension using a small number of slices	152
Figure 5.7: (a) The initial 3-bar tensegrity prism; (b) SolidWorks® dimensional drawing of the 3-bar tensegrity prism	152
Figure 5.8: SolidWorks® dimensional drawing of the 3-bar tensegrity prism with cables approximated by elastic springs and the three bottom nodes rigidly attached to the base.....	154
Figure 5.9: Picture of the spring fabricated to approximate the linear cable of the initial 3-bar tensegrity prism	154
Figure 5.10: The variation of forces in the six springs as a linear actuator is driven (a forced oscillatory motion) through a distance of 13 cm	156
Figure 5.11: The degree of stability of the initial 3-bar tensegrity prism (measured by the natural log of the norm of the nodal residual forces, $\ \mathbb{A} \cdot \mathbb{q}\ _2$) as its height is varied by increasing the lengths of the bars equally from 45 cm to 75 cm.....	157
Figure 5.12: Examples of three regular 3-bar minimal tensegrity prisms (with $r_t = r_b$, $l_1 = l_2 = l_3 = l_4 = l_5 = l_6 = 40.8750$ cm, $q_1 = q_2 = q_3 = q_4 = q_5 = q_6 = 2.5745$ N/cm, $q_7 = q_8 = q_9 = 4.4591$ N/cm, and $q_{10} = q_{11} = q_{12} = -4.4591$ N/cm in the three structures).....	159
Figure 5.13: The 3-bar tensegrity prism with electromechanical or active material based actuator embedded in-line with the tensile structural members	161
Figure 5.14: (a) and (b) are tensile structural members with electromechanical actuator positioned in-line at the middle and at the end of cable, respectively	161
Figure 5.15: Picture of the short spring fabricated to form part of the vertical tensile structural member	164
Figure 5.16: Two structural members with each member made up of two nodes	167

Figure 5.17: An illustration of the shortest distance between any two bars of the initial 3-bar tensegrity prism.....	169
Figure 5.18: An illustration of a structural member that makes an angle of θ with the plane containing nodal points P_1 , P_2 and P_3	172
Figure 5.19 (a): (i) and (ii) are the plane containing the three top nodes and the translation of the top triangle in the x - y plane, respectively.	173
Figure 5.19 (b): Rotation of the top triangle about the x and y axes.....	174
Figure 5.20: The translation of the initial 3-bar tensegrity prism (Before translation: cable = blue, bar = black; after translation: cable = red, bar = brown)	177
Figure 5.21: (a) Rotation of the top-triangle of the initial 3-bar tensegrity prism about the z -axis; (b), (c) and (d) are the variation of the norm of the nodal residual forces as rotation of the top triangle is carried-out about the x , y and z axes, respectively.	179
Figure 5.22: The translation and rotation of the initial 3-bar tensegrity prism (Before translation: cable = blue, bar = black; after translation: cable = red, bar = brown)	180
Figure 5.23: A sectional-view of a flexible (morphing) wing turbine blade loaded with tensegrity prisms	183
Figure 6.1: A setup for a computer control system of a tensegrity structure showing the relation among the various constituent components.....	186
Figure 6.2: (a) The PJ board with a 14×1 straight 0.1” male header strip and two 2-pin 3.5 mm terminal blocks; (b) The PJ board with the header strip and terminals soldered unto the board.....	188
Figure 6.3: A labelled top-view picture of the PJ board.....	189
Figure 6.4: A configuration of a potentiometer used as a sensor	190
Figure 6.5: The wiring of the PJ board.....	191
Figure 6.6: The PJ board configuration utility dialog box.	193
Figure 6.7: The workflow for executing serial port communication in MATLAB.	194
Figure 6.8: The workflow involving the implementation of the ‘stop motor’ and the ‘set target-position’ commands.....	197
Figure 6.9: The workflow involving the implementation of the ‘read feedback sensor’ and ‘send me feedback reading’ commands	199
Figure 6.10: The structure of the implementation of PID control algorithm of the PJ board.....	200
Figure 6.11: Flow chart for the determination of the PID controller parameters for the PJ board	204
Figure 6.12: System responses at the beginning and at the end of the iteration process	206
Figure 6.13: Block diagram of the control system for each actuator.....	207
Figure 6.14: A general block diagram for the control of the tensegrity structure that uses the proposed multistable design approach	208
Figure 6.15: Control strategy for the monostable 3-bar tensegrity prism involving multiple SISO control loops (the bottom nodes are rigidly attached to the base)	210

Figure 6.16: Control strategy for the multistable 3-bar tensegrity prism involving multiple SISO control loops (the bottom nodes are rigidly attached to the base)	211
Figure 6.17: Pictures of the set-up for the calibration of the 6 electromechanical actuators	212
Figure 6.18: Pictures of the final structure after assemblage of all the constituent components	213
Figure 6.19 (a): The plots of the stroke lengths versus time as the multistage 3-bar tensegrity structural system changes its shapes through tensegrity structures 5.20 (a), (b), (c) and (d).215	
Figure 6.19 (b): The plots of the stroke lengths versus time as the multistage 3-bar tensegrity structural system changes its shapes through tensegrity structures 5.22 (a), (b) and (c).	216
Figures 6.20 (a): A graphical user interface developed using MATLAB graphical user interface development environment (GUIDE) for deployment of the 3-bar tensegrity prism.....	217
Figures 6.20 (b): A graphical user interface developed using MATLAB graphical user interface development environment (GUIDE) for the six-DOF position control system of the 3-bar tensegrity prism	217
Figure 6.21: A standard, a monostable and a multistable 3-bar tensegrity structures	219
Figure 6.22: Dynamic response plots: The plots of nodal displacements (cm) Vs time (sec) of the structures of Figure 6.21 (a), (b) and (c).....	221
Figure 6.23: Frequency response plots of the structures of Figure 6.21 (a), (b) and (c).....	222
Figure 6.24: Dynamic response plots: The plots of nodal displacements (cm) Vs time (sec) of the structures of Figure 5.20 (a), (b), (c) and (d).....	223
Figure 7.1: Assumed structural system for controller design	227
Figure 7.2: (a), (b) and (c) are the plots of the open- and closed-loop poles of the structural systems of Figure 6.21 (a), (b) and (c), respectively, in the complex plane for the output matrix $C = B^T$ ('o' – open-loop poles; 'x' – closed-loop poles).	236
Figure 7.3 (a): (a) and (b) are the plots of the dynamic responses (nodal velocities [cm^2/s] Vs time [sec]) and the control efforts (actuator forces [N] Vs time [sec]) at Node 6 in the structural system of Figure 6.21 (a), respectively, for the output matrix $C = B^T$	237
Figure 7.3 (b): (c) and (d) are the plots of the dynamic responses (nodal velocities [cm^2/s] Vs time [sec]) and the control efforts (actuator forces [N] Vs time [sec]) at Node 5 in the structural system of Figure 6.21 (b), respectively, for the output matrix $C = B^T$	238
Figure 7.3 (c): (e) and (f) are the dynamic responses (nodal velocities [cm^2/s] Vs time [sec]) and the control efforts (actuator forces [N] Vs time [sec]) at Node 5 in the structural system of Figure 6.21 (c), respectively, for the output matrix $C = B^T$	239
Figure 7.4: (a), (b) and (c) are the plots of the open- and closed-loop poles of the structural systems of Figure 6.21 (a), (b) and (c), respectively, in the complex plane for the output matrix $C = B^T W_c^{-1}$ ('o' – open-loop poles; 'x' – closed-loop poles).....	241
Figure 7.5 (a): (a) and (b) are the dynamic responses (nodal velocities cm^2/s] Vs time [sec]) and the control efforts (actuator forces [N] Vs time [sec]) at Node 6 in the structural system of Figure 6.21 (a), respectively, for the output matrix $C = B^T W_c^{-1}$	242
Figure 7.5 (b): (c) and (d) are the dynamic responses (nodal velocities [cm^2/s] Vs time [sec]) and the control efforts (actuator forces [N] Vs time [sec]) at Node 5 in the structural system of Figure 6.21 (b), respectively, for the output matrix $C = B^T W_c^{-1}$	243

Figure 7.5 (c): (e) and (f) are the dynamic responses (nodal velocities [cm^2/s] Vs time [sec]) and the control efforts (actuator forces [N] Vs time [sec]) at Node 4 in the structural system of Figure 6.21 (c), respectively, for the output matrix $C = B^T W_c^{-1}$.	244
Figure 7.6: Simulation results for the cases of $P \neq I$ and $P = I$ computed with (7.28 – 7.29) and (7.30), respectively, for the tensegrity structures of Figure 6.21(a–c).	248
Figure 7.7: Simulation results for the (non-collocated) tensegrity structural system of Figure 6.21(c) using output-feedback controllers designed with pole-placement and optimization approaches.	251
Figure 7.7 (continued): Simulation results for the (non-collocated) tensegrity structural system of Figure 6.21(c) using output-feedback controllers designed with pole-placement and optimization approaches.	252
Figure 7.8: Simulation results for the robust tracking control for the (non-collocated) tensegrity structural system of Figure 6.21(c) using linear observer designed with pole-placement and optimization approaches.	253
Figure 7.8 (continued): Simulation results for the robust tracking control for the (non-collocated) tensegrity structural system of Figure 6.21(c) using linear observer designed with pole-placement and optimization approaches.	254
Figure 7.9: A 2-stage 3-order active tensegrity structure	258
Figure A.1: (a) and (b) are the time-invariant deterministic and stochastic linear optimal regulators, respectively.	289
Figure A.2: Block diagram of a time-invariant linear observer.	292
Figure A.3: A structure of a linear output-feedback control system	293
Figure A.4: A structure of the optimal linear feedback control system for a system with state excitation and measurement noises	294
Figure A.5: A block diagram of a linear tracking control system	296
Figure A.6: A block diagram of an Integral Control System	298
Figure A.7: A structure of the optimal linear tracking system with integral action	300

LIST OF TABLES

Table 2.1: Types of structural assemblies.....	22
Table 2.2: An illustration on obtaining vectors of nodal coordinates from the nullspaces of the force density matrix	26
Table 2.3: Descriptions of two methods for obtaining tensegrity structures: The Nullspaces approach .	28
Table 2.4: The Interior Point Algorithm for Constrained Optimization	31
Table 2.5: Relationship between the vector of tension coefficients and kinematic form-finding method.....	41
Table 2.6: Descriptions of two methods for obtaining tensegrity structures using constrained optimization approach	43
Table 2.7: Parameters of tensegrity structures of Figure 2.10 obtained using form-finding methods A, B and C	48
Table 2.8: Length and tension coefficient associated with each member of the class 2 tensegrity structure	50
Table 2.9: The constrained optimization form-finding algorithm	53
Table 3.1: Length and tension coefficient of each of the structural members of the tensegrity structure shown in Figure 3.1	70
Table 3.2: Tension coefficients, material and physical properties of the structural members of the tensegrity structure shown in Figure 3.1.....	76
Table 3.3: Length and tension coefficient of each of the structural members of the tensegrity structure shown in figures 3.10 and 3.11	84
Table 3.4: Nodal coordinates of the structural systems of figures 3.10 and 3.11	85
Table 3.5: Nodal coordinates, length and tension coefficient of each of the structural members of the tensegrity structure shown in Figures 3.19	95
Table 4.1: The additive and relative model reduction errors (ϵ_{∞} and $\epsilon_{r\infty}$, respectively) for the tensegrity structural systems of Figures 4.3 – 4.7.....	131
Table 4.2: Nodal coordinates of the tensegrity structure of Figure 4.4 and the tension coefficient of each of its members.....	131
Table 5.1: Structural parameters of the initial 3-bar tensegrity prism with the following constraints: $l_1 = l_2 = l_3 = l_4 = l_5 = l_6$, $l_7 = l_8 = l_9$ and $l_{10} = l_{11} = l_{12}$	146
Table 5.2: Technical Specification of the 12” stroke linear actuator with feedback	148
Table 5.3: The extended length l_e for the electromechanical actuators of Figure 5.12 (a-c).....	162

Table 5.4: A picture and technical details of the 2” stroke linear actuator with feedback (LD series actuator) manufactured by Concentric International	164
Table 6.1: Technical Specification of the PJ board	188
Table 7.1: Poles of the open-loop and closed-loop structural systems for $C = B^T$	234
Table 7.2: Poles of the open-loop and closed-loop structural systems for $C = B^T W_c^{-1}$	240
Table 7.3: Open-loop and closed-loop poles of the reduced-model of the structural system (non-collocated case) of Figure 6.21(c)	249

LIST OF MAIN SYMBOLS AND ABBREVIATIONS

Symbols

A	Equilibrium matrix, p. 18
A	System matrix of the state-space representation, p. 73
A	Equilibrium matrix, p. 20
A, B, C, D	Linear time-invariant system, p. 101
A_i	Cross-sectional area of the i^{th} member
B	Input matrix of the state-space representation, p. 73
B	Matrix of nodal coordinate differences; $B = [u \ v \ w]$, p. 56
\mathbb{B}	Transpose of the equilibrium matrix, $\mathbb{B} = A^T$
C	Connectivity matrix, p. 19
C	Damping matrix, p. 63
C	Output matrix of the state-space representation, p. 73
D	Force density matrix, p. 21
D	Feed-forward matrix of the state-space representation, p. 73
D	Mean spring diameter, p. 153
\mathbb{D}	Matrix of tensor product of I_3 (3-by-3 identity matrix) and D
E_i	Young's modulus of the i^{th} member
F	Force in a tensile member
G	Transfer matrix of the linear time-invariant system, p. 105
G	Shear modulus, p. 153
G_{ij}	Transfer function from the j^{th} input to the i^{th} output
H	Transformation matrix determined by the choice of the controlled variable z of a control system
K	Stiffness matrix, p. 58
K	Constant feedback gain matrix, p. 226
\underline{K}	Optimal value of the constant gain of the integral control system

K_e	Elastic stiffness matrix
K_e^i	Elastic stiffness matrix of the i^{th} member in the global coordinate system
K_f	Scaling factor for converting feedback voltage reading between 0 to 5 V to 0 – 4095 digital scale
K_i	Stiffness matrix of the i^{th} member in the global coordinate system
K^o	Optimal regulator gain
K_p, K_i, K_d	Parameters of the PID controller
K_q	Pre-stress (or geometric) stiffness matrix
K_q^i	Pre-stress stiffness matrix of the i^{th} member in the global coordinate system
L	Diagonal matrix of vector l , p. 20
L	Length of a tensile member, p. 160
L	Constant feedback gain matrix, p. 231
L	Estimator gain, p. 249
M	Mass matrix
M_a	Vector obtained by taking the norm of each row of T_a
M_s	Vector obtained by taking the norm of each row of T_s
N	Matrix of nodal coordinates; $N = [x \ y \ z]^T$
P	Vector of time-varying nodal forces of a structural system, p. 63
P	Parameter of the algebraic Riccati equation of the closed-loop system, p. 246
P_c	Controllability matrix
P_e	Vector of loads on elastic nodes
P_o	Observability matrix
P_r	Vector of loads on inelastic (unrestricted) nodes
P_x, P_y, P_z	Vectors of x, y and z components of nodal forces, respectively
Q	Diagonal matrix of vector q , p. 20
Q	Parameter of the algebraic Riccati equation of the observer, p. 292
R_1	Weighting matrix representing limit on state variables
R_2	Weighting matrix representing limit on the control effort
S	Diagonal matrix of singular values of \mathfrak{X} in descending order of magnitude
T	Transformation matrix of the Guyan (static) model reduction, p. 68
T	State transformation matrix, p. 103
T_a	Placement matrix of actuators
T_a'	Vector obtained by taking the norm of each column of T_a

T_s	Placement matrix of sensors
T_s'	Vector obtained by taking the norm of each column of T_s
U	Left-orthonormal matrix of the singular value decomposition of D
U	Left-orthonormal matrix of the singular value decomposition of A
\bar{U}	Right-hand side partition of U
U, V, W	Diagonal matrices of vectors u, v and w , respectively
V	Intensity of the white noise
\mathcal{V}	Diagonal matrix of singular values of D in descending order of magnitude
\mathbb{V}	Diagonal matrix of singular values of A in descending order of magnitude
W	Weight of an ideal extensible bar with uniform cross-sectional area
\mathcal{W}	Right-orthonormal matrix of the singular value decomposition of D
\mathbb{W}	Right-orthonormal matrix of the singular value decomposition of A
$\bar{\mathbb{W}}$	Right-hand side partition of \mathbb{W}
W_c	Controllability grammian
W_o	Observability grammian
b	Number of structural members
b_i	Vector of coordinate differences which uniquely defines the i^{th} member connecting nodes h and j ; $b_i = n_h - n_j$.
c_q	Scaling factor for the tension coefficients
c_x	Scaling factor for the nodal coordinates
d	Wire diameter of a spring, p. 153
d	Shortest distance between the two lines (or any two bars of the initial 3-bar tensegrity prism), p. 168
d	Vector of nodal displacements
e	Error or error due to state reconstruction
e	Vector of member elongation coefficients
f	Vector of member forces
k	Number of kinematic constraints, p. 17
k	Spring constant, p. 153
k_e^i	Component of the elastic stiffness matrix due to the i^{th} member in the local coordinate system
k_q^i	Component of the stiffness matrix of the i^{th} member due to pre-stress in the local coordinate system
k^i	Stiffness matrix of the i^{th} member in the local coordinate system

k_{mA}	Scaling factor for converting feedback current reading into 0 – 255 digital scale
l	Vector of member lengths
l_{ao}	Retracted length of an electromechanical actuator inline with a tensile member
l_e	Extended length of an electromechanical actuator
l_o	Original length of a spring
lb	Lower bound on the tension coefficients
m	Number of independent inextensible mechanisms
m_i	Mass matrix of the i^{th} member in the local coordinates system
\acute{m}_i	Mass matrix of the i^{th} member in the global coordinates system
n	Number of nodes, p. 17
n	Number of state variables, p. 73
n	Number of active coils of a spring, p. 153
n	Normal vector perpendicular to a plane, p. 171
n_i	Nodal coordinates of the i^{th} node; $n_i = [x_i \ y_i \ z_i]^T$
p	Vector of nodal forces, p. 18
\mathbb{P}	Vector of nodal forces, p. 20
\mathbf{p}	Vector of nodal forces, p. 56
p	Number of bars of a tensegrity prism, p. 141
p_{ji}	Nodal force at node j due the strain of the i^{th} member
\check{p}_i	Vector representing forces at nodes of the i^{th} member due to its strain
p_o	Vector of desired closed-loop poles
q	Vector of tension coefficients
\mathbb{Q}	Vector of tension coefficients
q_b	Tension coefficient of a cable of the bottom polygon of a tensegrity prism
q_t	Tension coefficient of a cable of the top polygon of a tensegrity prism
q_{vb}	Tension coefficient of a vertical bar of a tensegrity prism
q_{vc}	Tension coefficient of a vertical cable of a tensegrity prism
r	Rank of the equilibrium matrix, p. 22
r	Circumradii of a polygon of a tensegrity prism, p. 141
r	Reference input of a control system, p. 226
r_b	Circumradii of the bottom polygon of a tensegrity prism
r_j	Radius of the j^{th} bar considered to be a circular cylinder
r_t	Circumradii of the top polygon of a tensegrity prism

s	Number of independent states of self-stress
u, v, w	Vectors of coordinate differences of connected nodes for the x , y and z axes, respectively, p. 20
u	Vector of input (control) variables, p. 73
u^o	Optimal control input
ub	Upper bound on the tension coefficients
w	White noise
w_1	State excitation (disturbance) noise
w_2	Measurement noise
x	Vector of state variables
\hat{x}	Vector of reconstructed state variables
x_b	Vector of state variables of the balanced linear time-invariant system
x, y, z	Vectors of Cartesian coordinates in the direction of the x , y and z axes, respectively
xyz	Matrix of nodal coordinates; $xyz = [x \ y \ z]$
\overline{xyz}	Vector of nodal coordinates; $\overline{xyz} = [x^T \ y^T \ z^T]^T$
y	Vector of output variables
z	Vector of controlled output variables of a control system
κ	Singular values of the closed-loop matrix
H	Diagonal matrix of Hankel singular values of the linear time-invariant system arranged in descending order of magnitudes on the diagonal
Σ	Diagonal matrix of vector p_o
Φ	Vector of nodal displacements
$\bar{\Phi}$	Modal matrix
$\underline{\Phi}$	Mode shape or amplitudes of the displacement Φ ; $\Phi = \underline{\Phi} e^{i\omega t}$
Φ_e	Vector of elastic nodal degrees of freedom
Φ_r	Vector of inelastic (unrestricted) nodal degrees of freedom
Ω	Diagonal matrix of natural frequencies
π	Potential energy of a structural assembly
ε_i	Strain of the i^{th} member
η	Vector of generalized coordinates (modal displacement)
$\dot{\eta}$	Vector of modal velocities
$\ddot{\eta}$	Vector of modal accelerations
η_i	i^{th} Hankel singular value of the linear time-invariant system
λ_i	i^{th} eigenvalue of the product of the observability and controllability grammians

ρ_i	Mass density of the i^{th} member
ζ_{ij}	weight assigned to the j^{th} actuator/sensor of the i^{th} state
σ_{max}	Largest singular value at a given frequency
ϵ_2	Additive error due to model reduction using the H_2 norm
ϵ_∞	Additive Error due to model reduction using the H_∞ norm
$\epsilon_{r\infty}$	Relative Error due to model reduction using the H_∞ norm
\emptyset	Characteristic angle of a polygon
α	Twist angle of a tensegrity prism
\mathcal{E}	Left-orthonormal matrix of the singular value decomposition of \mathfrak{X}
\mathfrak{Z}	Right-orthonormal matrix of the singular value decomposition of \mathfrak{X}
γ	Gain of a linear time-invariant system, p. 105
γ	Tension coefficient scaling factor for a tensegrity prism, p. 141
δ	Impulse function
θ	Angle between a member and a plane
λ	Transformation matrix
ζ	Damping constant
ξ	Angle between the normal vector and the vector of coordinate differences which uniquely defines a member
σ	Ratio of the circumradius of the top polygon to that of the bottom polygon of a tensegrity prism
σ_{a_i}	i^{th} element of T_a' or M_a
σ_{ij}^a	Actuator placement index of the i^{th} state and j^{th} actuator location
σ_{ij}^s	Sensor placement index of the i^{th} state and j^{th} sensor location
σ_{s_i}	i^{th} element of T_s' or M_s
v	Number of candidate actuators
ω	Angular frequency of vibration, p. 64
ω	Number of candidate sensors, p. 113
$\phi(x)$	Variation (or function) of axial displacement x
\otimes	Kronecker product
\times	Cross (vector) product operator

Functions

$(\cdot)^*$	Complex conjugate transpose of a matrix
-------------	---

$\ \cdot\ _2$	2-norm of a linear time-invariant system
$\ \cdot\ _\infty$	Infinity-norm of a linear time-invariant system
$\ \cdot\ _h$	Hankel norm of a linear time-invariant system
$\ \mathbb{A} \cdot \mathbb{q}\ _2$	Norm of the vector of nodal residual forces
$\sup(\cdot)$	Supremum operation (the smallest upper bound of a set)
$E[\cdot]$	Expected value operation
$diag(\cdot)$	Diagonalization of a vector to form a matrix (such that the elements of the vector are the diagonal elements of the matrix with all other elements zero) or (conversely) formation of a vector from the diagonal elements of a matrix.
$tr(\cdot)$	Trace of a matrix
$vec(\cdot)$	Vector valued function of a matrix such that $vec(X_{p \times q}) = [x_1^T \ x_2^T \ \dots \ x_q^T]^T$ where $x_i \in \mathbb{R}^{p \times 1}$ is the i^{th} column vector of X

Abbreviations

BFGS	Broydon-Fletcher-Goldfarb-Shanno
DOF	Degree-of-freedom
FEM	Finite Element Method
GUIDE	Graphical User Interface Development Environment
ISE	Integral of Squared Error
LED	Light Emitting Diode
LQG	Linear system – Quadratic cost – Gaussian noise
MPC	Model Predictive Control
PID	Proportional Integral Derivative
PJ board	Pololu Jrk 12v12 USB motor controller with feedback
PWM	Pulse Width Modulation
SISO	Single-Input Single-Output
USB	Universal Serial Bus
tol	Tolerance value

Chapter 1

INTRODUCTION

1.1 Definition of Tensegrity Structures

Tensegrity structures date back to the late 1940s when Buckminster Fuller used the term *tensegrity* as a contracted form of the two words *tension* and *integrity* to describe Kenneth Snelson's structure [1]. Despite their long presence, the structures have only received a surge in interest from the 1990s. From an engineering perspective, this class of structures are ideal candidates for deployable structures [2], [3] as they are capable of undergoing large displacements and can be of very lightweight. Moreover, these pre-stressed structures are obtained by the optimal arrangement of material components, each of which must either be in tension or compression.

Furthermore, tensegrity structures, similar to other tension structures, have aesthetic value which, although impossible to measure or quantify, emerges naturally in the optimization process. In a research carried-out at the University of Stuttgart's Institute of Lightweight Structures between 1964 and 1991 that focused on structural forms of lightweight structures, it was found that, although the objective was not to create structures with beauty, aesthetic value is inherently rooted in the optimal structural shapes of lightweight structures; that is, shapes that would satisfy functional, durability and strength requirements at minimum cost [4], [5].

Tensegrity structures consist of two components, or structural members as they are often called, as shown in Figure 1.1, namely, the tensile and the compressive structural members, often called as cables and bars, respectively; besides, strings and struts are also common terms for these two components in the literature, respectively. It should be noted that in Figure 1.1 no bar is allowed to touch any other bar at the connection points, or *nodes*, while the cables form a continuous network and these

cables are connected (that is, they make contact) at every node. Thus, traditionally, tensegrity structures are described as ‘*islands of compression inside an ocean of tension*’ [1] or as ‘*continuous tension, discontinuous compression structures*’ [6]. They have also been defined as structures which are ‘*established when a set of discontinuous compression components interacts with a set of continuous tensile components to define a stable volume in space*’ [7], and ‘*as system in a stable self-equilibrated state comprising a discontinuous set of compressed components inside a continuum of tensioned components*’ [8].

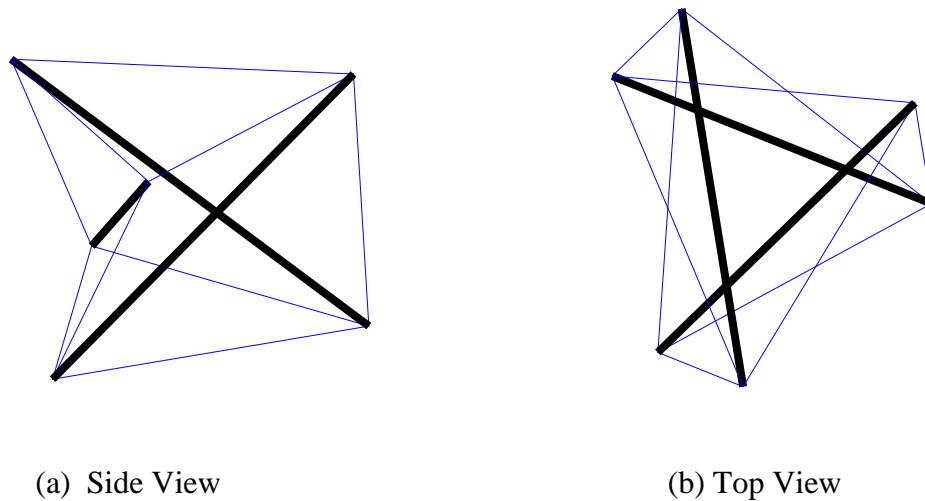


Figure 1.1: A simple tensegrity structure with 3 bars (thick black lines) and 9 cables (thin blue lines).

In order to incorporate structures, excluded in the traditional definitions, that consist of simple tensegrity modules that are connected together to form structures wherein bars are connected, the extended definition, given in [9], describes tensegrity structures as systems ‘*whose rigidity is the result of a state of self-stress equilibrium between cables under tension and compression elements and independent of all fields of action*’.

In addition, since the bars of a tensegrity structure can be considered as inelastic rigid bodies to a good approximation, the structural system is only stabilized by the presence of tensile forces in the cables alone in the absence of external forces. For this reason, in [2], a tensegrity structure is described as a system which is composed of a given set of cables connected to a *configuration* of rigid bodies and stabilized by

internal forces of the cables in the absence of external forces. In other words, a configuration of rigid bodies is a tensegrity system if it can be, or it is, stabilized by a set of cable connectivity in the absence of external forces. Here, stability (*integrity*) of the system denotes an equilibrium state or configuration in which the system returns to when disturbed by an arbitrary small perturbation.

Also, since the new definition now excludes the necessity for bars to be discontinuous or for cables to form a continuous network, different classes of tensegrity structures are distinguished by counting the number of bars present at the nodes [10]. For example, if only one bar is present at every node, the structure is classified as a class 1 tensegrity structure; if at most two bars are present in at least one node, a class 2, and so on. To be precise, '*a tensegrity configuration that has no contacts between its rigid bodies is a class 1 tensegrity system, and a tensegrity system with as many as k rigid bodies in contact is a class k tensegrity system*' [2]. Figure 1.2 shows a simple example of a tensegrity system constructed with 3 cables and 3 bars.

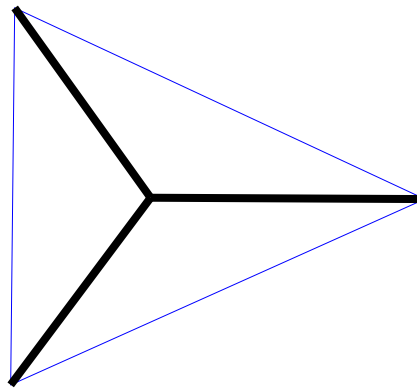


Figure 1.2: A simple example of class 3 tensegrity structures.

As a result of the wide range of definitions of tensegrity structures, it is difficult to make a distinction between tensegrity structures and other pre-stressed spatial structural systems. For instance, tensegrity structures have been classified as a special type of truss structures [11], as a type of cabled structures [4], and as internally pre-stressed free-standing pin-jointed cable-strut systems [12], [13]. However, it is explicitly understood that tensegrity structures (or systems) exclude all structures (or configuration of rigid bodies) which are not stabilized (or cannot be stabilized) with the

pre-stressed cables alone in the absence of external forces. An example of such a structure that is not a tensegrity structure is shown in Figure 1.3; it will be observed that there is no way this structure that consists of two bars and one cable can be stabilized, such that the cable is in tension while the bars remain in compression and with none of these structural members touching each other except at the three nodes (as shown in the figure), without the influence of an external force or forces.

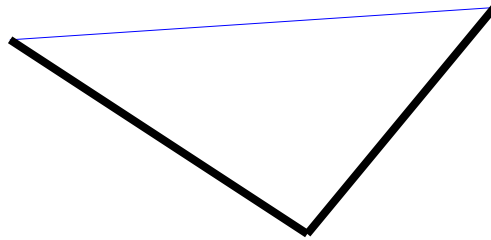
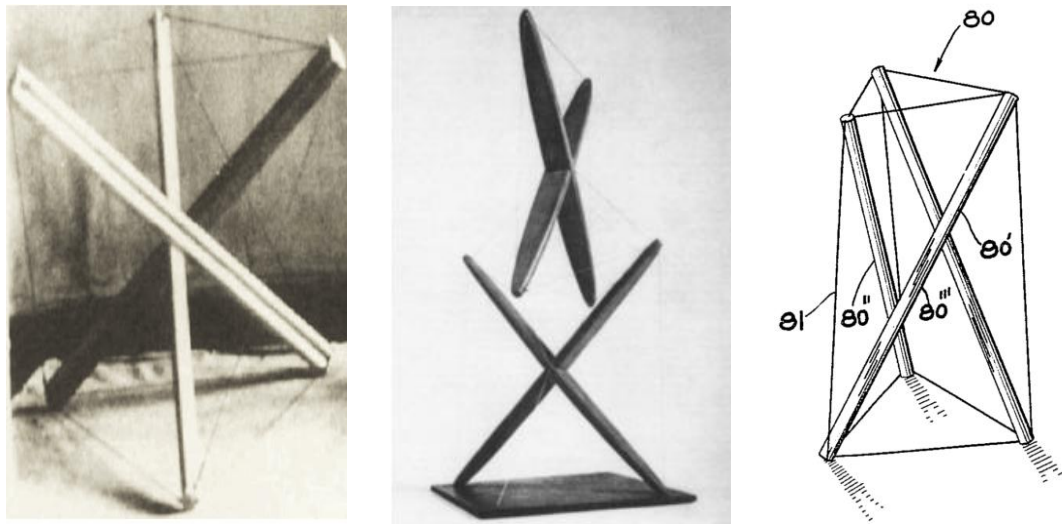


Figure 1.3: A simple structural system that cannot be stabilized in the absence of external forces.

1.2 Origin of Tensegrity Structures

There has been a controversy on the origin of tensegrity systems as Kenneth Snelson, Richard Buckminster Fuller and David Georges Emmerich have all claimed originality of the concept of tensegrity and have all applied for patents in this regards [6], [14], [15]. It has also been claimed that Karl Ioganson has presented the same idea in his study of balance between 1921 and 1922 [16]. With the exception of Ioganson, all the other three have described exactly the tensegrity structures in their patents and a detailed account about the controversy on the origin of tensegrity structures can be found in [1], [9], [10], [16], for example. It can be deduced from these references that, indisputably, Fuller coined and popularized the word tensegrity, a short form of ‘tension integrity’, and Snelson was the first to build a tensegrity structure known as the ‘X-Piece’ that inspired Fuller. Furthermore, from Ioganson’s structure, which although has a tensegrity impression, it cannot be concluded that Ioganson has envisioned that he would obtain a tensegrity structure as it is being defined today. In other words, on seeing Ioganson’s structure, as Snelson puts it, ‘*no one on Earth would have been able to discern the nature of IX without prior acquaintance with tensegrity primary*’ [17]; IX denotes the number 9 – the minimum number of cables that can be used to construct a

three-dimensional class 1 tensegrity structure with three bars, popularly known as a *simplex* tensegrity structure. Furthermore, Emmerich discovered tensegrity, perhaps independently, but he is known to have seen the Ioganson's sculpture [8] and cited it as a precedent to his work [18]. Figure 1.4 shows a piece of construction by Ioganson around 1920-1921, Snelson's X-piece and the simplex tensegrity structure obtained from the original Snelson's patent of 1965.



(a) Ioganson's Sculpture (b) Snelson's X-piece, 1948 (c) Snelson's Patent, 1965

Figure 1.4: Ioganson's Sculpture [16], Snelson's X-piece [16] and Snelson's simplex [6]

1.3 Research and Application of Tensegrity Structures and Concept

Sculptors, artists and architects have long been captivated by the beauty of tensegrity structures ever since they first started to be built. In the arts, these structures are of interest because of their aesthetic value [9]. They have been used to show how geometric arrangements of rods and strings give structures of complex configuration and striking beauty. Also, direct applications of tensegrity structures in civil engineering and architecture have been significant in the last few decades. Tensegrity structures are used in cable domes [19–22], bridges [23], [24] and towers [25]. They can also be used for deployable structures such as retractable roofs, tents and shelters [2], [26]. In these designs, their use has been primarily due to their lightweight and aesthetic property [3].

At conceptual level, tensegrity structures have been used in different unrelated areas; for example, in the sciences, it has been used to explain the structure of the spider

fibre [27]. In man and many types of animals, bones (rigid bodies) and tendons (elastic bodies) are connected together and are moved from one equilibrium configuration to another by tensile forces in the tendons alone. Thus, in osteology, different configurations are classified as different classes of tensegrity structures [2].

Moreover, it has been argued that tensegrity structures can be used to explain how cells obtain their shapes and movements; in explaining cytoskeletal mechanics as well as the sensing and response of cells to mechanical forces, tensegrity also play an important role [28]. Ingber [28–30], for instance, has made extensive publication on how tensegrity structures can be used to model a cell at molecular level and how this structural basis can be organized hierarchically from molecule to organism to model living systems. A simple tensegrity module – the icosahedrons module – has also been used to model biological organisms, like viruses, as well as systems and subsystems of other biological systems [31–33]. The role of tensegrity structures as a model for cytoskeletal organization to aid the understanding of the mechanical behaviour of living cells has also been investigated for many years; see, for example, [34–38]. In addition, the significance of tensegrity concepts for osteopathic medicine has also been studied [39].

Furthermore, tensegrity structures have also been reported as being capable of forming building blocks for modelling DNA for studying cellular mechanotransduction, molecular forces and other fundamental biological processes [33], [38]. In chemistry, the behaviour of tensegrity structures have been used to describe the overall properties of sodium caseinate aggregates and casein micelles structures [40]. They have also been used to describe the geometry of gas molecules [41].

Other areas where tensegrity structures and concept have been used include furniture manufacturing [42], [43], robots [44], [45], electrical transducers [46], underwater morphing wing applications [47] and flight simulators [48].

Mathematicians and engineers have tried to analyse tensegrity structures to understand and unveil the meaning of this very interesting structural concept from a mathematical viewpoint. Thus, mathematical answers to the questions such as ‘what are tensegrity structures?’ and ‘why they are stable?’ have been proposed. Using group and representation theories, mathematicians, such R. Connelly *et al.* [27], [49], [50], have tried to find answers to these questions and have used powerful graphical and

computational capabilities of modern computers to find a proper three-dimensional generalization for tensegrity structures. The role of tensegrity structural concept in rigidity [51–53], geometry [54], energy [55], graph theory [56], [57] are also increasing.

As a follow-up to the interesting role of tensegrity structures in rigidity, geometry, energy and graph theories developed by mathematicians, the mathematical analysis of these structures, mainly due to their pre-stressed nature, has also been thoroughly investigated by engineers. Maxwell's rule for the study of the static and kinematic determinacy, or otherwise, of pin-jointed frameworks has been extended to tensegrity structures [58]. Equilibrium matrix analyses [59], static analysis [60], first order infinitesimal mechanisms [61–63], properties revealed by singular value decomposition of equilibrium matrix [64–66], and stiffness matrix analyses [67], [68] of pin-jointed frameworks, in general, and of tensegrity structures, in particular, have all been presented.

The largest mathematical and engineering literatures on tensegrity structures are related to form-finding of these structures [2]. It normally involves using information on the mathematical properties of tensegrity structures to search and/or define a configuration that satisfies the conditions of static equilibrium for the pre-stressed structure. Examples of form-finding methods include the analytical method [69], algebraic form-finding methods [70], [71] [72], the finite element method [73], the energy method [54] and the dynamic relaxation method [74]. Computational techniques that have been used in association with the different form-finding methods include the genetic algorithm [75], [76], neural networks [77] and the sequential quadratic programming methods [78], for instance.

An extension of mathematical research into the equilibrium properties (statics) of tensegrity structures is the study of their dynamic properties. Modal analyses in which critical values of resonance modes and damping parameters [79] and, vibration and damping characteristics [80–82], are to be determined as well as the linearised equation of motion [83] for tensegrity structure have been presented. A method for systematic and efficient formulation of equation of motion represented in simple form for constrained and unconstrained tensegrity systems is given in [2]. Research in tensegrity dynamics is still an emerging field. A review on the current research and open problems on the dynamics of tensegrity structures is presented in [84].

Quite recently, examples of actively controlled tensegrity structure have appeared in the literature. These include control of three-stage tensegrity structure [85], tensegrity mobile robot [44], [45], and tensegrity flight simulator [48], among others. An illustrative example on the way structural design and controller design can be integrated when designing a tensegrity system can be found in [86]. Other issues, such as open-loop control, input/output selection, and optimal dynamic performance, related to controlled tensegrity structures are presented in [86–90].

1.4 Project Motivation and Description

Structures containing sensors and actuators and that have the abilities to modify themselves due to their changing environments are referred to as active structures [91]. The development of this field stems from the recent advancement in the fields of structural engineering and control engineering. Active control of structural systems was originally proposed in the early 1970's as a concept and means to counteract extreme conditions such as earthquakes in buildings and undesirable vibrations in space-structure [92]. Thus, it provides a mechanism of enhancing the performance (dynamic behaviour) of complex structural systems in changing and uncertain environments. Over the past decade, research in active structural control has increased to meet the requirements of new challenges faced in extreme environments where many structural systems must function. This has also been due to the advancement in the development of viable sensors, actuators and microprocessor technologies that can be used to perform a wide range of engineering tasks [91].

For structural systems such as large buildings and bridges, most active control systems will not be reliable enough over their service lives without expensive maintenance in place which may be difficult to justify economically. Thus, for the structural systems that involve catastrophic collapse, loss of life, or other safety criteria, passive control mechanisms – for instance, through the use of tuned-mass dampers which are less effective in dealing with inelastic modes or in reducing vibrations that are due to high frequency modes [93] – are used as the common standard. However, for structures that are not governed by these safety criteria, active control is most practical [92]. An important feature of active structures is their possession of computational control systems that support certain functions such as control objectives that arise from

multiple and/or changing performance goals, adaptation of structural geometry to improve performance by sensing the changes in behaviour and in loading, and autonomous and continuous control of several coupled structural subsystems [91], [92].

Active control structures are capable of interacting with complex environments. Moreover, some researchers have pointed out the necessity to expand the concepts of control theory to embrace the larger concept of system design [94]; this means a system design approach where structural design and control systems design can be integrated (that is, designed simultaneously in a single framework – not as independents or ‘afterthoughts’ – one after the other – approach). A major obstacle against integrated design of active control systems during the design process of structures is, however, the computational cost involved. To create an approach that tackles this unique problem offers a promising and major step in the future of man-made structures. In addition, an integrated structural and control design, in particular, and active control techniques, in general, are most efficient when the appropriate types of structural systems are chosen. Tensegrity structures, not only provide an important platform for exploring advanced computational active control technologies but, have been found, so far, to be the only type of structural system suitable for integrated structural and control design [2].

More so, with tensegrity structures, it is possible for a structural component to simultaneously be a load-carrying member, an actuator, a sensor, a thermal insulator and/or an electric conductor. Thus, proper choice of material for tensegrity structures offers excellent opportunities for the physical integration of structural designs with controller designs. Furthermore, compared to other structures, tensegrity structures are highly suitable alternatives for the design of structural systems with highly complex and variable topological configurations. Structural modification (shape morphing), adaptation and adjustment may be easier for tensegrity structures than for conventional structures [2]. Other attractive features of tensegrity structures from an engineering perspective, such as mass efficiency, modularity, redundancy, scalability, deployability and shape/stiffness flexibility, have been emphasized extensively in the literature; see [2], [10], [24], [26], [70], [95], [96], for example.

Deformation of components of tensegrity structures is only one-dimensional in individual component (since structural members are only axially loaded). As such, modelling can be much easier than it would have been if bending of components is allowed or possible. Therefore, since components have predefined directions, equations

of motion are greatly simplified and relatively accurate dynamic models of tensegrity structures can be obtained. Although no component undergoes bending moment, the whole structure undergoes global bending when subjected to external loads. This feature, in particular, is likely to be the most important scientific feature of tensegrity structures for future applications [2]. The consequence of accurate modelling is that precision control of tensegrity structures is possible. While one would expect that the active control technologies that would be deployed for tensegrity structures will be similar to those in civil and mechanical engineering, their application to tensegrity structures involves solving unique set of problems. Moreover, many of these challenges are interdisciplinary in nature. Finding solutions to these problems will create new possibilities for innovative active control and new application areas.

Therefore, the objectives of this project are as follows:

1. To develop new algorithms for the form-finding of tensegrity structures that will be applicable to small and large tensegrity structures with or without a complex connectivity of structural members.
2. To develop a modelling technique and investigate the static and dynamic properties of tensegrity structures.
3. To investigate the effect of including additional structural members (than strictly necessary) on the dynamics of tensegrity structures and to examine how the resulting changes in their geometric properties can be explored for self-diagnosis and self-repair in the event of structural failure.
4. To outline the procedures for model reduction and optimal placement of actuators and sensors for tensegrity structures.
5. To develop a design strategy that can be adopted for the physical realization of tensegrity structure that can be actively controlled and to offer strategies for preventing and discovering collisions between structural members of tensegrity structures.
6. To develop methods for designing collocated and non-collocated control systems for vibration suppression and precise positioning of tensegrity structural systems.

In general, the thesis can also be viewed as a contribution in the process of meeting the needs of design challenges given that it highlights some of the most

important aspects of system designs that must be considered for the physical realization of tensegrity structures. The contents of this thesis are outlined in the next section.

1.5 Thesis Outline

In this chapter, tensegrity structures and concept have been broadly introduced. Brief accounts on the origin as well as the traditional and more recent definitions of tensegrity structures were given. The chapter also includes areas of research and a summary of direct and conceptual applications of tensegrity structures in the literature. In addition, the chapter addresses the main motivation and the overall goals of this thesis. Specifics of these goals are pointed out in the paragraphs that follow.

The objective of Chapter 2, titled ‘Form-finding of Tensegrity Structures’, is to find shapes for which the structure is pre-stressed and in a state of static equilibrium in the absence of external forces. Thus, the chapter presents a new algorithm for the form-finding of tensegrity structures. The use of computation techniques, which is inevitable for large structures, is adopted in general. As such, the new method is based on the interior point constrained optimisation technique and the efficacy of the method is demonstrated with a number of examples. The chapter concludes with a short review of other form-finding methods.

Chapter 3, titled ‘Modelling, Static and Dynamic Analyses of Tensegrity Structures’, outlines the theory behind modelling, static and dynamic analyses of tensegrity structures. The derivation of the mass and stiffness matrices is described using the FEM. Thereafter, the solution procedure for carrying out pseudo-static analysis of a tensegrity structure is presented. Subsequently, the dynamic equations of motion governing a general tensegrity structure, written in the time domain, are converted into a state-space representation. With this representation, the study of the dynamic responses tensegrity structures is easily carried-out. The effect of including additional structural members (than strictly necessary) on the dynamics of n-stage tensegrity structures is also examined. The chapter concludes by demonstrating the possibility of a tensegrity structure with a highly complex configuration to change its geometric properties – making them suitable as a platform for the design of active structures capable of shape morphing – in the event of structural failure through self-diagnosis and self-repair.

Chapter 4, titled ‘Model Reduction and Optimal Actuator and Sensor Placement’, presents model reduction technique that can be employed for the reduction of models of tensegrity structural systems. The model reduction operation is carried-out to facilitate further analysis and design of control systems in subsequent chapters. Also treated in this chapter is the procedure for the optimal placement of actuators and sensors. The procedure has the potential to minimize the control efforts and determine the credibility of the output feedback signals and, thus, must be considered part of the structural design, dynamic analysis and controller design to achieve best performance. It should be noted that selecting the number and locations of the actuators and sensors first, without taking into account during the selection process the future control problem to be solved, is not the most effective way of dealing with tensegrity related design problems. The applicability of the theory on model reduction and optimal actuator and sensor placement procedures presented in this chapter is demonstrated with several examples.

The design procedure for the physical realization of tensegrity structures proposed in this thesis are covered in two chapters, namely, Chapters 5 and 6. Within the context of these two chapters, an experimental simplex deployed tensegrity structure (a 3-bar multistable tensegrity prism) was designed, assembled and tested. This experimental prototype is available in the Intelligent Systems Laboratory of the Department of Automatic Control and Systems Engineering of the University of Sheffield. Thus, Chapter 5, titled ‘Physical Realization of Tensegrity Structural Systems: Part I Physical Structure Design’, deals with the design of tensegrity structural systems that are capable of changing their shapes significantly. The discussion is focused on practical structural design and optimization issues and brings together many novel concepts. In particular, it introduced a new physical realization approach that makes it possible to combine the control of the cable and bar lengths simultaneously, thereby combining the advantages of both bar control and cable control techniques of tensegrity structural systems together. The chapter also includes the design of the tension and compression structural members and the methods for form-finding and deployment of simple and complex tensegrity structures. A collision avoidance technique that may be employed for tensegrity structures in general is also described. The chapter concludes by suggesting that shape-change capability of wind turbine blades which relies on controlled deformation of the blade’s shape is possible under the action of several tensegrity prisms located inside the blade box.

Chapter 6, titled ‘Physical Realization of Tensegrity Structural Systems: Part II Hardware Architecture and a Decentralized Control Scheme’, presents details of the hardware, hardware configuration, serial communication protocol using the Universal Serial Bus (USB) interface and the implementation of the software and the control system architecture for the 3-bar multistable tensegrity prism designed in Chapter 5. There are three main tasks involved in this project for the realization of a tensegrity structural system: the first task entails the structural optimization and related design issues, and this is covered in Chapter 5. The second task involves the configuration of the hardware and the control architecture, and the third task is associated with the design of application software user interface and the implementation of the control algorithm. These last two tasks are essentially the focus of Chapter 6. Chapter 6 also includes mathematical modelling and structural analyses of the tensegrity structures designed in Chapter 5 using realistic structural parameters. Moreover, the control of a 3-bar multi-stable tensegrity structure is achieved through decentralized (independent) multiple Single-Input Single-Output (SISO) control systems. Hence, for the implementation of a decentralized control scheme for tensegrity structures, Chapter 6 should be considered a first attempt.

Chapter 7, titled ‘Control System Design for Tensegrity Structures’, presents the active control of tensegrity structures in a multivariable and centralized control context. In the field of control of active structures, the choice of the measured output divides active structural systems into two, namely, collocated and non-collocated systems. Collocated control systems are those in which actuators and sensors are paired together for the suppression of vibration requiring low amount of force typically. Non-collocated control systems are commonly used as high-authority controllers which, in addition to providing damping forces, are capable of making structural systems undergo significant movement (shape change) often requiring the use of powerful actuators to provide significant amount of force. Consequently, the control system design presented in Chapter 7 is divided into these two classes of controllers. On the one hand, in relation to collocated controller, a new method is presented that can be used for the determination of the feedback gain to reduce the control effort as much as possible while the closed-loop stability of the system is unconditionally guaranteed. On the other hand, the LQG controllers are suitable for both collocated and non-collocated control systems. Techniques for the design of LQG controllers are given in the Appendix; these techniques are subsequently applied in Chapter 7 to actively control tensegrity structural

systems for vibration suppression (low-authority controllers) and precise positioning or tracking (high-authority controllers). Chapter 7 concludes with a detailed discussion of new results and the importance of these findings in relation to the remaining chapters of this thesis and other previous work on active control of flexible structures, in general, and tensegrity structures, in particular.

Chapter 8, titled ‘Conclusions and Future Work’, summarizes the main findings of this thesis. It also presents recommendations for future research.

Chapter 2

FORM-FINDING OF TENSEGRITY STRUCTURES

2.1 Introduction

The most basic issue in the design of tensegrity structures, similar to other internally pre-stressed stable structures, lies in the selection and definition of their optimal structural forms – a process called form-finding [4]. Thus, it is not coincidental that the majority of scientific research on tensegrity structures is related to the form-finding process [2]. The models of tensegrity structures as a function of structural geometry and/or geometrical restrictions, member forces, external forces and joint types, are nonlinear and difficult to describe by simple mathematical functions. As such, except for small scale tensegrity structures with a few structural members, the analytical solutions necessary to obtain optimal structural forms are not possible. Even for the small scale systems where analytical solutions may be obtained, significant simplifications and several assumptions, especially in relation to the type of joint connecting the members, symmetry (similarity) of structural members and the influence of external forces, have to be made. Thus, resorting to the use of computational techniques is inevitable for analysis when dealing with large structures. Computational methods also reveal many properties of these structures that would otherwise not be obvious from analytical techniques.

For the purpose of employing computational methods for the form-finding of a tensegrity structure, the term ‘form-finding’ will be used to mean finding all shapes for which the structure is pre-stressed and in a state of static equilibrium in the absence of external forces. In other words, the objective is to determine all shapes for which all member forces are non-zero and the algebraic sum of all forces at each of the

connection points, or nodes, of the structures are zero. Thus, this chapter outlines a new method for the form-finding of tensegrity structures using a constrained optimization approach. It also explains the use of the four fundamental spaces of the static equilibrium matrices in conjunction with the constrained optimization approach for form-finding of large tensegrity structures with a complex connectivity of members. The new method offers control of both forces and lengths of structural members and it will be described via several examples. This chapter also discusses other methods of form-finding and the last section summarizes the chapter.

2.2 Form-finding Method for Tensegrity Structures: The Constrained Optimization Approach

2.2.1 Matrix Analysis of Tensegrity Structures

An investigation into the matrix form of the equations of equilibrium of structural assemblies, tensegrity structures not being an exception, reveals the static, kinematic and pre-stress properties, among others, of these assemblies. These properties are very useful in the design of optimal structural shapes of structural assemblies in general [59], [64], [65], [97]. In this section, the properties of tensegrity structures revealed by matrix analysis of the equations of equilibrium will be introduced. The works of Pellegrino and Calladine on matrix analysis of statically and kinematically indeterminate frameworks [59], [64], [65] and Schek's force density method for computations of general cable networks [98] will be used as a source of main reference in the definitions and notations that follow. Moreover, the concepts will be applied to tensegrity structures directly which are only a class of statically and kinematically indeterminate frameworks or networks. Likewise, in the form-finding methods to be discussed in the subsequent sections, except where otherwise stated, the following assumptions will be made: i) members are connected at the nodes in pin-jointed manner; that is, each of the joints transmits only forces and is not affected by kinetic friction and offers no resistance to rotation; ii) the cables are in tension at all times and can be elastic and/or inflexible; likewise, the bars are in compression at all times and the possibility of buckling is ignored; iii) the influence of external force fields (e.g. self-weight due to gravity, pre-stress due to temperature variation, etc.) are neglected; iv) the structure is only loaded at the nodes.

2.2.1.1 Definitions and Notations

Consider a tensegrity structure with n nodes and b structural members, the forces of tension (for cables) and compression (for bars), a total of b forces, assembled together form a vector of $f \in \mathbb{R}^b$. Likewise, the assemblage of external forces at the nodes in three-dimensional Euclidean space, a total of $3n$, will form a vector of $p \in \mathbb{R}^{3n}$. Here, it has been assumed that the tensegrity structure is not connected to an external body (rigid foundation) for support. Note that, tensegrity structures, as defined traditionally, do not need or require any rigid foundation (support constraints) to prevent rigid body motion. However, if rigid foundations are present to constrain the movement of the structure, a total of $3n - k$ external forces will be present where k is the number of kinematic constraints (in which case, $p \in \mathbb{R}^{3n-k}$) with a maximum value of 6 when the structure is fully constrained and a minimum value of 0 when the structure is free in space. Thus, for an unconstrained node i connected to nodes j and h through structural members of lengths l and m , respectively, as shown in Figure 2.1, the three equations of equilibrium (that is, the algebraic sum of forces acting) for the node i may be written as follows [59]:

$$\begin{aligned} (x_i - x_j) \frac{f_l}{l} + (x_i - x_h) \frac{f_m}{m} &= p_{i,x} \\ (y_i - y_j) \frac{f_l}{l} + (y_i - y_h) \frac{f_m}{m} &= p_{i,y} \\ (z_i - z_j) \frac{f_l}{l} + (z_i - z_h) \frac{f_m}{m} &= p_{i,z} \end{aligned} \quad (2.1)$$

where $\frac{f_l}{l}$ and $\frac{f_m}{m}$ in (2.1) are force-length ratios, which can be denoted by q_l and q_m respectively, and are called force density coefficients or tension coefficients; thus, (2.1) can then be re-written as follows:

$$\begin{aligned} (x_i - x_j) q_l + (x_i - x_h) q_m &= p_{i,x} \\ (y_i - y_j) q_l + (y_i - y_h) q_m &= p_{i,y} \\ (z_i - z_j) q_l + (z_i - z_h) q_m &= p_{i,z} \end{aligned} \quad (2.2)$$

The matrix form of (2.2) for an overall tensegrity structure is as follows [59]:

$$\begin{pmatrix} \vdots & \vdots \\ \cdots(x_i - x_j)\cdots(x_i - x_h)\cdots \\ \cdots(y_i - y_j)\cdots(y_i - y_h)\cdots \\ \cdots(z_i - z_j)\cdots(z_i - z_h)\cdots \\ \vdots & \vdots \end{pmatrix} \begin{pmatrix} q_1 \\ \vdots \\ q_l \\ \vdots \\ q_m \\ \vdots \\ q_b \end{pmatrix} = \begin{pmatrix} \vdots \\ p_{i,x} \\ p_{i,y} \\ p_{i,z} \\ \vdots \end{pmatrix} \quad (2.3)$$

Equivalently, (2.3) may be written as follows:

$$A \cdot q = p \quad (2.4)$$

where $A \in \mathbb{R}^{(3n-k) \times b}$ is called the *equilibrium matrix*; $q \in \mathbb{R}^b$ and $p \in \mathbb{R}^{3n-k}$ are vectors of tension coefficients and external forces, respectively. It is worth noting that since tensegrity structures are in a state of static equilibrium, the algebraic sum of all forces at every node is zero and, as such, p is a zero vector. As for the entries of vector q , $q_i > 0$ for structural members in tension (cables) and $q_j < 0$ for structural members in compression (bars).

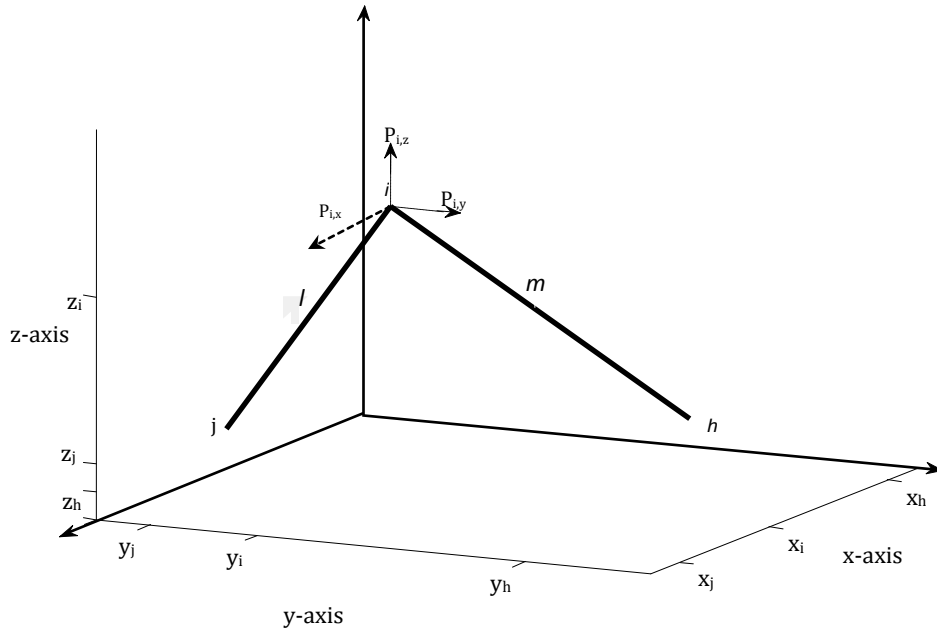


Figure 2.1: A view of an unconstrained node i connected to nodes j and h through members l and m , respectively.

Tensegrity structures are defined by, and are strongly dependent on, the connectivity of nodes by the branches. Thus, a branch-node connectivity matrix [98], [99], called the *incidence matrix* [100] and denoted C ($C = [c_{i,j}]_{b \times n}$), may be defined with the aid of a connectivity graph; for the structural member i connected to two matched nodes numbered $j(i)$ and $h(i)$ (where $j(i) < h(i)$), one can write the following equation:

$$c_{i,j} = \begin{cases} +1 & \text{for } j(i) = 1 \\ -1 & \text{for } h(i) = 1 \\ 0 & \text{otherwise} \end{cases} \quad (2.5)$$

For the class 3 tensegrity structure of Figure 2.2, for example, the connectivity matrix is as follows:

$$C = \begin{matrix} & \xrightarrow{\text{n, nodes}} \\ \downarrow & \begin{pmatrix} 0 & 1 & -1 & 0 \\ 1 & 0 & -1 & 0 \\ 1 & -1 & 0 & 0 \\ 0 & 0 & 1 & -1 \\ 1 & 0 & 0 & -1 \\ 0 & 1 & 0 & -1 \end{pmatrix} \\ \text{b, structural members} & \end{matrix}$$

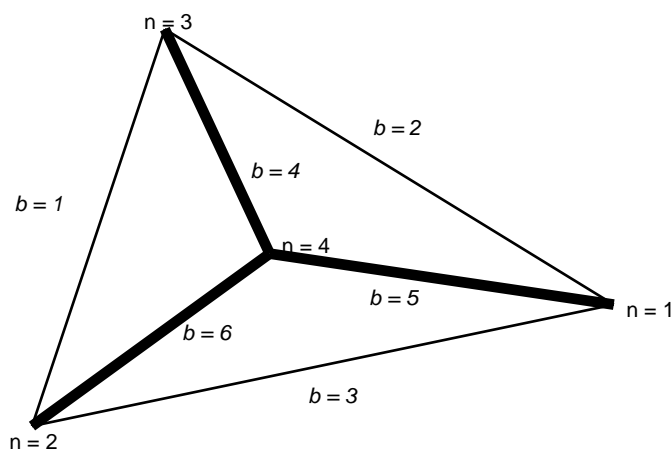


Figure 2.2: A class 3 tensegrity structure (thick and thin lines represent bars and cables, respectively)

Let the nodal coordinates of all points in 3-dimensional Euclidean space be assembled into column vectors $x \in \mathbb{R}^n$, $y \in \mathbb{R}^n$ and $z \in \mathbb{R}^n$; thus, (x_i, y_i, z_i) represents the coordinates of node i , and the lengths of structural members are assembled into vector $l \in \mathbb{R}^b$. Two nodes are said to be connected if they have a structural member in common. The coordinate difference of the connected nodes can be written as follows:

$$u = Cx, \quad v = Cy, \quad w = Cz \quad (2.6)$$

Thus, the equilibrium equation of the whole structure in (2.3) can be written in the following forms:

$$\begin{pmatrix} C^T U \\ C^T V \\ C^T W \end{pmatrix} \cdot L^{-1} f = \begin{pmatrix} P_x \\ P_y \\ P_z \end{pmatrix}, \quad (2.7)$$

$$\mathbb{A} \cdot \mathbb{q} = \mathbb{p} \quad (2.8)$$

where \mathbb{A} , \mathbb{q} and \mathbb{p} are defined as follows:

$$\mathbb{A} = \begin{pmatrix} C^T U \\ C^T V \\ C^T W \end{pmatrix}, \quad \mathbb{q} = L^{-1} f, \quad \mathbb{p} = \begin{pmatrix} P_x \\ P_y \\ P_z \end{pmatrix}, \quad (2.9)$$

and $(\cdot)^T$ denotes the linear algebraic transpose of a matrix. Likewise, U , V , W , and L are diagonal matrices of vectors u , v , w , and l , respectively; P_x , P_y and P_z are vectors of the x , y and z components of external forces at nodes, respectively. Equivalently, using the following identities [98]:

$$U\mathbb{q} = Qu, \quad V\mathbb{q} = Qv, \quad W\mathbb{q} = Qw, \quad (2.10)$$

where Q is a diagonal matrix of q , the equation of equilibrium in (2.3) can be written as follows:

$$D \cdot [x \quad y \quad z] = [P_x \quad P_y \quad P_z]. \quad (2.11)$$

where D is given by the following equation:

$$D = (C^T Q C). \quad (2.12)$$

$D \in \mathbb{R}^{n \times n}$ in equation (2.12) is a matrix of force density coefficients and is called the *force density matrix* [100]. It is worth noting that while both equations (2.4) and (2.8) represent equations of equilibrium in a matrix form with the matrices having the same dimensions, the way the elements of the matrices are ordered in both equations is different – hence, the reason for the slight difference in the notations used for the two equations. Also, for the same reason, as noted in (2.4), that tensegrity structures are in a state of static equilibrium, P_x , P_y and P_z are all zero vectors. Importantly, it is also worth noting that equations (2.8) and (2.11) are systems of linear equations with tension coefficients and nodal coordinates as their variables, respectively. Moreover, the matrix D is a positive-semidefinite matrix as long as $\mathbb{q}_i > 0$ for cables (in tension) and $\mathbb{q}_j < 0$ for bars (in compression) – which is the case for tensegrity structures.

2.2.1.2 Matrix Decompositions related to Equations of Equilibrium

In statically and kinematically determinate structures, the equilibrium matrix and its transpose can be used to uniquely determine the tension coefficients and geometry, respectively, of a given structural assembly since the two matrices are nonsingular. However, on the one hand, when additional structural members than strictly required are added, additional stresses in all other members will be introduced in general and, since there are now more unknowns than can be determined by the equations of equilibrium alone, the solution for the set of tensions in members will not be unique. Thus, a *statically indeterminate* structure is now obtained and the structure is said to be in a *state of self-stress*. On the other hand, if a structural member is removed from the structural assembly, the geometry of structure can no longer be uniquely determined in general and the structure is said to be *kinematically indeterminate* and a number of *independent inextensional mechanisms* is, as a result, introduced into the structural assembly. The introduction of the independent inextensional mechanisms (also called zero-energy deformation modes or higher-order stiffness) means that it is possible for the node(s) of the structure to move infinitesimally without any change in the length of members [59], [64], [65]. Thus, the number of independent states of self-stress s and the number of independent inextensional mechanisms m determine the class a structural assembly belong to as shown in Table 2.1 [65]. Tensegrity structures are pre-stressed stable structures with a number of inextensional mechanisms and, therefore, fall in type IV in the table [65].

Table 2.1: Types of structural assemblies

Type of assembly		Value of s	Value of m
I	Statically and kinematically determinate	$s = 0$	$m = 0$
II	Statically determinate and kinematically indeterminate	$s = 0$	$m > 0$
III	Statically indeterminate and kinematically determinate	$s > 0$	$m = 0$
IV	Statically and Kinematically indeterminate	$s > 0$	$m > 0$

Furthermore, the *rank* of equilibrium matrix r can be used to determine the values of m and s using a modified form of Maxwell's formula which, in three-dimension, leads to the following expressions [59]:

$$m = 3n - k - r \quad , \quad s = b - r \quad (2.13)$$

A wealth of other information about tensegrity structures (similar to other structural assemblies) can be obtained from the four fundamental spaces (the *row space*, the *column space*, *nullspace* and *left nullspace*) of the equilibrium matrix that are obtained by factorizing the equilibrium matrix using the *singular value decomposition* as shown in Figure 2.3 [59], [65]. For tensegrity structures, and other structures with $m > 0$, the initial configuration is not unique but one can still set up an initial configuration to obtain the equilibrium matrix by assuming that small-deflection theory holds [65]. The singular value decomposition of the equilibrium matrix in (2.8) is as follows:

$$\mathbb{A} = \begin{pmatrix} C^T U \\ C^T V \\ C^T W \end{pmatrix} = \mathbb{U} \mathbb{V} \mathbb{W}^T \quad (2.14)$$

where $\mathbb{U} \in \mathbb{R}^{(3n-k) \times (3n-k)}$ and $\mathbb{W} \in \mathbb{R}^{b \times b}$ are left and right orthonormal matrices, respectively, and $\mathbb{V} \in \mathbb{R}^{(3n-k) \times b}$ is a diagonal matrix with singular values on the diagonal in descending order of magnitude (note that orthonormality of \mathbb{U} means that each of its column or row are orthogonal unit vectors; that is $\mathbb{U}^T \cdot \mathbb{U} = I$ where I is the identity matrix). More so, \mathbb{U} and \mathbb{W} can be further partitioned as follows [64]:

$$\begin{aligned} \mathbb{U} &= [\mathbb{u}_1, \mathbb{u}_2, \dots, \mathbb{u}_r \mid \mathbb{u}_{r+1}, \mathbb{u}_{r+2}, \dots, \mathbb{u}_{3n-k-r}] \\ \mathbb{W} &= [\mathbb{w}_1, \mathbb{w}_2, \dots, \mathbb{w}_r \mid \mathbb{w}_{r+1}, \mathbb{w}_{r+2}, \dots, \mathbb{w}_{b-r}] \end{aligned} \quad (2.15)$$

where a matrix $\overline{\mathbb{W}}$, deduced from \mathbb{W} in (2.15), is defined as follows:

$$\overline{\mathbb{W}} = [\mathbb{w}_{r+1}, \mathbb{w}_{r+2}, \dots, \mathbb{w}_{b-r}] \quad (2.16)$$

The vectors in \overline{W} represent all states of self-stress s that pre-stress the structure. Likewise, the transpose of the equilibrium matrix $\mathbb{B} = \mathbb{A}^T$ is related to the elongations of structural members defined by the following equation:

$$\mathbb{B} \cdot \mathbb{d} = \mathbb{e} \quad (2.17)$$

where $\mathbb{d} \in \mathbb{R}^{(3n-k)}$ is the vector of nodal displacements and $\mathbb{e} \in \mathbb{R}^b$ is a vector of member elongation coefficients (unlike tension coefficient that is force-to-length ratio, elongation coefficient is the product of member elongation and length). Thus, the following equation:

$$\overline{U} = [\mathbb{u}_{r+1}, \mathbb{u}_{r+2}, \dots, \mathbb{u}_{3n-k-r}] \quad (2.18)$$

can be deduced from \mathbb{U} in (2.15); here the column vectors in \overline{U} represent all modes of inextensional mechanisms. Importantly, the row and column spaces of \mathbb{A} are orthogonal to subspaces \overline{W} and \overline{U} , respectively. Also, the relationships between m , r , s and \overline{U} , \mathbb{V} , \overline{W} are depicted in Figure 2.3.

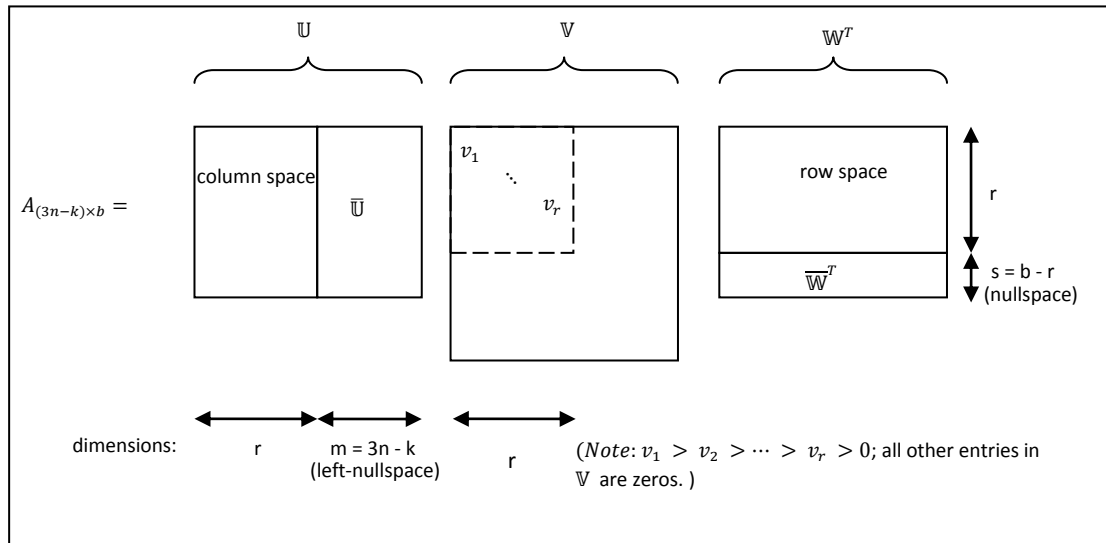


Figure 2.3: Singular value decomposition of the equilibrium matrix illustrating the relationships between m , r , s and \overline{U} , \mathbb{V} , \overline{W} .

The use of the equations presented so far in this section will be illustrated with an example: For the simplex tensegrity structure of Figure 2.4 which has 6 nodes and 12 structural members of which 9 are cables in tension and the other 3 are bars in

compression, the rank of the equilibrium matrix is 11; thus, using (2.13), and with the structure not attached to any rigid foundation ($k = 0$), the values of m and s are 7 and 1, respectively.

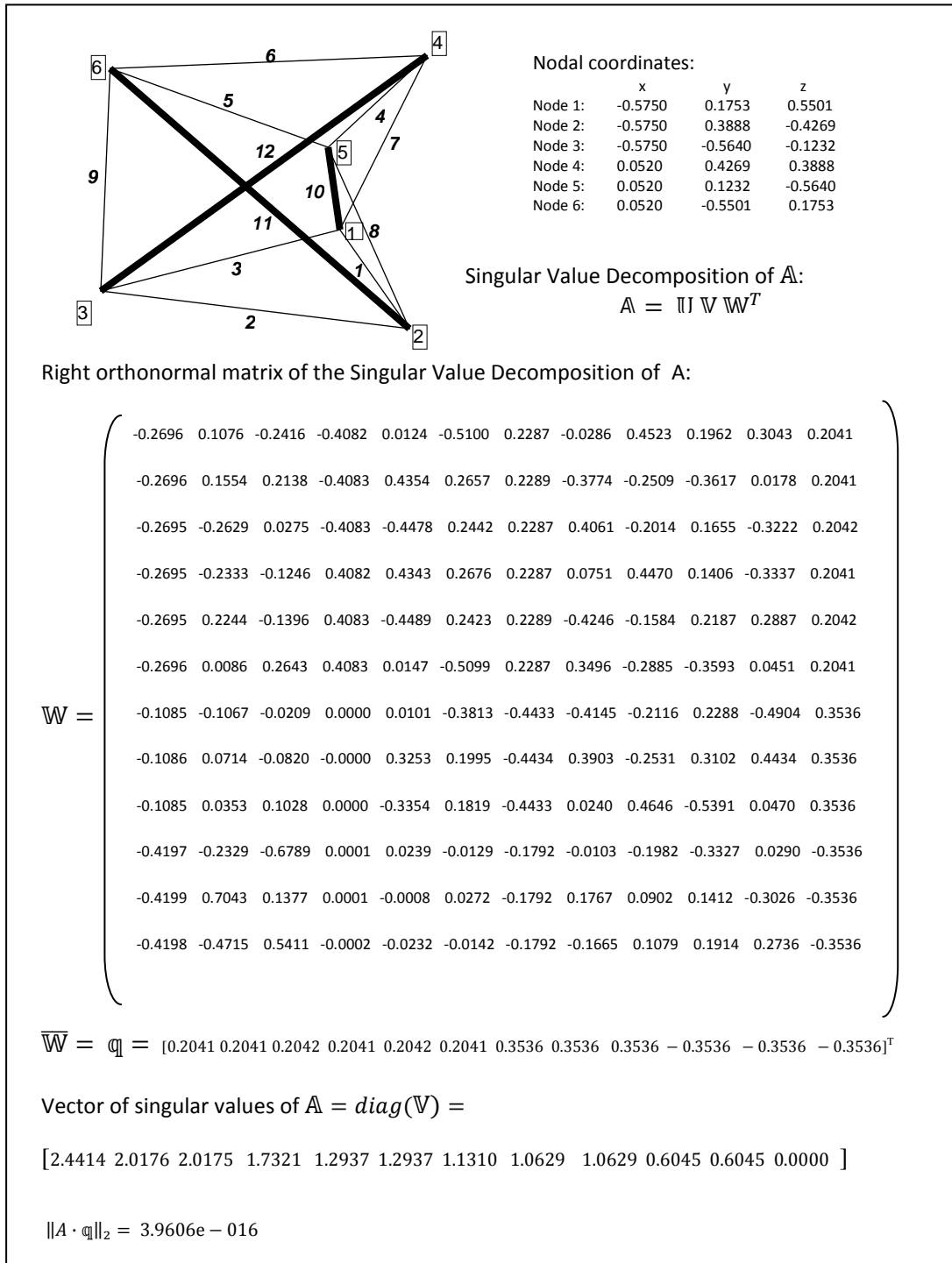


Figure 2.4: An illustrating on obtaining tension coefficients from the right orthonormal matrix.

As tensegrity structures are pre-stressed stable structures, the implication of $s = 1$ is that, of all the orthogonal unit vectors in the \mathbb{W} , only a particular set of column vector(s) of $\overline{\mathbb{W}}$ (which, in this case, is a single column vector) solves the equation of equilibrium (2.8) and it is this vector of tension coefficients that will pre-stress the overall tensegrity structure and will make it attain stability (that is, being in a state of static equilibrium) due to pre-stress. Thus, from Figure 2.4, the vector of tension coefficients is as follows:

$$\mathbb{q} = [0.2041 \ 0.2041 \ 0.2041 \ 0.2041 \ 0.2041 \ 0.2041 \ 0.3536 \\ 0.3536 \ 0.3536 \ -0.3536 \ -0.3536 \ -0.3536] ^T.$$

In addition, since $s = 1$, the number of zero singular values (which make up the diagonal of \mathbb{V}) will be 1. Thus, the example presented in Figure 2.4 illustrates the way tension coefficients are obtained from the right orthonormal matrix of the singular value decomposition of the equilibrium matrix. The 2-norm of the vector of external forces $\|A \cdot \mathbb{q}\|_2$ (that is, $\|\mathbb{p}\|_2$) is used as a test of the level of static equilibrium as shown in the figure. Similar to the singular value decomposition of the equilibrium matrix A , a singular value decomposition of the force density matrix D leads to the following equation:

$$D = (C^T Q C) = \mathcal{U} \mathcal{V} \mathcal{W}^T \quad (2.19)$$

where \mathcal{U} , \mathcal{V} and \mathcal{W} are square matrices of order n . Just as the nullspace of the equilibrium matrix A in (2.8) is linked to vectors of tension coefficients, the nullspace of the force density matrix D in (2.11) is linked to nodal coordinates. From linear algebra, recall that for an original space of \mathbb{R}^3 , the possible subspaces, by definition of a subspace of a vector space [101], are: (i) \mathbb{R}^3 space itself; (ii) any plane (that is, \mathbb{R}^2) through the origin; (iii) any line (that is, \mathbb{R}^1) through the origin; and (iv) the origin (the zero vector) since the zero vector belongs to every subspace – thus, a total of four subspaces are in a space of \mathbb{R}^3 . For tensegrity structures, the significance of this is that, to satisfy the equilibrium equation in the force density form in (2.11), the dimension of the nullspace of D must be four for a 3-dimensional (or three for a 2-dimensional) tensegrity structure. Stated differently, the number of zero singular values on the diagonal of \mathcal{V} in (2.19) must be four and any of the corresponding four vectors in \mathcal{U} and \mathcal{W} can be selected to represent the nodal coordinate vectors – x , y and z . This concept is the same as the *maximal rank* concept of rigidity theory in mathematics

which is described in [50], [102], where the matrix D is called the rigidity or stress matrix; the matrix D must be of maximal rank for the structural system to be *infinitesimally rigid* (that is, to be in a state of static equilibrium due to pre-stress). Since D is a square matrix of order n , its maximal rank implies that its rank must be four less than n for any given 3-dimensional tensegrity structure to be in a state of static equilibrium due to pre-stress.

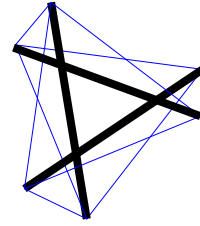
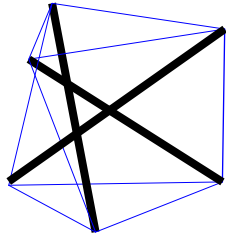
Furthermore, in the selection of the vectors x , y and z (of a 3-dimensional structure) from the four vectors of \mathcal{U} or \mathcal{W} (either case will work), the preferred vectors that leads to a unique structural shape that covers maximum volume in space – which can be chosen in any manner to represent x , y and z – would be the three vectors corresponding to \mathbb{R}^3 space itself, the plane \mathbb{R}^2 through the origin and the line \mathbb{R}^1 through the origin of the nullspaces – the last column vector is excluded; that is, the last vector, which corresponds to the zero vector, is a subspace of, not only the nullspace of D but, every subspace of D and, therefore, when selected as a vector of coordinates leads to a structure that is not unique (that is, it leads to a different structure for every different combinations with other nullspace vectors) and may tend towards a structure of a lower dimension (for example, a 3-dimension to a 2-dimension structure). The implication of this is that, as long as one has a *valid set* of tension coefficients and a tensegrity configuration defined by matrix C , the vectors x , y and z may be selected from the nullspace of D . Here, a valid set of tension coefficients are those that will lead to exactly four zero singular values of D . Using the valid vector of tension coefficients obtained in the last example (see Figure 2.4), different selections of nodal coordinates from the nullspace of the D matrix are shown in Table 2.2 with their associated structures shown in Figure 2.5.

Table 2.2: An illustration on obtaining vectors of nodal coordinates from the nullspaces of the force density matrix

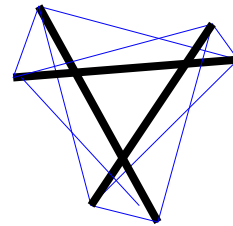
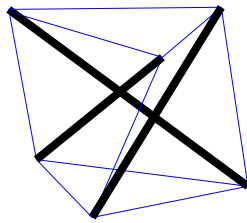
Description	n	Nodal Coordinates			Description	n	Nodal Coordinates		
		x	y	z			x	y	z
a) Nodal coordinates selected from \mathcal{U}	1	0.6375	-0.1998	-0.1700	c) Nodal coordinates selected from \mathcal{W} including its last vector	1	0.6455	-0.0739	0.4934
	2	-0.1900	-0.0951	-0.7126		2	-0.1193	0.1589	0.5556
	3	0.1111	0.6490	-0.1301		3	-0.2152	-0.5769	0.5258
	4	0.0494	-0.6739	0.2566		4	0.3358	0.6338	0.2190
	5	-0.7323	-0.1234	-0.0335		5	-0.6027	0.4777	0.2736
	6	-0.0808	0.2458	0.6159		6	-0.2165	-0.0815	0.2204
b) Nodal coordinates from \mathcal{W}	1	0.0332	0.6455	-0.0739	d) Another set of Nodal coordinates selected from \mathcal{W} including its last vector:	1	0.0332	0.0739	0.4934
	2	-0.5643	-0.1193	0.1589		2	-0.5643	0.1589	0.5556
	3	0.1054	-0.2152	-0.5769		3	:0.1054	-0.5769	0.5258
	4	0.3230	0.3358	0.6338		4	0.3230	0.6338	0.2190
	5	0.0198	-0.6027	0.4777		5	0.0198	0.4777	0.2736
	6	0.7514	-0.2165	-0.0815		6	0.7514	-0.0815	0.2204

Side View

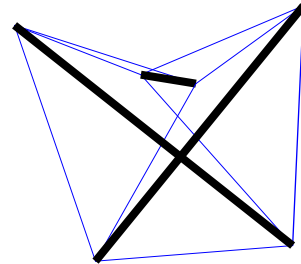
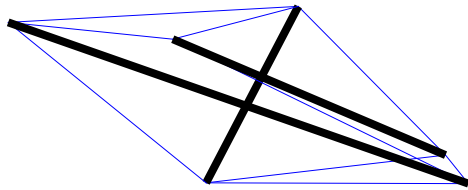
Top View



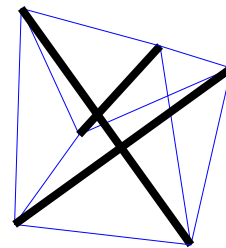
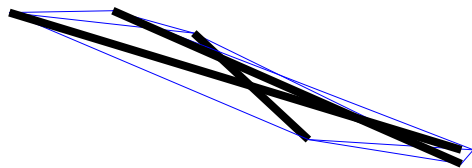
(a)



(b)



(c)



(d)

Figure 2.5: Tensegrity structures associated with nodal coordinates defined in Table 2.2.

2.2.2 Penalty Function Method of Constrained Optimization

From the discussions so far, what seems to be a simple approach to obtain a tensegrity structure from an initial tensegrity configuration would be to follow any of the two algorithmic methods in Table 2.3.

**Table 2.3: Descriptions of two methods for obtaining tensegrity structures:
The Nullspaces approach**

Method 1	Method 2
<p>Algorithm: Step 1: Define the initial configuration (in matrix C) and a starting feasible geometry (vectors of nodal coordinate vectors x, y and z). Here, feasibility means that the nodal coordinates defined correspond to the structural configuration defined in C.</p> <p>Step 2: Compute A</p> <p>Step 3: Obtain the vector of tension coefficients \mathbb{q}, such that bars are in compression and cables are in tension, from the nullspace of A.</p> <p>Step 4: Check if the equation of equilibrium is satisfied; if satisfied, terminate the process. Otherwise, continue the next step.</p> <p>Step 5: Compute D using \mathbb{q} from Step 3.</p> <p>Step 6: Find new nodal coordinate vectors x, y and z for the structure from the nullspace of D and go back to Step 2.</p>	<p>Algorithm: Step 1: Define the initial configuration (in matrix C) and a starting set of tension coefficients in vector \mathbb{q}.</p> <p>Step 2: Compute D.</p> <p>Step 3: Obtain vectors of nodal coordinates from the nullspace of D.</p> <p>Step 4: Check if the equation of equilibrium is satisfied; if satisfied, terminate the process. Otherwise, continue the next step.</p> <p>Step 5: Compute A using vectors of nodal coordinates obtained in Step 3.</p> <p>Step 6: Find a new set of tension coefficient from the nullspaces of A and go back to Step 2.</p>

Figure 2.6 shows an example of an initial tensegrity configuration transformed to a tensegrity structure using Method 1. The sums of all the initial and final lengths of structural members of the initial configuration and the obtained tensegrity structure are 19.3921 and 12.7552, respectively. The vector of tension coefficient of the obtained tensegrity structure is as follows:

$$\mathbb{q} = [0.2041 \ 0.2041 \ 0.2041 \ 0.2041 \ 0.2041 \ 0.2041 \ 0.3536 \\ 0.3536 \ 0.3536 \ -0.3536 \ -0.3536 \ -0.3536]^T$$

The 2-norm of the vector of external forces has been used to verify whether the equation of static equilibrium is satisfied with the size of the tolerance set to 10^{-8} ; that is, the algorithm terminates at the 11th iteration when $\|A \cdot \mathbb{q}\|_2 = 1.5631 \times 10^{-9} < 10^{-8}$.

The algorithms presented in Table 2.3 provide overall characteristics and important elements of form-finding via the nullspace approach. Other algorithms that use the nullspace approach in the literature are a particular case of these more general algorithms. For instance, a special case of how a tensegrity structure can be obtained from the algorithm of Method 2 on Table 2.3 has been presented in [103], [104]. There, the starting set of tension coefficients has been termed ‘prototypes’ as they define which structural members are cables ($q_i > 0$) and those that are bars ($q_j < 0$). The description also details the way the matrix D may be improved during the current iteration process so that the selection of vectors of nodal coordinates from its nullspace is optimal – where optimality means that the lengths of structural members must not be zero but must be as small as possible. Furthermore, the selection of tension coefficients from vectors in the right orthonormal matrix W is determined by which vector matches the prototypes the most; that was achieved using a least-square fit procedure. The algorithm tries to find a valid set of tension coefficients that will give exactly four zero singular values of D in the next iteration and continues until the state of self-stress $s > 0$ is found; that is, $s > 0$ is the test for static equilibrium.

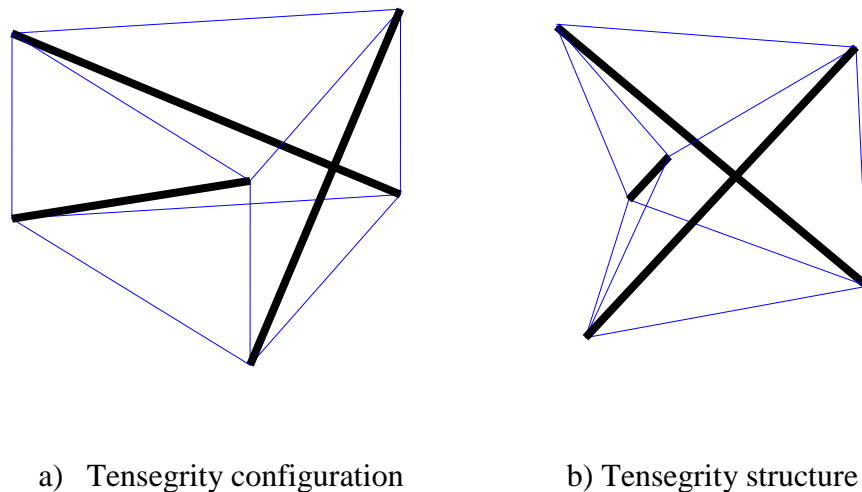


Figure 2.6: An illustrative example of the implementation of algorithm in Method 1.

Using any of the two methods on Table 2.3, and also the algorithm provided in [103], [104], to form-find tensegrity structures suffer from a number of drawbacks. These drawbacks are as follows:

1. Because the vectors of tension coefficients and nodal coordinates are chosen from the nullspaces of equilibrium matrices, there is no control over what these unit length vectors should be. The implication is that, for any tensegrity structure, one cannot specify that a particular set of members should have predefined set of tension coefficients or lengths. The most that can be done is that, during each iteration, one post-processes the equilibrium matrices [103], [104] in the expectation that a solution would be found in the next iteration.

2. By defining a tensegrity configuration with the C matrix and ensuring that the starting set of tension coefficients are uniform (that is, all tension coefficients are the same for all cables and all bars except for their differences in signs; $q_j < 0$ for bars and $q_i > 0$ for cables), the procedure finds a tensegrity structure in the first few iterations (in fact, in many cases, in the first iteration for Class 1 3-dimensional tensegrity structures), otherwise, it fails by not leading to a valid structure of maximum volume in space (for example, a 3-dimensional structure collapses to a 2-dimensional structure). Note that using tension coefficients of 1 for cables (or -1 for compressive structural members) as starting values has been found to produce reasonable results [4], [98], [103], [104] for cable and pre-stressed structures in general. Moreover, when non-uniform starting set of tension coefficients are used, the procedure may not only fail but, for cases where a tensegrity structure is found, the number of iterations may increase in a way that is difficult to predict in general.

3. Finally the following *orthonormality constraint* $xyz^Txyz = I$, where $xyz = [x \ y \ z]$ and x , y and z are the vectors of nodal coordinates and $I \in \mathbb{R}^{n \times 3}$ denote the identity matrix, is another constraint imposed on the tensegrity structure that results from these methods of form-finding. The consequence is that, only tensegrity structures satisfying this orthonormality constraint can be obtained with the methods, and these form only a class of tensegrity structures with special meaning as will be shown later in Section 2.2.3.

In the next few sections, another procedure which does not involve the use of the nullspaces of \mathbb{A} or D to determine vectors of tension coefficients and nodal coordinates from equilibrium matrices will be presented. The procedure uses constrained optimization algorithm – and in particular, the interior point algorithm for constrained optimization. The main idea of the interior point algorithm is summarized in the remainder of this section.

Let an initial optimization problem, with inequality constraints, be written as follows:

$$\begin{aligned} \min_x \quad & f(x) \\ \text{subject to:} \quad & g_i(x) \leq 0, i = 1, 2, \dots, e \end{aligned} \quad (2.20)$$

This problem is converted to an unconstrained optimization problem by defining the following function:

$$\min_x \quad f_\mu(x, s) = f(x) - \mu \sum_{i=1}^e \ln(s_i) \quad (2.21)$$

where s_i is some function of $g_i(x)$ (for example, $s_i = -g_i(x)$) and $\mu > 0$ is the penalty term which, when given a decreasing sequence of values, the solution may converge to that of the original problem of (2.20) [105–107]. The algorithm for the iteration procedure of this method of constrained optimization is shown in Table 2.4 [105].

Table 2.4: The Interior Point Algorithm for Constrained Optimization

Algorithm:

Step 1: Define initial values of μ_k and feasible points x_k satisfying the constraints with $k = 1$.

Step 2: Minimize (2.21) using any unconstrained optimization method to obtain the solution x_k^* .

Step 3: Using a stopping criterion, test if x_k^* is the optimal solution; if it is, terminate the process. Otherwise, go to the next step.

Step 4: Find $\mu_{k+1} = c \cdot \mu_k$ where $c < 1$.

Step 5: Set $k = k + 1$ and $x_{k+1} = x_k^*$; then go to step 2.

This straightforward algorithm can be extended to include equality constraints as well as lower and upper bounds on the design variables in x [105], [106], [108]. The solution to the constrained optimization problem in (2.20) using the interior point method may be obtained, for example, using the '*fmincon*' function in MATLAB [109]. Thus, to obtain the vector of tension coefficients for a tensegrity configuration

from its equilibrium matrix \mathbb{A} using a constrained optimization approach, the optimization problem may be defined, for instance, as follows:

$$\begin{aligned}
& \min_{\mathbb{q}} \quad \sqrt{\mathbb{p}^T \mathbb{p}} \\
& \text{subject to: } \quad h_i(\mathbb{q}) = 0, \quad i = 1, 2, \dots, r \\
& \quad \quad \quad g_i(\mathbb{q}) \leq 0, \quad i = 1, 2, \dots, e \\
& \quad \quad \quad lb_i \leq \mathbb{q}_i \leq ub_i, \quad i = 1, 2, \dots, b
\end{aligned} \tag{2.22}$$

where $h_i(\mathbb{q})$ and $g_i(\mathbb{q})$ are the equality and inequality constraints, respectively, for the i^{th} structural member; r and e are the total numbers of the equality and inequality constraints, respectively; lb and ub are the lower and upper bounds on the tension coefficients, respectively; and, as before, b is the number of structural members and \mathbb{p} is a vector of external forces given by (2.8). The objective function $\sqrt{\mathbb{p}^T \mathbb{p}}$ is the 2-norm of \mathbb{p} . $h_i(\mathbb{q})$ enables us to dictate tension coefficients for some structural members while $g_i(\mathbb{q})$ may be used to prevent these coefficients from exceeding certain limits. Also, the constraint $lb_i \leq \mathbb{q}_i \leq ub_i$ allows one to define members in compression and those in tension.

Because the interior point algorithm will be used to solve the constrained optimization problem in (2.22), the following optimization options in relation to the algorithm of Table 2.4 are used:

1. For Step 1, the starting value of μ_k is 0.1.
2. For Step 2, the unconstrained optimization method used is the well-known Broydon-Fletcher-Goldfarb-Shanno (BFGS) quasi-Newton algorithm that calculates the Hessian by a dense quasi-Newton approximation and the line search routine used for this constrained optimization problem is the backtracking algorithm as described in [110].
3. For Step 3, the two stopping criteria used are: $\|\mathbb{q}_{k+1} - \mathbb{q}_k\| < tol$ or $\|f(\mathbb{q} + 1) - f(\mathbb{q})\| < tol$ where $tol = 10^{-8}$; that is, the iteration terminates if any or both of the two criteria is satisfied.
4. For Step 4, optimal c will be obtained for each iteration. The initial starting value c_k , with $k = 1$, is \sqrt{b} . For subsequent iterations, c_k are obtained using the conjugate gradient method as the line search algorithm in which c_k are constrained to have strictly positive values within a defined trust region [106], [107], [111].

2.2.2.1 Obtaining Tension Coefficients from the Equilibrium Matrix

Consider the two structures of Figure 2.7 in which (a) and (b) are a tensegrity configuration and a tensegrity structure, respectively. The vector of tension coefficients for these structures may be obtained by minimizing the norm of the vector of external force \mathbb{p} ; the optimization model is as follows:

$$\begin{aligned} \min_{\mathbb{q}} \quad & \sqrt{\mathbb{p}^T \mathbb{p}} \\ \text{subject to:} \quad & lb_i \leq \mathbb{q}_i \leq ub_i, \quad i = 1, 2, \dots, 12, \end{aligned} \quad (2.23)$$

where \mathbb{p} is as defined in (2.8); the constraints $0.1 \leq \mathbb{q}_i \leq 10$ for cables ($i = 1, 2, \dots, 9$) and $-10 \leq \mathbb{q}_i \leq -0.1$ for bars ($i = 10, 11, 12$) are defined by the following vectors:

$$\begin{aligned} lb &= [0.1 \ 0.1 \ 0.1 \ 0.1 \ 0.1 \ 0.1 \ 0.1 \ 0.1 \ 0.1 \ -10 \ -10 \ -10]^T \\ ub &= [10 \ 10 \ 10 \ 10 \ 10 \ 10 \ 10 \ 10 \ 10 \ -0.1 \ -0.1 \ -0.1]^T \end{aligned} \quad (2.24)$$

The initial starting value of vector \mathbb{q} is as follows:

$$\mathbb{q} = [0.1 \ 0.1 \ 0.1 \ 0.1 \ 0.1 \ 0.1 \ 0.1 \ 0.1 \ 0.1 \ -0.1 \ -0.1 \ -0.1]^T$$

The solutions to the optimization problem for both structures are given in Figure 2.7. Recall that the equilibrium matrix \mathbb{A} has the dimension $(3n - k) \times b$ with $(3n - k) > b$. For the example is currently being considered, $k = 0$, $\mathbb{A} \in \mathbb{R}^{(3n) \times b}$ and $3n > b$; thus, the solution to the system of linear equations of equilibrium will not be unique (there is an infinite number of solutions). This is true for the tension coefficients found for tensegrity systems; moreover, for tensegrity structures, it is known that the geometry (nodal coordinates) are preserved under affine transformations [49], [70], [112]. As such, the tension coefficients of the tensegrity structure obtained using the nullspace method (see Figure 2.6) and those obtained using the constrained optimization method presented here are the same in that the bar-to-cable tension coefficient ratios are the same as the vectors of tension coefficients are scalar multiple of each other. Accordingly, in addition to the fact that the constraints of (2.24) define members that are in tension and those in compression, they also define the working scale of our tension coefficients. In other words, if an initial starting value of vector \mathbb{q} is chosen at random for a given tensegrity structure, the bar-to-cable tension coefficient ratios will

be the same although actual magnitudes of these tension coefficients will be different in general.

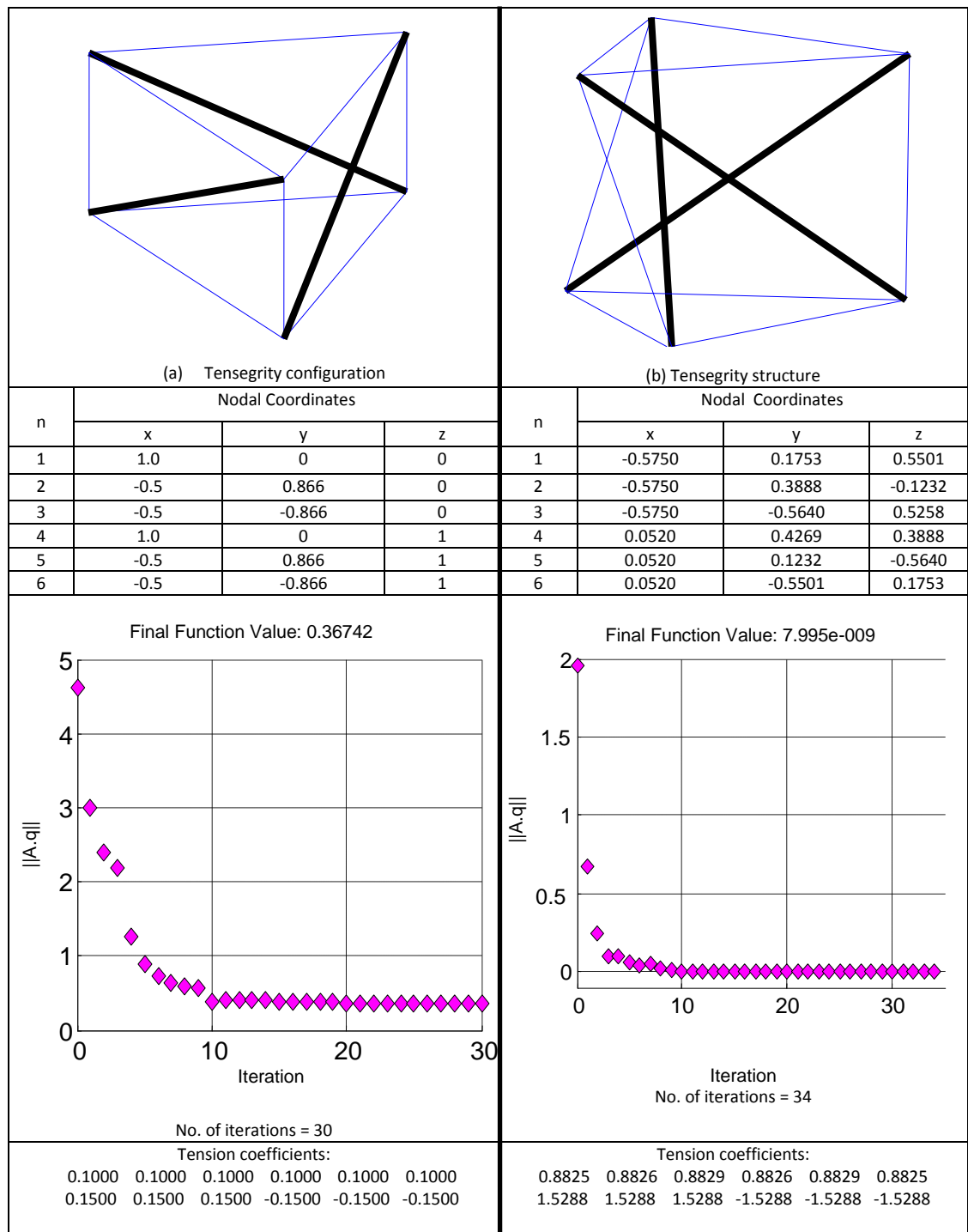


Figure 2.7: Tension coefficients obtained from the equilibrium matrix using a constrained optimization approach.

Note that in Figure 2.7, the final values of $\|\mathbb{A} \cdot \mathbb{q}\|_2$ in figures (a) and (b) are 0.3674 and 7.9950×10^{-9} , respectively. In other words, with the associated tension coefficients obtained from the constrained optimization, structure (b) is a tensegrity structure while structure (a) is only a tensegrity configuration and not a tensegrity structure since it does not satisfy the condition that the algebraic sum of nodal forces is zero at every node. As such, the main task of form-finding, from a constrained optimization perspective, will be to find a tensegrity structure (for example, (b) in Figure 2.7), given a tensegrity configuration (for example, (a) in Figure 2.7).

2.2.2.2 Obtaining Nodal Coordinates from the Force Density Matrix

Similarly, given a valid set of tension coefficients and starting values of nodal coordinates of a tensegrity configuration, it is possible to obtain the nodal coordinates of the associated tensegrity structure. The corresponding optimization model is as follows:

$$\begin{aligned} \min_{\overline{xyz}} \quad & \sqrt{\mathbb{p}^T \mathbb{p}} \\ \text{subject to:} \quad & lb_i \leq l_i \leq ub_i, \quad i = 1, 2, \dots, 12, \end{aligned} \quad (2.25)$$

where l_i denotes the length of the i^{th} structural member and is a function of the nodal coordinates; thus, $lb_i \leq l_i \leq ub_i$ represents the length constraints with lb_i and ub_i representing the lower and the upper bound on the length of the i^{th} structural member, respectively. Of course, other equality and inequality constraints can be introduced. Let $\overline{xyz} = [x^T \quad y^T \quad z^T]^T$, the relationship between \overline{xyz} and \mathbb{p} is obtained by rewriting (2.11) as follows [50]:

$$\begin{bmatrix} D & 0 & 0 \\ 0 & D & 0 \\ 0 & 0 & D \end{bmatrix} \cdot \begin{bmatrix} x \\ y \\ z \end{bmatrix} = \begin{bmatrix} P_x \\ P_y \\ P_z \end{bmatrix}, \quad (2.26)$$

$$\mathbb{D} \cdot \overline{xyz} = \mathbb{p} \quad (2.27)$$

where \mathbb{D} is defined as follows:

$$\mathbb{D} = \begin{bmatrix} D & 0 & 0 \\ 0 & D & 0 \\ 0 & 0 & D \end{bmatrix} \quad (2.28)$$

Equivalently, \mathbb{D} can also be written as follows:

$$\mathbb{D} = I_3 \otimes D \quad (2.29)$$

where I_3 is the 3-by-3 identity matrix and \otimes is the symbol for the tensor product of two matrices. Thus, given the valid set of tension coefficients of the tensegrity structure of Figure 2.7 (b) and using, as starting values, the nodal coordinates of the tensegrity configuration of Figure 2.7 (a) (and shown in Figure 2.8(a)) and without constraining the length of any member (and, as such, the BFGS quasi-Newton unconstrained optimization algorithm [110] can be used directly), the nodal coordinates of the tensegrity structure is shown in Figure 2.8 (a). Figure 2.8 (b) shows the final tensegrity structure as well as the nodal coordinates for the case in which six structural members have been constrained to have unit lengths using an equality constraint $l_i = 1$ for $i = 1, 2, \dots, 6$ as given in the constraint equation for (2.25).

2.2.2.3 Obtaining Nodal Coordinates from Geometric Consideration

So far, the procedure of obtaining tension coefficients and nodal coordinates of tensegrity structures from equations of static equilibrium has been shown. However, tensegrity structures possess remarkable *geometric*, or *kinematic*, properties. It is thus possible to obtain, by form-finding, tensegrity structures from a geometric consideration alone and many analytical and numerical methods have been proposed for doing this [7], [51], [113–115]. In general, these methods constrain the lengths of the cables and maximize the lengths of the bars or constrain the lengths of the bars and minimize the lengths of the cables without explicitly requiring that cables should be in tension and bars should be in compression [100], [114]. However, these are, indeed, implied as maximizing the lengths of bars and minimizing the lengths of cable correspond to putting the bars in a state of compression and the cables in a state of tension, respectively. Moreover, the methods implicitly minimize the total length of structural members and are independent of the material properties (such as the mechanical, electrical and thermal properties) of the of bars and cables or the cross-sectional areas of these structural members. Importantly, these methods inherently assume that the magnitudes of tension coefficients in all cables and bars are equal as will be shown shortly. Furthermore, it will also be shown that these methods do not necessary mean that the equations of static equilibrium will be satisfied because, by *a priori* dictating that the magnitudes of tension coefficients for all structural members be equal, the possibility that optimal set of tension coefficient exist (in which structural members may have different magnitudes of tension coefficients) for a given structural configuration is ignored.

Consider the general nonlinear constrained optimization form-finding method for tensegrity structures proposed in [114], given the tensegrity configuration shown in Figure 2.9 with the structural members labelled $c1, c2, \dots, c9$ for the cables, $b1, b2, b3$ for the bars and nodes $n1, n2, \dots, n6$, the objective would be to maximize the length of only a single member, the bar $b1$, subject to the constraints that all cables are of unit length and that all bars have the same length; the optimization model is as follows [100], [114]:

$$\begin{aligned} \min_{x,y,z} \quad & -l_{b1}^2 \\ \text{subject to:} \quad & l_i - 1 = 0, \quad i = c1, c2, \dots, c9 \\ & l_i - l_{b1} = 0, \quad i = b2, b3 \end{aligned} \quad (2.30)$$

where $l_i = l_i(x_j, y_j, z_j, x_h, y_h, z_h)$ denotes the length of the i^{th} structural member connected to nodes j and h (and is a function of the nodal coordinates of nodes j and h). The approximate solution to (2.30) which satisfies all the constraints given in [100] is $l_{b1} = 1.468$ compared to the exact value of $\sqrt{1 + 2/\sqrt{3}} \approx 1.4679$ obtained analytically. Now, consider the following four cases:

Case 1: Another approach to pose the optimization problem of (2.30) is to minimize, instead of the negative squared length of a single member, the weighted squared lengths of all structural members.

Thus, the optimization model for minimizing the squared length of all members (and of course, subject to cable symmetry) may be written as follows:

$$\begin{aligned} \min_{x,y,z} \quad & l^T \cdot (\text{diag}([\rho \ \rho \ -\rho \ -\rho \ -\rho])) \cdot l \\ \text{subject to:} \quad & l_i - 1 = 0, \quad i = c1, c2, \dots, c9 \end{aligned} \quad (2.31)$$

Equivalently, the optimization model of (2.31) may be written as follows:

$$\begin{aligned} \min_{x,y,z} \quad & l^T \cdot (\text{diag}(\hat{\rho})) \cdot l \\ \text{subject to:} \quad & l_i - 1 = 0, \quad i = c1, c2, \dots, c9 \end{aligned} \quad (2.32)$$

where $|\rho| > 0$, $\hat{\rho} = [\rho \ \rho \ -\rho \ -\rho \ -\rho]$, $\text{diag}(\hat{\rho})$ is the diagonal matrix of vector $\hat{\rho}$ and l is a vector whose elements are the lengths of the structural members. Notice that the constraint $l_i - l_{b1} = 0$ for $i = b2, b3$ is no longer required. Furthermore, the negative elements of $\hat{\rho}$ shows that squared lengths of bars are being

maximized. With $\rho = 1$, for example, the solution to (2.31) is $l = [1 \ 1 \ 1 \ 1 \ 1 \ 1 \ 1 \ 1 \ 1 \ 1.4679 \ 1.4679 \ 1.4679]^T$ as shown on Table 2.5. Notice that $l_{b_1} = 1.4679$ in this solution correspond to the exact solution of (2.30) and the sum of the lengths of all the structural members is 13.4037. Also, the value of the objective function $l^T(\text{diag}(\hat{\rho})) l$ at this solution is 2.5359.

Case 2: Now, instead of using $\rho = 1$, the elements of $\hat{\rho}$ are replaced with the optimal tension coefficients determined previously for the structure in Figure 2.7 (b) which has the same configuration as the structure in Figure 2.9; thus, $\hat{\rho}$ is as follows:

$$\hat{\rho} = [0.8825 \ 0.8826 \ 0.8829 \ 0.8826 \ 0.8829 \ 0.8825 \ 1.5288 \\ 1.5288 \ 1.5288 \ -1.5288 \ -1.5288 \ -1.5288]$$

With the constraints and initial starting values of nodal coordinates same as in Case 1, $l = [1 \ 1 \ 1 \ 1 \ 1 \ 1 \ 1 \ 1 \ 1 \ 1.4679 \ 1.4679 \ 1.4679]^T$ is again the solution to (2.32) but the value of the objective function for this solution is 8.1451×10^{-5} . Thus, the sum of the lengths of all structural members is again 13.4037.

Case 3: To be convinced that not any arbitrary value of $\hat{\rho}$ gives the desired tensegrity structure, consider the following choice of $\hat{\rho}$:

$$\hat{\rho} = [0.8825 \ 0.8826 \ 0.8829 \ 0.8826 \ 0.8829 \ 0.8825 \ 1.5288 \ 1.5288 \ 1.5288 \ -1 \ -2 \ -3]$$

With the constraints and initial starting values of nodal coordinates same as in Case 1, the solution to (2.32) with these set of tension coefficients is $l = [1 \ 1 \ 1 \ 1 \ 1 \ 1 \ 1 \ 1 \ 1 \ 0.5176 \ 1.4142 \ 1.9319]^T$ which forms a collapsed (or 2-dimensional) structure and the sum of the lengths of all structural members is 12.8637.

Case 4: Lastly, now consider using the following optimal tension coefficient vector again for the optimization problem in (2.32):

$$\hat{\rho} = [0.8825 \ 0.8826 \ 0.8829 \ 0.8826 \ 0.8829 \ 0.8825 \ 1.5288 \\ 1.5288 \ 1.5288 \ -1.5288 \ -1.5288 \ -1.5288]$$

This time the constraints would just be that none of the member length should be less than a positive scalar. Equivalently, the length of any member (the distance between two connected nodes) should be at least non-zero. This constraint can be written in the following form:

$$u^T \cdot u - \tau = 0 \quad , \quad v^T \cdot v - \tau = 0 \quad , \quad w^T \cdot w - \tau = 0 \quad (2.33)$$

where u , v , and w are already defined in (2.6), and τ is a positive scalar.

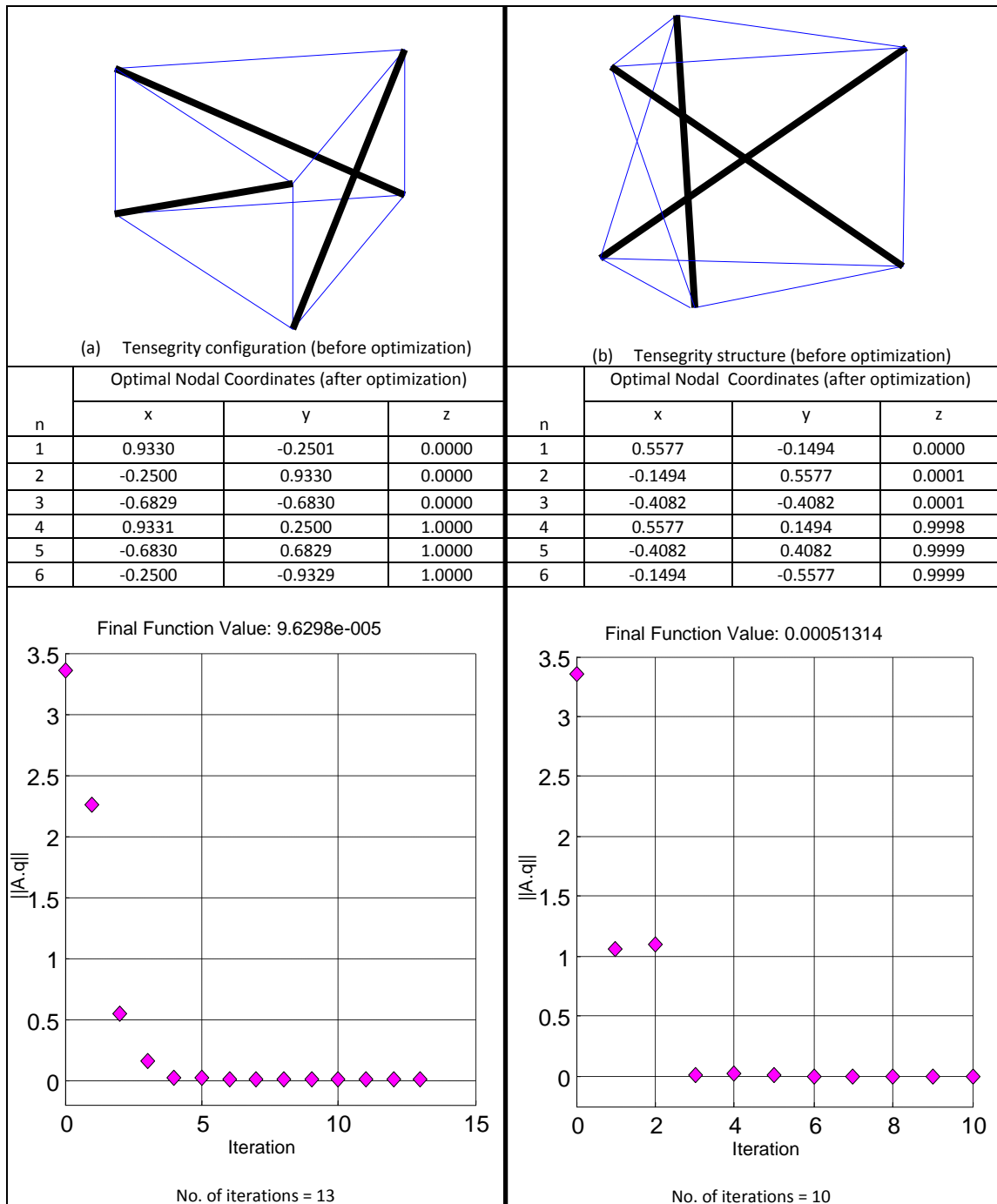


Figure 2.8: Nodal coordinates obtained from the force density matrix of valid set of tension coefficients using an optimization approach.

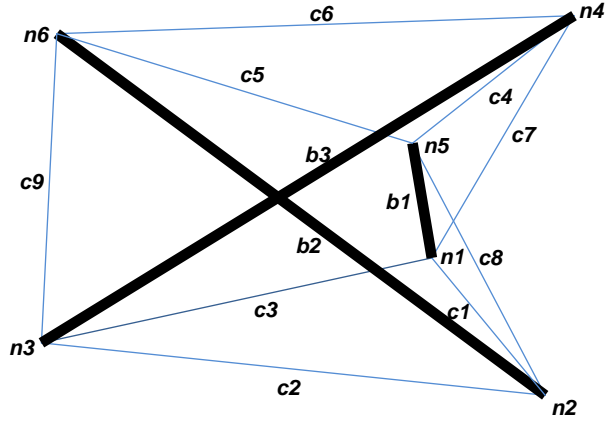


Figure 2.9: Tensegrity structure to be determined from geometric consideration

Let $\tau = 5$, for instance, so that (2.32) is re-written as follows:

$$\begin{aligned} \min_{x,y,z} \quad & l^T \cdot (\text{diag}(\hat{\rho})) \cdot l \\ \text{subject to: } & u^T \cdot u - 5 = 0, \quad v^T \cdot v - 5 = 0, \quad w^T \cdot w - 5 = 0 \end{aligned} \quad (2.34)$$

The solution to (2.34) is as follows:

$$l = [1 \ 1 \ 1 \ 1 \ 1 \ 1 \ 0.9606 \ 0.9606 \ 0.9606 \ 1.4413 \ 1.4413 \ 1.4413]^T$$

The sum of the lengths of all structural members is 13.2055. The results of the above four cases are summarized in Table 2.5.

From the above, it can be seen that the lengths of all structural members and the sum of their lengths remain the same for the first two cases (cases 1 and 2) though they had different elements for the vector $\hat{\rho}$. Furthermore, although the vector $\hat{\rho}$ is the same for case 2 and 4 and the lengths of members c_1, c_2, \dots, c_6 are also the same in both cases, the sum of the lengths of all structural members in case 4 is smaller compared to that of case 2. The implication is that, the choice of the vector $\hat{\rho}$ does indeed determine the optimal solution of the length minimization problems in (2.30), (2.32) and (2.34). Thus, the optimal selection of the vector $\hat{\rho}$ would be of utmost importance in the form-finding involving geometric consideration alone. Indeed, the vector $\hat{\rho}$ is obtained from the vector of tension coefficients as these cases illustrate. Moreover, the values of $\|A \cdot \mathfrak{q}\|_2$, where $\mathfrak{q} = \hat{\rho}^T$, are 1.7932, 5.1314×10^{-4} , 4.8506 and 5.8696×10^{-5} for cases 1, 2, 3 and 4, respectively. Thus, case 1 which is the equivalence of (2.30) proposed in

[114] has much larger residual forces at the nodes than case 2 or case 4 since it does not take into account optimal selection of the vector of tension coefficients for that particular structural configuration. It is well-known that form-finding method that does not take into account forces (tension coefficients) of the structural members does not lead to an outcome of structural assembly whose stability (due to pre-stress) is guaranteed [116].

Table 2.5: Relationship between the vector of tension coefficients and kinematic form-finding method

Case	Parameter	members $c1, c2, \dots, c6$	members $c7, c8, c9$	members $b1, b2, b9$	Total length	$\ A \cdot q\ _2$
1	Length	1, 1, 1, 1, 1, 1	1, 1, 1	1.4679 1.4679 1.4679	13.4037	1.7932
	Tension coefficient	1, 1, 1, 1, 1, 1	1, 1, 1	-1, -1, -1		
2	Length	1, 1, 1, 1, 1, 1	1, 1, 1	1.4679 1.4679 1.4679	13.4037	5.131×10^{-4}
	Tension coefficient	0.8825, 0.8826, 0.8829, 0.8826, 0.8829, 0.8825	1.5288 1.5288 1.5288	-1.5288 -1.5288 -1.5288		
3	Length	1, 1, 1, 1, 1, 1	1, 1, 1	0.5176 1.4142 1.9319	12.8637	4.8506
	Tension coefficient	0.8825, 0.8826, 0.8829, 0.8826, 0.8829, 0.8825	1.5288 1.5288 1.5288	-1 -2 -3		
4	Length	1, 1, 1, 1, 1, 1	0.9606 0.9606 0.9606	1.4413 1.4413 1.4413	13.2055	5.8696×10^{-5}
	Tension coefficient	0.8825, 0.8826, 0.8829, 0.8826, 0.8829, 0.8825	1.5288 1.5288 1.5288	-1.5288 -1.5288 -1.5288		

Thus, a more general approach for form-finding tensegrity structures from a geometric consideration alone (or in the context of the subject of this section, obtaining nodal coordinates from geometric consideration) is to find, for instance, the solution of the following optimization problem:

$$\min_{x,y,z} \quad l^T \cdot (\text{diag}(\hat{p})) \cdot l$$

$$\text{subject to: } u^T \cdot u - \tau_1 = 0, v^T \cdot v - \tau_2 = 0, w^T \cdot w - \tau_3 = 0 \quad (2.35)$$

where \hat{p} is the optimal vector of tension coefficients and the positive scalars τ_1 , τ_2 and τ_3 (which may be equal or different) are the scaling factors that define the magnitudes of the lengths of the structural members.

Lastly, the advantage of this method of obtaining nodal coordinates, from a geometric consideration, is that it establishes a relationship between the static and kinematic form-finding methods which renders the control of forces of structural member possible for these methods. More so, it is thought that kinematic form-finding methods are only applicable to systems with a small number of structural members supposedly due to the large constraints that would be required for any larger systems [100]. Writing the form-finding problem as an optimization problem as in (2.35), for instance, alleviates this obstacle and makes this form-finding process feasible for larger systems and there are many other ways of expressing the constraints in simpler forms. Moreover, the method of obtaining nodal coordinates from a valid vector of tension coefficients using the force density matrix presented in the preceding section (see equation (2.25)) has the special advantage in that constraints may not be necessary to obtain an optimal solution as the example in Figure 2.8 shows.

2.2.3 A Constrained Optimization Approach for the Form-finding of Tensegrity Structures

Given a tensegrity configuration, the main task of form-finding involves finding an optimal set of tension coefficients and/or nodal coordinates for which the structure is in a state of static equilibrium due to pre-stress in the absence of external forces. From the nullspaces and constrained optimization methods of obtaining tension coefficients and nodal coordinates for a tensegrity configuration, two form-finding methods that may be deduced, are summarized in Table 2.6.

In methods A and B, the process of form-finding tensegrity structures from an initial configuration has been divided into two main tasks. The first main task, Step 3 in both methods, involves using the constrained optimization method given in (2.22) to obtain the optimal vector of tension coefficients for a given tensegrity configuration. Also, in methods A and B, the second main task (steps 5 and 4 in methods A and B, respectively) involves determining the nodal coordinates for a given set of tension coefficients. The reason for dividing the task into two is that the equation of equilibrium is a nonlinear function of nodal coordinates and member forces. By expressing the

equation in the tension coefficients form, as in (2.8) for example, the equation has been linearised into a set of linear equations of tension coefficients. Conversely, when the equation is expressed in the force density form, as in (2.11) for example, the equation has been linearised into a set of linear equations of nodal coordinates.

Table 2.6: Descriptions of two methods for obtaining tensegrity structures using constrained optimization approach

Method A	Method B
<p>Step 1: Define the initial configuration (in matrix C) and a starting vector of tension coefficients and a feasible geometry.</p> <p>Step 2: Compute A</p> <p>Step 3: Obtain the vector of tension coefficients \mathbb{q} from the optimization model in (22):</p> $\min_{\mathbb{q}} \quad \sqrt{\mathbb{p}^T \mathbb{p}}$ <p>subject to: $h_i(\mathbb{q}_i) = 0,$ $g_i(\mathbb{q}_i) \leq 0,$ $lb_i \leq \mathbb{q}_i \leq ub_i, \quad i = 1, 2, \dots, b$</p> <p>Step 4: Compute D using \mathbb{q} from Step 3.</p> <p>Step 5: Find new nodal coordinate vectors x, y and z for the structure from the nullspace of D.</p> <p>Step 6: Check if the equation of equilibrium is satisfied (for example, $\ A \cdot \mathbb{q}\ _2 < tolerance$ or state of self-stress, $s > 0$, is found); if satisfied, a tensegrity structure is found, terminate the process. Otherwise, go back to Step 2.</p>	<p>Step 1: Define the initial configuration (in matrix C) and a starting vector of tension coefficients and a feasible geometry.</p> <p>Step 2: Compute A</p> <p>Step 3: Obtain the vector of tension coefficients \mathbb{q} from the optimization model in (22):</p> $\min_{\mathbb{q}} \quad \sqrt{\mathbb{p}^T \mathbb{p}}$ <p>subject to: $h_i(\mathbb{q}_i) = 0,$ $g_i(\mathbb{q}_i) \leq 0,$ $lb_i \leq \mathbb{q}_i \leq ub_i, \quad i = 1, 2, \dots, b$</p> <p>Step 4: Find new nodal coordinate vectors x, y and z for the structure from the optimization model:</p> $\min \quad l^T \cdot (diag(\hat{\rho})) \cdot l$ <p>subject to: $h_i(l_i) = 0,$ $g_i(l_i) \leq 0, \quad i = 1, 2, \dots, b$</p> <p>Step 5: If $r_{k+1} - r_k < tolerance$, terminate the process (where $r_k = \sqrt{\mathbb{p}^T \mathbb{p}}$). Otherwise, go back to Step 2.</p>

In other words, by fixing the nodal coordinates (that is, defining the tensegrity configuration) and determining the tension coefficients for the configuration, the first task ‘assumes’ that tension coefficients are independent of nodal coordinates which is not the case. Recall that tension coefficient is the force-to-length ratio and the length is dependent on the nodal coordinates, so the tension coefficient is also dependent on it. Similarly, by fixing the tension coefficients and determining the nodal coordinates, the second task ‘assumes’ that the nodal coordinates are independent on the tension

coefficients. Thus, an optimization model that combine these two equations takes advantage of finding solutions to two linear equations at every iteration which may be simpler and less computational expensive than iteratively finding a solution to a single but nonlinear equation.

Furthermore, in the second main task, different approaches have been used for the two methods. For method A, the nodal coordinates in Step 5 are obtained from the nullspaces of the force density matrix since optimal vector of tension coefficients, for the particular configuration, has been determined from Step 3. For method B, the nodal coordinates are obtained in Step 4 by finding solution to the constrained optimization problem of (2.25); the optimization model in (2.35) – involving a set of linear equations – may also be used instead of (2.25). It is worth noting that method A fails if the set of tension coefficients, from which the vectors x , y and z which satisfies the orthonormality constraint $xyz^Txyz = I$ (where $xyz = [x \ y \ z]$) are obtained, does not produce exactly four zero singular values from the D matrix during any iteration and the iteration process continues until a solution is found. Recall that x , y and z form an orthonormal set since they are obtained from the nullspace of the same matrix. Such an orthonormality constraint is not required in method B but, in fact, it can be included. To reveal certain properties of tensegrity structures that satisfy this constraint, the constraint will be include in method B and the new method will be called method C; thus, with all other steps of method B remaining the same for method C, the Step 4 for method C is written as follows:

Step 4: Find new nodal coordinate vectors x , y and z for the structure from the optimization model:

$$\begin{aligned} \min \quad & l^T \cdot (\text{diag}(\hat{\rho})) \cdot l \\ \text{subject to:} \quad & h_i(l_i) = 0, \\ & g_i(l_i) \leq 0, \quad i = 1, 2, \dots, b \\ & xyz^T \cdot xyz = I. \end{aligned} \tag{2.36}$$

Figure 2.10 shows the results of tensegrity structures obtained from initial configurations using the form-finding methods A, B and C. It is worth noting that the main distinction between methods B and C is the orthonormality constraint present in Step 4 of method C; all other similarity constraints are exactly the same. While the three methods are capable of finding tensegrity structures for the first configuration, the first method (method A) fails to find the second and the third configurations as shown in Figure 2.10. The nullspace form-finding methods presented in Section 2.2 (including

the method in [103], [104]) also fail to find tensegrity structures when the second and third initial configurations were defined for them which are an obvious limitation of those methods.

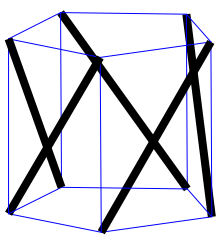
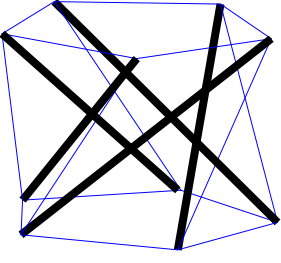
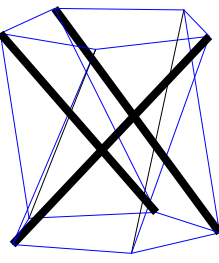
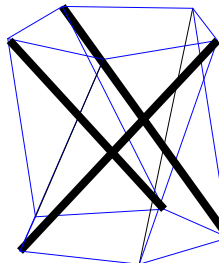
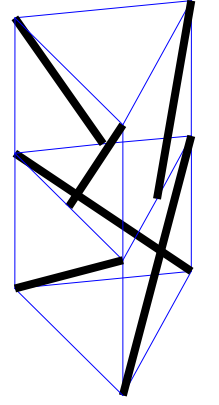
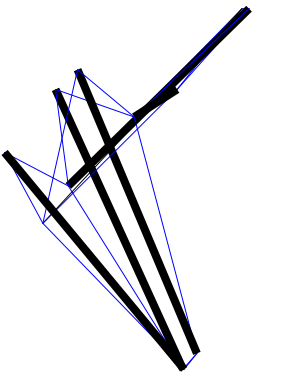
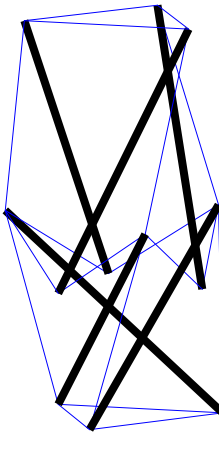
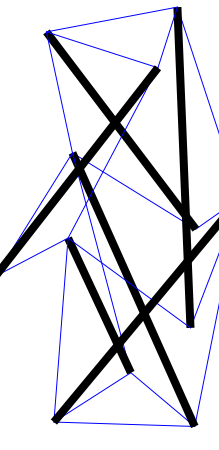
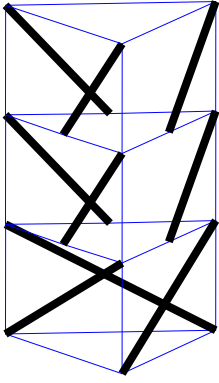
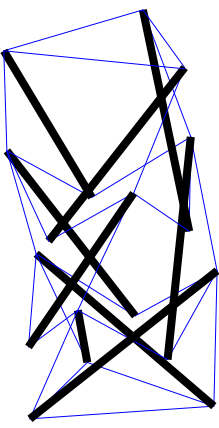
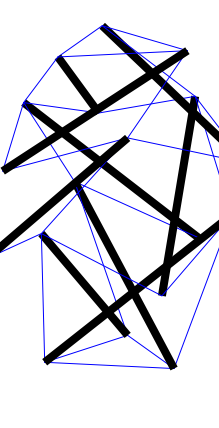
Tensegrity configuration	Tensegrity Structures		
	Method A	Method B	Method C
1) 			
2) 	 Method failed (a 2D structure – top view)		
3) 	Method failed (no solution found)		

Figure 2.10: Tensegrity structures obtained using form-finding methods A, B and C.

The important question, however, is what the difference between the tensegrity structures obtained using methods B and C is. To answer this question, consider the following: In configuration 1, noting that the lengths of the side cables of the top and bottom polygons are the same for both the tensegrity structures of methods B and C, the

area of the surface of the top and bottom polygons must be the same. However, the heights of the configurations are different. The height of the structure, measured by the distance between the top and the bottom parallel polygons, are 1.1063 and 0.8447 for methods B and C, respectively. Thus, in addition to obtaining a solution to a static equilibrium problem, method C solves a minimum total surface area and volume problem. This can be seen more clearly when heights are compared for larger structures; for example, using methods B and C, the heights are 2.2197 and 1.2960, respectively, for configuration 2, and 2.1863 and 1.2776, respectively, for configuration 3. Parameters of the tensegrity structures in Figure 2.10 are shown in Table 2.7.

The form-finding algorithm Method B will be used in the remainder of this thesis for obtaining tensegrity structures. It should be observed that the convergence of this algorithm depends on the convergence of the interior point algorithm for solving constrained optimization problem that is employed twice at any given iteration. The proof convergence of the interior point algorithm can be found, for instance, in [105].

2.2.4 Examples of Applications of the Constrained Optimization Form-finding Algorithm

The constrained optimization method, the method B in particular, described in the previous sections for form-finding of practical tensegrity structures will be used to demonstrate its applicability to a wide range and complex problems. A class 2 tensegrity configuration, given in [2], that can be used as a shelter on a disaster site for temporary hospital or housing is shown in Figure 2.11.

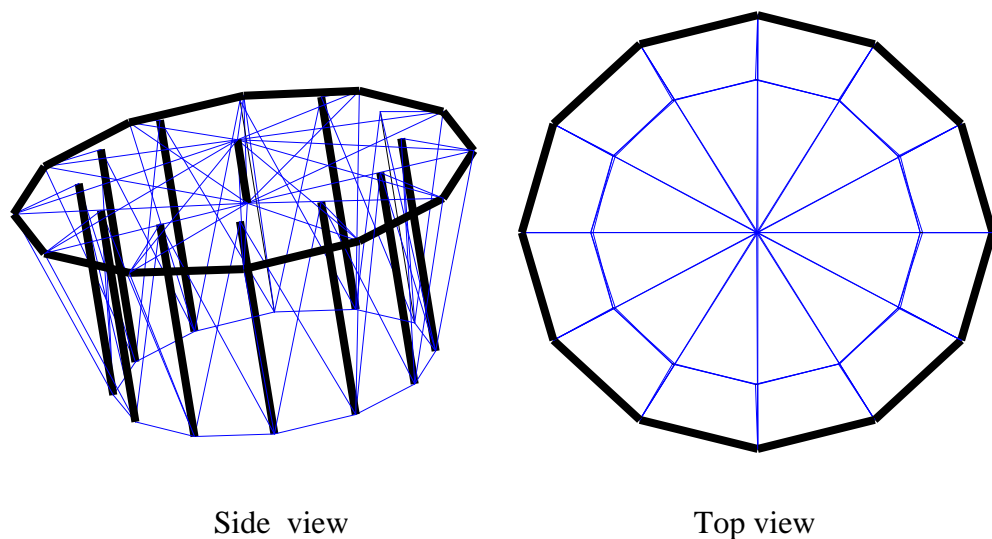


Figure 2.11: A class 2 tensegrity configuration [2].

The large structure of Figure 2.11 includes 84 cables, 25 bars and 38 nodes. From the symmetric nature of the structure, the following constraints are used:

Constraints on tension coefficients:

$$q_i - q_{11} = 0 \text{ for } i = 2 \text{ to } 12$$

$$q_i - q_{13} = 0 \text{ for } i = 14 \text{ to } 24$$

$$q_i - q_{25} = 0 \text{ for } i = 26 \text{ to } 36$$

$$q_i - q_{37} = 0 \text{ for } i = 38 \text{ to } 48$$

$$q_i - q_{49} = 0 \text{ for } i = 50 \text{ to } 60$$

$$q_i - q_{61} = 0 \text{ for } i = 62 \text{ to } 72$$

$$q_i - q_{73} = 0 \text{ for } i = 74 \text{ to } 84$$

$$q_i - q_{85} = 0 \text{ for } i = 86 \text{ to } 96$$

$$q_i - q_{97} = 0 \text{ for } i = 98 \text{ to } 109$$

Length constraints:

$$l_i - l_1 = 0 \text{ for } i = 2 \text{ to } 12$$

$$l_i - l_{13} = 0 \text{ for } i = 14 \text{ to } 24$$

$$l_i - l_{25} = 0 \text{ for } i = 26 \text{ to } 36$$

$$l_i - l_{37} = 0 \text{ for } i = 38 \text{ to } 48$$

$$l_i - l_{49} = 0 \text{ for } i = 50 \text{ to } 60$$

$$l_i - l_{61} = 0 \text{ for } i = 62 \text{ to } 72$$

$$l_i - l_{73} = 0 \text{ for } i = 74 \text{ to } 84$$

$$l_i - l_{85} = 0 \text{ for } i = 86 \text{ to } 96$$

$$l_i - l_{97} = 0 \text{ for } i = 98 \text{ to } 109$$

$$l_1 - 1.8117 = 0$$

Node constraints:

$$\tilde{y}_j - y_j = 0 \text{ for } j = 1 \text{ to } 38.$$

i and j denote member and node, respectively; the constraints $\tilde{y}_j - y_j = 0$ for $j = 1$ to 38 fix the y coordinate values of the nodes.

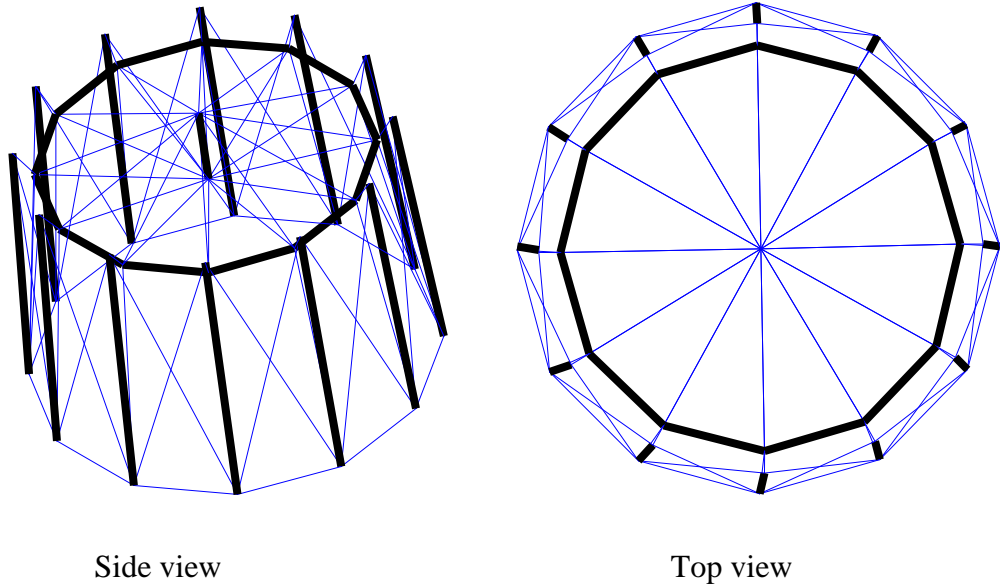


Figure 2.12: Tensegrity structure obtained from a class 2 tensegrity configuration using constrained optimization form-finding approach.

Using the constrained optimization form-finding method, the final tensegrity structure is shown in Figure 2.12. With the defined configuration and a feasible

geometry that takes into account the symmetric nature of the structure for which the original length of the cable member $i = 1$ is 1.8117, the optimization model is constrained to have $l_1 - 1.8117 = 0$. The stopping criterion is $|r_{k+1} - r_k| < 10^{-3}$ where $r_k = \sqrt{\mathbb{p}^T \mathbb{p}}$. The value of $\|A \cdot \mathbb{q}\|_2$ reduces from 3.3401 in the first iteration to 1.4373 as the form-finding algorithm terminates after the 9th iteration. The initial and final sums of the lengths of the structural members are 439.3161 and 362.2277, respectively.

Table 2.7: Parameters of tensegrity structures of Figure 2.10 obtained using form-finding methods A, B and C.

Tensegrity configuration		Tensegrity Structures		
		Method A	Method B	Method C
1)	$\ A \cdot \mathbb{q}\ _2$	1.8526×10^{-7}	1.8472×10^{-4}	1.8526×10^{-7}
	l_{1-10}	1	1	1
	l_{11-15}	1.0730	1.3491	1.1534
	l_{16-20}	1.6890	1.8765	1.7412
	Sum of lengths	23.8097	26.1285	24.4727
2)	$\ A \cdot \mathbb{q}\ _2$		2.3003×10^{-7}	0.0831
	l_{1-3}		1	1
	l_{4-9}		0.7378	0.9198
	l_{10-15}		1.1667	0.8571
	l_{16-18}		1	1
	l_{19-25}		1.6705	1.5292
	Sum of lengths		27.4503	25.8365
3)	$\ A \cdot \mathbb{q}\ _2$		6.1776×10^{-7}	0.0844
	l_{1-3}		1	1
	l_{4-9}		0.6509	0.9753
	l_{10-18}		0.7876	0.7725
	l_{19-24}		0.6509	0.9752
	l_{25-27}		1	1
	l_{28-36}		1.3322	1.5436
	Sum of lengths		32.8896	38.5503

As another example, Figure 2.13 shows a truss-like class 2 tensegrity configuration with 36 cables and 13 bars. Note that the eight middle bars which make contact at the middle can be considered as four ‘X’ pieces or rigid bodies as in the original patent of Snelson [6]. Using the constrained optimization form-finding approach, and with each of the four rigid bodies still considered as two independent bars, the constraints used for form-finding are as follows:

Constraints on tension coefficients:

$$q_i - q_1 = 0 \quad \text{for } i = 2 \text{ to } 20$$

$$q_i - q_{21} = 0 \quad \text{for } i = 22 \text{ to } 36$$

$$q_i - q_{37} = 0 \quad \text{for } i = 38 \text{ to } 40$$

$$q_i - q_{41} = 0 \quad \text{for } i = 42 \text{ to } 44$$

$$q_i - q_{45} = 0 \quad \text{for } i = 46 \text{ to } 49$$

Length constraints:

$$l_i - l_1 = 0 \quad \text{for } i = 2 \text{ to } 20$$

$$l_i - l_{21} = 0 \quad \text{for } i = 22 \text{ to } 36$$

$$l_i - l_{37} = 0 \quad \text{for } i = 38 \text{ to } 40$$

$$l_i - l_{41} = 0 \quad \text{for } i = 42 \text{ to } 44$$

$$l_i - l_{45} = 0 \quad \text{for } i = 46 \text{ to } 49$$

$$l_1 - 1 = 0$$

Node constraints:

$$\check{x}_j - x_j = 0 \quad \text{for } j = 1 \text{ to } 20.$$

i and j denote member and node, respectively; the constraints $\check{x}_j - x_j = 0$ for $j = 1$ to 20 fix the x coordinate values of the nodes.

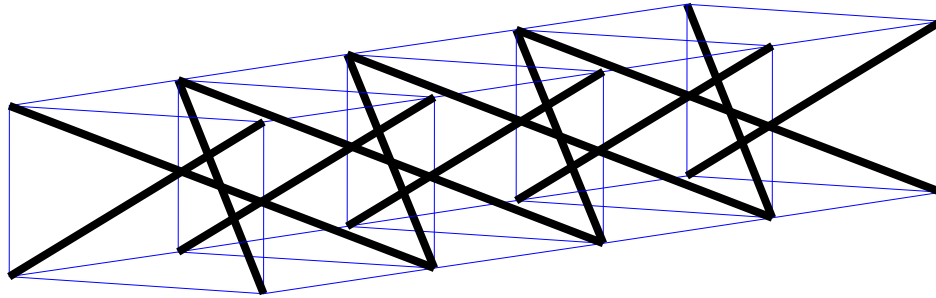


Figure 2.13: A truss-like class 2 tensegrity configuration and structure

With these constraints, the structural geometry (therefore, lengths of structural members) of the final tensegrity structure remains exactly the same as the original configuration in Figure 2.13 but the optimal set of tension coefficients has been found for the structure and algorithm terminates at the second iteration when $\|A \cdot q\|_2 = 0.2966$. The length and tension coefficient associated with each member are shown in Table 2.8. Note that the node constraints are necessary for obtaining Figure 2.12 or 2.13 to keep the overall shape of the structure the same but optimal as desired. Without these constraints, the optimization obtains an arbitrary shape or a collapsed structure in which there are members with zero lengths.

**Table 2.8: Length and tension coefficient associated with each member of the class
2 tensegrity structure**

Member	1 - 12	13 - 24	25 - 36	37 - 48	49 - 60	61 - 72	73 - 84	85 - 96	97 - 109
Length	1.8117	5.2903	5.3111	4.5403	0.5925	3.0655	2.9406	5.0082	1.5000
α	0.1000	0.1000	0.1000	0.1000	0.6073	0.1247	0.2075	-0.2749	-0.9137

2.2.5 Discussions

In this section, the main findings in the preceding sections will be summarized and the main advantages, as well as limitations, of using the constrained optimization method for form-finding of tensegrity structures will be presented.

Firstly, the wealth of information on tensegrity structures contained in their four fundamental spaces of the equilibrium matrices can be used for form-finding of these structures. However, using only the information obtained from the fundamental spaces for form-finding purposes limits their application to tensegrity structures with few structural members and whose member connectivity are relatively simple. Although, in some cases, form-finding is possible with only minimal knowledge of the connectivity and type of each member – compressive or tensile – these methods offer little or no control over member forces or lengths. This is not to mean that the fundamental spaces of the equilibrium matrices are not useful for form-finding; in fact, it is the contrary. They reveal limitations of these form-finding methods and they may be used, in conjunction with other methods, to design optimal tensegrity structures. In particular, these have been used, as demonstrated in this chapter, in conjunction with a new constrained optimization approach for form-finding of tensegrity structures and it has been demonstrated that they can be used for very large tensegrity structures with complex connectivity of members. This new method allows for the control of member forces and lengths.

Secondly, the well-known advantage of the kinematic form-finding method is that it allows the control of lengths of structural members but the stability of the structure obtained using this method is not guaranteed [117]. Moreover, it is thought that it is only applicable to systems with a few structural members due to, it is argued, the large number of constraints that would be required for larger systems. Not only has a relationship between the kinematic form-finding method and the forces in structural members with guaranteed stability of the resulting structure been established, but also a

simple way to alleviate the problem of handling large constraints by writing them in simpler forms has been shown. The use of this new approach was described using a class 2 tensegrity configuration given in [2] that can be used as a shelter on a disaster site for a temporary hospital or housing, for instance.

Thirdly, for the new constrained optimisation framework for form-finding of tensegrity structures proposed in the preceding section, the process of form-finding these structures from initial tensegrity configurations has been divided into two main tasks: obtaining the optimal vector of tension coefficients for the given configuration and determining the nodal coordinates for the optimal set of tension coefficients. Thus, the optimization model takes advantage of finding solutions to two linear equations at every iteration which may be simpler and less computationally expensive than iteratively finding a solution to a single but nonlinear set of equations.

Lastly, as with other form finding methods, the constrained optimization method is not without its disadvantages. The main disadvantage is the requirement that feasible initial nodal coordinates must be defined for the tensegrity configuration. This can be a daunting task for very large structures. However, this shortcoming can be overcome by using a pre-processing software, such as the Formian programming language [118] as suggested in [8], for example, to obtain initial feasible nodal coordinates. The use of the form-finding algorithm is also limited to idealized structures satisfying the assumptions discussed at the beginning of the chapter (see Section 2.2.1).

2.3 Other Form-finding Methods

It has been shown that it is possible to obtain tensegrity structures from geometric considerations alone (the kinematic form-finding methods). Moreover, the equations of static equilibrium in the form of tension coefficients, or force densities, for form-finding of tensegrity structures via the nullspace and the constrained optimization approaches have also been presented. Other methods also exist that use these and other equations for the form-finding of tensegrity structures. A brief discussion on some of these other methods is presented in what follows.

An analytical method, presented in [69], finds the valid set of tension coefficients to satisfy the maximal rank condition. Many methods that search for self-equilibrium

tensegrity structures arbitrarily using the so-called *minimal information* – connectivity of members and their types being the only initial starting parameters – have also been proposed [12], [104]. Algebraic form-finding methods that render the required mathematical elegance to the form-finding process are given in [70], [71] but they require extensive use of software capable of handling symbolic variables and computations. Symmetry can greatly simplify the form-finding process of pre-stressed structural assemblies in general; a technique that takes advantage of symmetry for finding all possible tensegrity structures with a given connectivity is given in [72]. The method presented in [71] also took advantage of symmetry in reducing the $n_c \times n_c$ equilibrium matrix (n_c denotes the number of cables), obtained from the virtual work principle (with the structural geometry defined by a set of generalised coordinates), to a square matrix whose dimension is only determined by the number of dissimilar cables.

Apart from the kinematic and static form-finding methods, there are the finite element method, the energy method and the dynamic relaxation method of form-finding. The equations from which these three methods originated are different from the equations used for the static and kinematic form-finding methods. In the finite element method [73], the total potential energy of a tensegrity configuration is minimized using an equation involving the column vector of nodal coordinates, the external load vector and the global stiffness matrix. Because the energy in a tensile member increases with increase in length and that in a compressive member increases with length decrease, the energy method of form-finding [54] minimizes an energy function by testing for the positive semi-definiteness of the stress matrix – a matrix identical to the force density matrix in equation (2.11). The dynamic relaxation method is a very successful and widely used form-finding and static analysis tool for tension structures [4]. It was used for form-finding of tensegrity structures in [74]. In this method, the mass of the structure is assumed to be concentrated at the nodes. As such, for a given configuration, the peak in kinetic energy is sorted so that the position of the nodal masses of the discretized structure is readjusted – which corresponds to the minimum potential energy for that configuration. The computation is repeated with every new configuration until the peak kinetic energy is very small – meaning that the system has settled to a static equilibrium position [4].

Some computational techniques that have been used in association with the different form-finding methods include the genetic algorithm [75], [76], neural

networks [77] and the sequential quadratic programming methods [78], among others. A review on state-of-the-art research on form-finding methods of tensegrity structures and the associated computational techniques can be found in [100], [116].

2.4 Summary

In this chapter the description of a new constrained optimization form-finding algorithm for tensegrity structures has been given. First, the description of the nullspace (matrix decomposition) approach to form-finding was presented then the form-finding technique was reformulated as a constrained optimization problem as shown in Table 2.9. The constrained optimization problem was solved using the interior point algorithm. The main characteristic of the constrained optimization form-finding algorithm is that the process of form-finding of a structure from an initial tensegrity configuration has been divided into two main tasks: obtaining the optimal vector of tension coefficients for the given configuration and determining the nodal coordinates for the optimal set of tension coefficients. Next, a number of examples were described to show that the presented form-finding method offers control of both forces and lengths of structural members. Lastly, the chapter concludes with a short review of other form-finding methods.

In the next chapter, the modelling of tensegrity structures using the Finite Element Method will be covered. The chapter will also include the static and dynamic analyses and the model simulation of tensegrity structures obtained using the form-finding method presented in this chapter.

Table 2.9: The constrained optimization form-finding algorithm

<p>Algorithm:</p> <p><i>Step 1:</i> Define the initial configuration (in matrix C) and a starting vector of tension coefficients and a feasible geometry.</p> <p><i>Step 2:</i> Compute A</p> <p><i>Step 3:</i> Obtain the vector of tension coefficients q from the following optimization model:</p> $\min_q \quad \sqrt{p^T p}$ <p>subject to: $h_i(q_i) = 0, \quad g_i(q_i) \leq 0, \quad lb_i \leq q_i \leq ub_i, \quad i = 1, 2, \dots, b$</p> <p><i>Step 4:</i> Find new nodal coordinate vectors x, y and z for the structure from the optimization model:</p> $\min_{x,y,z} \quad l^T \cdot (\text{diag}(\hat{p})) \cdot l$ <p>subject to: $h_i(l_i) = 0, \quad g_i(l_i) \leq 0, \quad i = 1, 2, \dots, b$</p> <p><i>Step 5:</i> If $r_{k+1} - r_k < \textit{tolerance}$, terminate the process (where $r_k = \sqrt{p^T p}$). Otherwise, go back to Step 2.</p>

Chapter 3

STATIC AND DYNAMIC ANALYSES OF TENSEGRITY STRUCTURES

3.1 Introduction

The study of (structural) systems in some state of rest (static equilibrium) or in a dynamic motion is an important aspect of the engineering study of such systems. Given the pre-stressed nature of any tensegrity structural system that is obtained from any form-finding method, an important step in the design process is to develop mathematical models that describe the behaviour of the system to allow static and dynamic analyses. Analyses of tensegrity structures are necessary to understand the properties of these structures in their equilibrium states and to establish the relationships among load response, geometry and stiffness. Modelling the dynamics of multivariable tensegrity structural systems accurately and effectively will enable the understanding of their behaviour over time and provide guidance on the control techniques that can be employed for their precision control. This chapter outlines the theory behind static and dynamic analyses of tensegrity structures. Firstly, the derivation of the mass and stiffness matrices is described using the Finite Element Method (FEM). Next, the solution procedure for carrying out pseudo-static analysis of a tensegrity structure is presented. Subsequently, the dynamic equations of motion governing a general tensegrity structure, written in the time domain, are converted into a state-space representation. With this representation, the study of the dynamic responses tensegrity structures can be easily carried-out. The state-space representation simplifies the analyses of tensegrity structures, particularly structures with several degrees of freedom, and provides a new insight into the behaviour of these interesting and yet challenging structures, at least from a control systems' viewpoint.

Thus, in this chapter, the three main tasks to be carried-out are as follows: the modelling via the FEM, the study of the pseudo-static properties, and the study of the dynamic responses via the state-space model representation of tensegrity structures.

3.2 Static and Dynamic Analyses of Tensegrity Structures Using the Finite Element Method

The FEM has been extensively explored in the field of solid and structural mechanics to solve a wide range of problems in the field [119–122]. The method will be employed in this section in the derivation of the element matrices. The matrices are used in the rest of the thesis for several specific modelling cases.

3.2.1 Derivation and Assembly of the Element Matrices

3.2.1.1 The Stiffness Matrix

In this section, the usage of the definitions and notations given in Section 2.2.1.1 will be continued. From the coordinates of the nodes of a tensegrity structure in 3-dimensional Euclidean space assembled into column vectors $x \in \mathbb{R}^n$, $y \in \mathbb{R}^n$ and $z \in \mathbb{R}^n$, the coordinates of node i is represented as (x_i, y_i, z_i) and n is the number of nodes in the structure. Thus, a matrix of nodal coordinates $N \in \mathbb{R}^{3 \times n}$ may be defined as follows:

$$\begin{aligned} N &= [x \quad y \quad z]^T \\ &= [n_1 \quad n_2 \quad \dots \quad n_i \quad \dots \quad n_n] \end{aligned} \quad (3.1)$$

where $n_i \in \mathbb{R}^3$, given by $n_i = [x_i \quad y_i \quad z_i]^T$, is the nodal coordinates of node i . Thus, the i^{th} column of N , n_i , corresponds to the coordinates of the i^{th} node of the structural system.

The i^{th} structural member connecting nodes h and j can be uniquely described by a Euclidean row vector $b_i \in \mathbb{R}^3$, given by $b_i = [x_h - x_j \quad y_h - y_j \quad z_h - z_j]$ and has the length $\|b_i\| = \|n_h - n_j\|$. Recalling the branch-node connectivity matrix C defined in equation (2.5), it will be noted that the i^{th} row of C , $C_i \in \mathbb{R}^n$, describes the structural configuration of the i^{th} structural member since the element of vector C_i has the value of +1 at the j^{th} entry and the value of -1 at the h^{th} entry and all other entries are zeros.

Thus, all members of the structural system can be assembled into a matrix $B \in \mathbb{R}^{m \times 3}$ as follows:

$$\begin{aligned} B &= [u \quad v \quad w] \\ &= [b_1^T \quad b_2^T \quad \dots \quad b_i^T \quad \dots \quad b_b^T]^T \\ &= C N^T \end{aligned} \quad (3.2)$$

where the vectors u , v , and w have already been defined in equation (2.6). Tensegrity structures are in the state of minimum potential energy and this energy (which is due to straining alone) for the i^{th} structural member can be written as follows:

$$\pi_i = \pi_i(\|b_i\|) \quad (3.3)$$

where (3.3) implies π_i is a function of $\|b_i\|$. Thus, the potential energy of the whole structural system can be written as follows:

$$\boldsymbol{\pi} = \sum_{i=1}^b \pi_i(\|b_i\|) \quad (3.4)$$

Note that $\boldsymbol{\pi}$ is a function of nodal coordinates (that is, $\boldsymbol{\pi} = \boldsymbol{\pi}(N)$) since b_i is a function of nodal coordinates (that is, $b_i = b_i(N)$). If p_i denotes a Euclidean column vector of nodal forces of the i^{th} node, vectors of nodal forces of the structural system can be obtained by differentiating the strain energy (which is a scalar function) with respect to the nodal displacements (which are vectors) and, assuming that the member forces and stresses are constants, the following relationship is obtained:

$$\mathbf{p}(N) = -\partial_N \boldsymbol{\pi}(N) \quad (3.5)$$

where $\mathbf{p}(N) \in \mathbb{R}^{3 \times n}$ is defined by $\mathbf{p}(N) = [p_i]_{1 \times n}$; that is, the nodal forces is computed by taking the negative of the directional derivative of the strain energy along the nodal displacement vectors). If the i^{th} structural member is connected to nodes h and j , the nodal force at node j due the strain of the i^{th} structural member is obtained as follows:

$$\begin{aligned} p_{ji} &= -\partial_{n_j} \pi_i(\|b_i\|) = \partial_{n_h} \pi_i(\|b_i\|) \\ &= -\pi_i' \cdot \partial_{n_j} \|b_i\| \\ &= -\pi_i' \cdot \frac{(n_h - n_j)}{\|n_h - n_j\|} \\ &= -\pi_i' \cdot \frac{b_i}{\|b_i\|} \end{aligned} \quad (3.6)$$

Therefore, Equation (3.6) may be written as follows:

$$p_{ji} = -q_i b_i \quad (3.7)$$

where q_i is the tension coefficient (or force density) of the i^{th} structural member and it is defined as follows:

$$q_i = \frac{\pi'_i}{\|b_i\|} \quad (3.8)$$

Thus, $q \in \mathbb{R}^b$ represents the vector of tension coefficients of structural members. Therefore, the forces at nodes h and j ($\check{p}_i \in \mathbb{R}^{1 \times 3n}$) due to the strain in the i^{th} structural member can be written as follows:

$$\check{p}_i = -q_i(C_i \otimes b_i) \quad (3.9)$$

where \otimes denotes the Kronecker product of two matrices. The nodal forces for the entire structural system can be written as follows:

$$\begin{aligned} P(N) &= \text{vec}(\mathbf{p}(N)) \\ &= \sum_{i=1}^b \check{p}_i \end{aligned} \quad (3.10)$$

where $\text{vec}(\cdot)$ is the vector valued function of a matrix defined as follows [123]:

$$\text{vec}(X_{p \times q}) = [x_1^T \ x_2^T \ \dots \ x_q^T]^T \quad (3.11)$$

Here, $x_i \in \mathbb{R}^{p \times 1}$ represents the i^{th} column vector of X . Thus, $P(N) \in \mathbb{R}^{1 \times 3n}$. In matrix form, $\mathbf{p}(N)$ can be written as follows:

$$\mathbf{p}(N) = B^T Q C \quad (3.12)$$

where Q is the diagonal matrix of the vector of tension coefficients $q \in \mathbb{R}^{b \times 1}$. Comparing (3.12) with the equilibrium equation (2.8) of Chapter 2 which is re-written here as follows:

$$\mathbb{A} \cdot \mathbb{q} = \mathbb{p} \quad (3.13)$$

where $\mathbb{A} = \begin{pmatrix} C^T U \\ C^T V \\ C^T W \end{pmatrix}$, $\mathbb{q} = L^{-1} f$ and $\mathbb{p} = \begin{pmatrix} P_x \\ P_y \\ P_z \end{pmatrix}$.

Noting that $P_x^T = q^T U^T C$, equation (3.12) can be rewritten as follows:

$$\mathbf{p}(N) = \begin{pmatrix} q^T U^T C \\ q^T V^T C \\ q^T W^T C \end{pmatrix} \quad (3.14)$$

Furthermore, assuming that the member forces and stresses are constants, the stiffness matrix of the structural system can be obtained by differentiating $\mathbf{p}(N)$ with respect to the nodal displacements as follows:

$$K(N) = -\partial_N P(N) \quad (3.15)$$

For the i^{th} structural member, the element stiffness in the global coordinate system can therefore be written as follows:

$$\begin{aligned} K_i(N) &= -\partial_{N_i} \check{p}_i(N_i) \\ &= -\partial_{N_i} (-q_i (C_i \otimes b_i)) \\ &= \partial_{N_i} (C_i \otimes q_i b_i) \end{aligned} \quad (3.16)$$

The following identity of matrix differentiation (see Lemma (6) in [124] for proof) should be recalled:

$$\frac{\partial(X \otimes Y)}{\partial Z} = \left(\text{vec}(X) \otimes \frac{\partial(Y)}{\partial Z} \right) \cdot (E_{nr \times nr} \otimes I_s) \quad (3.17)$$

where $Z \in \mathbb{R}^{p \times q}$, the elements of $X \in \mathbb{R}^{1 \times n}$ are constants with respect to Z , the elements of $Y \in \mathbb{R}^{r \times s}$ are differentiable functions of the elements of Z , $I_s \in \mathbb{R}^{s \times s}$ is an identity matrix and $E \in \mathbb{R}^{nr \times nr}$ is a permutation matrix given by $E = [e_{g,h}]_{nr \times nr}$ such that:

$$e_{g,h} = \begin{cases} 1, & \text{if } g = n(j-1) + k, \quad h = (k-1) + j \\ 0, & \text{otherwise} \end{cases} \quad \text{for } 1 \leq g \leq n, 1 \leq h \leq n \quad (3.18)$$

where $0 < k \leq n$ and $j = 1$. Thus, $E_{nr \times nr}$ is a square matrix with a single '1' in each row and each column; it can be thought to be an identity matrix with some rows/columns interchanged [124].

Substituting (3.8) into (3.16) and expanding the resulting matrix differential equation using the identity of matrix differentiation in (3.17) leads to the following results:

$$\begin{aligned}
K_i(N) &= -\partial_{N_i}(-q_i(C_i \otimes b_i)) \\
&= \partial_{N_i}(C_i \otimes q_i b_i) \\
&= (C_i^T \otimes (\frac{\pi_i'' b_i b_i^T}{\|b_i\|^2} + q_i (I_3 - \frac{b_i b_i^T}{\|b_i\|^2}))) \cdot (E_{n \times n} \otimes I_3) \quad (3.19)
\end{aligned}$$

The expression in (3.19) can also be represented, as given in [2], in the following forms:

$$K_i(N) = (C_i C_i^T \otimes [\frac{\pi_i'' b_i b_i^T}{\|b_i\|^2} + q_i (I_3 - \frac{b_i b_i^T}{\|b_i\|^2})]) \quad (3.20)$$

$$= (C_i C_i^T \otimes \kappa_i) \quad (3.21)$$

where κ_i is given as follows:

$$\kappa_i = \frac{\pi_i'' b_i b_i^T}{\|b_i\|^2} + q_i (I_3 - \frac{b_i b_i^T}{\|b_i\|^2}) \quad (3.22)$$

Thus, for the tensegrity structural system, the stiffness matrix can be expressed as follows:

$$K(N) = \sum_{i=1}^b K_i(N) \quad (3.23)$$

Writing κ_i in the form $\kappa_i = q_i I_3 + (\pi_i'' - q_i) \frac{b_i b_i^T}{\|b_i\|^2}$ and noting that $aa^T \otimes A = (a \otimes I)A(a^T \otimes I)$, the expression in (3.23) may be written as follows [2]:

$$K(N) = K_q(N) + K_e(N) \quad (3.24)$$

where $K_q(N)$ and $K_e(N)$ are defined as follows:

$$K_q(N) = C^T Q C \otimes I_3 \quad (3.25)$$

$$K_e(N) = (C^T \otimes I_3) \text{diag}[(\pi_i'' - q_i) \frac{b_i b_i^T}{\|b_i\|^2}] (C^T \otimes I) \quad (3.26)$$

K_q is called the pre-stress (or geometric) stiffness matrix and it is mainly a function of tension coefficients, while K_e is called the elastic stiffness matrix and it is mainly a function of material properties of the structural members [2], [68], [125].

3.2.1.2 The Relationship between the Geometric and Elastic Stiffness Matrices and the Stiffness Matrix of the Conventional Finite Element Method

The relationship between K_q and K_e and the stiffness matrix K of the conventional finite element method can be obtained as follows: The strain energy stored in a structural element i with two nodes n_j and n_h under axial deformation is given by $\pi_i = \frac{A_i E_i}{2} \int_0^{l_i} \varepsilon_i^2 dx$ where A_i , E_i , l_i , and ε_i are the cross-sectional area, Young's modulus, length and strain of the i^{th} member, respectively; the expression for strain is $\varepsilon_i = \frac{\partial \phi}{\partial x}$ where $\phi(x)$ is the variation axial displacement x ($\phi(x=0) = \bar{n}_j$ and $\phi(x=l_i) = \bar{n}_h$). Assuming ϕ is a linear function of x so that $\phi(x)$ may be written as $\phi(x) = \bar{n}_j + (\bar{n}_h - \bar{n}_j) \frac{x}{l_i}$, then $\frac{\partial \phi}{\partial x} = \frac{\bar{n}_h - \bar{n}_j}{l_i}$. Therefore, π_i can be expressed as follows:

$$\begin{aligned} \pi_i &= \frac{A_i E_i}{2} \int_0^{l_i} \varepsilon_i^2 dx \\ &= \frac{A_i E_i}{2 l_i} (\bar{n}_j^2 + \bar{n}_h^2 - 2 \bar{n}_j \bar{n}_h) \\ &= \frac{1}{2} \frac{A_i E_i}{l_i} \begin{bmatrix} \bar{n}_j \\ \bar{n}_h \end{bmatrix}^T \begin{bmatrix} 1 & -1 \\ -1 & 1 \end{bmatrix} \begin{bmatrix} \bar{n}_j \\ \bar{n}_h \end{bmatrix} \end{aligned} \quad (3.27)$$

$$\begin{aligned} \pi_i' &= \frac{A_i E_i}{l_i} \begin{bmatrix} 1 & -1 \\ -1 & 1 \end{bmatrix} \begin{bmatrix} \bar{n}_j \\ \bar{n}_h \end{bmatrix} \\ &= \frac{A_i E_i}{l_i} [(\bar{n}_j - \bar{n}_h) \quad -(\bar{n}_j - \bar{n}_h)]^T \end{aligned} \quad (3.28)$$

$$\pi_i'' = \frac{A_i E_i}{l_i} \quad (3.29)$$

where the variation in π_i' and π_i'' has been taken with respect to nodal displacements alone. Let the stiffness matrix of the i^{th} structural member be k^i using the local coordinate system; the component of the elastic stiffness matrix due to this i^{th} structural member can be expressed as follows:

$$\begin{aligned} k_e^i &= (\pi_i'' - q_i) \begin{bmatrix} 1 & -1 \\ -1 & 1 \end{bmatrix} \\ &= \left(\frac{A_i E_i}{l_i} - q_i \right) \begin{bmatrix} 1 & -1 \\ -1 & 1 \end{bmatrix} \end{aligned} \quad (3.30)$$

Thus, the stiffness matrix of the i^{th} structural member in the global coordinate system is as follows:

$$K_e^i = \lambda^T k_e^i \lambda \quad (3.31)$$

where $\lambda \in \mathbb{R}^{6 \times 6}$ is a transformation matrix defined as follows:

$$\lambda = \frac{1}{l_i} \begin{bmatrix} 1 & 0 \\ 0 & 1 \end{bmatrix} \otimes b_i \quad (3.32)$$

It should be noted that, since tensegrity structures are statically indeterminate and kinematically indeterminate structures [65], the pre-stressed structure is in a state of static equilibrium under zero external load and, as such, there are a number of zero-energy deformation mode, or mechanisms. For this reason, it is the pre-stress level, or state of self-stress, that stiffens the structural system such that at least one mechanism is excited without deformation in the structural members. Thus, the equilibrium and kinematic equations of the structure, $\mathbb{A} \cdot \mathbb{q} = \mathbb{p}$ and $\underline{\mathbb{A}} \cdot \bar{n} = e$, respectively, becomes $\mathbb{A} \cdot \mathbb{q} = 0$ and $\underline{\mathbb{A}} \cdot \bar{n} = 0$ where \mathbb{A} , \bar{n} and e are the kinematic matrix, the nodal displacement vector and the member elongation vector, respectively (note that, $\mathbb{A} = \underline{\mathbb{A}}^T$). Since there is no member elongation, l_i – which should have been the rest length of the i^{th} structure member – has been taken as the length of the i^{th} member at the equilibrium state; thus, l_i can be expressed as follows:

$$l_i = \| b_i \| \quad (3.33)$$

For analysis where ϕ is a nonlinear function of axial displacement, the component of the stiffness of the i^{th} structural member mainly due to its material properties, k_e^i , in the local coordinate system is as follows:

$$k_e^i = \iiint_v \mathbf{B}^T \mathbf{D} \mathbf{B} dV - q_i \begin{bmatrix} 1 & -1 \\ -1 & 1 \end{bmatrix} \quad (3.34)$$

where $\mathbf{B} = \mathbf{L}\mathbf{N}$; \mathbf{L} , \mathbf{N} , \mathbf{D} and V are the strain displacement operator, vector of element shape function, elasticity matrix and the volume of the i^{th} structural member, respectively. Likewise, the component of the stiffness of the i^{th} structural member mainly due to pre-stress, k_q^i , in the local coordinate system is as follows:

$$k_q^i = q_i \begin{bmatrix} 1 & -1 \\ -1 & 1 \end{bmatrix} \quad (3.35)$$

Equation (3.35) in the global coordinate system can be written as follows:

$$K_q^i = k_q^i \otimes I_3 \quad (3.36)$$

Since the total number of nodal degrees of freedom is $3n$ (where n is the number of nodes), from (3.31) and (3.36), $K_e(N)$ and $K_q(N)$ can be written, respectively, as follows:

$$K_e(N) = \sum_{i=1}^b \underline{K}_e^i \quad (3.37)$$

$$K_q(N) = \sum_{i=1}^b \underline{K}_q^i \quad (3.38)$$

where \underline{K}_e^i and \underline{K}_q^i ($3n \times 3n$ matrices) are the expanded matrices of K_e^i and K_q^i , respectively, obtained by identifying the locations of the i^{th} structural member in the global system and including zeros in the remaining locations. It is easy to see from (3.30) and (3.35) that if the structure is not in a state of stress $k_e^i = \left(\frac{A_i E_i}{l_i}\right) \begin{bmatrix} 1 & -1 \\ -1 & 1 \end{bmatrix}$ and $k_q^i = 0_{2 \times 2}$.

For the properties of the stiffness matrix of tensegrity structures, see [68], [70], [83], [125], for instance.

3.2.1.3 The Mass Matrix

The mass matrix of a tensegrity structure, similar to other space structures, may be written in the consistent mass matrix [126] form. There are also several other simpler forms of expressing the mass matrices in structural dynamic problems – the simplest of which is the lumped mass matrix [119]. The lumped mass matrix of a structural element can be obtained by dividing its total mass by the number of nodal displacement degrees of freedom and assigning the result of the division to each of its end node. Consider the i^{th} structural member with length l_i , cross-sectional area A_i , and mass density ρ_i , by dividing the total mass of the member between its two nodes, the lumped mass matrix is purely a diagonal matrix that can be obtained using the following equation [119]:

$$m_i = \frac{\rho_i A_i l_i}{2} \begin{bmatrix} 1 & 0 \\ 0 & 1 \end{bmatrix} \quad (3.39)$$

It should be noted that the lumped mass matrix ignores any cross, or dynamic, coupling between point masses placed at the nodes of the structural member because it

assumes each point mass behaves like a rigid body and is independent of the remainder of the structural member when in motion.

The consistent mass matrix is given as follows [126]:

$$m_i = \iiint_V \rho_i \mathbf{N}^T \mathbf{N} dV \quad (3.40)$$

where \mathbf{N} and V are the vector of element shape function and the volume of the i^{th} structural member. If the i^{th} structural member is assumed to deform linearly in the axial direction only, then Equation (3.40) leads to the following expression [119]:

$$m_i = \frac{\rho_i A_i l_i}{6} \begin{bmatrix} 2 & 1 \\ 1 & 2 \end{bmatrix} \quad (3.41)$$

The lumped and consistent mass matrices in (3.39) and (3.41) are in a local coordinates system; the transformation to the global coordinate system of either can be obtained using the following expression:

$$M = \sum_{i=1}^b \underline{m}_i \quad (3.42)$$

where \underline{m}_i is obtained from m_i , the global mass matrix, by identifying the locations of the i^{th} structural member in the global system and including zeros in the remaining location; the global mass matrix m_i is defined as follows:

$$m_i = \lambda^T m_i \lambda \quad (3.43)$$

Thus, M is the mass matrix of the entire structure and $\lambda \in \mathbb{R}^{6 \times 6}$ is a transformation matrix computed using (3.32).

3.2.2 Basic Equations and Solution Procedure

3.2.2.1 Equations of Motion of a Discretized System

Consider a discretized elastic structural system with n nodal degrees of freedom whose dynamic is governed by the equations of motion given by the following:

$$M \ddot{\Phi}(t) + C \dot{\Phi}(t) + K \Phi(t) = P(t) \quad (3.44)$$

where $\ddot{\Phi}(t)$, $\dot{\Phi}(t)$ and $\Phi(t)$ are $n \times 1$ vectors of nodal accelerations, velocities and displacements, respectively, in the global coordinate system. $M_{n \times n}$ is the symmetric positive definite mass matrix, $C_{n \times n}$ is the damping matrix, $K_{n \times n}$ is the symmetric

positive semi-definite stiffness matrix, and $P_{n \times 1}$ is the external nodal force vector. If the structural system is a tensegrity structure, M and K may be obtained from (3.42) and (3.24), respectively. The case where M , C and K are time independent matrices while $\ddot{\Phi}(t)$, $\dot{\Phi}(t)$, $\Phi(t)$ and $P(t)$ are time dependent vectors is the subject of discussion throughout the remainder of this chapter.

A common and computationally effective method for solving (3.44) is the mode superposition method which involves transforming the vector $\Phi(t)$ - before any integration method is employed - using the following matrix transformation:

$$\Phi(t)_{n \times 1} = \bar{\Phi}_{n \times n} \eta(t)_{n \times 1} \quad (3.45)$$

where $\bar{\Phi}$ and $\eta(t)$ are called the time independent modal matrix and time dependent vector of generalized coordinates, respectively. In structural dynamic problems using the FEM, η is called the vector of modal coordinates. The columns of $\bar{\Phi}$ are eigenvectors obtained by solving the ‘linear’ eigenvalue problem of equation (3.44) for an undamped systems. The term ‘linear’ signifies that both M and K are time independent matrices. The basis of the mode superposition method is that the modal matrix can be used to diagonalize M , C and K matrices to transform equation (3.44) into uncoupled equations of motion. The solution of the resulting independent second order differential equations can then be found by any standard algorithm and the final solution is obtained by the superposition of all the individual solutions [119], [127], [128].

3.2.2.2 Eigenvalue Problem and Uncoupled Equations of Motion

By assuming that the structure is undamped and the external force vector is zero, the equations of motion in (3.44) for the harmonic nodal displacements of the form $\Phi = \underline{\Phi} e^{i\omega t}$ give the following eigenvalue problem:

$$[K - \omega^2 M] \underline{\Phi} = 0 \quad (3.46)$$

where $\underline{\Phi}$ is the amplitudes of the displacement Φ , and ω is the natural frequency of vibration. Also, $\underline{\Phi}$ is called the mode shape, or eigenvector, and ω is the corresponding eigenvalue. For a whole structural system, the mode shape (eigenvector) corresponding to the j^{th} natural frequency ω_j (eigenvalue) can be designated as $\underline{\Phi}_j$. Thus, the natural frequencies of the structure given by equation (3.46) are $\omega_1, \omega_2, \dots, \omega_n$ and the

corresponding eigenvectors are $\underline{\Phi}_1, \underline{\Phi}_2, \dots, \underline{\Phi}_n$. Therefore, the modal matrix is defined as follows:

$$\bar{\Phi} = [\underline{\Phi}_1 \ \underline{\Phi}_2 \ \dots \ \underline{\Phi}_n] \quad (3.47)$$

It is worth noting that only the shape of the mode $\underline{\Phi}_j$ is important, not the amplitude; thus, $\underline{\Phi}_j$ can be scaled arbitrarily and can therefore be written as $a_j \underline{\Phi}_j$ where a_j is an arbitrary nonzero constant. As such, each of the column vectors of $\bar{\Phi}$ in (3.47) can easily be scaled so that the following matrix relation is satisfied [119]:

$$\bar{\Phi}^T M \bar{\Phi} = I \quad (3.48)$$

where $I_{n \times n}$ is the identity matrix. Equation (3.46) is written for a single structural mode; for all the modes, the following expression is obtained:

$$\Omega^2 M \bar{\Phi} = K \bar{\Phi} \quad (3.49)$$

where Ω is a diagonal matrix of natural frequencies defined as follows:

$$\Omega = \text{diag}([\omega_1 \ \omega_2 \ \dots \ \omega_n]) \quad (3.50)$$

Pre-multiplying equation (3.49) by $\bar{\Phi}^T$ and using the identity of (3.48) in the resulting equation, the following matrix relation is obtained:

$$\Omega^2 = \bar{\Phi}^T K \bar{\Phi} \quad (3.51)$$

Hence, for an undamped structural system, the transformation in equation (3.45) simplifies and uncouples the original equations of motion of (3.44) into the following form:

$$\ddot{\eta}(t) + \Omega^2 \eta(t) = \bar{\Phi}^T P(t) \quad (3.51)$$

Generally, the elements of the damping matrix C are unknown. A choice for which C is proportional to a linear combination of M and K , called a proportional damping, is usually chosen to enable the diagonalization of C ; in particular, C of the following form:

$$C = aM + bK \quad (3.52)$$

where a and b are constants that are chosen to suit a specific problem, is called Rayleigh damping [127].

Thus, with the form of C in (3.52), (3.51) may be written as follows:

$$\ddot{\eta}(t) + (aI + b\Omega^2)\dot{\eta}(t) + \Omega^2 \eta(t) = \bar{\Phi}^T P(t) \quad (3.53)$$

Note that the matrix $(aI + b\Omega^2)$ is diagonal, and as such, the second order differential equation of motion of the j^{th} mode obtained from the decoupled equations of motion (3.53) is written as follows:

$$\ddot{\eta}_j(t) + 2\zeta_j\omega_j\dot{\eta}_j(t) + \omega_j^2 \eta_j(t) = \underline{\Phi}_j^T P(t) \quad (3.54)$$

where $\zeta_j = \frac{(aI + b\omega_j^2)}{2\omega_j}$ is the damping constant for the j^{th} mode; in matrix form, (3.54) may be written as follows:

$$\ddot{\eta}(t) + 2\zeta\Omega\dot{\eta}(t) + \Omega^2 \eta(t) = \bar{\Phi}^T P(t) \quad (3.55)$$

where $\zeta = \text{diag}(\zeta_j)$. Thus, while Equation (3.44) is expressed in terms of nodal coordinates, Equation (3.55) is in the terms of modal coordinates. Typical values of $\zeta_j \cong 0.001 - 0.005$ are common choices for satellite and space structures where strain levels are usually low, values of $\zeta_j \cong 0.01 - 0.02$ for mechanical engineering applications where most dissipation takes place in the joints, and value of $\zeta_j \cong 0.05$ for civil engineering applications [129].

Also, it has been assumed that rigid body degrees of freedom have been eliminated in (3.46) from matrices M and K . This is easily achieved, for example, by imposing some support constraints at some nodes which corresponds to deleting the rows and columns associated with these nodes. The significance of applying these boundary conditions for fixed structures is to ensure that the matrix K is nonsingular so as to prevent the structure from undergoing rigid body motion in which the structure is free to undergo translations and rotation without bound. A rigid body mode shape $\underline{\Phi}_j$ correspond to the case where $\omega_j = 0$ and in which $K\underline{\Phi}_j = 0$. For a general unrestrained structure, there will be six rigid body, or zero energy, modes in the structure. Other modes are called elastic modes.

Furthermore, for practical designs or form-finding of tensegrity structures, it is convenient that sets of structural members are constrained to have similar lengths, leading to a structure with repetitive mode-patterns, as a result of which, modal analysis will reveal repeated natural frequencies. It is as such necessary that the eigenvectors $\underline{\Phi}_1$,

$\underline{\Phi}_2, \dots, \underline{\Phi}_n$ in $\bar{\Phi}$ of (3.47) are linearly independent for the modal superposition technique to be valid. As it is well known, existence of repeated natural frequencies does not invalidate the existence of mutually orthogonal eigenvectors in $\bar{\Phi}$ and eigenvectors of the same natural frequency only form a subspace of dimension equal to the multiplicity of frequencies [127].

3.2.2.3 Rigid Body Modes and Static Model Reduction

In this section, it will be assumed that the columns and rows of the mass matrix M and the stiffness matrix K have been renumbered such that the columns and rows, which would have been deleted in for obtaining (3.46) when the boundary conditions are applied to make K nonsingular, are placed at the end of the matrices. It will also be assumed that the diagonal matrix of natural frequencies is as follows:

$$\Omega = \text{diag}([\omega_1 \ \omega_2 \ \dots \ \omega_e \ \underline{\omega}_1 \ \dots \ \underline{\omega}_r]) \quad (3.56)$$

such that $\omega_i \neq 0$ and $\underline{\omega}_i = 0$; e and r correspond to the number of flexible and rigid degrees of freedom, respectively. Thus, Φ and $\bar{\Phi}$ are partitioned as follows:

$$\Phi = \begin{bmatrix} \Phi_e \\ \Phi_r \end{bmatrix}, \quad \bar{\Phi} = \begin{bmatrix} \bar{\Phi}_e \\ \bar{\Phi}_r \end{bmatrix} \quad (3.57)$$

For undamped structures with rigid body modes, (3.44) can thus be written as follows:

$$\begin{bmatrix} M_{11} & M_{12} \\ M_{21} & M_{22} \end{bmatrix} \begin{bmatrix} \ddot{\Phi}_e \\ \ddot{\Phi}_r \end{bmatrix} + \begin{bmatrix} K_{11} & K_{12} \\ K_{21} & K_{22} \end{bmatrix} \begin{bmatrix} \Phi_e \\ \Phi_r \end{bmatrix} = \begin{bmatrix} P_e \\ P_r \end{bmatrix} \quad (3.57)$$

where Φ_e is the vector of elastic nodal degrees of freedom, Φ_r is the vector of unrestricted nodal degrees of freedom, P_e is the vector of loads on the elastic nodes, and P_r is the vector of loads (reactions) at points where Φ_r is specified. Note that $\bar{\Phi}_e$ and $\bar{\Phi}_r$ are $e \times n$ and $r \times n$ matrices, respectively. Let $\Phi_e = \bar{\Phi}_e \eta$ and $\Phi_r = \bar{\Phi}_r \eta$ so that the following equation is obtained:

$$\Phi = \begin{bmatrix} \Phi_e \\ \Phi_r \end{bmatrix} = \bar{\Phi} \eta = \begin{bmatrix} \bar{\Phi}_e \\ \bar{\Phi}_r \end{bmatrix} \eta = \begin{bmatrix} \bar{\Phi}_e \eta \\ \bar{\Phi}_r \eta \end{bmatrix} \quad (3.58)$$

where η is the time dependent vector of generalized coordinates; then the first partition in (3.57) can be written as follows:

$$M_{11}\bar{\Phi}_e\ddot{\eta} + M_{12}\bar{\Phi}_r\ddot{\eta} + K_{11}\bar{\Phi}_e\eta + K_{12}\bar{\Phi}_r\eta = P_e \quad (3.59)$$

The eigenvalue problem of (3.49) can be written as follows:

$$\left[\begin{bmatrix} K_{11} & K_{12} \\ K_{21} & K_{22} \end{bmatrix} - \Omega^2 \begin{bmatrix} M_{11} & M_{12} \\ M_{21} & M_{22} \end{bmatrix} \right] \begin{bmatrix} \bar{\Phi}_e \\ \bar{\Phi}_r \end{bmatrix} = 0 \quad (3.60)$$

where $\Omega = \begin{bmatrix} \Omega_e & 0 \\ 0 & \Omega_r \end{bmatrix}$, and Ω_e and Ω_r are defined as follows:

$$\Omega_e = \text{diag}([\omega_1 \ \omega_2 \ \cdots \ \omega_e]) \ , \ \Omega_r = \text{diag}([\underline{\omega}_1 \ \underline{\omega}_2 \ \cdots \ \underline{\omega}_r]) \quad (3.61)$$

If $\Omega_r \cong 0$, re-arranging the second partition of (3.60) (that is, $K_{21}\bar{\Phi}_e + K_{22}\bar{\Phi}_r = 0$) gives the following expression:

$$\bar{\Phi}_r = T \bar{\Phi}_e \quad (3.62)$$

where

$$T = -K_{22}^{-1}K_{21} \quad (3.63)$$

The transformation matrix in (3.63) is the matrix of the Guyan reduction method [130] commonly used for static model reduction. Substituting (3.62) into (3.59) and pre-multiplying the result with $\bar{\Phi}_e^T$ give the following equation:

$$\bar{\Phi}_e^T (M_{11} + M_{12}T)\bar{\Phi}_e\ddot{\eta} + \bar{\Phi}_e^T (K_{11} + K_{12}T)\bar{\Phi}_e\eta = \bar{\Phi}_e^T P_e \quad (3.64)$$

For studying pseudo-static deflection properties (where $\ddot{\eta} = 0$), the following equations are obtained from (3.64):

$$\Phi_e = \bar{\Phi}_e \left[\bar{\Phi}_e^T (K_{11} + K_{12}T)\bar{\Phi}_e \right]^{-1} \bar{\Phi}_e^T P_e \quad (3.65)$$

3.2.2.4 Pseudo-Static Deflection Properties of a 2-stage Tensegrity Structure

Let the matrix of nodal coordinates $X \in \mathbb{R}^{n \times 3}$ be defined as $X = N^T$ where N is defined in (3.1). It is worth noting that static rigidity of tensegrity structures are preserved under affine transformation [131]. A transformation of X such that $X \mapsto X \cdot$

$c_x I_{3 \times 3}$ is an affine transformation of the nodal coordinates of a tensegrity structure which corresponds to the scaling of the tensegrity structure by a factor of c_x ; c_x is a constant and $I_{3 \times 3}$ is a 3×3 identity matrix. Also, let c_q be a scaling factor for the tension coefficients of the tensegrity structure, that is, $q \mapsto c_q q$ where q is the vector of tension coefficient of the tensegrity structure.

For the 2-stage tensegrity structure with three bar per stage (in short form, 2-stage 3-order tensegrity structure) shown in Figure 3.1, it is assumed that the cables are made of copper of Young's modulus 117 GPa, cross-sectional area $1.5 \times 10^{-6} \text{ m}^2$ and mass density 8920 kg/m^3 and the bars are hollow circular steel cylinders of Young's modulus 200 GPa, cross-sectional area $6 \times 10^{-6} \text{ m}^2$, mass density 7850 Kg/m^3 and nodes 1, 2, and 3 are constrained (rigid) in each of the x , y and z directions. Also, the figure shows the nomenclature that will be adopted throughout this thesis, except where otherwise stated, for numbering the structural members of minimal multistage tensegrity structures. The length and tension coefficient of each structural member is shown in Table 3.1.

Figures 3.2 (a) and (b) show the solution of equation (3.65) for the various point loads, 1N, 10N, 50N, 100N and 200N, each placed at nodes 10, 11 and 12 in the downward (vertical) direction as tension coefficients scaling factor c_q varies. It can be seen that, for a given load, as the tension coefficients of the tensegrity structure is increased, nodal displacements reduces in a nonlinear manner. Furthermore, Figure 3.3 shows the solution of equation (3.65) as point loads in the downward (vertical) direction at nodes 10, 11 and 12 vary for various level of pre-stress defined by c_q . Here, it can be seen that, for a given pre-stress level, the displacements are proportional to the point loads.

Also, Figure 3.4 is a plot of the nodal coordinates scaling factor c_x against vertical displacements of nodes 10, 11, and 12 for various loads and for the tension coefficient scaling factor $c_q = 10$. It reveals that, for a given load, the nodal displacements of the tensegrity structure increases linearly with c_x . Lastly, as shown in Figure 3.5, the vertical displacements of nodes 10, 11, and 12 increases linearly with c_x for the three 1KN loads, each placed in the vertical downward direction at nodes 10, 11 and 12. The implication of results of Figure 3.4 and Figure 3.5 in tensegrity structural designs is that, although tensegrity structures are scalable, the tension coefficient scaling factor c_q has

to be increased as the scale (defined by c_x) of the tensegrity structure increases to maintain the same level of rigidity. It should be noted that the staggered nature of the plots of Figure 3.2 – 3.5, and similar plots drawn in Chapter 5, is because the plots' data points were first obtained discretely using equally spaced data points and then joined together to form a continuous (but staggered) lines.

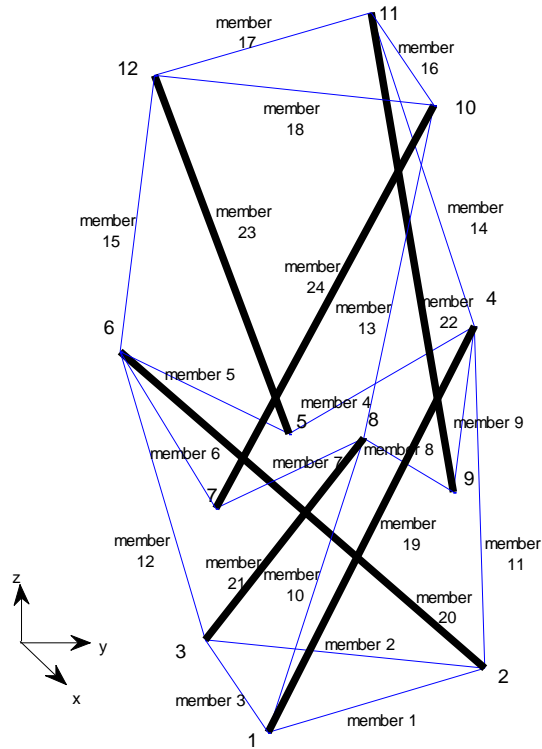
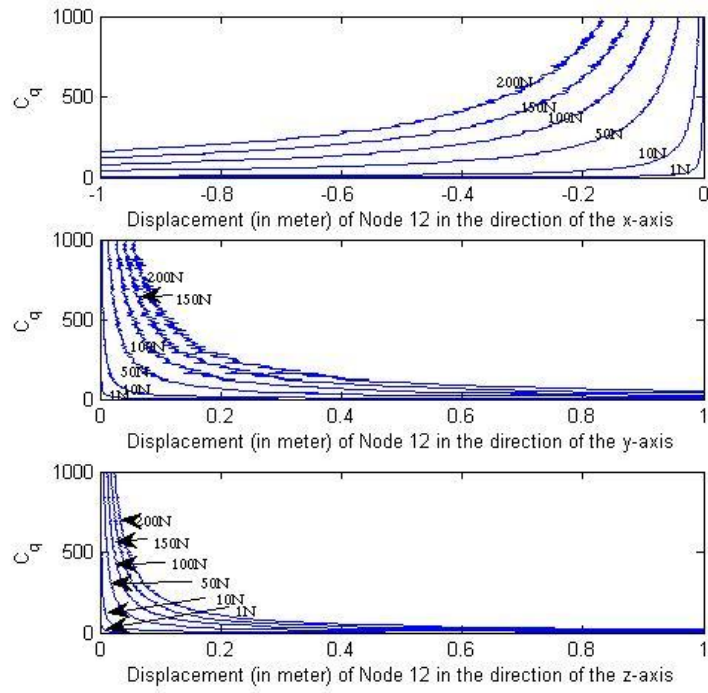


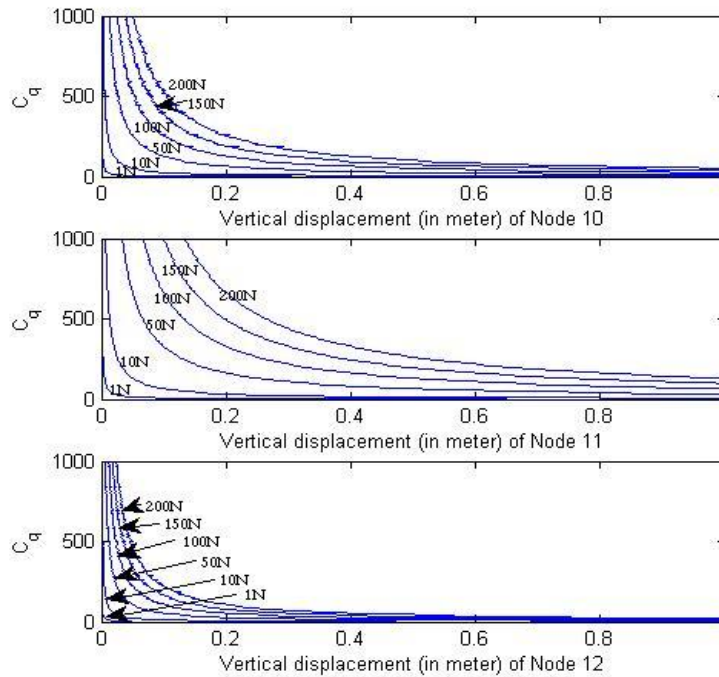
Figure 3.1: A 2-stage tensegrity structure with three bars per stage

Table 3.1: Length and tension coefficient of each of the structural members of the tensegrity structure shown in Figure 3.1

Member No.	1-3	4	5	6	7	8	9	10-12	13-15	16-18	19-21	22-24
Length (m)	10.00	7.38	7.38	7.38	7.38	7.38	7.38	11.67	11.67	10.00	16.71	16.71
Tension coefficient (N/m)	3.106	3.015	4.909	3.015	4.909	3.015	4.909	4.346	2.730	0.7423	-4.346	-2.030



(a)



(b)

Figure 3.2: (a) Displacements in the x-,y- and z-axis of node 12 as tension coefficients scaling factor c_q varies on loads 1N, 10N, 50N, 100N and 200N. (b) Vertical displacements of nodes 10, 11, and 12 as tension coefficients scaling factor c_q is varied on vertical loads 1N, 10N, 50N, 100N and 200N.

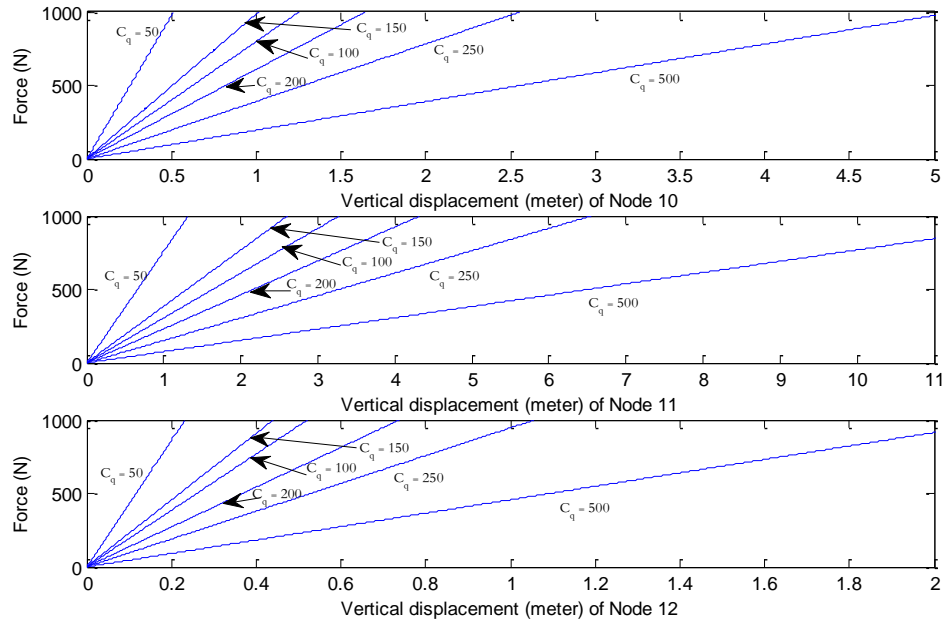


Figure 3.3: Vertical displacements of nodes 10, 11, and 12 as static loads on these nodes are varied for various tension coefficients scaling factor c_q .

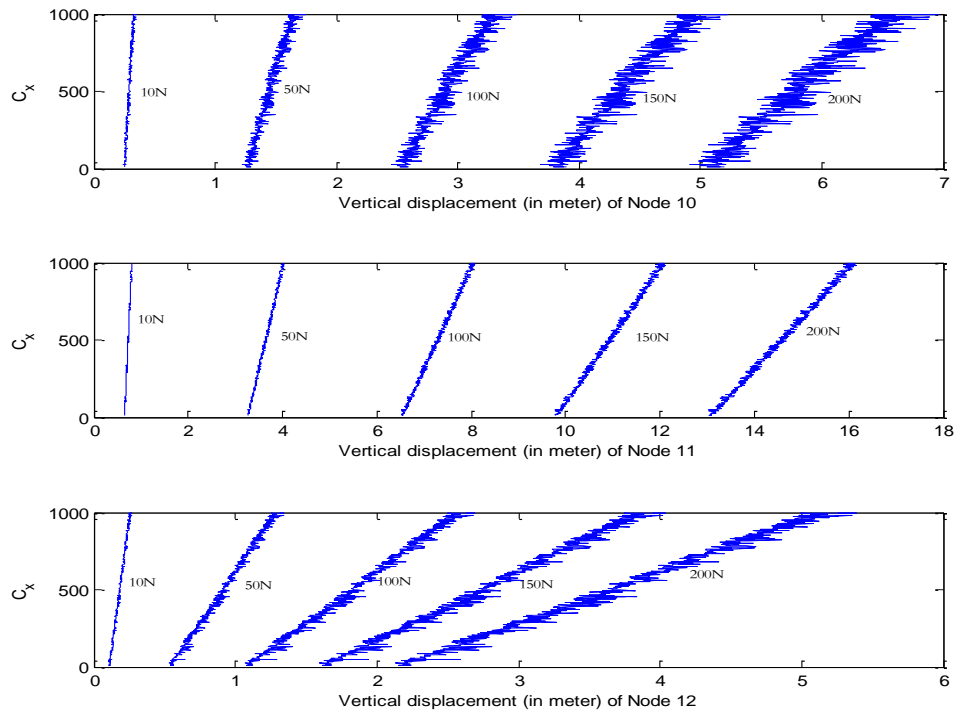


Figure 3.4: Vertical displacements of nodes 10, 11, and 12 for the tension coefficients scaling factor of $c_q = 10$ as the nodal coordinates scaling factor varies on loads 10N, 50N, 100N, 150N and 200N.

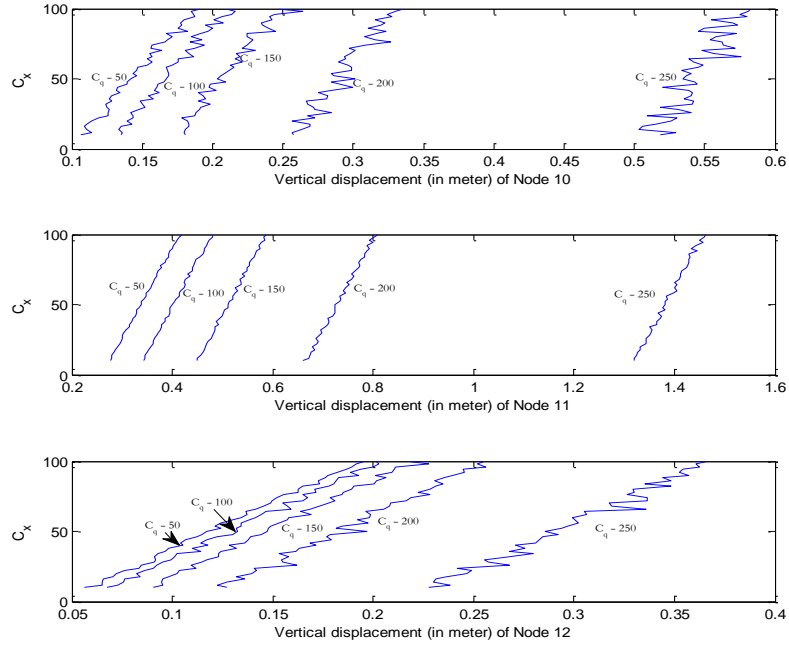


Figure 3.5: Vertical displacements of nodes 10, 11, and 12 for loads 1KN placed vertically on these nodes as the nodal coordinates scaling factor varies for the tension coefficient scaling factor c_q of values 50, 100, 150, 200 and 250.

3.2.3 State-Space Model Representation

In structural analysis, a common way of finding the solution to the second order linear equations of motion defined in (3.44) is to transform the equation into a state variable form called the state-space model. The state-space model of a linear time invariant system is given by a set of first order linear equations as follows:

$$\dot{x} = A x + B u \quad (3.66)$$

$$y = C x + D u \quad (3.67)$$

where x , u and y are n -dimension vectors of state variables, inputs and outputs, respectively; n – number of state variables, m – number of inputs and p – number of outputs; $A_{n \times n}$, $B_{n \times m}$, $C_{p \times n}$ and $D_{p \times m}$ are the system matrix, the input matrix, the output matrix and the feed-forward, or feed-through, matrix. The state-space formulation is a convenient way of converting higher order linear differential equations into a set of first order differential equations. Equations (3.66) and (3.67) are called the state differential equation and the output equation, respectively. State variables are a set whose knowledge provides the future state and output of a system given the input function and

the equation describing the dynamics of the system. The state variables are a non-unique set chosen as small as possible to avoid redundant variables and a convenient choice is a set of variables that can be easily measured in the output [132]. For equation (3.44), choosing vectors of nodal displacements and velocities as state-variables results to the following:

$$x_1 = \Phi(t) \quad , \quad x_2 = \dot{\Phi}(t). \quad (3.68)$$

Thus, the state vector and its differential are as follows:

$$x = \begin{bmatrix} x_1 \\ x_2 \end{bmatrix} \quad , \quad \dot{x} = \begin{bmatrix} \dot{x}_1 \\ \dot{x}_2 \end{bmatrix} \quad (3.69)$$

Hence, transforming (3.44) into the state-space model of (3.66) gives the following:

$$\dot{x} = \begin{bmatrix} 0 & I \\ -M^{-1}K & -M^{-1}C \end{bmatrix} \begin{bmatrix} x_1 \\ x_2 \end{bmatrix} + \begin{bmatrix} 0 \\ M^{-1} \end{bmatrix} P(t) \quad (3.70)$$

The vector u and matrices A and B are as follows:

$$u = P(t) \quad . \quad A = \begin{bmatrix} 0 & I \\ -M^{-1}K & -M^{-1}C \end{bmatrix} \quad , \quad B = \begin{bmatrix} 0 \\ M^{-1} \end{bmatrix} \quad (3.71)$$

Depending on which output is measured, the measured output y of displacements sensors (that is, $y = x_1$), velocities sensors (that is, $y = x_2$) and acceleration sensors (that is, $y = \dot{x}_2$) are respectively is obtained from the following expressions:

- With displacement sensor: $x_1 = [I \quad 0] x$ (3.72)

and from which $C = [I \quad 0]$ and $D = 0$.

- With velocity sensor: $x_2 = [0 \quad I] x$ (3.73)

and from which $C = [0 \quad I]$ and $D = 0$.

- With acceleration sensor: $\dot{x}_2 = [-M^{-1}K \quad -M^{-1}C] x + [M^{-1}]P(t)$ (3.74)

and from which $C = [-M^{-1}K \quad -M^{-1}C]$ and $D = [M^{-1}]$.

The above state-space formulation (3.70-3.74) directly involves the nodal coordinates of the structural systems (for example, $\Phi(t) = y = [I \quad 0] x$) and therefore called the nodal state-space model. This model may be impractical since the size of the

state vectors, therefore the number of differential equations to be solved, is twice the actual number of degrees of freedom of the system [129]. As such, it is common to transform (3.44), firstly, into modal coordinate form of equations of motion (3.55). Equations (3.69 – 3.74) can then be written as follows:

$$x = \begin{bmatrix} x_1 \\ x_2 \end{bmatrix} = \begin{bmatrix} \eta \\ \dot{\eta} \end{bmatrix} \quad (3.75)$$

$$\dot{x} = \begin{bmatrix} \dot{x}_1 \\ \dot{x}_2 \end{bmatrix} = \begin{bmatrix} 0 & I \\ -\Omega^2 & -2\zeta\Omega \end{bmatrix} \begin{bmatrix} x_1 \\ x_2 \end{bmatrix} + \begin{bmatrix} 0 \\ \bar{\Phi}^T \end{bmatrix} P(t) \quad (3.76)$$

$$u = P(t) \quad , \quad A = \begin{bmatrix} 0 & I \\ -\Omega^2 & -2\zeta\Omega \end{bmatrix} \quad , \quad B = \begin{bmatrix} 0 \\ \bar{\Phi}^T \end{bmatrix} \quad (3.77)$$

Depending on which output is measured, the measured output y of modal displacements sensors (that is, $y = \eta$), modal velocities sensors (that is, $y = \dot{\eta}$) and modal acceleration sensors (that is, $y = \ddot{\eta}$) are respectively is obtained from the following expressions:

- Modal displacements: $\eta = [I \quad 0] x \quad (3.78)$

and from which $C = [I \quad 0]$ and $D = 0$. In this case, the vector of nodal displacements is $\Phi(t) = \bar{\Phi} y$.

- Modal velocities: $\dot{\eta} = [0 \quad I] x \quad (3.79)$

and from which $C = [0 \quad I]$ and $D = 0$. In this case, the vector of nodal velocities is $\dot{\Phi}(t) = \bar{\Phi} y$.

- Modal accelerations: $\ddot{\eta} = [-\Omega^2 \quad -2\zeta\Omega] x + [\bar{\Phi}^T] P(t) \quad (3.80)$

and from which $C = [-\Omega^2 \quad -2\zeta\Omega]$ and $D = [\bar{\Phi}^T]$. In this case, the vector of nodal accelerations is $\ddot{\Phi}(t) = \bar{\Phi} y$.

As the state variables in vector x are not a unique set, apart from those in (3.75), another common choice of these variables in the literature (which of course gives different forms of matrices A , B , C and D) is as follows [129], [133]:

$$x = \begin{bmatrix} x_1 \\ x_2 \end{bmatrix} = \begin{bmatrix} \Omega\eta \\ \dot{\eta} \end{bmatrix}. \quad (3.81)$$

An important advantage of the transformation into modal state-space model is that the state vector can be reduced to contain only those modes that fall into the frequency bandwidth of interest by eliminating all other modes [129]. As an example, Figures 3.6 – 3.9 show the dynamic simulation of the tensegrity structure of Figure 3.1 using equations (3.75-3.79) when three vertically downward loads, each of 300N, are placed suddenly on nodes 10, 11 and 12 at time $t = 0$ (sec) with zero initial conditions of nodal displacements and velocities. Nodes 1, 2, and 3 are constrained (rigid) in each of the x , y and z directions. The physical and material properties (the length l , Young's modulus E , cross-sectional area A , and mass densities ρ) and the tension coefficient q of each of the structural members of the structure are shown in Table 3.2. The damping constant $\zeta_j = 0.02$ and the mass matrix, written in the consistent mass matrix form of Equations (3.40-3.43), have been employed for the simulation with the integration step-size of 0.02 sec.

It can be seen on Figures 3.6 – 3.9 that not all the nodes of the structure (structure modes) are significantly affected by the application of the external loading forces. Therefore, it may be convenient to eliminate the least affected modes in the state space model by transforming the equations of motion (3.44) into a reduced modal coordinate form using techniques such as the Guyan reduction method [130] (see Section 3.2.2.3). These techniques can prove particularly useful for large structures. In the next section, the dynamic simulation of several tensegrity structures will be investigated using the state space model equations (3.75 – 3.78).

Table 3.2: Tension coefficients, material and physical properties of the structural members of the tensegrity structure shown in Figure 3.1

Member No.	1-3	4	5	6	7	8	9	10-12	13-15	16-18	19-21	22-24
l (m)	10.00	7.38	7.38	7.38	7.38	7.38	7.38	11.67	11.67	10.00	16.71	16.71
q N/m	31.06	30.15	49.09	30.15	49.09	30.15	49.09	43.46	27.30	7.423	-43.46	-20.30
E (GPa)	117	117	117	117	117	117	117	117	117	117	200	200
ρ (kg/m ³)	8920	8920	8920	8920	8920	8920	8920	8920	8920	8920	7850	7850
A ($\times 10^{-6}$ m ²)	1.5	1.5	1.5	1.5	1.5	1.5	1.5	1.5	1.5	1.5	6	6

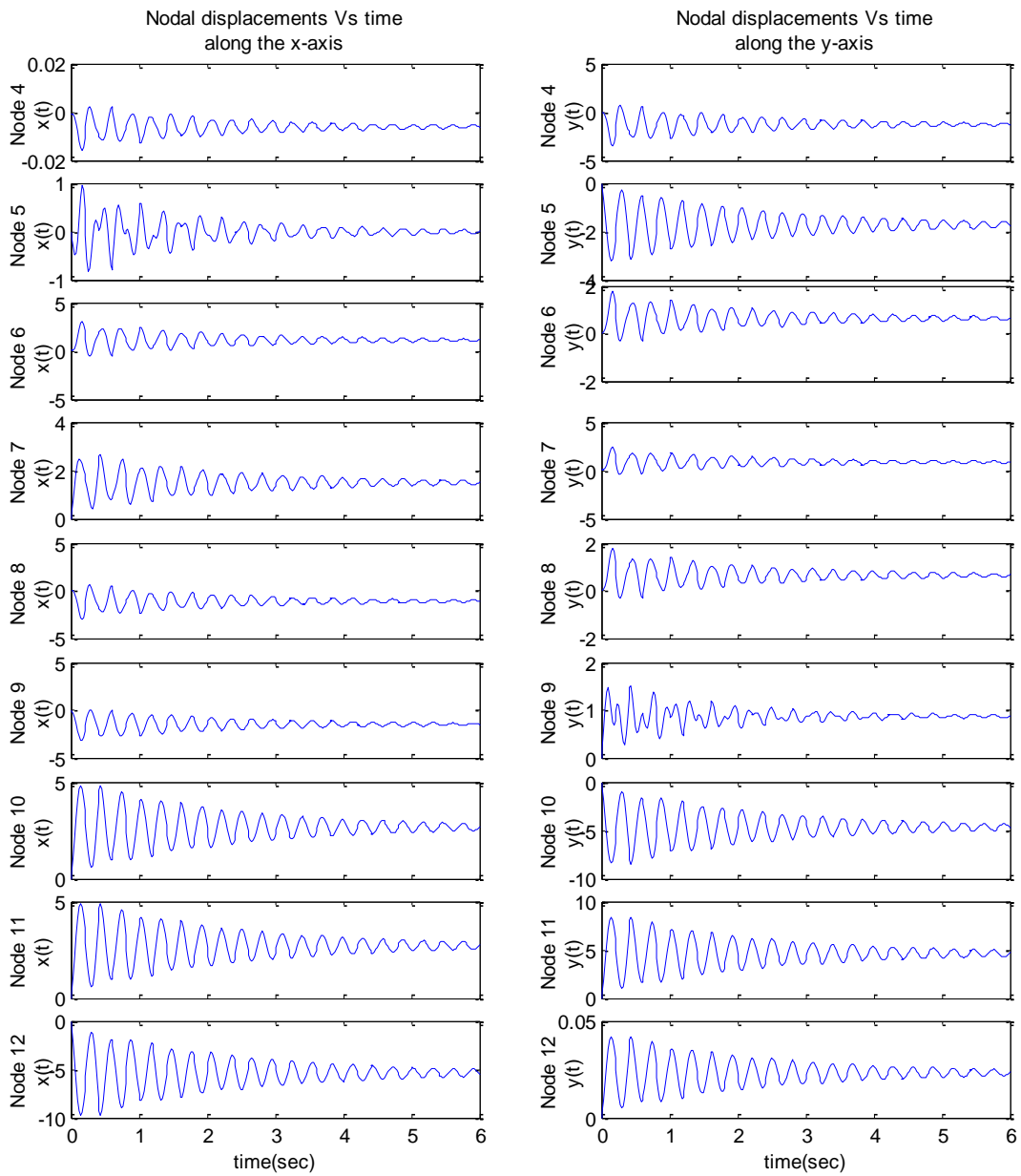


Figure 3.6: Dynamic response of the 2-stage tensegrity structure to three vertically downward loads of 300N on nodes 10, 11, and 12 suddenly applied at time $t = 0$ (sec): Nodal Displacements (meter) Vs time (sec) for the x and y axes.

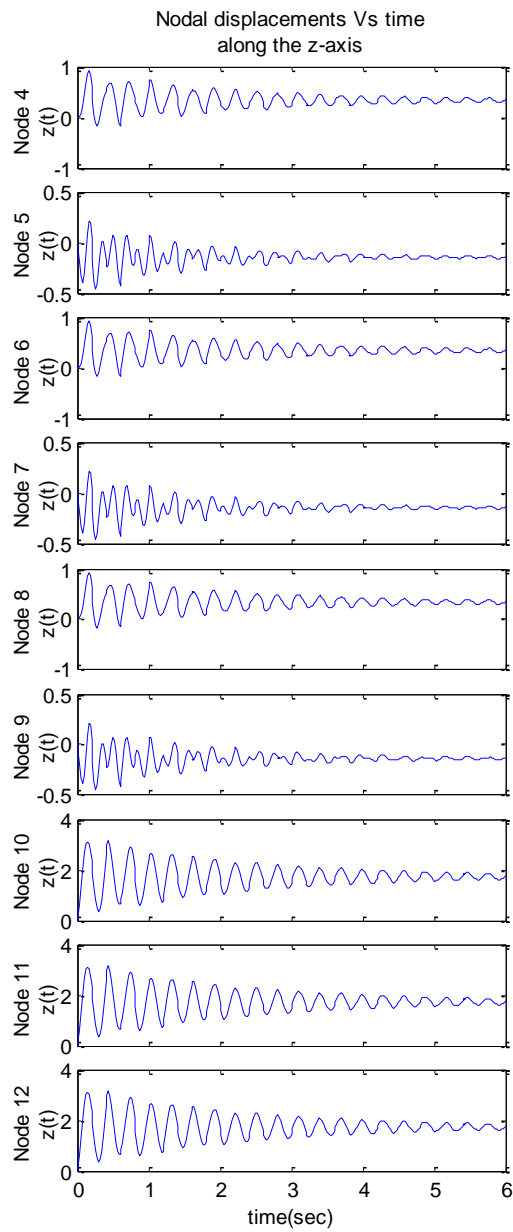


Figure 3.7: Dynamic response of the 2-stage tensegrity structure to three vertically downward loads of 300N on nodes 10, 11, and 12 suddenly applied at time $t = 0$ (sec): Nodal Displacements (meter) Vs time (sec) for the z axis.

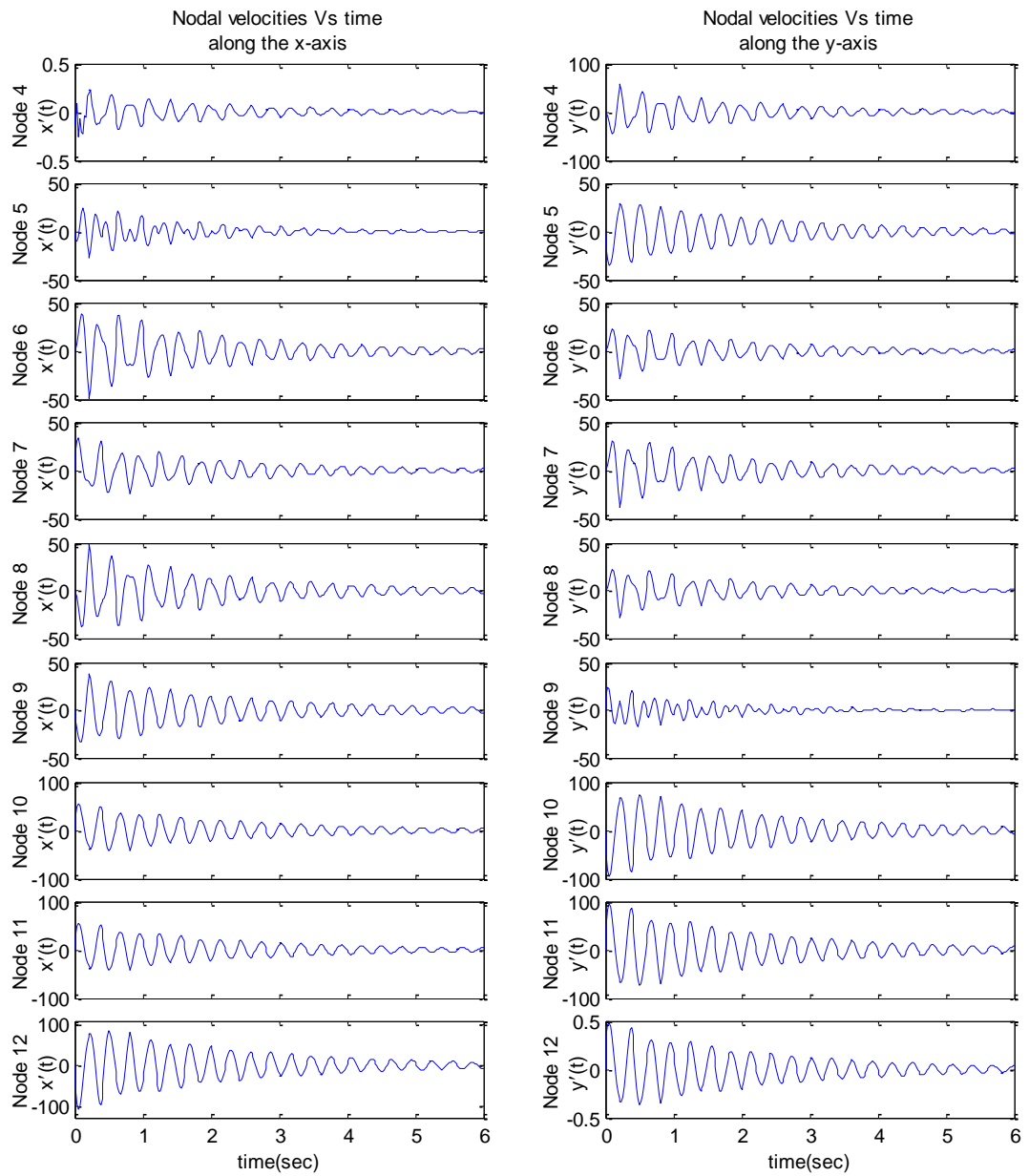


Figure 3.8: Dynamic response of the 2-stage tensegrity structure to three vertically downward loads of 300N on nodes 10, 11, and 12 suddenly applied at time $t = 0$ (sec): Nodal Velocities (meter/sec) Vs time (sec) for the x and y axes.

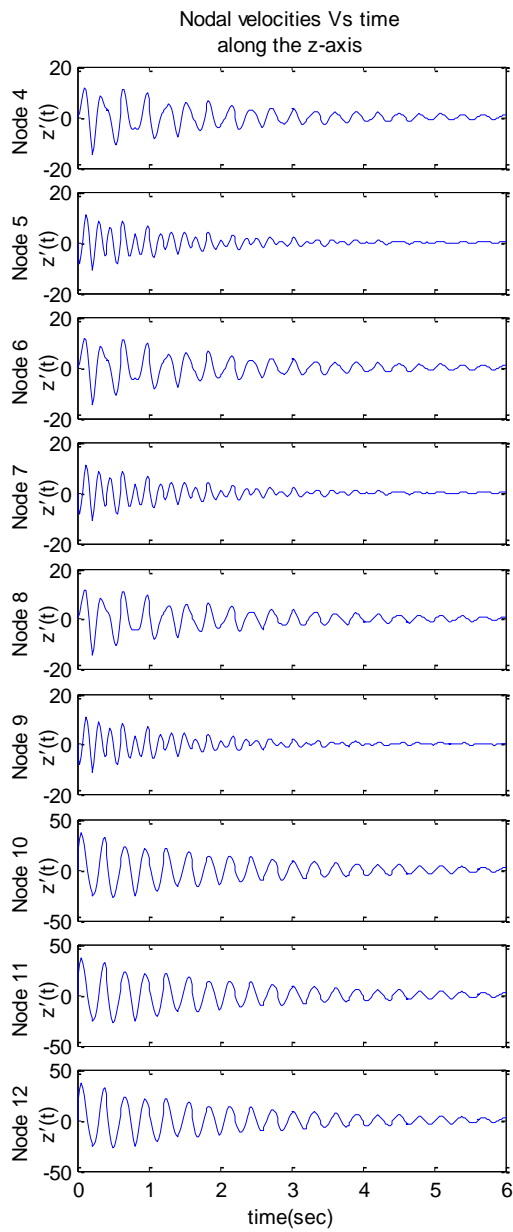


Figure 3.9: Dynamic response of the 2-stage tensegrity structure to three vertically downward loads of 300N on nodes 10, 11, and 12 suddenly applied at time $t = 0$ (sec): Nodal Velocities (meter/sec) Vs time (sec) for the z axis.

3.2.4 Dynamic Model Simulation of n-stage Tensegrity Structures

In this section, the simulation of the dynamic models obtained using the techniques presented in the preceding sections of this chapter will be carried-out on a number of tensegrity structures. Moreover, one of the purposes of the simulation study to be carried-out is to investigate the effect of including additional structural members (than strictly necessary) on the dynamics of n-stage tensegrity structures. The constrained optimisation form-finding algorithm in Chapter 2 has been used to obtain all the structural assemblies that will be considered. Figures 3.10 and 3.11 show two 2- and 3-stage tensegrity structures of 3-order, respectively. The main difference between the tensegrity structures of Figure 3.10 (a) and (b) (likewise Figure 3.11 (a) and (b)) is the additional structural members – shown in red in the figure – introduced in 3.10 (b) (likewise Figure 3.11 (b)). The nomenclature adopted for the structural assemblies of figures 3.10 (b) and 3.11 (b) are shown in Figure 3.12. It is assumed that the cables are made of copper of Young's modulus 117 GPa, cross-sectional area $1.5 \times 10^{-6} \text{ m}^2$ and mass density 8920 kg/m^3 and the bars are hollow circular steel cylinders of Young's modulus 200 GPa, cross-sectional area $6 \times 10^{-6} \text{ m}^2$ and mass density 7850 Kg/m^3 . Table 3.3 gives the length l and the tension coefficient q of each of the structural members of these structures. The nodal coordinates of the structures are given in Table 3.4. The damping constant $\zeta_j = 0.02$ and the mass matrix, written in the consistent mass matrix form of Equations (3.40-3.43), have been employed. Figures 3.13 – 3.18 show the dynamic simulation of the tensegrity structure of figures 3.10 and 3.11 using equations (3.75-3.79) when three vertically downward loads, each of 300N, are suddenly placed on the three top-most nodes at time $t = 0$ (sec) with zero initial conditions of nodal displacements. Nodes 1, 2, and 3 are constrained (rigid) in each of the x , y and z directions. The integration step-size for the simulation in all cases is 0.02 sec.

As can be seen from Figures 3.13 – 3.18, the additional structural members introduced in the tensegrity structures of Figure 3.10 (a) and (b) cause increase in the stiffness of these structural assemblies. This results in the significant reduction in the amplitudes of vibration of the structures (compare Figures of 3.13 (a), 3.14 (a), 3.15 (a), 3.16 (a), 3.17 (a) and 3.18 (a) with Figures 3.13 (b), 3.14 (b), 3.15 (b), 3.16 (b), 3.17 (b) and 3.18 (b), respectively).

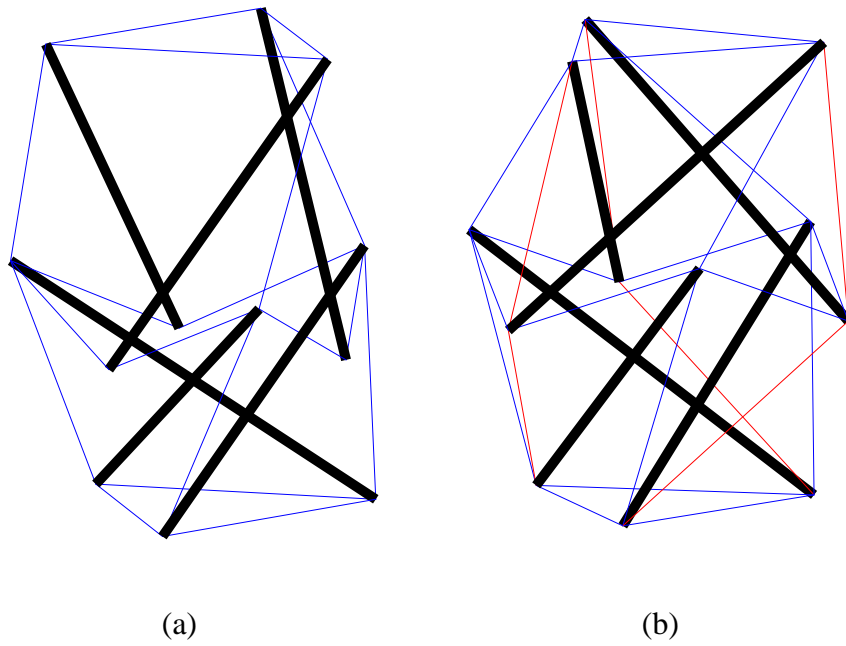


Figure 3.10: (a) A minimal 2-stage 3-order tensegrity structure; (b) A 2-stage 3-order tensegrity structure with additional structural members (shown in red).

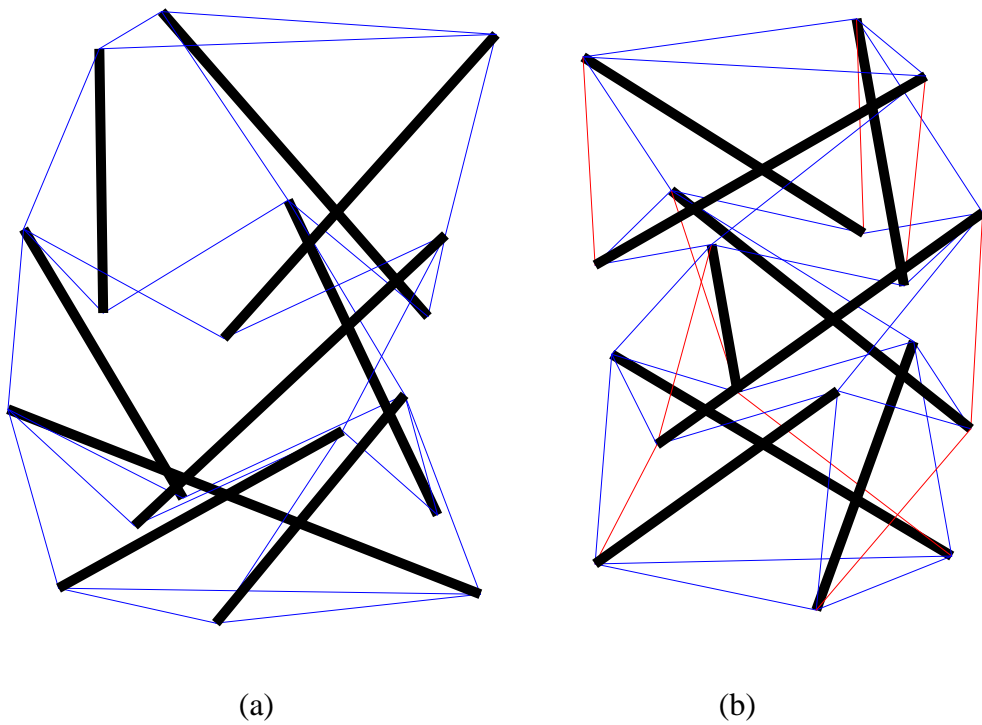


Figure 3.11: (a) A minimal 3-stage 3-order tensegrity structure; (b) A 3-stage 3-order tensegrity structure with additional structural members (shown in red).

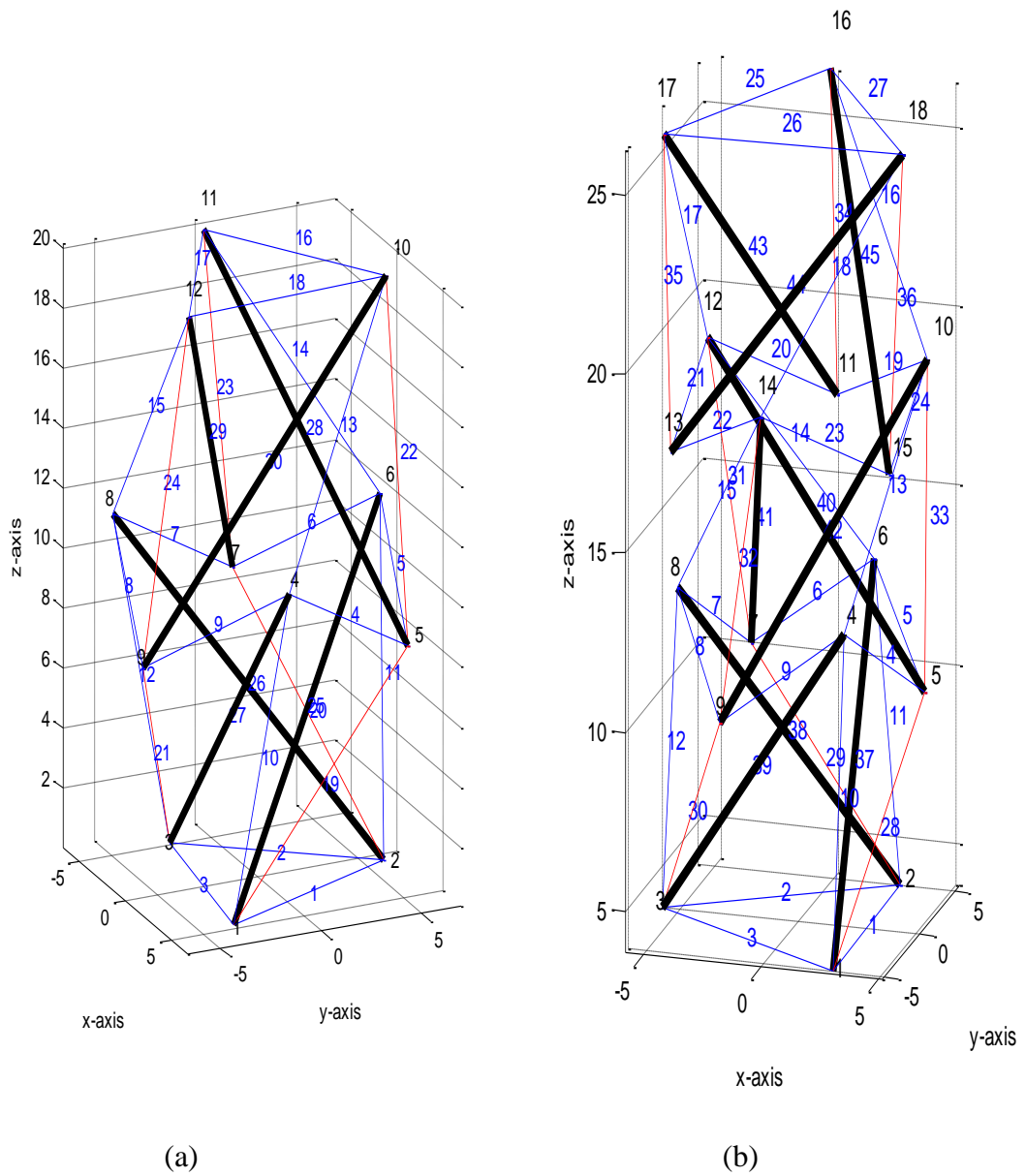


Figure 3.12: (a) and (b) show the nomenclature adopted for numbering the structural members of figures 3.10 (b) and 3.11 (b), respectively; in both cases, the numberings of structural members and nodes are in blue and black, respectively. [Scale of Plots: meter in all axes].

Table 3.3: Length and tension coefficient of each of the structural members of the tensegrity structure shown in figures 3.10 and 3.11

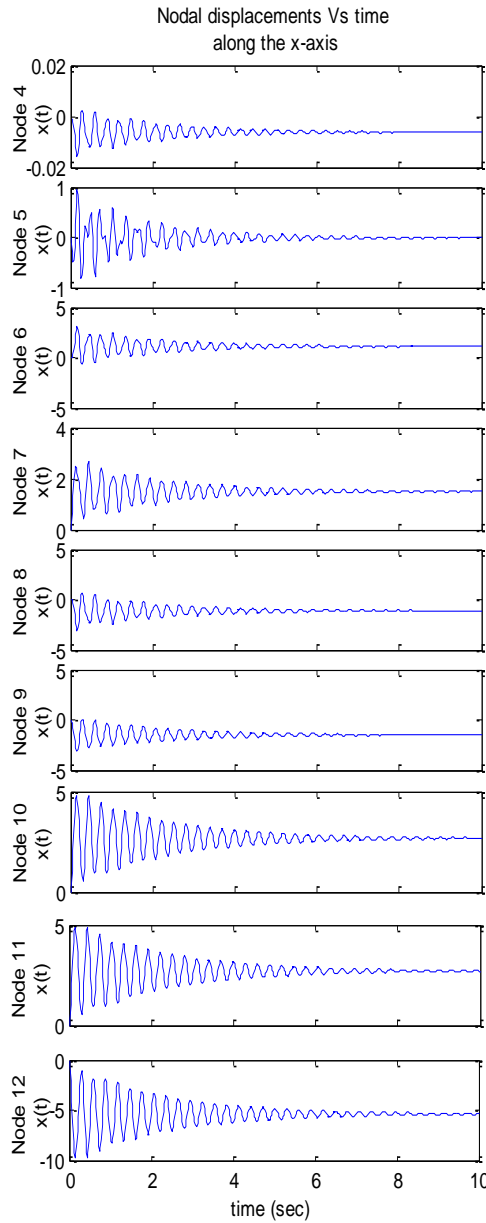
Structural Member	Structural Assembly of Figure 3.10 (a)		Structural Member	Structural Assembly of Figure 3.10 (b)	
	Length (m)	Tension-coefficient (N/m)		Length (m)	Tension-coefficient (N/m)
1	9.9991	31.0610	1	9.9994	31.0619
2	9.9993	31.0610	2	9.9998	31.0619
3	9.9991	31.0610	3	9.9996	31.0619
4	7.3784	30.1540	4	7.7119	35.3930
5	7.3786	49.0920	5	7.7112	71.1659
6	7.3782	30.1540	6	7.7113	35.3930
7	7.3785	49.0920	7	7.7111	71.1659
8	7.3780	30.1540	8	7.7126	35.3930
9	7.3784	49.0920	9	7.7120	71.1659
10	11.6675	43.4610	10	11.7571	40.2307
11	11.6676	43.4610	11	11.7568	40.2307
12	11.6675	43.4610	12	11.7570	40.2307
13	11.6666	27.2950	13	11.7565	24.6689
14	11.6666	27.2950	14	11.7569	24.6689
15	11.6665	27.2950	15	11.7570	24.6689
16	9.9991	7.4230	16	9.9998	23.8699
17	9.9991	7.4230	17	10.0002	23.8699
18	9.9993	7.4230	18	9.9997	23.8699
19	16.7052	-43.4610	19	11.9401	14.0456
20	16.7051	-43.4610	20	11.9403	14.0456
21	16.7051	-43.4610	21	11.9397	14.0456
22	16.7046	-20.3020	22	11.9393	26.7644
23	16.7047	-20.3020	23	11.9397	26.7644
24	16.7047	-20.3020	24	11.9407	26.7644
			25	16.7044	-50.4584
			26	16.7051	-50.4584
			27	16.7050	-50.4584
			28	16.7045	-44.9305
			29	16.7046	-44.9305
			30	16.7050	-44.9305

Structural Member	Structural Assembly of Figure 3.11 (a)		Structural Member	Structural Assembly of Figure 3.11 (b)	
	Length (m)	Tension-coefficient (N/m)		Length (m)	Tension-coefficient (N/m)
1	10.0001	27.3560	1	10.0005	27.3560
2	9.9999	27.3560	2	9.9996	27.3560
3	10.0000	27.3560	3	10.0001	27.3560
4	6.5092	35.7330	4	5.7183	52.7697
5	6.5094	83.5550	5	5.7172	151.0325
6	6.5091	35.7330	6	5.7176	52.7697
7	6.5089	83.5550	7	5.7174	151.0325
8	6.5088	35.7330	8	5.7180	52.7697
9	6.5092	83.5550	9	5.7179	151.0325
10	7.8768	47.3920	10	9.2110	34.7695
11	7.8769	47.3920	11	9.2109	34.7695
12	7.8768	47.3920	12	9.2109	34.7695
13	7.8769	63.4360	13	9.2097	27.3560
14	7.8766	63.4360	14	9.2103	27.3560
15	7.8767	63.4360	15	9.2103	27.3560
16	7.8759	25.4280	16	9.2105	50.7727
17	7.8760	25.4280	17	9.2103	50.7727
18	7.8760	25.4280	18	9.2104	50.7727
19	6.5091	14.3240	19	5.7169	63.2471
20	6.5089	33.4950	20	5.7180	127.8346
21	6.5088	14.3240	21	5.7174	63.2471
22	6.5092	33.4950	22	5.7179	127.8346
23	6.5092	14.3240	23	5.7180	63.2471
24	6.5094	33.4950	24	5.7167	127.8346
25	10.0001	4.3970	25	9.9997	27.3560
26	9.9999	4.3970	26	9.9997	27.3560
27	10.0000	4.3970	27	9.9999	27.3560
28	13.3228	-47.3920	28	9.0081	50.7180
29	13.3224	-47.3920	29	9.0073	50.7180
30	13.3227	-47.3920	30	9.0076	50.7180
31	13.3228	-41.4130	31	9.0070	50.1709
32	13.3228	-41.4130	32	9.0069	50.1709
33	13.3230	-41.4130	33	9.0067	50.1709
34	13.3225	-16.6010	34	9.0074	32.1433
35	13.3225	-16.6010	35	9.0074	32.1433
36	13.3226	-16.6010	36	9.0074	32.1433
			37	13.3226	-72.7943
			38	13.3223	-72.7943
			39	13.3224	-72.7943
			40	13.3220	-72.7943
			41	13.3219	-72.7943
			42	13.3216	-72.7943
			43	13.3220	-72.7943
			44	13.3220	-72.7943
			45	13.3219	-72.7943

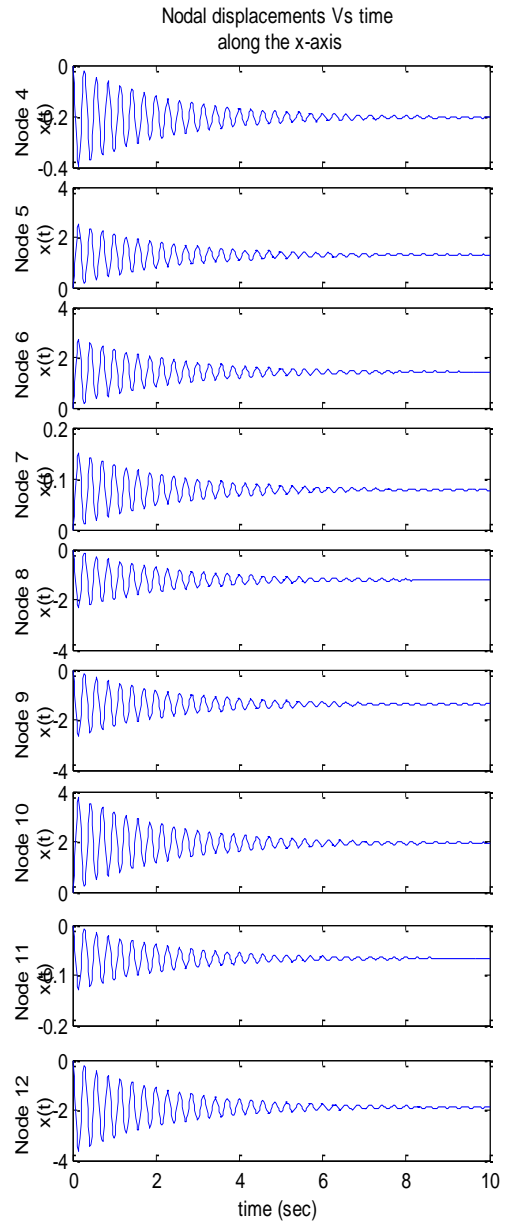
Table 3.4: Nodal coordinates of the structural systems of figures 3.10 and 3.11

Node	Structural System of Figure 3.10(a)			Structural System of Figure 3.10(b)		
	x	y	z	x	y	z
1	4.9870	-2.9080	-0.1430	4.6070	-3.3260	0.0540
2	0.0250	5.7730	-0.1430	0.8020	5.9210	0.1070
3	-5.0120	-2.8650	-0.1430	-5.3040	-1.9980	0.0520
4	7.1470	-0.0310	10.9560	6.8970	-1.5930	11.4550
5	2.4200	4.1500	7.1330	4.9220	5.2070	8.4000
6	-3.5470	6.2050	10.9560	-1.9230	6.9420	11.4980
7	-4.8040	0.0210	7.1330	-6.8030	1.8580	8.3670
8	-3.6000	-6.1740	10.9560	-4.9050	-4.9630	11.4220
9	2.3840	-4.1710	7.1330	1.9600	-6.6220	8.3230
10	5.0120	2.8650	22.0540	2.7500	5.1590	20.1400
11	-4.9870	2.9080	22.0540	-5.7570	-0.0970	20.0990
12	-0.0250	-5.7730	22.0540	3.0490	-4.8360	20.0790

Node	Structural System of Figure 3.11(a)			Structural System of Figure 3.11(b)		
	x	y	z	x	y	z
1	3.9520	-4.2090	5.3600	2.9370	-4.9710	3.8350
2	1.6690	5.5270	5.3600	2.8360	5.0290	3.8350
3	-5.6210	-1.3180	5.3600	-5.7730	-0.0580	3.8350
4	5.5260	-1.6690	12.6480	3.1040	-3.9260	12.9850
5	3.2230	3.0260	8.7720	5.1580	0.7560	10.4240
6	-1.3180	5.6200	12.6480	1.8480	4.6510	12.9850
7	-4.2320	1.2780	8.7720	-3.2330	4.0890	10.4240
8	-4.2080	-3.9510	12.6480	-4.9520	-0.7250	12.9850
9	1.0090	-4.3040	8.7720	-1.9250	-4.8450	10.4240
10	5.6200	1.3180	19.9360	4.6880	2.6720	19.2120
11	1.2780	4.2320	16.0600	0.0300	5.3630	17.2770
12	-3.9510	4.2080	19.9360	-4.6590	2.7240	19.2120
13	-4.3040	-1.0090	16.0600	-4.6600	-2.6560	17.2770
14	-1.6690	-5.5260	19.9360	-0.0300	-5.3970	19.2120
15	3.0260	-3.2230	16.0600	4.6300	-2.7070	17.2770
16	4.2090	3.9520	27.2230	-0.3630	5.7620	26.2670
17	-5.5270	1.6690	27.2230	-4.8090	-3.1950	26.2670
18	1.3180	-5.6210	27.2230	5.1710	-2.5670	26.2670

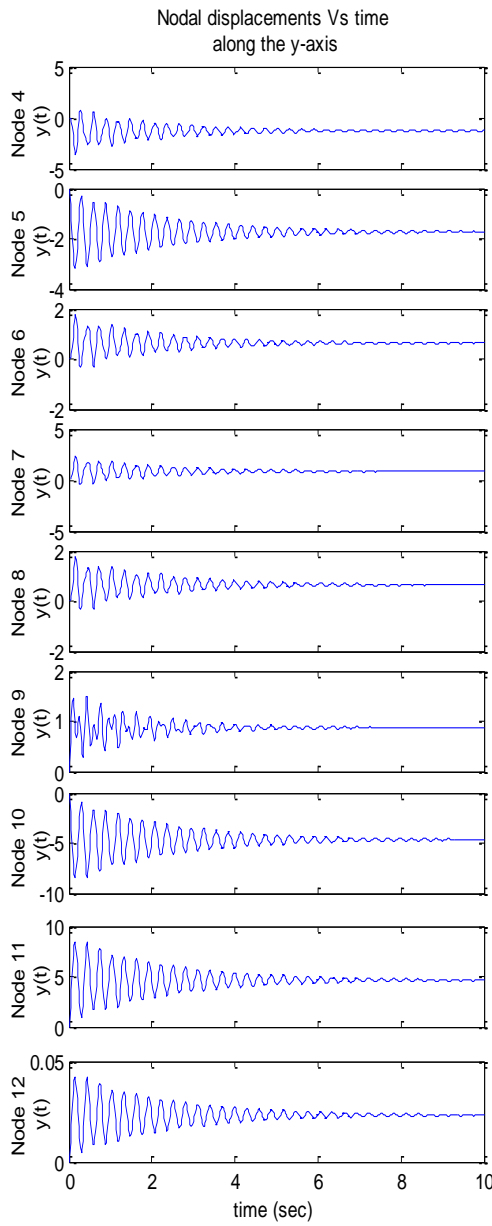


(a)

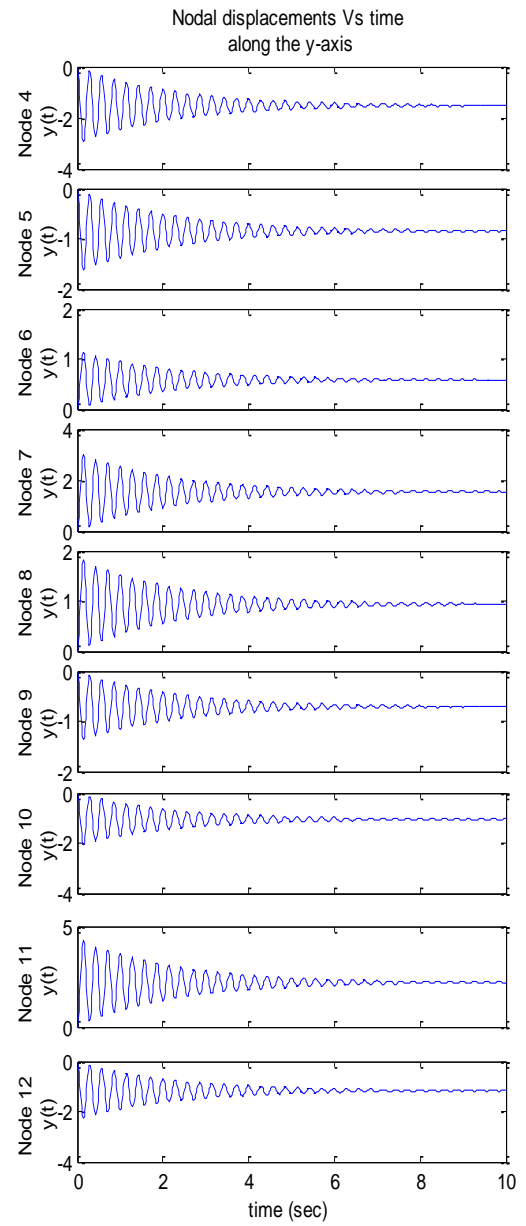


(b)

Figure 3.13: (a) and (b) are the dynamic response (nodal displacements (meter) Vs time (sec) along the x-axis) of the 2-stage 3-order tensegrity structures of Figure 3.10 (a) and (b), respectively, to three vertically downward loads of 300N on nodes 10, 11, and 12 suddenly applied at time $t = 0$ (sec)

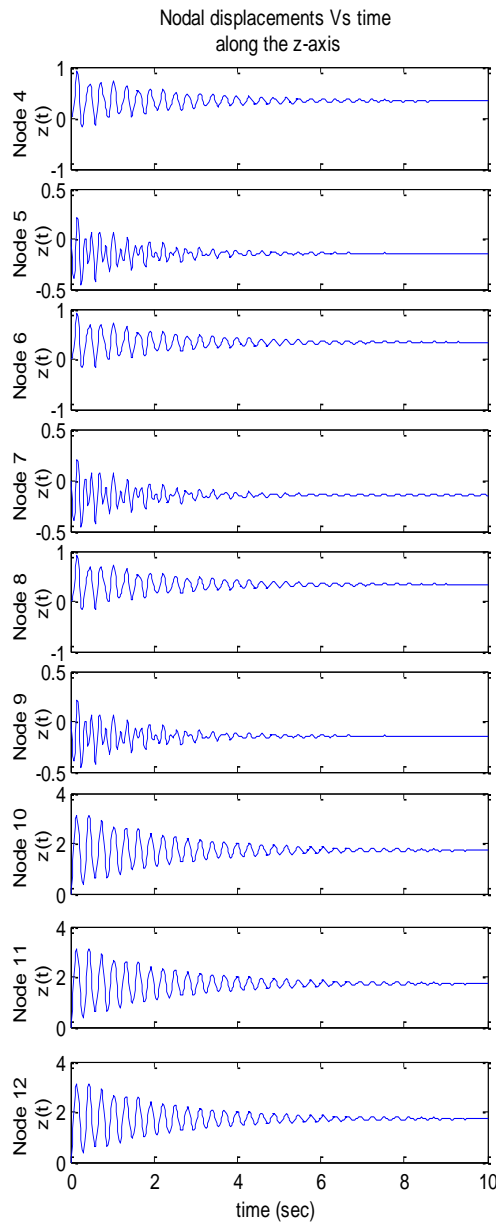


(a)

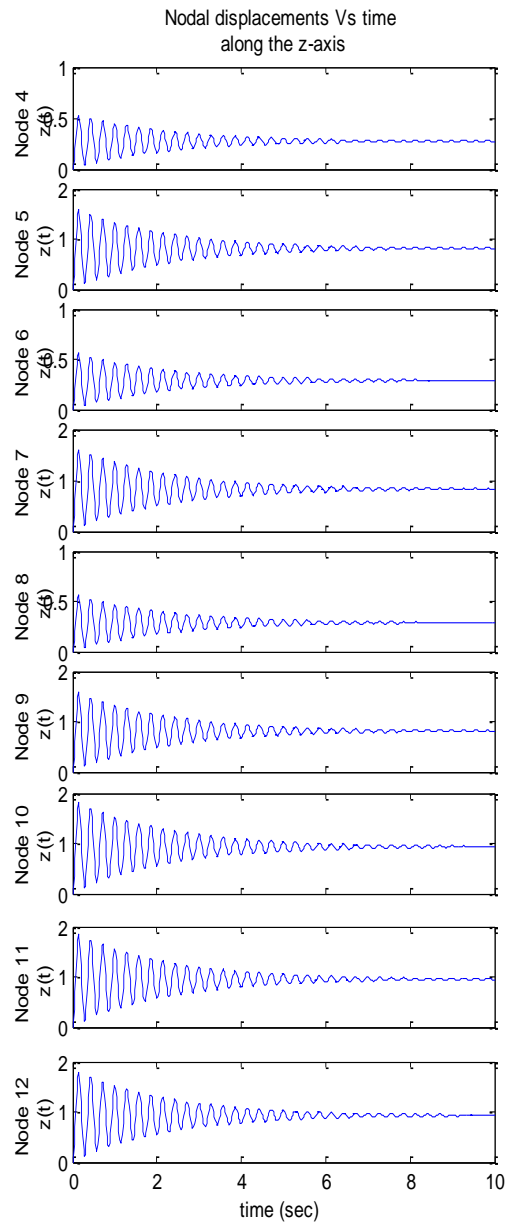


(b)

Figure 3.14: (a) and (b) are the dynamic response (nodal displacements (meter) Vs time (sec) along the y-axis) of the 2-stage 3-order tensegrity structures of Figure 3.10 (a) and (b), respectively, to three vertically downward loads of 300N on nodes 10, 11, and 12 suddenly applied at time $t = 0$ (sec)

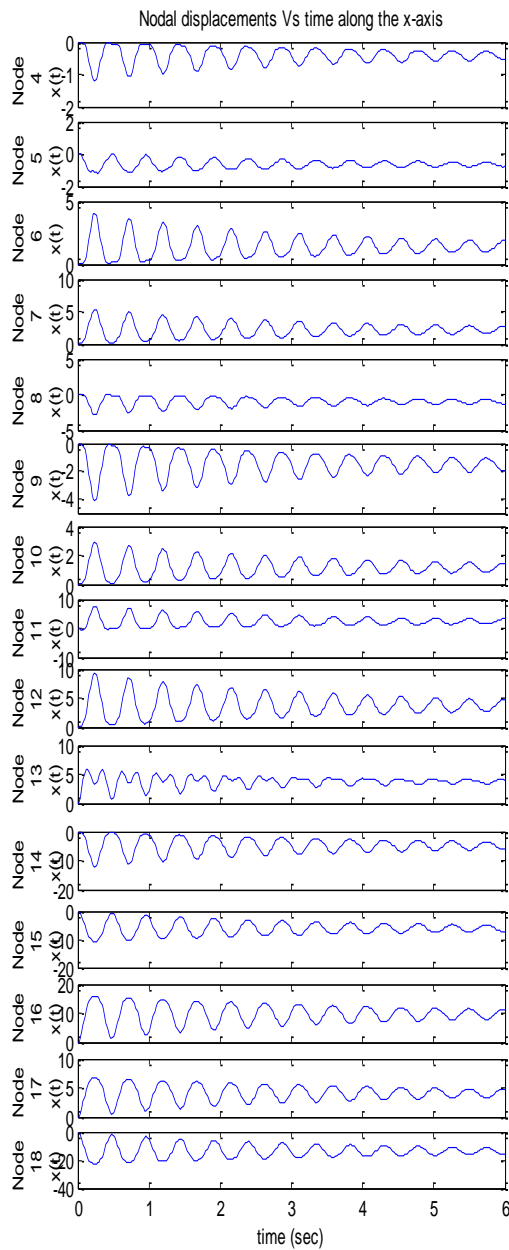


(a)

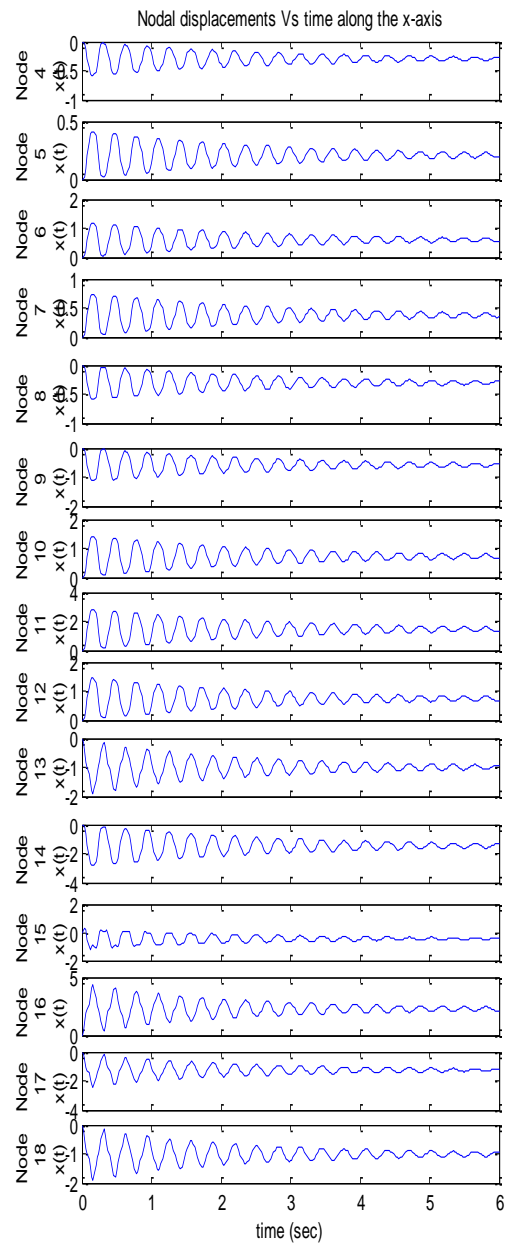


(b)

Figure 3.15: (a) and (b) are the dynamic response (nodal displacements (meter) Vs time (sec) along the z-axis) of the 2-stage 3-order tensegrity structures of Figure 3.10 (a) and (b), respectively, to three vertically downward loads of 300N on nodes 10, 11, and 12 suddenly applied at time $t = 0$ (sec)

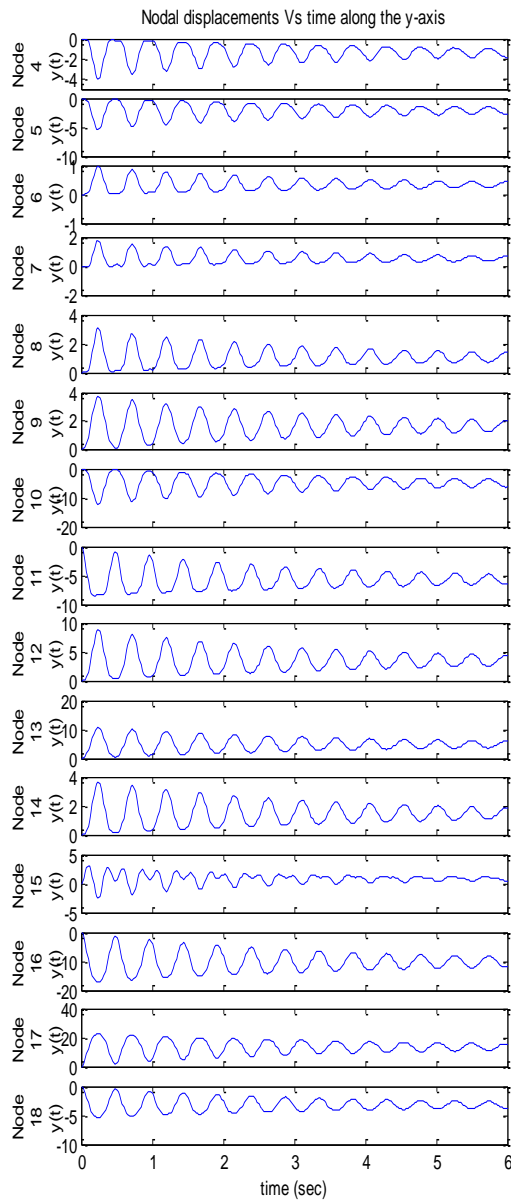


(a)

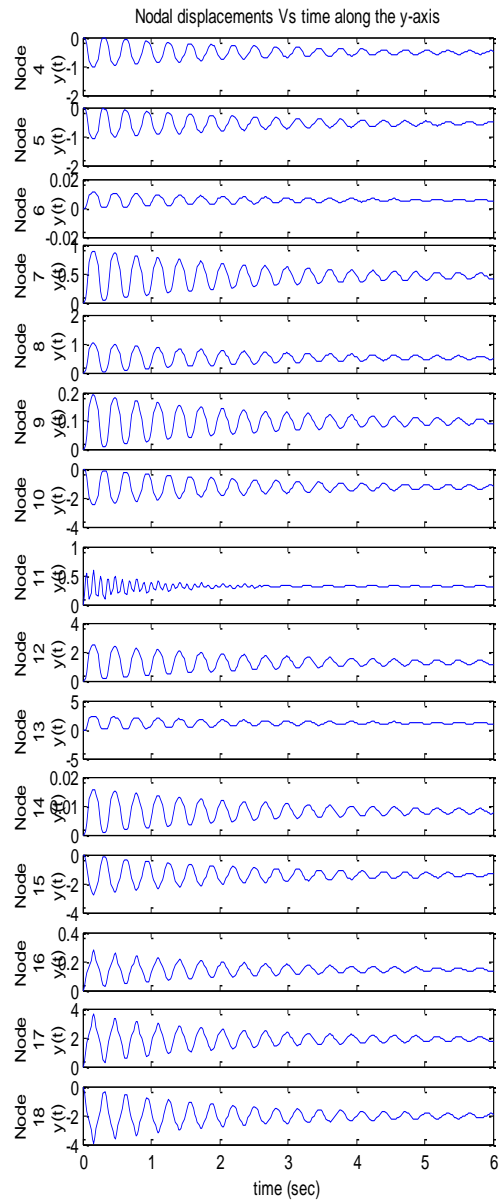


(b)

Figure 3.16: (a) and (b) are the dynamic response (nodal displacements (meter) Vs time (sec) along the x-axis) of the 3-stage 3-order tensegrity structures of Figure 3.11 (a) and (b), respectively, to three vertically downward loads of 300N on nodes 16, 17, and 18 suddenly applied at time $t = 0$ (sec)

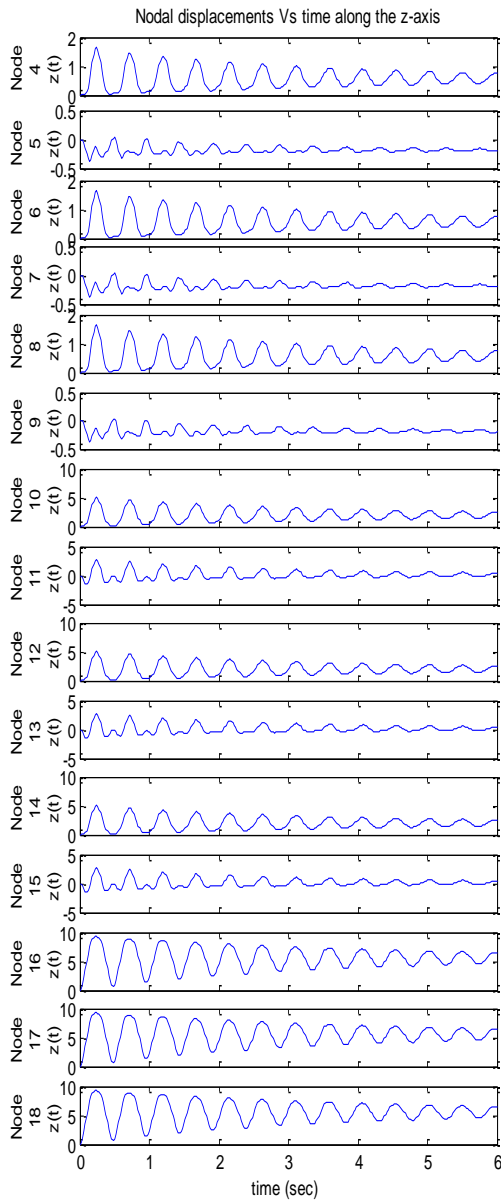


(a)

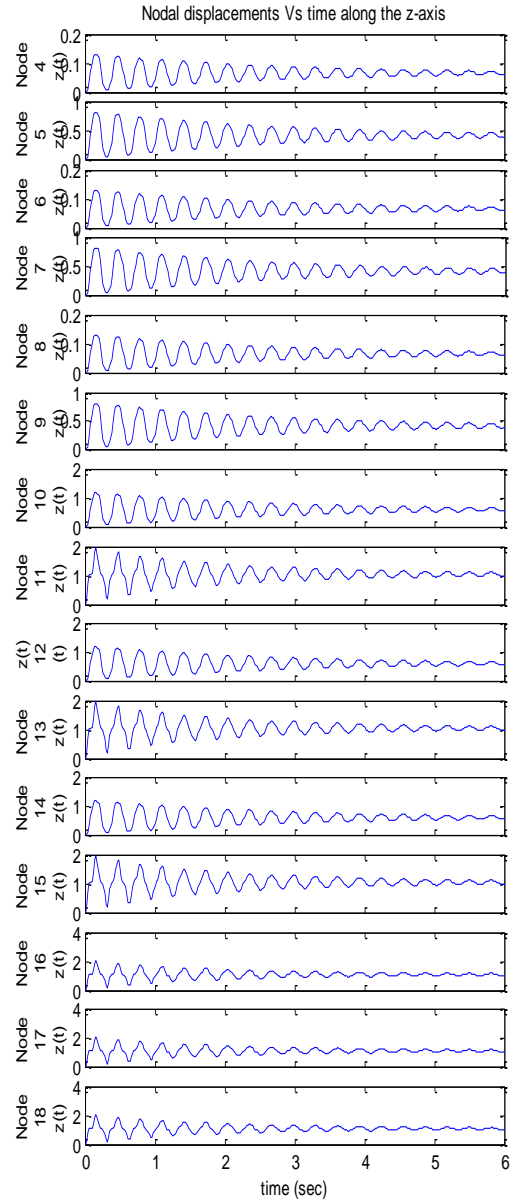


(b)

Figure 3.17: (a) and (b) are the dynamic response (nodal displacements (meter) Vs time (sec) along the y-axis) of the 3-stage 3-order tensegrity structures of Figure 3.11 (a) and (b), respectively, to three vertically downward loads of 300N on nodes 16, 17, and 18 suddenly applied at time $t = 0$ (sec)



(a)



(b)

Figure 3.18: (a) and (b) are the dynamic response (nodal displacements (meter) Vs time (sec) along the z-axis) of the 3-stage 3-order tensegrity structures of Figure 3.11 (a) and (b), respectively, to three vertically downward loads of 300N on nodes 16, 17, and 18 suddenly applied at time $t = 0$ (sec)

3.3 Discussions

For the 3-stage 3-order tensegrity structure of Figure 3.11, (a) is the minimal form of the structural assembly while (b) is the non-minimal since it contains 9 additional structural members (cables) than strictly necessary. Figure 3.11 (b) is not the only non-minimal form of a 3-stage 3-order tensegrity structure. Figure 3.11 shows another non-minimal 3-stage 3-order tensegrity structures with 12 additional structural members (instead of 9 as in Figure 3.11 (b)); the structural parameters of this structure are given in Table 3.5 and the structural assembly has the same nomenclature as that of the structure in Figure 3.12 (b).

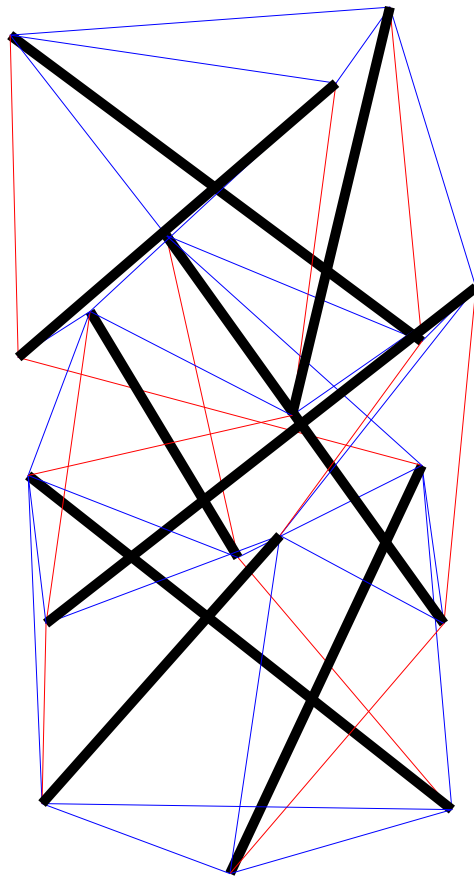
The possibility of having different possible configurations or structural assemblies for the 3-stage 3-order tensegrity structure being discussed highlights a very important feature of tensegrity structural systems; this feature symbolises the possibility of a tensegrity structure with a highly complex configuration to change its geometric properties, as such, making it suitable as a platform for the design of active structures capable of shape morphing, self-diagnosis and self-repair.

Active control of structural systems was originally proposed in the early 1970's as a concept and means to counteract extreme conditions such as earthquakes in buildings and undesirable vibrations in space-structure [92], [134–136]. For these structural systems, most active control systems will not be reliable enough over their service lives without expensive maintenance in place the economic cost of which may be difficult to justify. Thus, for the structural systems that involve catastrophic collapse, loss of life, or other safety criteria, passive control mechanism – through the use of tuned-mass dampers, for instance – are used as the common standard. However, for structures that are not governed by these safety criteria, active control is most practical [91], [92]. An important feature of active structures is their possession of feedback control systems that support certain functions such as control objectives that arise from multiple and/or changing performance goals, adaptation of structural geometry to improve performance by sensing the changes in behaviour and in loading, and autonomous and continuous control of several coupled structural subsystems [91], [92].

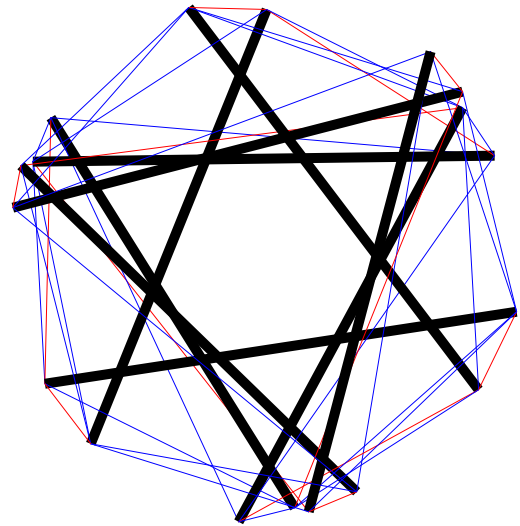
Active control structures are capable of interacting with complex environments. Moreover, active control techniques are the most efficient for the appropriate structural systems; one of such structural systems is the tensegrity structure. In particular, consider

a cable cut in the tensegrity structure of Figure 3.19; with the employment of knowledge-based computational (active) control system that is capable of reasoning, planning and learning, this structure can be transformed into that in Figure 3.11 (b), or the structure in Figure 3.11 (b) transformed into that in 3.11 (a), by disengaging certain cables and adjusting the lengths and forces in the remaining structural members while the structure continues to perform the task it was designed for. The structural transformation from Figure 3.19 to Figure 3.11 (b) and from Figure 3.11 (b) to Figure 3.11 (a) is depicted in Figure 3.20. Also, the structural configurations of figures 3.11 (a) and (b) can be considered as subsets of the 3-stage 3-order tensegrity structure of Figure 3.19. Figure 3.11 (b) is the minimal realizable 3-stage 3-order tensegrity structure and any failure (such as cut) in any of its structural member will to a total collapse of the structure. While there are other possible subsets that can be obtained from the tensegrity structure of the original set of Figure 3.19 by the removal of some structural members (cables), structure members can also be added to Figure 3.19 to expand the domain of the possible subsets of the original set, creating the possibility to explore other possibilities of structural transformation apart from those depicted in Figure 3.20.

Thus, an active tensegrity structure demonstrates the potential of a framework for advanced computational control technologies. While the active control technologies will be similar to those in civil and mechanical engineering, their application to tensegrity structures involves meeting new and unique challenges the solutions of which will create new possibilities for innovative active structures and new application areas. In addition, compared to other structures, tensegrity structures are highly suitable alternative for the design of structural systems with highly complex and variable topological configurations. Some researchers have pointed out the necessity to expand the concepts of control theory to embrace the larger concept of system design [94]. A major obstacle against integrated design of active control systems during the design process of structures is the computational cost involved. Nonetheless, to create an approach that tackles this unique problem offers a promising and major step in the evolvement process of human-made structures and tensegrity structures provide an important platform for exploring this problem.



(a) Side view



(b) Top view

Figure 3.19: An example of non-minimal 3-stage 3-order tensegrity structure (additional structural members are shown in red).

Table 3.5: Nodal coordinates, length and tension coefficient of each of the structural members of the tensegrity structure shown in Figures 3.19

Node	x	y	z
1	2.9200	-4.9710	5.2260
2	2.9860	5.0280	5.3630
3	-5.7070	0.0870	5.1890
4	3.6930	-4.2460	13.5760
5	5.5920	0.3400	10.9370
6	1.7190	5.2540	13.6810
7	-3.1210	4.6320	10.8880
8	-5.5210	-1.2050	13.5030
9	-2.4800	-5.0590	10.7630
10	5.2540	1.9920	19.0060
11	1.5030	5.4680	16.6720
12	-4.6260	3.4360	18.9040
13	-5.6900	-1.5280	16.4880
14	-0.9350	-5.8430	18.8230
15	3.9670	-4.2600	16.5700
16	0.3170	5.5340	24.8300
17	-5.4010	-2.6680	24.6470
18	4.5620	-3.5200	24.7590

Structural Member	Length (m)	Tension-coefficient (N/m)
1	10.0002	27.3560
2	10.0006	27.3560
3	10.0005	27.3560
4	5.6216	36.4469
5	6.8321	110.4727
6	5.6226	36.4469
7	6.8315	110.4727
8	5.6222	36.4469
9	6.8323	110.4727
10	8.4170	34.6820
11	8.4170	34.6820
12	8.4158	34.6820
13	8.4163	16.6500
14	8.4169	16.6500
15	8.4169	16.6500
16	8.4166	48.5014
17	8.4167	48.5014
18	8.4172	48.5014
19	5.6214	42.9237
20	6.8319	99.1674
21	5.6223	42.9237
22	6.8324	99.1674
23	5.6224	42.9237
24	6.8321	99.1674
25	10.0001	27.3560
26	10.0000	27.3560
27	10.0000	27.3560
28	8.2439	47.2194
29	8.2449	47.2194
30	8.2440	47.2194
31	8.2433	49.0676
32	8.2441	49.0676
33	8.2433	49.0676
34	8.2440	31.7848
35	8.2433	31.7848
36	8.2439	31.7848
37	10.4280	16.6500
38	10.4292	16.6500
39	10.4289	16.6500
40	13.3222	-66.4335
41	13.3221	-66.4335
42	13.3220	-66.4335
43	13.3216	-66.4335
44	13.3217	-66.4335
45	13.3221	-66.4335
46	13.3214	-66.4335
47	13.3222	-66.4335
48	13.3219	-66.4335

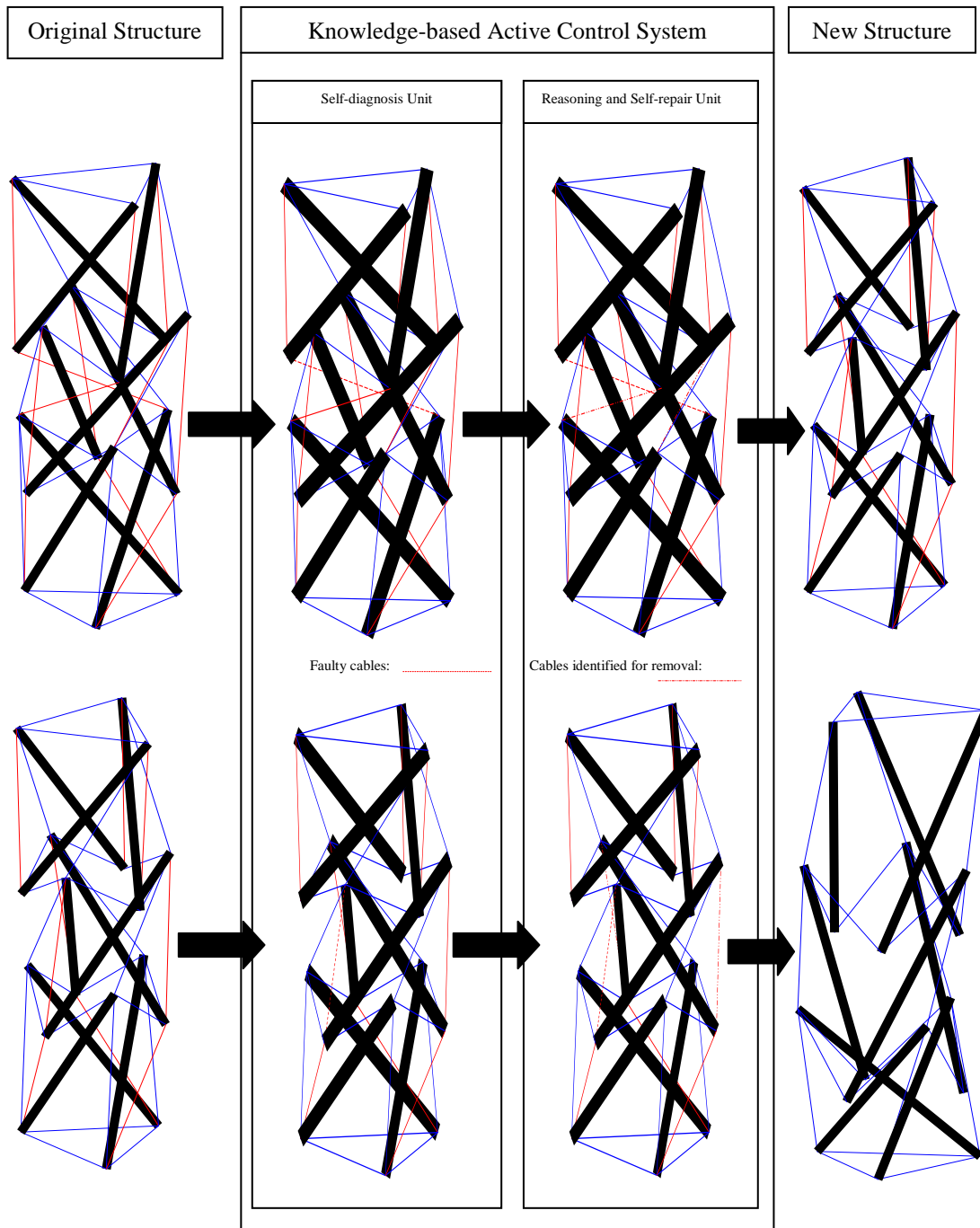


Figure 3.20: Examples of possible structural transformation as a result of failure (e.g. cable cut) in some structural members

3.4 Summary

In this chapter, the theory behind static and dynamic analyses of tensegrity structures has been outlined. Firstly, the derivation of the mass and stiffness matrices was described using the FEM. Next, the solution procedure for carrying out pseudo-static analysis of a tensegrity structure was presented and state-space model representation was used to simplify the dynamic analysis and model simulation of tensegrity structures of several tensegrity structures. The analysis and simulation provide an insight into the dynamic behaviour of tensegrity structures. It was also demonstrated that additional structural members introduced in a minimal tensegrity structural assembly causes increase in the stiffness of the overall structural system. In addition, it was noted that tensegrity structures are important candidates for structural design applications with shape morphing, self-diagnosis and self-repair capabilities due to their lightweight, ability to form complex variable geometry, possibility of structural transformation and adjustable stiffness.

The models of the tensegrity structures obtained from the FEM presented in this chapter may be reduced by techniques such as the Guyan reduction method [130] or dynamic sub-structuring method [137]. From a control theory viewpoint, not only are the reduced models still too large [138], but the input-output behaviour are only well approximated in the neighbourhood of the zero excitations frequency [139] and are very dependent on the initial choice of nodal degrees-of-freedom. Furthermore, for the design of lighter and stronger controlled flexible tensegrity structures, actuators and sensors must be placed at locations that will excite the desired state(s) most effectively. Thus, to facilitate further analysis and design of control systems for tensegrity structures, efficient and computationally simple model reduction and optimal actuator and sensor placement techniques will be presented in the next chapter.

Chapter 4

MODEL REDUCTION AND OPTIMAL ACTUATOR AND SENSOR PLACEMENT

4.1 Introduction

Model order reduction, or simply model reduction, is the process of approximating a dynamic model of high-order, or high number of states, by a simpler one of a low-order. This operation is carried-out to facilitate further analysis and design of control systems. In classical structural dynamics, the model of structures, usually obtained from a finite element analysis, is reduced by techniques such as the Guyan reduction method [130] or dynamic sub-structuring method [137]. The main idea of these techniques is that, to reduce the dimension of the mass and stiffness matrices, the designer focuses only on nodal coordinates of interest and eliminates or condenses all other degrees-of-freedom to the degrees of freedom of interest using matrix transformation that usually preserves the stiffness matrix but eliminates the masses of the removed nodes. From a control theory viewpoint, not only is the reduced model still too large [138], but the input-output behaviours are only well approximated in the neighbourhood of the zero excitations frequency and are very dependent on the initial choice of nodal degrees-of-freedom [139].

Many model reduction techniques, such as optimal projection method [140], the aggregation method [141], and the internal balancing method [142–144] (see [140], for example, for the relationships among these methods), have extensively been developed in control literature and these methods use optimization methods (for calculating the H_2 norm, H_∞ norm and Hankel-norm, and others) to reduce complex high order models to less complex low-order approximations in order to preserve the dynamic behaviour of the systems over well-defined frequency ranges. Moreover, these techniques provide a

means for controller design, for instance, using optimal and robust control methods, and the complexity and performance of model-based controllers are dependent on the order of the model to a large extent. The truncation and residualization reduction techniques of the internal balancing method [142–144] which, compared to other methods, may be less accurate but computationally simpler and relatively efficient [133], are employed in this chapter for the reduction of models of tensegrity structural systems obtained using the modelling method presented in Chapter 3.

Also, in developing the dynamic model of a structural system written in the modal state-space form, for instance, the system's states (state variables) may be chosen as the modal displacements and velocities. The design of lighter and stronger controlled flexible structures requires that actuators and sensors be placed at locations that will excite the desired states most effectively. This task commonly involves the determination of the precision requirement for each actuator/sensor as well as the minimum number and/or location of the required actuators/sensors. Moreover, in collocated structural systems, where structural members also serve as actuators and/or sensors, or where actuators and sensors are placed at the same locations, actuators and sensors affect the structural dynamics of the integrated structure and, as such, their numbers and locations must be considered part of the structural design, dynamic analysis and controller design to achieve best performance. Thus, the optimal location or placement of actuators and sensors, which has the potential to minimize the control efforts and affect the credibility of the output feedback signals, is a very important step in the design of controlled flexible structures. Since it will not be possible, in general, to relocate the actuators and sensors online while the structure is operational, and it may even require a complete redesign or disassembling and reassembling to alter the location of the actuators and sensors, the design of controller are mostly done after the locations of actuators and sensors have been determined. Clearly, selecting the number and locations of the actuators and sensors first, without taking into account during the selection process the future control problem to be solved, is not the most effective way of dealing with this engineering design problem.

Different techniques have thus been proposed for the simultaneous selection of actuator and sensors and the design of output feedback control systems (see, for example, [145], [146]). The problem of finding the optimal numbers and locations of actuators and sensors of structural systems, in general, is a complicated nonlinear

optimization problem. For a given structure, the optimal number of actuators and sensors directly relate to the number of states to be controlled and observed. The optimal location of actuators and sensors has been extensively studied in the past for general structural systems (see [147] for a review) and in this chapter, the optimal actuator and sensor placement method presented in [133], [148], for its numerical simplicity, will be applied to tensegrity structural systems. Moreover, optimal actuator and sensor placement is of particular importance in the design of active tensegrity structures containing very large number of structural members and which are capable of undergoing a wide range of nodal displacements (for shape control, for instance) since they often require the use of a large number of actuators and sensors. The approach employed uses the model of a structural system to determine optimal actuator and sensor placement since both the optimal actuator and sensor placement and the controller design (that is, a model-based controller design) are dependent on the information contained in the structural model.

4.2 Definitions and Notations

The dynamics of a multivariable system described by the state-space model is a function of several state variables but, in general, not all these states are necessarily measurable (observable) when the system is excited by the inputs. Likewise, not all these states are necessarily driven (controllable) by the inputs. Controllability and observability are terms, when used in structural dynamics, describe whether the inputs of the structural system drive all structural modes and whether all states are measurable, respectively. However, this information, although very useful, does not tell us the degrees by which the systems are, or are not, controllable and observable. A more quantitative answer that represents these degrees can be obtained by the controllability and observability grammians. Moreover, these grammians are useful for system optimization that enables us to determine optimal locations to place the actuators and sensors just from the preliminary information on structural properties. They are also useful for reducing the order of dynamic models written in state-space format. In this section, more precise definitions of controllability, observability, grammians and norms in systems analysis are given for linear time-invariant systems that will be considered later in the chapter.

4.2.1 Controllability, Observability and Grammians

Controllability: An n -dimensional linear time-invariant system (A, B, C, D) is said to be completely controllable if there exists an unconstrained control (piecewise continuous) input u that can transfer any initial state $x(t = t_0)$ to any final state $x(t = t_f)$ within the finite time $t_f - t_0$; otherwise, the system is uncontrollable. Let P_c be a controllability matrix defined as follows:

$$P_{c_{n \times mn}} = [B \quad AB \quad A^2B \quad \dots \quad A^{n-1}B] \quad (4.1)$$

where n and m are the number of states and inputs, respectively. A common criterion for determining the controllability of a system is as follows [149]:

$$\det(P_c) = |P_c| \neq 0 \quad (4.2)$$

That is, if P_c is full rank (spans the n -dimensional space), then the system is completely controllable.

Observability: An n -dimensional linear time-invariant system (A, B, C, D) is said to be completely observable on the interval $t \in [t_0, t_f]$ if any initial state $x(t = t_0)$ is uniquely determined by observing the output $y(t)$ between the interval $t \in [t_0, t_f]$; otherwise, the system is unobservable. Let P_o be an observability matrix defined as follows:

$$P_{o_{pn \times n}} = \begin{bmatrix} C \\ CA \\ \vdots \\ CA^{n-1} \end{bmatrix} \quad (4.3)$$

where p is the number of outputs, a common criterion for determining the complete observability of a system is as follows [149]:

$$\det(P_o) = |P_o| \neq 0 \quad (4.4)$$

That is, if P_o is full rank (spans the n -dimensional space), the system is completely observable.

As a result of numerical overflow that may result in finding the determinants or ranks of controllability and observability matrices, the use of equations (4.1) and (4.3) are limited to systems with few numbers of states. For better numerical properties, the

grammians are used to study the controllability and observability properties of state-space models [10].

Grammians: The controllability and observability grammians are defined, respectively, by the following equations [149]:

$$W_c(t) = \int_0^t e^{A\tau} B B^T e^{A^T \tau} d\tau \quad (4.5)$$

$$W_o(t) = \int_0^t e^{A^T \tau} C^T C e^{A\tau} d\tau \quad (4.6)$$

for $0 < t < \infty$. Equations (4.5) and (4.6) are solutions to the following differential equations [149]:

$$\frac{dW_c(t)}{dt} = A W_c(t) + W_c(t) A^T + B B^T \quad (4.7)$$

$$\frac{dW_o(t)}{dt} = A^T W_o(t) + W_o(t) A + C^T C \quad (4.8)$$

From of equations (4.7) and (4.8), if $\frac{dW_c(t)}{dt} = W_c$ and $\frac{dW_o(t)}{dt} = W_o$ exist as $t \rightarrow \infty$, stationary solutions of W_c and W_o are obtained using the following Lyapunov equations [149]:

$$A W_c(t) + W_c(t) A^T + B B^T = 0 \quad (4.9)$$

$$A^T W_o(t) + W_o(t) A + C^T C = 0 \quad (4.10)$$

A numerical algorithm given in [150] can be used to solve equations (4.9) and (4.10) for W_c and W_o . Furthermore, stability is an important property of systems and involves whether or not the solutions of the system's state differential equations tend to grow indefinitely as $t > \infty$. The linear time-invariant system (A, B, C, D) is said to be asymptotically stable if and only if all the eigenvalues of A have strictly negative real parts; where asymptocity in this definition implies that initial deviations (at $t = 0$) of the solutions are in the vicinity of the nominal solution [151].

Matrices W_c and W_o only exist for stable systems and are both positive definite for $t > 0$ [149]. The square roots of the eigenvalues of the product of W_c and W_o are called the Hankel singular values of the system and are given by the following equations [152]:

$$\eta_i = \sqrt{\lambda_i(W_c W_o)}, i = 1, 2 \dots n \quad (4.11)$$

where η_i and λ_i are the i^{th} Hankel singular value and the i^{th} eigenvalue of the product of W_c and W_o for the n -order state-space model, respectively. While the eigenvalues of A of the system (A, B, C, D) define its stability, the Hankel singular values provide a measure of energy for each state in the system. Thus, by keeping only the states of a system with larger energy, most system characteristics in terms of stability, frequency and time response are preserved [144], [152]. This idea is the basis for the model reduction discussed later in this chapter.

Furthermore, a system is said to be open-loop balanced, or simply balanced, if its controllability and observability grammians are diagonal and equal; diagonality implies that each state can be independently controlled and observed while equality implies that each state is controllable in the same degree as it is observable. The grammians of a balanced system satisfies the following equalities [144]:

$$W_c = W_o = H \quad (4.12)$$

where $H = \text{diag}(\eta_1, \eta_2, \dots, \eta_n)$ and $\eta_i \geq 0$ is the i^{th} Hankel singular value. A stable but unbalanced system (A, B, C, D) can be balanced using the following state transformation:

$$x_b = T x \quad (4.13)$$

where x and x_b are the original state and the new state variables (for the balanced system), respectively. Thus, the corresponding state-space model of the system can be written in terms of x_b as follows:

$$\dot{x}_b = T A T^{-1} x_b + T B u \quad , \quad y = C T^{-1} x_b + D u \quad (4.14)$$

The grammians of the balanced system are obtained as follows:

$$W_c^b = T W_c T \quad , \quad W_o^b = T^{-T} W_o T^{-1} \quad (4.15)$$

The algorithms to find T such that $W_c^b = W_o^b = H$ can be found in [144], [150], [152]. It should be noted that since T can be arbitrarily scaled and $x = T^{-1} x_b$, both x and x_b can be chosen as the state variables of state-space model of the original system; T can, as such, be freely chosen to suite any problem at hand [151]. Moreover, since grammians of structure with rigid body modes (that is, structure whose dynamic models have a number of poles at the origin) do not exist since they reach infinity value – although the structural system may be controllable and observable [133], it may be

convenient to remove the rigid body modes by simply applying boundary conditions first (as in Chapter 3, for example) before transforming it to the modal model and then computing the grammians.

If the unbalanced system (A, B, C, D) is unstable (that is, not all system eigenvalues have strictly negative real parts), it can be decomposed into its stable and unstable subspaces. It should be recalled that, using the eigen decomposition, $A_{n \times n}$ can be diagonalized in the form $A = \mathbb{T}\Lambda\mathbb{T}^{-1}$ where \mathbb{T} is a matrix of eigenvectors and Λ is a diagonal matrix of eigenvalues (eigenvalues assumed to be distinct and \mathbb{T} assumed to be nonsingular). The stable subspace of the system is the subspace spanned by the eigenvectors that correspond to eigenvalues with strictly negative real parts (stable system poles) while the other eigenvectors (unstable system poles) form the unstable subspace. It is obvious that the stable part of the system correspond to the stable subspace; this part can be isolated and balanced using the method of the preceding paragraphs. Since the whole of the n -dimensional space is the direct sum of the stable and unstable subspaces [151], the unstable part of the system can then be added back to the balanced part to form the state differential equations of the whole system. Thus, the state vector is partitioned as follows:

$$x^T = [(x_{unstable})^T (x_{stable})^T] \quad (4.16)$$

The balancing of the stable subspace is done using the following state transformation:

$$x_b = T x_{stable} \quad (4.17)$$

Finally, the state vector of the unstable but ‘balanced’ system is obtained as follows:

$$(x'_b)^T = [(x_{unstable})^T x_b^T] \quad (4.18)$$

4.2.2 The H_2 , H_∞ and Hankel Norms

The transfer function of a linear system is the ratio of the Laplace transform of the output variables to the Laplace transform of the input variables with all initial conditions assumed to be zero. The transfer matrix of the system (A, B, C, D) is given by [132], [151]:

$$G(s) = \frac{y(s)}{u(s)} = C(sI - A)^{-1}B + D \quad (4.19)$$

where s is a complex variable, y and u are the transforms of the output and control vectors, respectively and I is the identity matrix. Each element $G_{ij}(s)$ of $G(s)$ is the transfer function from the j^{th} input to the i^{th} output. In scalar systems (where both $y(t)$ and $u(t)$ are one-dimensional), the transfer matrix reduces to a scalar transfer function. Also, transfer function is invariant under coordinate transformation of the states [151].

The frequency response of a system is the steady state response of the system to a sinusoidal input signal. It is simply obtained by substituting $s = j\omega$ in equation (4.19) where j and ω are the imaginary unit and angular frequency, respectively [132]. The gain of a system γ at frequency ω is defined as follows [153]:

$$\gamma = \|G(\omega)\|_2 = \frac{\|y(\omega)\|_2}{\|u(\omega)\|_2} \quad (4.20)$$

where $\|\cdot\|_2$ represents the 2-norm of a system and provides quantitative information about the average system gain over all frequencies.

The impulse function $\delta(t)$ is a piecewise function that is defined as follows [132]:

$$\delta(t) = \begin{cases} +\infty, & t = 0 \\ 0, & \text{otherwise} \end{cases} \quad (4.21)$$

and satisfies $\int_{-\infty}^{\infty} \delta(t) dt = 1$, and the response of a system to an impulse input $\delta(t)$ is its impulse response. The definitions of the 2-norm and other types of norms in system analysis follow.

The H_2 Norm: The 2-norm, or H_2 norm, of the system (A, B, C, D) with transfer matrix $G(s)$ is the root-mean-square of its impulse response. It is defined as follows [153]:

$$\|G\|_2 = \sqrt{\frac{1}{2\pi} \int_{-\infty}^{\infty} \text{tr}(G(\omega)^* \cdot G(\omega)) d\omega} \quad (4.22)$$

Equivalently, (4.22) may be written as follows [133]:

$$\|G\|_2 = \sqrt{\text{tr}(C^T C W_c)} = \sqrt{\text{tr}(B B^T W_o)} \quad (4.23)$$

where $\text{tr}(\cdot)$ and $G(\cdot)^*$ denotes the trace and complex conjugate transpose of a matrix, respectively. $\|G\|_2$ can also be obtained by taking the square root of the trace of the

stationary covariance of the system output when the system is driven by white noise [154]. $\|G\|_2 < \infty$ only if $G(s)$ has poles strictly on the left-hand plane of the complex plane and $D = 0$.

The H_∞ Norm: The infinity-norm, H_∞ norm, of the system (A, B, C, D) with transfer matrix $G(s)$ is the peak gain of the frequency response. It is defined as follows [153]:

$$\|G(\omega)\|_\infty = \sup_{\omega(-\infty, \infty)} (\|G(\omega)\|_2) = \sigma_{max} \quad (4.24)$$

where ‘sup’ is the abbreviation for supremum (that is, the smallest upper bound of a set) and σ_{max} is the largest singular value of matrix $G(\omega)$; in scalar systems, $\|G(\omega)\|_\infty = \max_{\omega(-\infty, \infty)} (|G(\omega)|)$. The largest singular value at frequency ω is obtained as follows:

$$\sigma_{max} = \sqrt{\lambda_{max}(G(\omega)^* \cdot G(\omega))} \quad (4.25)$$

where λ_{max} is the largest eigenvalue of the product of $G(\omega)^*$ and $G(\omega)$. A fast algorithm to compute $\|G(\omega)\|_\infty$ is given in [155].

The Hankel Norm: The Hankel singular values of a system provide a measure of energy for each of the states of the system [144], [152]. The largest Hankel singular value, called the Hankel norm, is a measure of total energy of the whole system and is obtained using the following equation [133]:

$$\|G(\omega)\|_h = \sqrt{\lambda_{max}(W_c \cdot W_o)} \quad (4.26)$$

where λ_{max} is the largest eigenvalue of the product of W_c and W_o . The relationship between $\|G(\omega)\|_\infty$ and $\|G(\omega)\|_h$ is given as follows [156]:

$$\|G(\omega)\|_h = \frac{1}{2} \cdot \|G(\omega)\|_\infty \quad (4.27)$$

4.3 Model Reduction

4.3.1 Truncation Method

Consider the structural system (A, B, C, D) with state vector x whose equation is written in the modal form which has now been transformed into a balanced system (A_b, B_b, C_b, D_b) with state vector x_b using the transformation matrix T (see equations 4.13 – 4.15). The matrices A_b, B_b, C_b and D_b are defined as follows:

$$A_b = TAT^{-1}, \quad B_b = TB, \quad C_b = CT^{-1}, \quad D_b = D \quad (4.28)$$

The controllability and observability grammians of the balanced system are as follows:

$$W_c^b = T W_c T, \quad W_o^b = T^{-T} W_o T^{-1}, \quad W_c^b = W_o^b = H \quad (4.29)$$

where H is a diagonal matrix whose diagonal element are the Hankel singular values arranged in descending order of magnitude (H is the same for the original and balanced system). Since the Hankel singular values provide a measure of energy of each states of the system, by keeping only the states of the system with larger energy and deleting, or truncating, all others, most of the dynamic behaviour of the original high-order model is approximated [144], [152]. Accuracy of the low-order system model may be improved by taking more states with higher energy. For a system that has unstable subspace, the Hankel singular values of unstable system poles are set to infinity and precedes other Hankel singular values on the leading diagonal of matrix H . The procedure of the truncation is outlined by the following set of equations:

$$\text{Modal Model:} \quad \dot{x} = A x + B u \quad y = C x + D u \quad (4.30)$$

$$\text{Balanced Model:} \quad \dot{x}_b = \begin{bmatrix} \dot{x}_1 \\ \dot{x}_2 \end{bmatrix} = A_b x_b + B_b u = \begin{bmatrix} A_{11} & A_{12} \\ A_{21} & A_{22} \end{bmatrix} \begin{bmatrix} x_1 \\ x_2 \end{bmatrix} + \begin{bmatrix} B_1 \\ B_2 \end{bmatrix} u \quad (4.31)$$

$$y = C_b x_b + D u = [C_1 \quad C_2] \begin{bmatrix} x_1 \\ x_2 \end{bmatrix} + D u \quad (4.32)$$

$$\text{Reduced Model:} \quad \dot{x}_1 = A_{11} x_1 + B_1 u \quad y = C_1 x_1 + D u \quad (4.33)$$

where equation (4.32) is the reduced model, x_1 is the retained state vector that contains states with larger energy and x_2 is the truncated state vector containing states with negligible energy.

4.3.2 Residualization Method

Instead of employing truncation as in the preceding section, a transformation that projects the subspace of the part to be truncated onto the retained part preserves the steady-state response (the ‘dc gain’) of the modal model. This is achieved by noting that the contribution of the states x_2 are negligible, \dot{x}_2 can therefore be set to zero; that is, $\dot{x}_2 = 0$. The model reduction procedure can therefore be written as follows:

$$\text{Modal Model:} \quad \dot{x} = A x + B u \quad y = C x + D u \quad (4.34)$$

$$\text{Balanced Model:} \quad \dot{x}_b = \begin{bmatrix} \dot{x}_1 \\ 0 \end{bmatrix} = A_b x_b + B_b u = \begin{bmatrix} A_{11} & A_{12} \\ A_{21} & A_{22} \end{bmatrix} \begin{bmatrix} x_1 \\ x_2 \end{bmatrix} + \begin{bmatrix} B_1 \\ B_2 \end{bmatrix} u \quad (4.35)$$

$$\Downarrow$$

$$\dot{x}_1 = A_{11} x_1 + A_{12} x_2 + B_1 u \quad (4.36)$$

$$x_2 = -A_{22}^{-1} A_{21} x_1 - A_{22}^{-1} B_2 u \quad (4.37)$$

$$y = C_b x_b + D u = [C_1 \quad C_2] \begin{bmatrix} x_1 \\ x_2 \end{bmatrix} + D u \quad (4.38)$$

$$\text{Reduced Model:} \quad \dot{x}_1 = (A_{11} - A_{12} A_{22}^{-1} A_{21}) x_1 + (B_1 - A_{12} A_{22}^{-1} B_2) u \quad (4.39)$$

$$y = (C_1 - C_2 A_{22}^{-1} A_{21}) x_1 + (D - C_2 A_{22}^{-1} B_2) u \quad (4.40)$$

where (4.39) and (4.40) are obtained by substituting (4.37) into (4.36) and (4.38), respectively. Of course, it is only possible to obtain the reduced model of equation if A_{22} is nonsingular.

4.3.3 Model Reduction Error

To determine the number of states in the balanced model with a higher energy to be retained in the reduced model, it is necessary to evaluate the model reduction error. As such, there is a trade-off between having a small sized model and having an accurate model. Let G , G_r and G_t be the transfer function of the modal model (for example, equation (4.30)), reduced model (for example, the first partition of equation (4.31)) and truncated model (for example, the second partition of equation (4.31)), respectively. The reduction error that provide absolute or relative approximation of the error that are commonly used are as follows:

a) Additive Error due to model reduction using the H_2 norm [157]:

$$\epsilon_2 = \|G - G_r\|_2 = \|G_t\|_2 \quad (4.41)$$

If n , r and t are the number of states in the modal, reduced and truncated models, respectively, ϵ_2 can simply be written as follows:

$$\epsilon_2 = \|G_t\|_2 = \sqrt{\sum_{i=r+1}^n (\|G_i\|_2)^2} \quad (4.42)$$

where G_i is the transfer function of the i^{th} state.

b) Additive Error due to model reduction using the H_∞ norm [158]:

$$\epsilon_\infty = \|G - G_r\|_\infty = \|G_t\|_\infty \leq 2 \sum_{i=r+1}^n \eta_i \quad (4.43)$$

where η_i is the i^{th} Hankel singular value of G .

c) Relative Error due to model reduction using the H_∞ norm [144], [159], [160]:

$$\begin{aligned} \epsilon_{r\infty} &= \|G^{-1}(G - G_r)\|_\infty = \|G^{-1}G_t\|_\infty \\ &= \frac{\sum_{i=r+1}^n \eta_i}{\sum_{i=1}^n \eta_i} \leq \prod_{i=r+1}^n [1 + 2\eta_i(\sqrt{1 + \eta_i^2} + \eta_i)] - 1 \end{aligned} \quad (4.44)$$

Figure 4.1 summarizes the model reduction procedure described in this section.

4.4 Optimal Actuator and Sensor Placement

For the structural system written in a modal form (see equation (3.55)), the state variables may be chosen simply as the modal displacements and velocities of the structure, for instance. In this case, it follows that the i^{th} structural mode is assigned two state variables – displacement and velocity – in the state-space model. For this reason, attention will be placed on the use of the terms i^{th} mode and i^{th} state of a structure. Also, the balanced model representation (equations (4.31-4.32) or (4.35 and 4.38)) will be used for the analysis in this section. While the reduced model representation (equations (4.33) or (4.39-4.40)) can directly replace the balanced model representation in the analysis, slight modifications in some equations and definitions will generally be required for the expressions to be valid for the modal model representation (equation (3.55)); nonetheless, the basic ideas remain the same for three model representations.

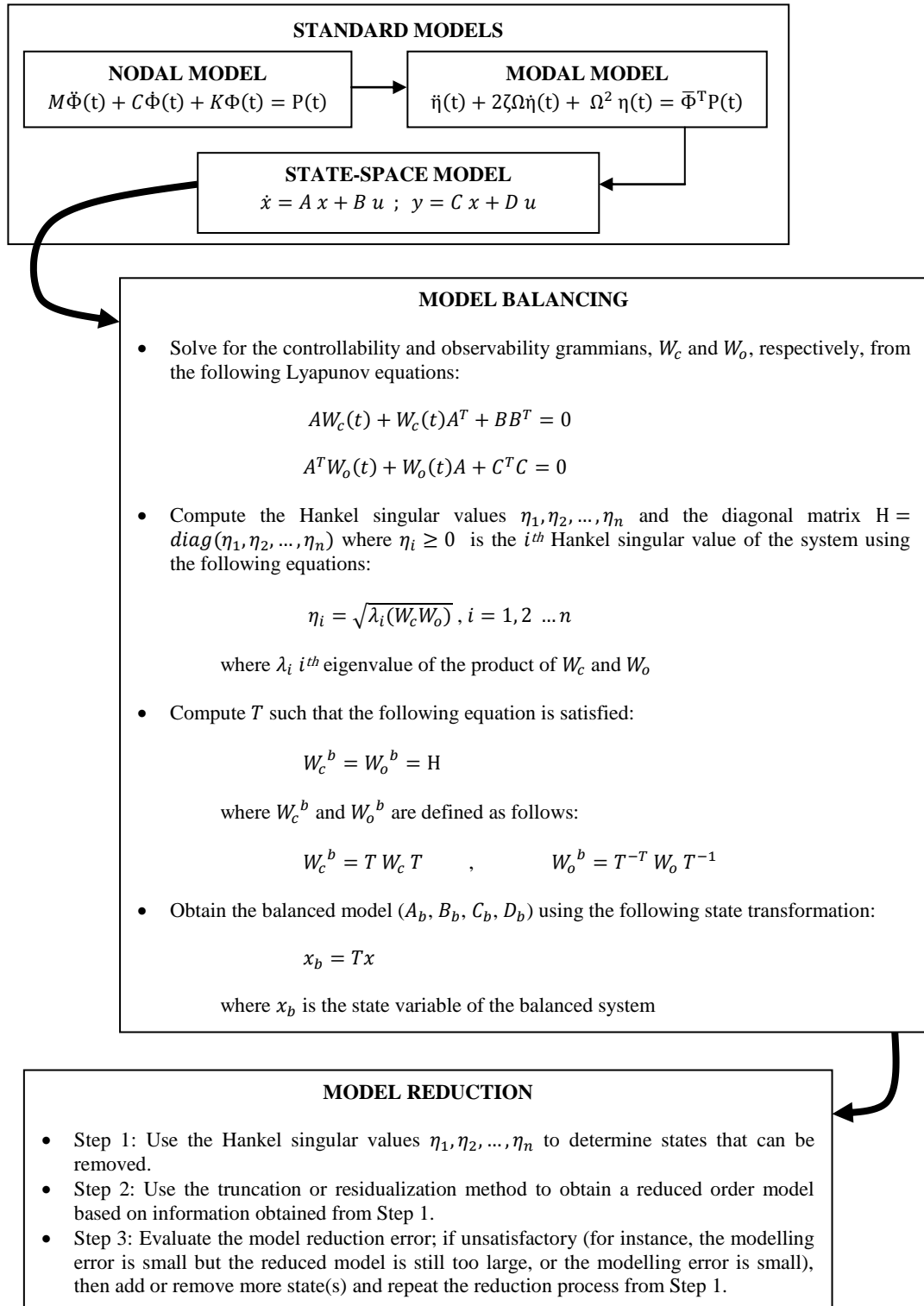


Figure 4.1: A block diagram of the model reduction procedure

The approximate norms of the i^{th} state and the corresponding j^{th} actuator and j^{th} sensor can be obtained using the following equations [133], [148]:

- The H_2 , H_∞ and Hankel norms of the i^{th} state:

$$\|G_i\|_2 \cong \frac{\|b_i\|_2 \|c_i\|_2}{2\sqrt{\zeta_i \omega_i}} \quad , \quad \|G_i\|_\infty \cong \frac{\|b_i\|_2 \|c_i\|_2}{2\zeta_i \omega_i} \quad , \quad \|G_i\|_h \cong \frac{\|b_i\|_2 \|c_i\|_2}{4\zeta_i \omega_i} \quad (4.52)$$

- The H_2 , H_∞ and Hankel norms of the i^{th} state, j^{th} actuator:

$$\|G_{ij}\|_2^a \cong \frac{\|b_{ij}\|_2 \|c_i\|_2}{2\sqrt{\zeta_i \omega_i}} \quad , \quad \|G_{ij}\|_\infty^a \cong \frac{\|b_{ij}\|_2 \|c_i\|_2}{2\zeta_i \omega_i} \quad , \quad \|G_{ij}\|_h^a \cong \frac{\|b_{ij}\|_2 \|c_i\|_2}{4\zeta_i \omega_i} \quad (4.53)$$

- The H_2 , H_∞ and Hankel norms of the i^{th} state, j^{th} sensor:

$$\|G_{ij}\|_2^s \cong \frac{\|b_i\|_2 \|c_{ij}\|_2}{2\sqrt{\zeta_i \omega_i}} \quad , \quad \|G_{ij}\|_\infty^s \cong \frac{\|b_i\|_2 \|c_{ij}\|_2}{2\zeta_i \omega_i} \quad , \quad \|G_{ij}\|_h^s \cong \frac{\|b_i\|_2 \|c_{ij}\|_2}{4\zeta_i \omega_i} \quad (4.54)$$

where ζ_i and ω_i are the damping factor and natural frequency of the i^{th} state. It should be noted that a pair of state variables (x_j and x_{j+1} , for instance) in the balanced model will have the same value of ζ_j and ω_j since each mode is represented with two state variables. It is also worth noting that the values of $\|G_i\|_2$, $\|b_i\|_2$ and $\|c_i\|_2$ change when a structural failure occurs (for example, a failure due to the damage of a structural member); thus, the ratio of the magnitudes of these changes to their original values are called modal, actuator and sensor indices of the structural damages, respectively, and these can be used to detect structural failures [133].

4.4.2 Placement Indices and Matrices

Next, to evaluate the importance of each actuator and sensor locations, the ratio of norms of each actuator and sensor to the system norm – referred to as the actuator and sensor placement indices, respectively – are obtained as follows [133], [148]:

- Actuator placement index of the i^{th} state and j^{th} actuator location:

$$\sigma_{ij}^a = \zeta_{ij} \cdot \frac{\|G_{ij}\|_2^a}{\|G\|_2} \quad (4.55)$$

- Sensor placement index of the i^{th} state and j^{th} sensor location:

$$\sigma_{ij}^s = \zeta_{ij} \cdot \frac{\|G_{ij}\|_2^s}{\|G\|_2} \quad (4.56)$$

where $\zeta_{ij} \geq 0$ is the weight assigned to the j^{th} actuator/sensor of the i^{th} state; the weight reflects the importance a designer associates with the i^{th} state and j^{th} actuator/sensor. Thus, the placement matrices of actuators and sensors (using (4.55) and (4.56), respectively) are written respectively as follows (where the superscripts a and s in σ_{ij}^a and σ_{ij}^s of (4.55) and (4.56), respectively, have been removed for brevity):

$$T_a = \begin{bmatrix} \sigma_{11} & \sigma_{12} & \dots & \sigma_{1j} & \dots & \sigma_{1v} \\ \sigma_{21} & \sigma_{22} & \dots & \sigma_{2j} & \dots & \sigma_{2v} \\ \vdots & & & \vdots & & \vdots \\ \sigma_{i1} & \sigma_{i2} & \dots & \sigma_{ij} & \dots & \sigma_{iv} \\ \vdots & & & \vdots & & \vdots \\ \sigma_{n1} & \sigma_{n2} & \dots & \sigma_{nj} & \dots & \sigma_{nv} \end{bmatrix}, \quad T_s = \begin{bmatrix} \sigma_{11} & \sigma_{12} & \dots & \sigma_{1j} & \dots & \sigma_{1\omega} \\ \sigma_{21} & \sigma_{22} & \dots & \sigma_{2j} & \dots & \sigma_{2\omega} \\ \vdots & & & \vdots & & \vdots \\ \sigma_{i1} & \sigma_{i2} & \dots & \sigma_{ij} & \dots & \sigma_{i\omega} \\ \vdots & & & \vdots & & \vdots \\ \sigma_{n1} & \sigma_{n2} & \dots & \sigma_{nj} & \dots & \sigma_{n\omega} \end{bmatrix} \begin{matrix} \rightarrow i^{\text{th}} \text{ state} \\ \\ \\ \\ \\ \end{matrix}$$

$$\begin{matrix} \downarrow & & & \downarrow \\ j^{\text{th}} \text{ actuator} & & & j^{\text{th}} \text{ sensor} \end{matrix} \quad (4.57)$$

where $v \leq m$ and $\omega \leq p$ are the numbers of candidate actuators and sensors, respectively. The H_2 has been used in equations (4.55-4.57), therefore, σ_{ij} , T_a and T_s are termed the H_2 norm actuator/sensor placement index, H_2 norm actuator placement matrix and H_2 norm sensor placement matrix, respectively; if H_∞ norm or Hankel-norm are to be used, they are prefixed in those terms. If the j^{th} element (that is, the j^{th} actuator/sensor placement index) of the i^{th} state in equation (4.57) is the largest element of the i^{th} state, then it is obvious that actuator or sensor location ij is the best, or optimal, location to excite or sense the i^{th} state as the case may be. Consequently, other actuator/sensor placement indices of the i^{th} state can be removed since they constitute the least significant placements. Moreover, a set of actuators/sensors with the largest indices can be selected as the optimal actuator/sensor placements.

More so, by taking the norm of each column of T_a and T_s , the following vectors are obtained:

$$T_a' = [\sigma_{a1} \quad \sigma_{a2} \quad \dots \quad \sigma_{aj} \quad \dots \quad \sigma_{av}]^T, \quad T_s' = [\sigma_{s1} \quad \sigma_{s2} \quad \dots \quad \sigma_{sj} \quad \dots \quad \sigma_{s\omega}]^T$$

$$\begin{matrix} \downarrow & & & \downarrow \\ j^{\text{th}} \text{ actuator} & & & j^{\text{th}} \text{ sensor} \end{matrix} \quad (4.58)$$

Depending on whether H_2 norm, H_∞ norm or Hankel-norm is used for the computation of elements of the vectors in (4.58), σ_{aj} and σ_{sj} are obtained as follows:

- Using the H_2 norm:

$$\sigma_{aj} = \sqrt{\sum_{i=1}^n (\sigma_{ij})^2}, \quad \sigma_{sj} = \sqrt{\sum_{i=1}^n (\sigma_{ij})^2} \quad (4.59)$$

- Using the H_∞ norm or Hankel-norm:

$$\sigma_{a_j} = \sup_i(\sigma_{ij}) \quad , \quad \sigma_{s_j} = \sup_i(\sigma_{ij}) \quad (4.60)$$

Therefore, σ_{a_j} and σ_{s_j} represent the (non-negative) contributions of the j^{th} actuator and sensor over all the states to the observability and controllability properties of the system, respectively.

On the other hand, if the norm of each row of matrices T_a and T_s are taken (instead of columns), the following vectors are obtained:

$$M_a = [\sigma_{a_1} \quad \sigma_{a_2} \quad \dots \quad \sigma_{a_i} \quad \dots \quad \sigma_{a_v}]^T \quad , \quad M_s = [\sigma_{s_1} \quad \sigma_{s_2} \quad \dots \quad \sigma_{s_i} \quad \dots \quad \sigma_{s_\omega}]^T \quad (4.61)$$

\downarrow
 $i^{\text{th}} \text{ state}$

\downarrow
 $i^{\text{th}} \text{ state}$

where σ_{a_i} and σ_{s_i} are obtained as follows:

- Using the H_2 norm:

$$\sigma_{a_i} = \sqrt{\sum_{j=1}^n (\sigma_{ij})^2} \quad , \quad \sigma_{s_i} = \sqrt{\sum_{j=1}^n (\sigma_{ij})^2} \quad (4.62)$$

- Using the H_∞ norm or Hankel-norm:

$$\sigma_{a_i} = \sup_j (\sigma_{ij}) \quad , \quad \sigma_{s_i} = \sup_j (\sigma_{ij}) \quad (4.63)$$

In this case, σ_{a_i} and σ_{s_i} are state indices that signify the importance of the i^{th} state for the given location of actuators and sensors, respectively, and can be used as indices for model reduction just as the Hankel singular values used in Section 4.3. That is, the magnitudes of σ_{a_i} and σ_{s_i} signify the importance of the i^{th} state and, as such, states with larger magnitudes affect the dynamic behaviour of the system the most and, therefore, should be retained while others may be eliminated. Moreover, the state indices can also be used as a recalibration index, that is, the actuators and sensors of states with lowest indices should be enhanced [133]. This statement answers the question of what should be the necessary precision for an actuator or sensor. Figure 4.2 summarizes the optimal actuator and sensor placement procedure described in this section.

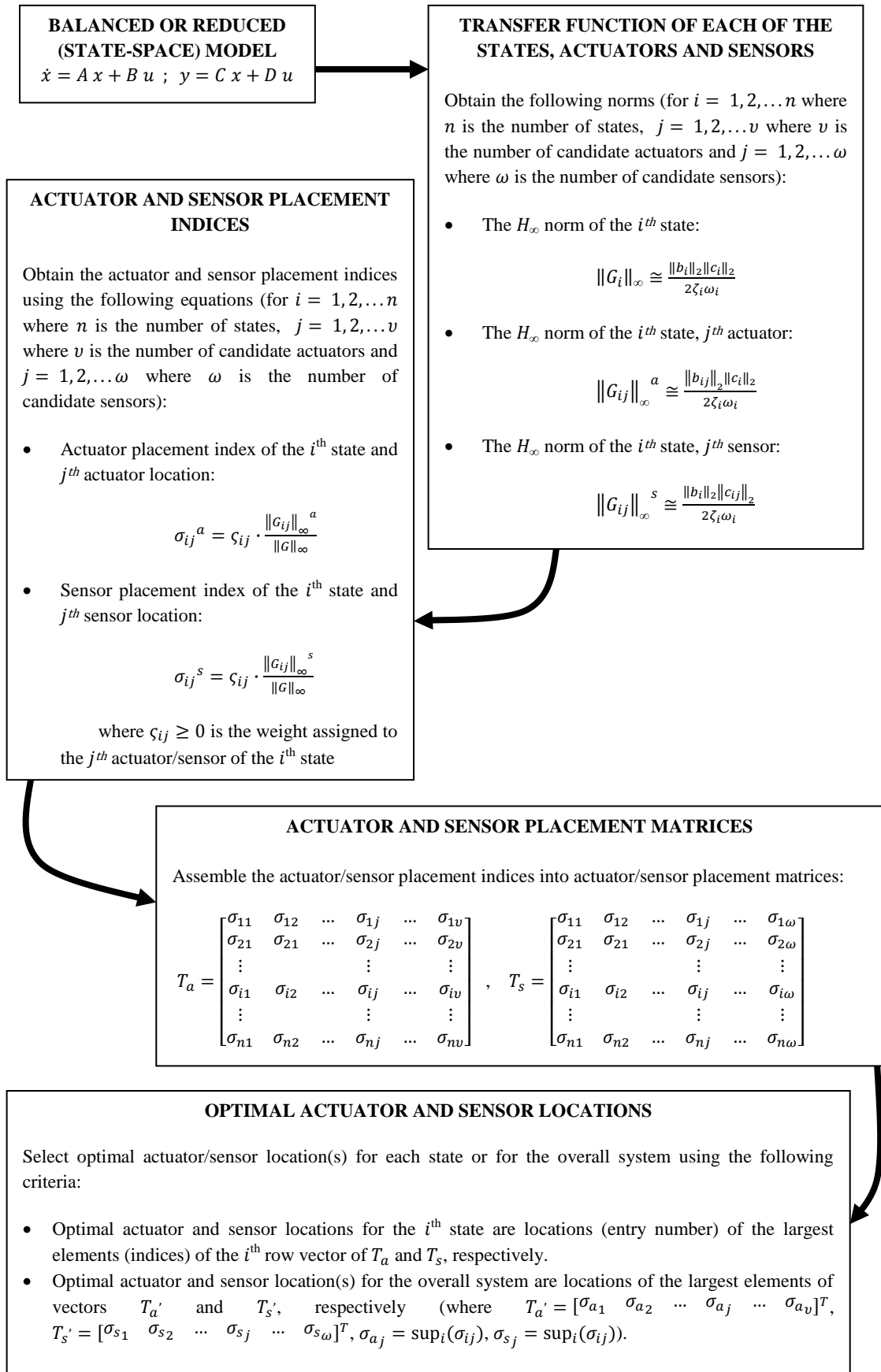


Figure 4.2: A block diagram of the optimal actuator and sensor placement procedure using the H_∞ norm

4.5 Numerical Applications

In this section, the applicability of the theory on model reduction and optimal actuator and sensor placement procedures presented in the preceding sections will be demonstrated. The structural models of the tensegrity structures to be considered are obtained using the Finite Element Method covered in Chapter 3 and the constrained optimisation form-finding algorithm in Chapter 2 has been used to obtain each of the structural assemblies. Moreover, for these structures, it is assumed that all the cables are made of copper of Young's modulus 117 GPa, cross-sectional area $1.5 \times 10^{-6} \text{ m}^2$ and mass density 8920 kg/m^3 and all the bars are hollow circular steel cylinders of Young's modulus 200 GPa, cross-sectional area $6 \times 10^{-6} \text{ m}^2$ and mass density 7850 Kg/m^3 . Also, the bottom nodes of the structures are constrained (rigid) in the x , y and z directions in all the analyses that will be considered.

4.5.1 Minimal Multistage Tensegrity Structures

Figures 4.3 – 4.7 show the plots of the Hankel singular values and the frequency response for 1-, 2-, 3-, 4- and 5-stage tensegrity structural systems of 3-order. In each case, the frequency response plot of the modal and the reduced models are shown. The reduced models are obtained using the residualization method (Section 4.3.2) by eliminating the states whose Hankel singular values are less than 10^{-3} (which corresponds to deleting high frequency modes as the figures clearly show). Each of the Hankel singular value plots also show the number of states that are chosen as the dominant states for model reduction. Table 4.1 shows the additive and relative model reduction errors (ϵ_{∞} and $\epsilon_{r\infty}$, respectively) for these structural systems.

While it is difficult to compare any set of geometrically and topologically different structures, nonetheless it can be seen that the number of dominant states (modes) increases with the number of stages generally. Moreover, the existence and finiteness of the Hankel singular values for all these cases confirms the previous knowledge that tensegrity structures are pre-stressed stable structural systems since the Hankel singular values do not exist (that is, are infinite) for unstable modes.

More so, Figures 4.8 and 4.9 show the plots of the Hankel singular values and the frequency response for 5- and 6-order tensegrity structures of 3-stage, respectively.

Compared with the 3-stage 3-order of Figure 4.5, the number of dominant states also increases as the order of the tensegrity structures increases.

Furthermore, Figures 4.10 and 4.11 show the plots of the Hankel singular values and the frequency response for the 6- and the 7-stage tensegrity structures of 3-order, respectively. An interesting feature of these structures is that they both have states which are unstable; it is worth noting that when minimal tensegrity structures are obtained using form-finding algorithms that take into account only the static and/or other properties (such as material, topological and geometric properties) of the structural systems, it is may be desirable (and even essential for very large structures) to investigate the degree of stability (for instance, controllability and observability grammians, Hankel singular values, etc.) of these structures if the structures are to be used for active control applications. As the current example of Figures 4.10 and 4.11 show, while it is possible that the constrained optimisation form-finding algorithm of Chapter 2 (which minimizes the lengths and tension coefficients of structural members in two separate steps and uses the state of static equilibrium due to pre-stress as the criteria for obtaining a valid tensegrity structure) is able to obtain the 6- and 7-stage tensegrity structures of 3-order (Figures 4.10 and 4.11), these structures still contain unstable states, thus, requiring additional consideration if these minimal tensegrity structures are to be actively controlled, or even physically realized. In fact, using the constrained form-finding algorithm, unstable states are present for the 3-order tensegrity structures with stages higher than 5; of course, it is possible to modify the similarity constraints in the form-finding algorithm to obtain a valid tensegrity structure of the 6- and 7-stage tensegrity structures of 3-order under consideration. Introducing additional structural members, for example, so that the structures become non-minimal can be used as a means for making all systems' states stable. Examples of non-minimal multistage tensegrity structures (introduced in Section 3.3) are discussed further in the next section.

In addition, Table 4.2 shows the nodal coordinates of the tensegrity structure of Figure 4.4 and the tension coefficient of each of its members. As defined in Section 3.2.2.4, c_x and c_q are the scaling factors of the physical size (in terms of its nodal coordinates) of a tensegrity structure and its vector of tension coefficients, respectively. Figure 4.12 shows the plots of the frequency response of the tensegrity structural of Figure 4.4 when $c_x = 10$ and $c_q = 10$. From the figure, it can be observed that for the first case where $c_x = 10$, the frequency response plot is shifted upwards and to the left

of the original plot, whereas for the second case where $c_q = 10$, the frequency response is shifted downwards and to the right indicating that the two scaling factors have opposite effect on the frequency response plot while the shape of the plot is mostly preserved.

4.5.2 Non-minimal Multistage Tensegrity Structures

Figures 4.13 (a) and (b) show the frequency response plots of minimal and non-minimal 2- and 3-stage tensegrity structures of 3-order (figures 3.10 (b) and 3.19, respectively) from sections 3.2.4 and 3.3, respectively. Unlike the effects of the scaling factors, c_x and c_q , in the preceding section where the shape of the frequency response is mostly preserved, the introduction of additional structural members than strictly necessary (in the non-minimal structures) significantly changes the frequency response of the structural systems. The addition has the effect of moving a significant number of system modes into the high-frequency region. Thus, the control design to attenuate vibration, for instance, has only a reduced number of dominant states to consider. Moreover, the reduced number of states available for control in the non-minimal structures implies that they are less amenable to undergo reasonably large displacements (compared to minimal structures), and therefore, are a less attractive option for structural system designs (for shape control) that need to be actively controlled for achieving large nodal displacements.

In addition, Figures 4.14 and 4.15 show the plots of the actuator placement indices of a few number of states, the actuator placement indices over all states (T_a'), the Hankel singular values ($\eta_1, \eta_2, \dots, \eta_n$), and the state-importance indices (M_a) of the 2- and 3-stage 3-order minimal and non-minimal tensegrity structures, respectively. It is worth noting that unit weights have been assumed for all the modes (meaning all modes have been assumed to be of equal importance) and the balanced model and H_∞ norm have been used for the analysis and computations. Results of this analysis can be summarized as follows: Firstly, in figures 4.14 (a) and 4.15 (a), it should be noted that the optimal balanced actuator placements are different for the 2-stage 3-order minimal and non-minimal structures and for the 3-stage 3-order minimal and non-minimal structures. Secondly, in figures 4.14 (b) and 4.15 (b), the Hankel singular values that are dominant in the minimal n-stage 3-order tensegrity structure are larger in number than those of the dominant in the n-stage 3-order non-minimal counterpart (the reason for

this follows from the discussion in the preceding paragraph). For instance, the largest 8 Hankel singular values are the dominant in the minimal 2-stage 3-order tensegrity structure while the largest 2 are the dominant in the non-minimal case as shown in Figure 4.14 (b). This implies that the model order of the reduced model of the non-minimal tensegrity structure is much smaller than the minimal counterpart, thus, it will require much less number of actuator and sensor to actively control the non-minimal structure. Thirdly, the state importance indices (M_a) is generally able to detect the most important states of the system and indicates that the high frequency modes are the least significant ones in the same ways as the Hankel singular values approach was able to detect and indicate.

4.6 Discussions

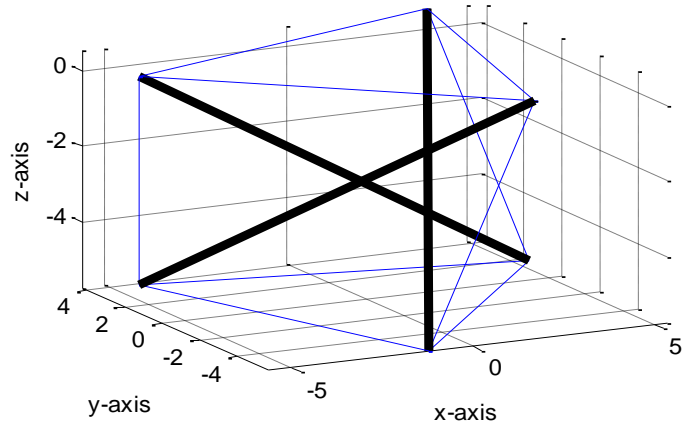
Although the actuator placement alone, sensor placement alone and the simultaneous placement of actuator and sensor are the three distinguishable problems of optimal actuator and sensor placement, only the placement of actuators was considered in the examples of the preceding section since the other two placements are obtained in mostly the same manner. Consider the 2-stage 3-order minimal tensegrity structures whose actuator placement indices are shown in Figure 4.14 (a) I, the procedure of actuator placement may be described as follows: To actuate state 1, the 27th actuator index is the largest index over all actuator; therefore, the 27th location is the optimal actuator location for actuating state 1 of the structural system. If other actuator locations are chosen instead of the 27th, the actuator will have to work harder and be capable of providing more force to achieve the same control objective. A similar statement can be made for states 3 and 5 with the 27th and 25th optimal actuator locations, respectively, as shown in Figure 4.14 (a) i.

Furthermore, it should be observed from the analysis of the tensegrity structures considered that each pair of states is described by two approximately equal Hankel singular values. This property is common to flexible structures (that is, lightly damped structures) in general [161].

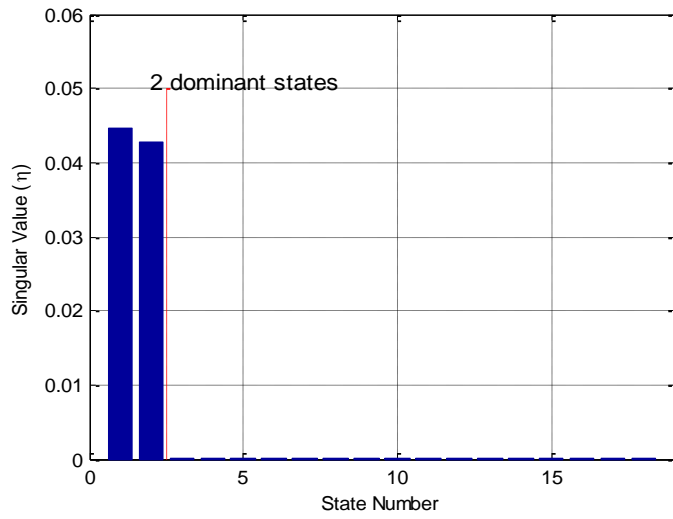
Importantly, actuator forces are assumed to be applied at the structural nodes of the structures in the x , y and z directions. In the physical system, if an electromechanical device (or a piezoelectric material) which will also serves as a

structural member will be used as an actuator, then every pair of connected nodes in which the device will be attached are a potential candidate actuator location. In this case, the problem will be finding the optimal set(s) of nodes (among other sets) to place a predetermined number of the actuator(s). An alternative (and, perhaps, more direct) way of determining the optimal location of actuators (instead of ‘optimal set of nodes’ as in this case) is to determine the optimal actuator location as described in this chapter but using the model representation expressed in terms of member length changes (presented later in Section 7.4) instead of those expressed in terms of nodal forces (as in the current case).

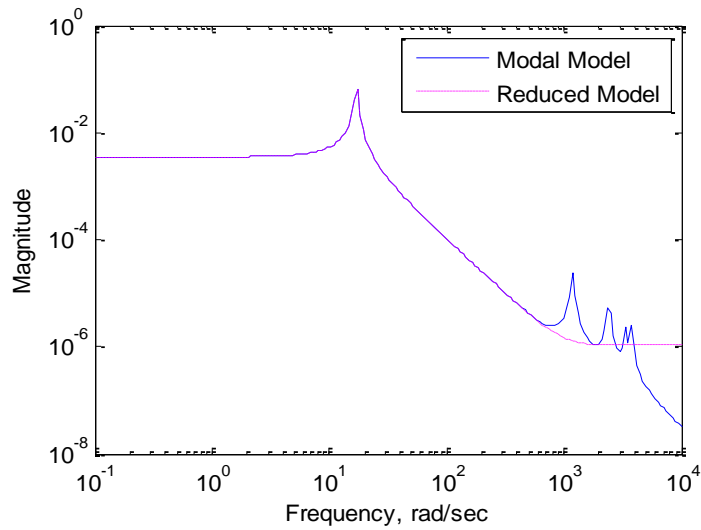
Given an open-loop system, the presentation of this chapter covered the procedures to determine the importance of each state using the Hankel singular values of the system with specific controllability and observability properties (that is, model balancing) for model order reduction, and to determine, for each state and for the whole system, the optimal location to place actuators or sensors using the controllability and observability properties. In this presentation, the selection of the numbers and locations of actuators and sensors are done first, while anticipating that the control design will be done later. However, the actuator and sensor placement and control design are dependent on each other as it is well known; thus, it is more efficient to integrate the placement and control design together (that is, to find optimal actuator and sensor placement for closed-loop control) and a number of techniques exist to tackle this problem that can be applied to structural systems in general (see for example [162–164]). An approach has also been proposed in [146] for optimal actuator and sensor placement of a simple tensegrity structure for closed-loop control in particular.



(a)



(b)



(c)

Figure 4.3: (a) A 1-stage 3-order tensegrity structure; (b) a plot of the Hankel singular values of the structure; and (c) a plot of the frequency response of the structure.

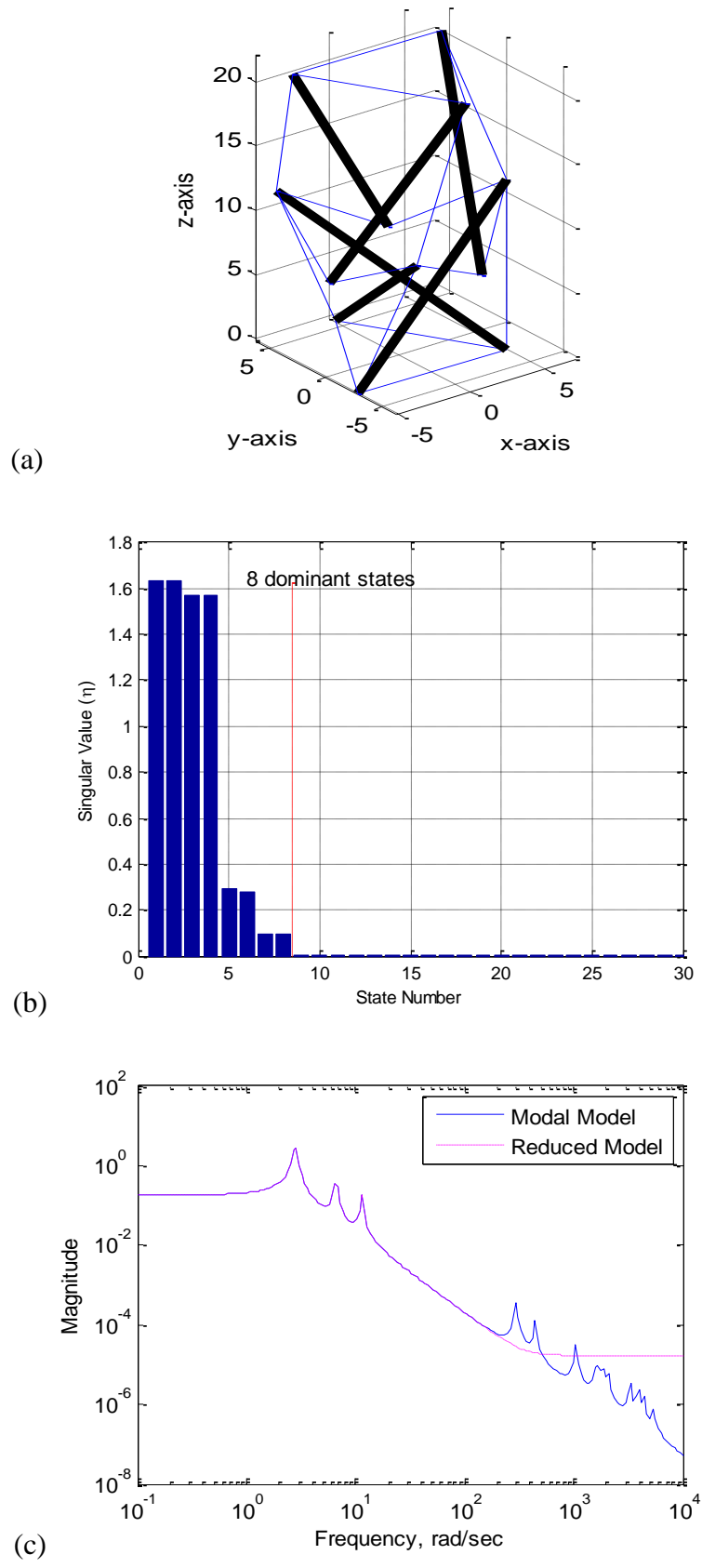
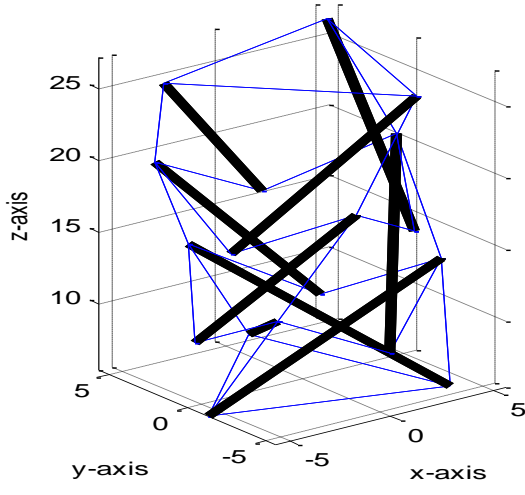
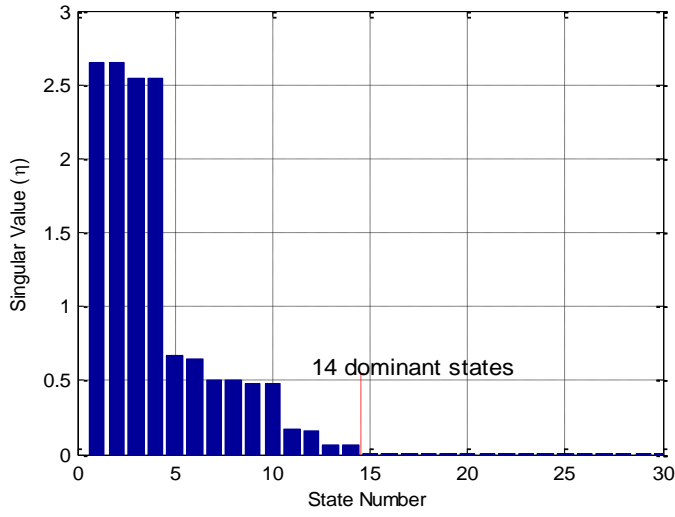


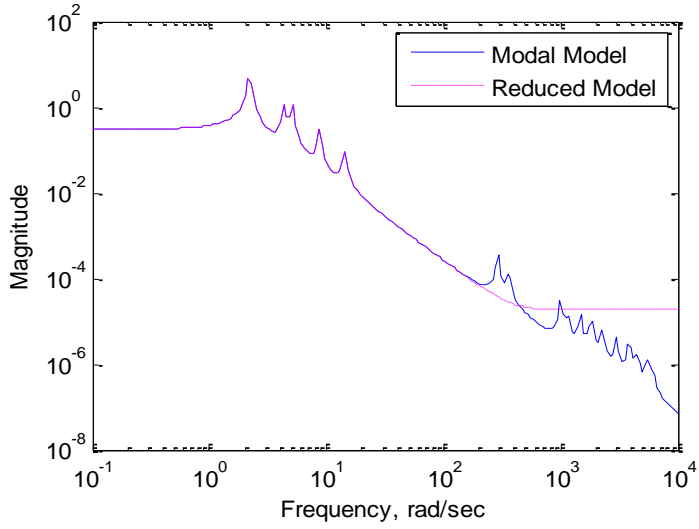
Figure 4.4: (a) A 2-stage 3-order tensegrity structure; (b) a plot of the Hankel singular values of the structure (only the largest 30 out of a total of 54 are shown); and (c) a plot of the frequency response of the structure.



(a)



(b)



(c)

Figure 4.5: (a) A 3-stage 3-order tensegrity structure; (b) a plot of the Hankel singular values of the structure (only the largest 30 out of a total of 90 are shown); and (c) a plot of the frequency response of the structure.

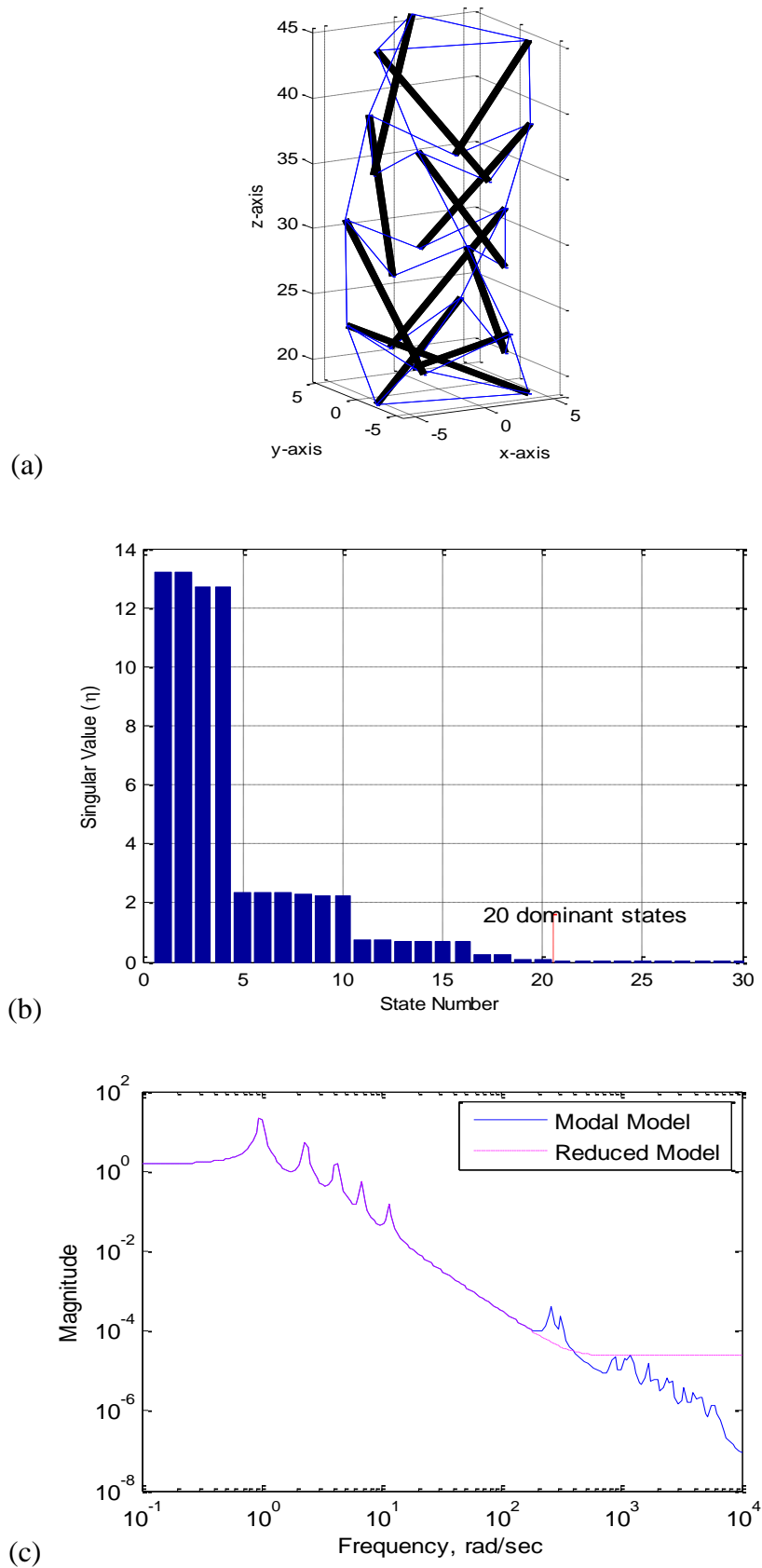
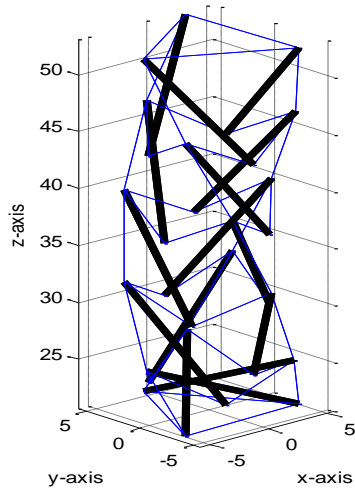
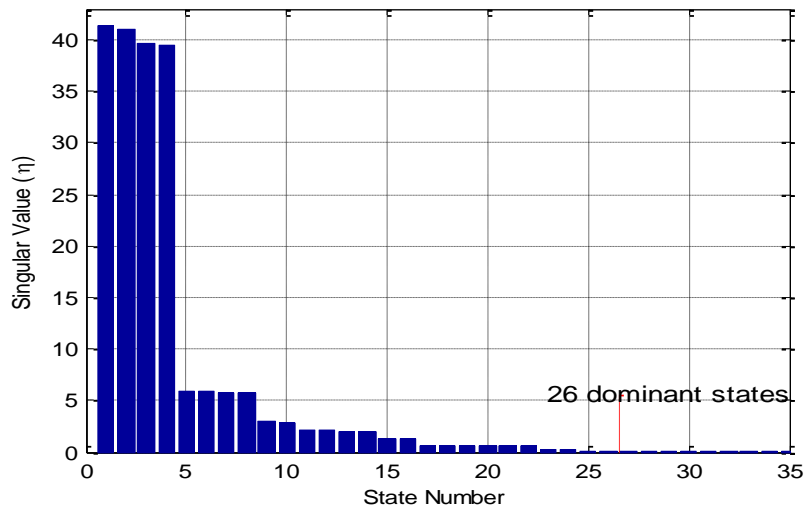


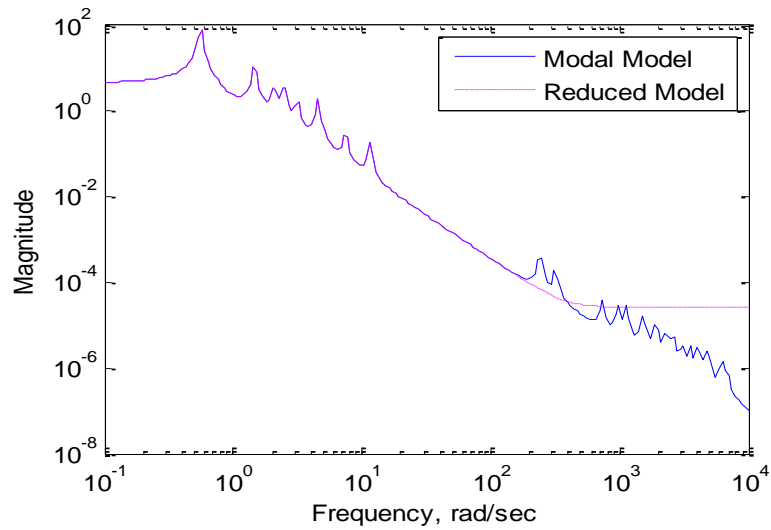
Figure 4.6: (a) A 4-stage 3-order tensegrity structure; (b) a plot of the Hankel singular values of the structure (only the largest 30 out of a total of 126 are shown); and (c) a plot of the frequency response of the structure.



(a)

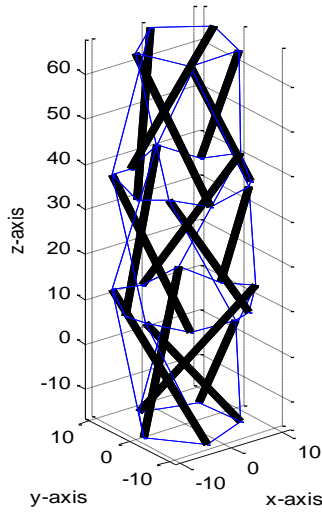


(b)

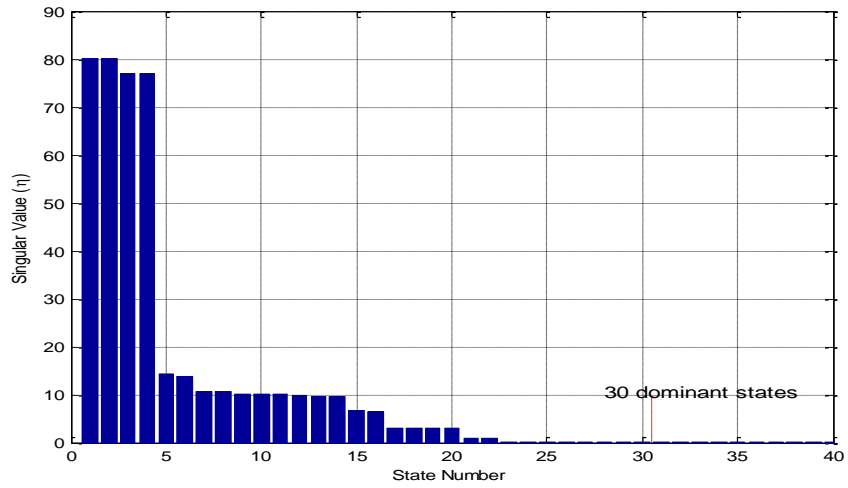


(c)

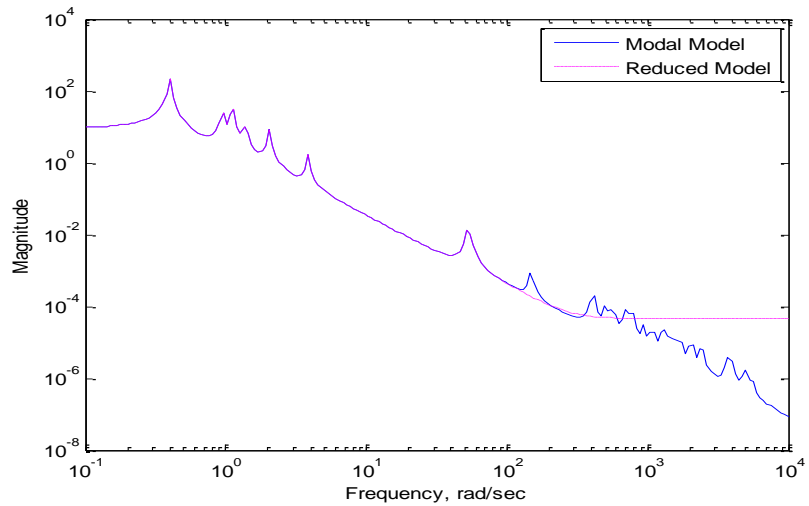
Figure 4.7: (a) A 5-stage 3-order tensegrity structure; (b) a plot of the Hankel singular values of the structure (only the largest 35 out of a total of 162 are shown); and (c) a plot of the frequency response of the structure.



(a)

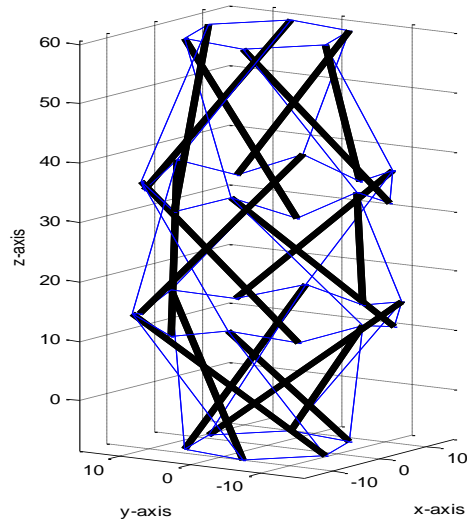


(b)

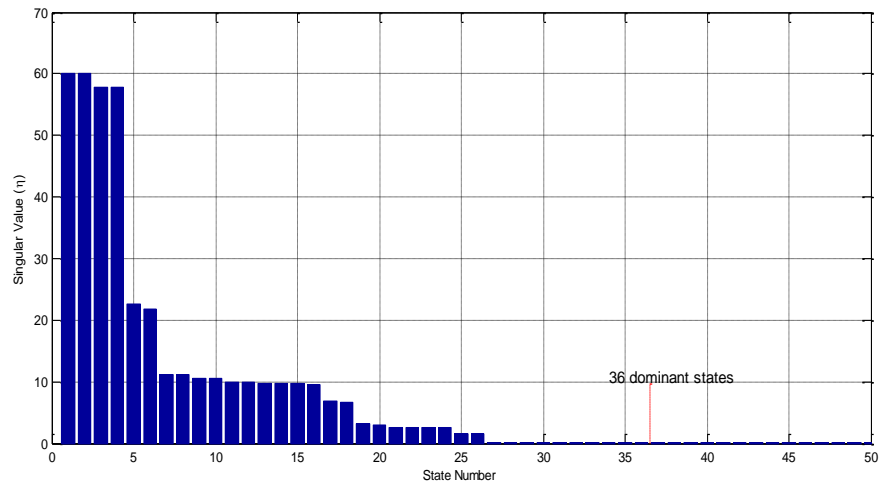


(c)

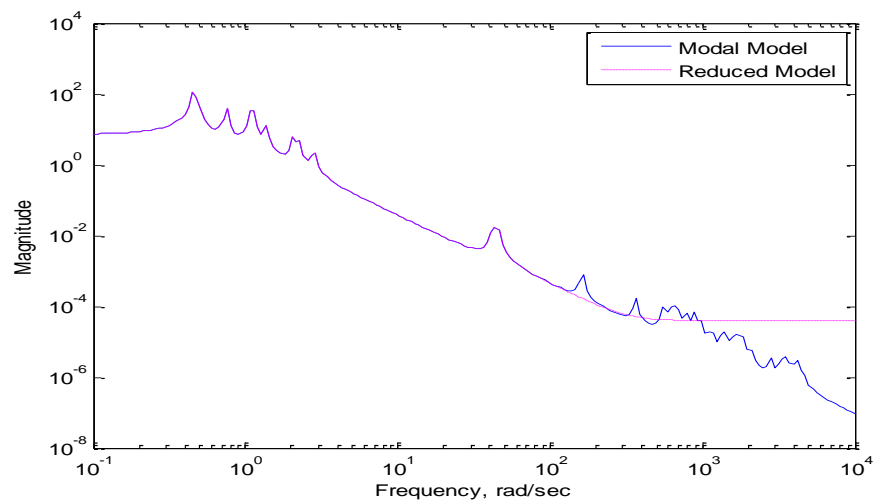
Figure 4.8: (a) A 3-stage 5-order tensegrity structure; (b) a plot of the Hankel singular values of the structure (only the largest 40 out of a total of 150 are shown); and (c) a plot of the frequency response of the structure.



(a)



(b)



(c)

Figure 4.9: (a) A 3-stage 6-order tensegrity structure; (b) a plot of the Hankel singular values of the structure (only the largest 50 out of a total of 180 are shown); and (c) a plot of the frequency response of the structure.

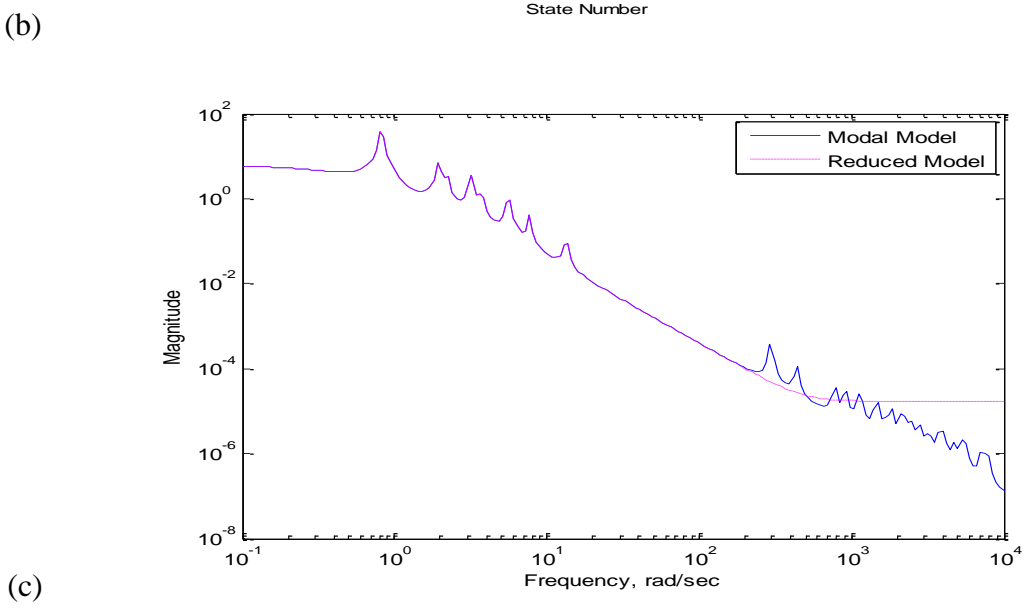
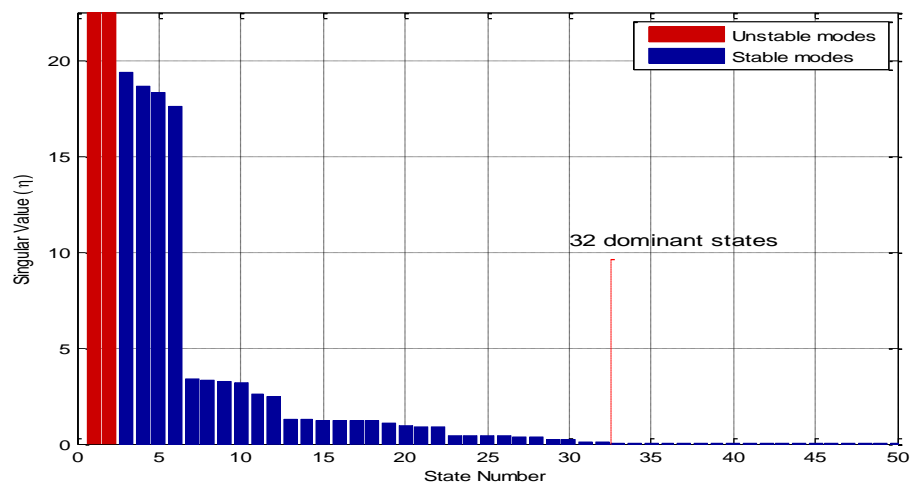
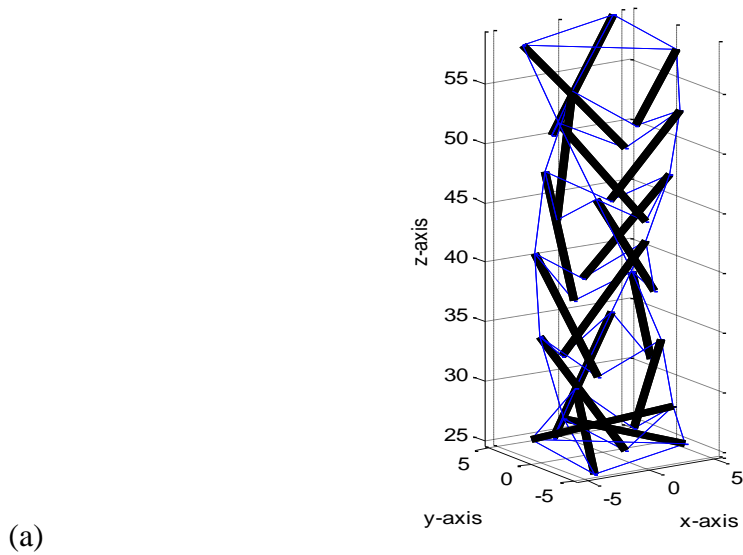
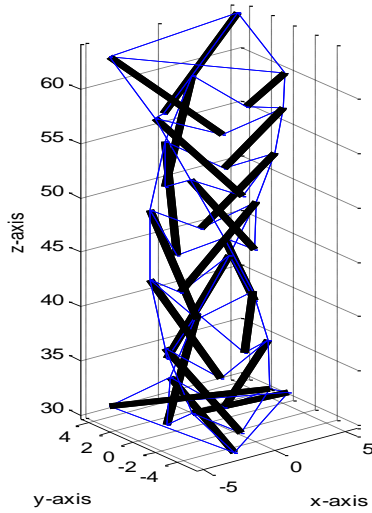
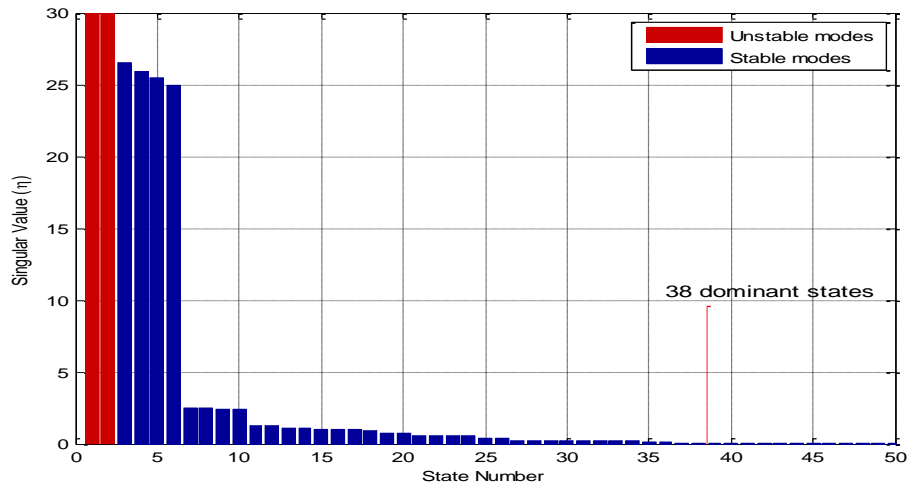


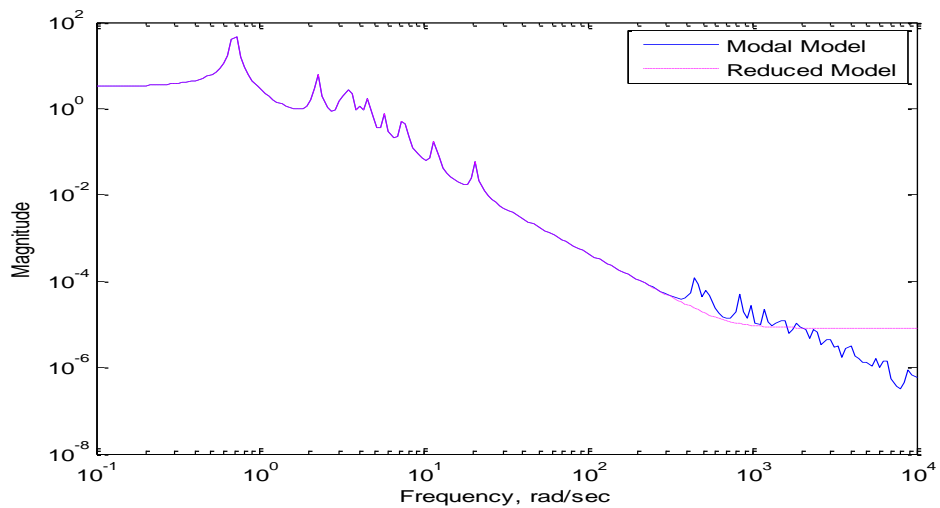
Figure 4.10: (a) A 6-stage 3-order tensegrity structure; (b) a plot of the Hankel singular values of the structure (only the largest 50 out of a total of 198 are shown; 2 of these are unstable); and (c) a plot of the frequency response of the structure.



(a)

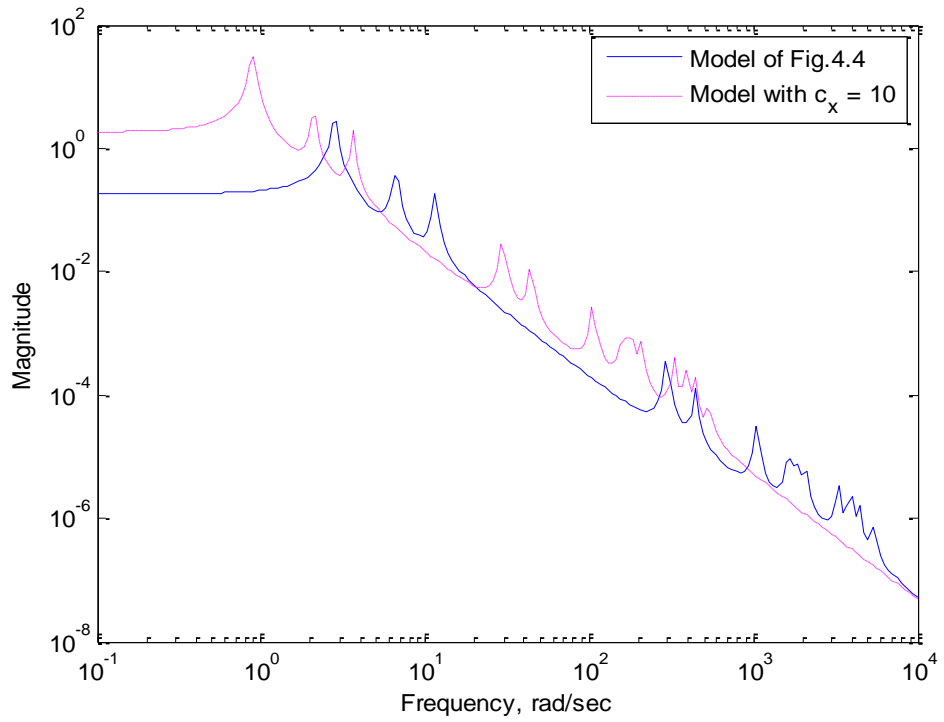


(b)

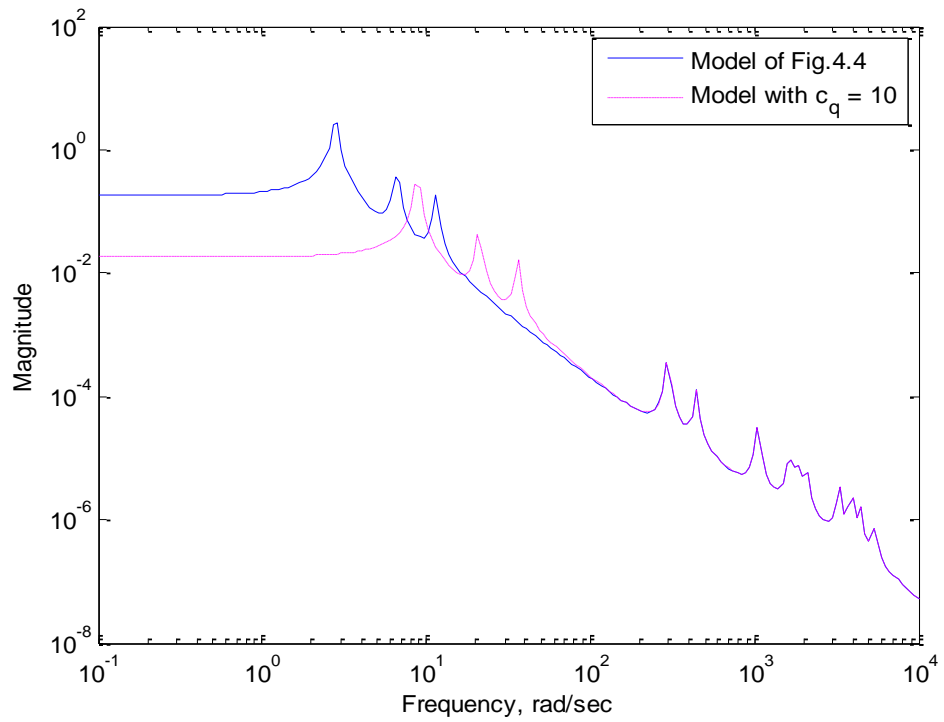


(c)

Figure 4.11: (a) A 7-stage 3-order tensegrity structure; (b) a plot of the Hankel singular values of the structure (only the largest 50 out of a total of 234 are shown; 2 of these are unstable); and (c) a plot of the frequency response of the structure.



(a)



(b)

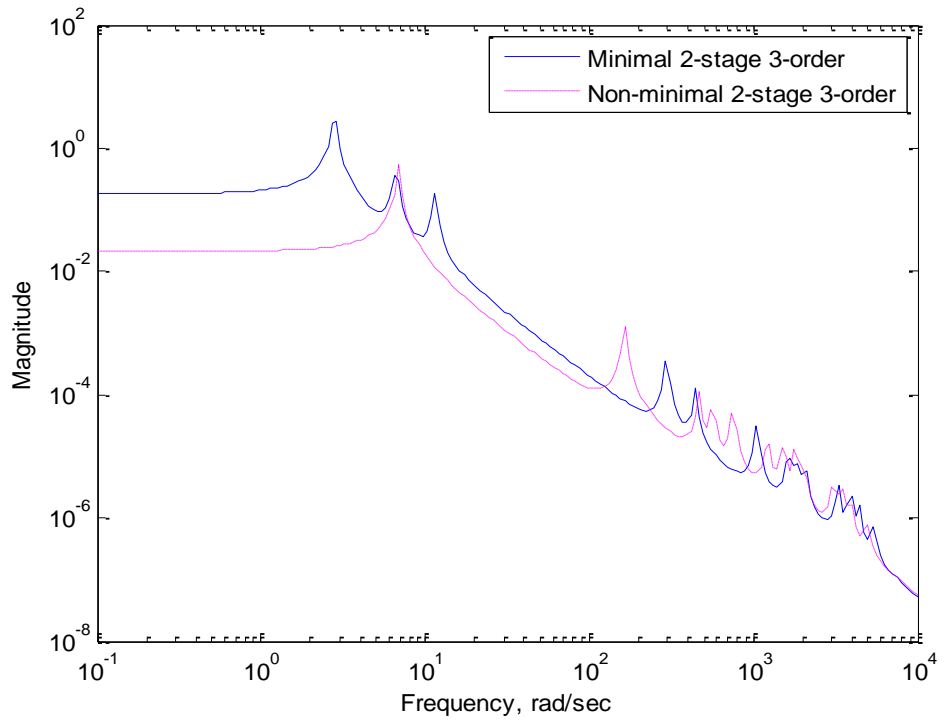
Figure 4.12: (a) A plot of the frequency response of the 2-stage 3-order tensegrity structure; and (b) a plot of the frequency response of the structure.

Table 4.1: The additive and relative model reduction errors (ϵ_{∞} and $\epsilon_{r\infty}$, respectively) for the tensegrity structural systems of Figures 4.3 – 4.7.

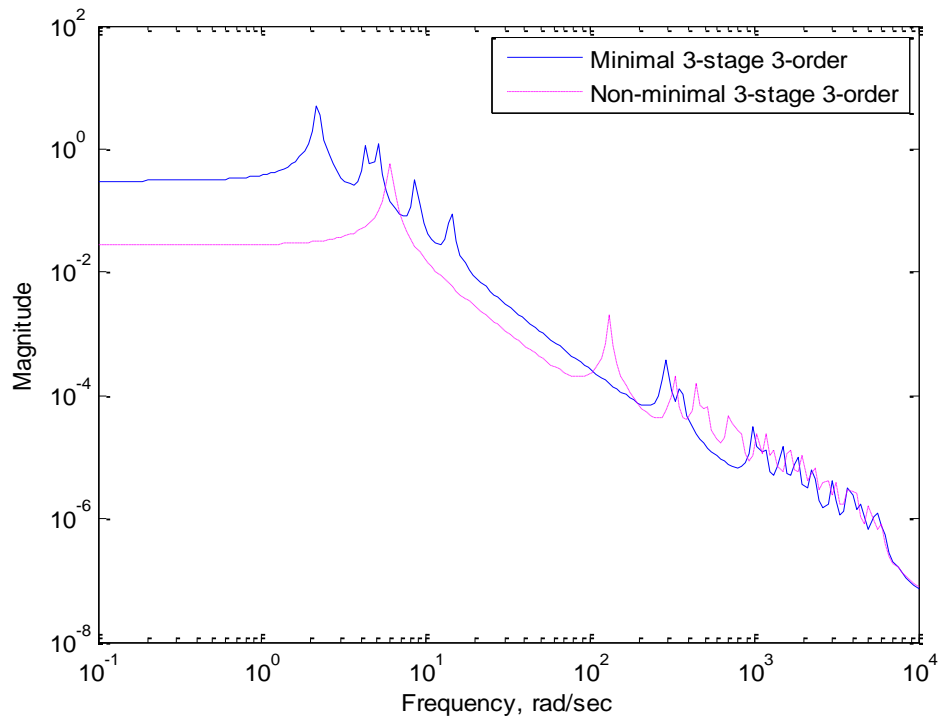
Structure Figure 4.3 – 4.7	Additive Error ϵ_{∞}	Relative Error $\epsilon_{r\infty}$
i) 1-stage 3-order	1.0890×10^{-4}	1.0891×10^{-4}
ii) 2-stage 3-order	1.6095×10^{-3}	1.6108×10^{-3}
iii) 3-stage 3-order	1.8917×10^{-3}	1.8934×10^{-3}
iv) 4-stage 3-order	2.4691×10^{-3}	2.4722×10^{-3}
v) 5-stage 3-order	2.8205×10^{-3}	2.8244×10^{-3}

Table 4.2: Nodal coordinates of the tensegrity structure of Figure 4.4 and the tension coefficient of each of its members

Node	Nodal Coordinates			Structural Member	Tension Coefficient (N/m)
	x	y	z		
1	4.9870	-2.9080	-0.1430	1	2.9999
2	0.0250	5.7730	-0.1430	2	2.9999
3	-5.0120	-2.8650	-0.1430	3	2.9999
4	7.1470	-0.0310	10.9560	4	2.9123
5	2.4200	4.1500	7.1330	5	4.7413
6	-3.5470	6.2050	10.9560	6	2.9123
7	-4.8040	0.0210	7.1330	7	4.7413
8	-3.6000	-6.1740	10.9560	8	2.9123
9	2.3840	-4.1710	7.1330	9	4.7413
10	5.0120	2.8650	22.0540	10	4.1975
11	-4.9870	2.9080	22.0540	11	4.1975
12	-0.0250	-5.7730	22.0540	12	4.1975
				13	2.6362
				14	2.6362
				15	2.6362
				16	0.7169
				17	0.7169
				18	0.7169
				19	-4.1975
				20	-4.1975
				21	-4.1975
				22	-1.9608
				23	-1.9608
				24	-1.9608

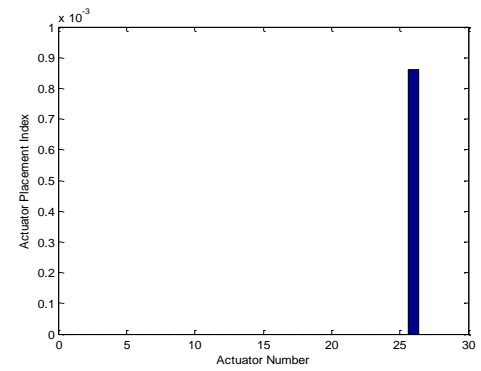
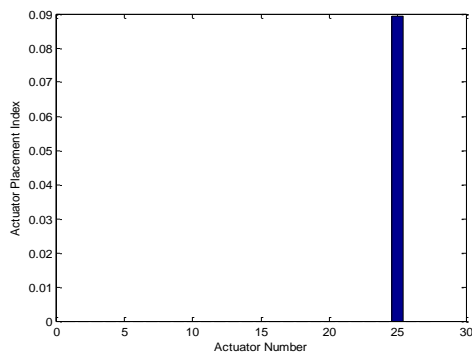
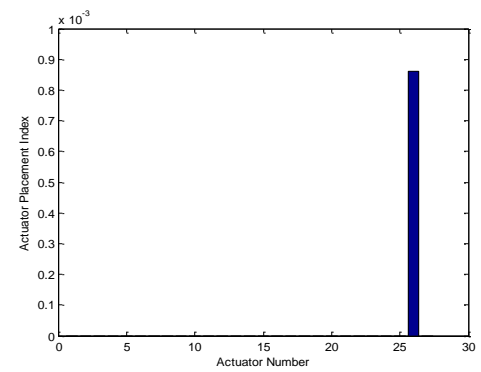
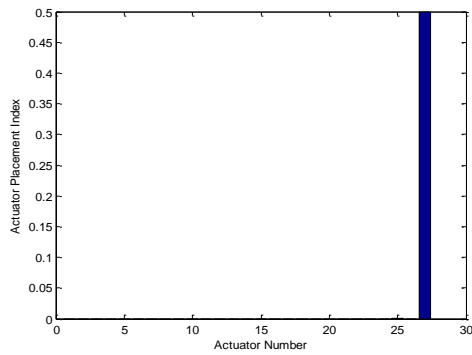
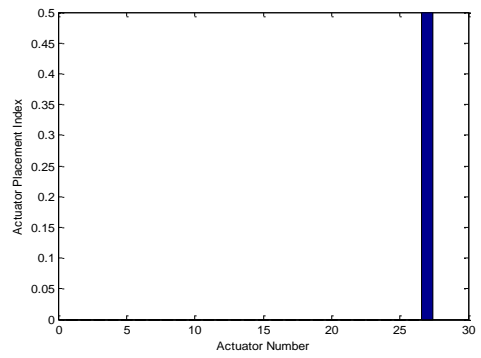
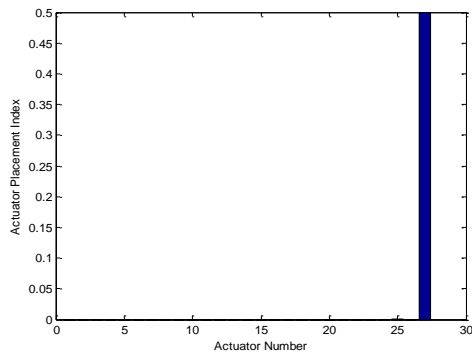


(a)



(b)

Figure 4.13: (a) Frequency response plots of minimal and non-minimal 2-stage 3-order tensegrity structure; and (b) frequency response plots of minimal and non-minimal 3-stage 3-order tensegrity structure.



(i)

(ii)

Figure 4.14 (a): (i) and (ii) are the plots of the actuator placement indices for the states 1, 3, and 5 of the 2-stage 3-order minimal and non-minimal tensegrity structures, respectively.

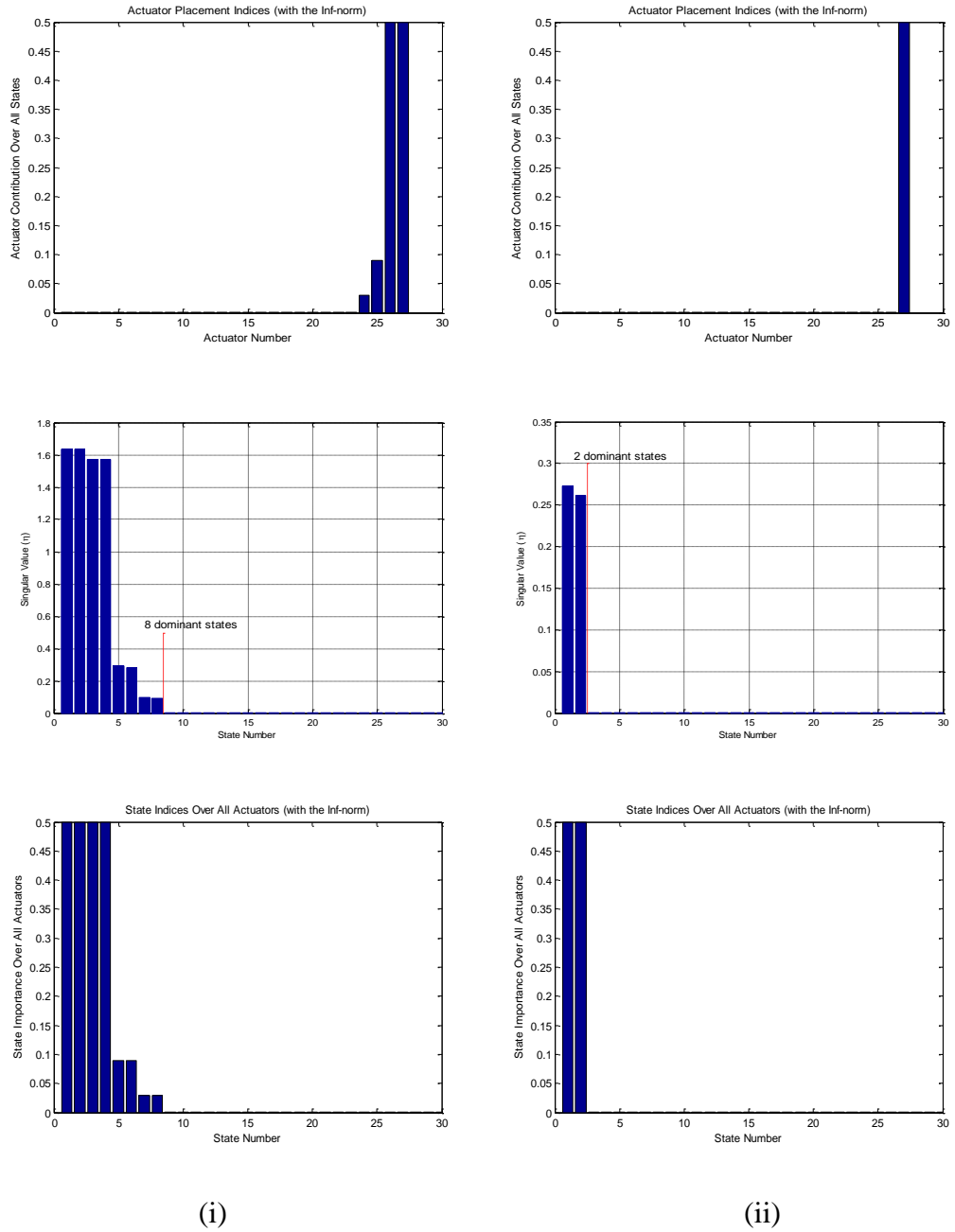


Figure 4.14 (b): (i) and (ii) are the plots of the actuator placement indices over all states (T_a'), the Hankel singular values ($\eta_1, \eta_2, \dots, \eta_n$ – only the largest 30 out of a total of 54 are shown), and the state importance indices (M_a) of the 2-stage 3-order minimal and non-minimal tensegrity structures, respectively.

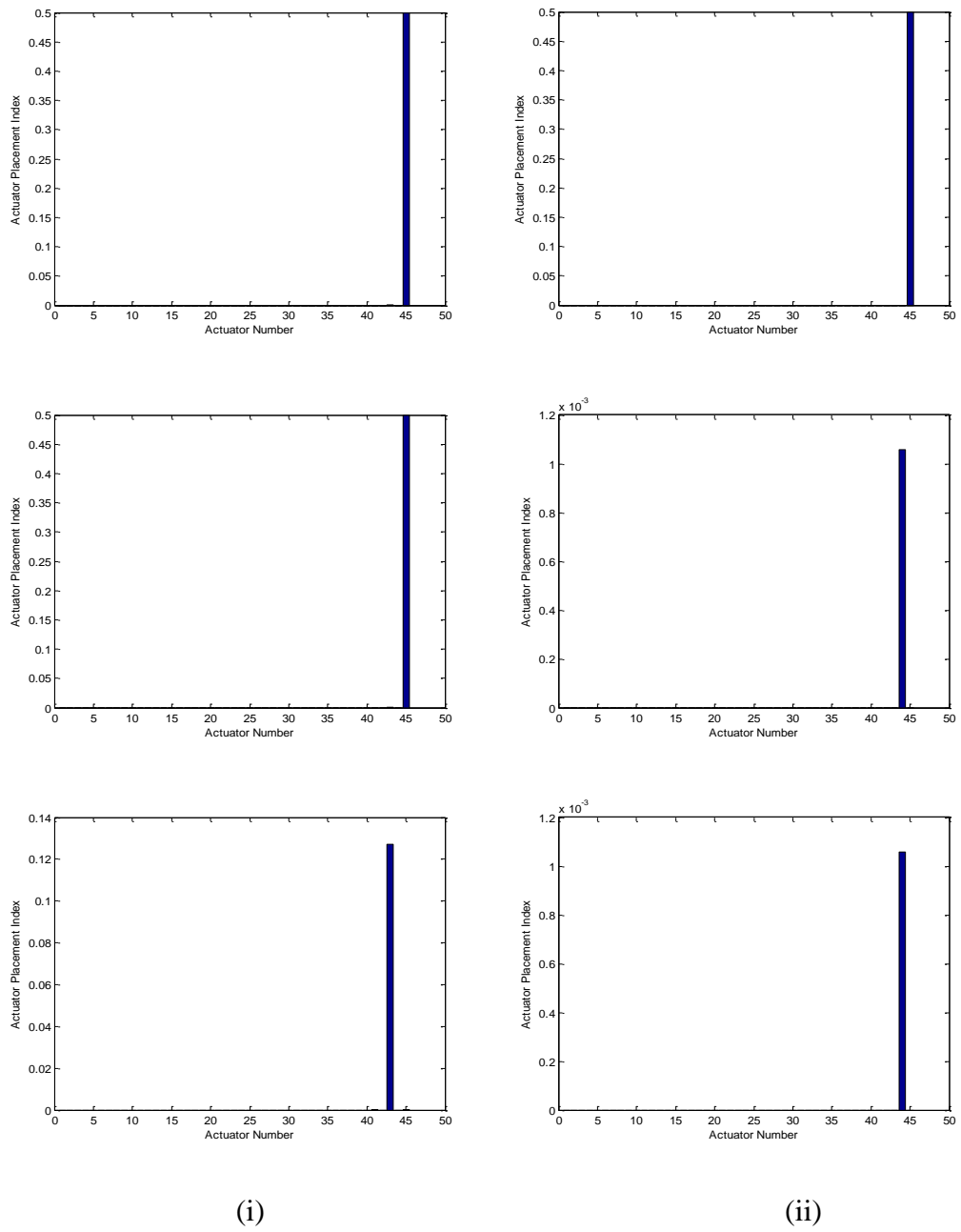
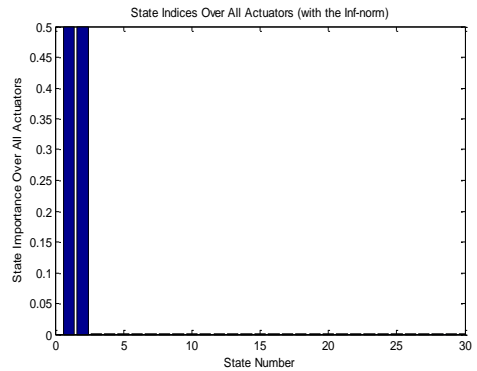
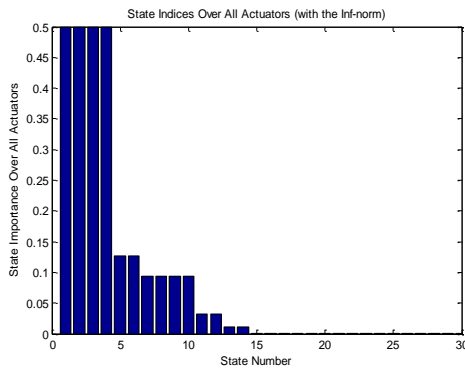
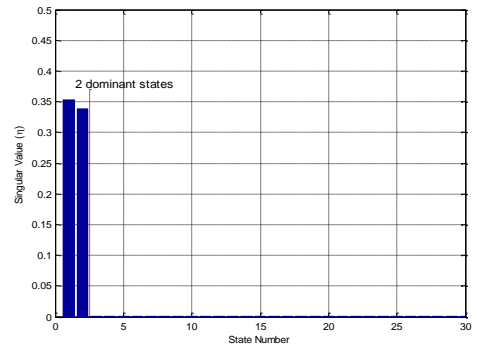
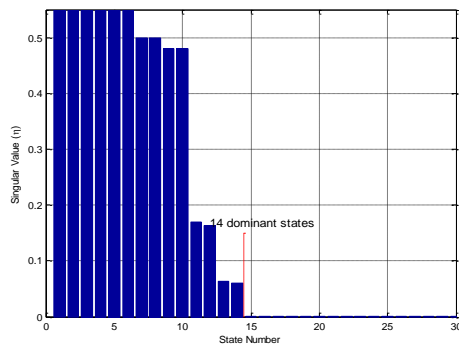
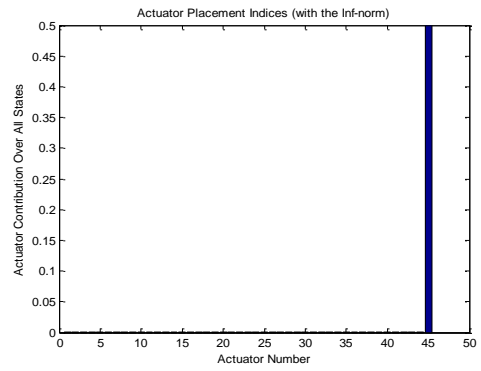
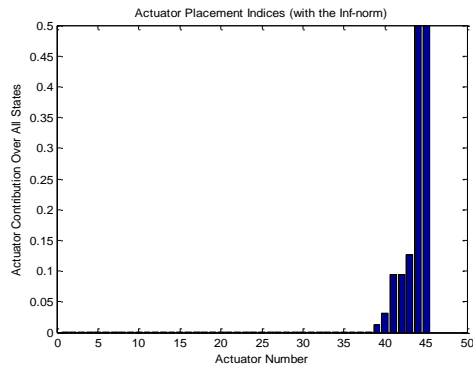


Figure 4.15 (a): (i) and (ii) are the plots of the actuator placement indices for the states 1, 3, and 5 of the 3-stage 3-order minimal and non-minimal tensegrity structures, respectively.



(i)

(ii)

Figure 4.15 (b): (i) and (ii) are the plots of the actuator placement indices over all states (T_a'), the Hankel singular values ($\eta_1, \eta_2, \dots, \eta_n$ – only the largest 30 out of a total of 90 are shown), and the state importance indices (M_a) of the 3-stage 3-order minimal and non-minimal tensegrity structures, respectively.

4.7 Summary

In this chapter, model order reduction of tensegrity structural systems has been presented. The approach employed the internal balancing technique which keeps only the states of the system with larger energy and deletes all others, thus, most of the dynamic behaviour of the original high-order model are retained in the reduced model. Also, the design of lighter and stronger controlled flexible structures requires that actuators and sensors be placed at locations that will excite the desired state(s) most effectively. This chapter covers the determination of optimal actuator and sensor placement using the balanced model representation since both optimal actuator and sensor placement and controller design are dependent on the information contained in the structural model and it is simpler to deduce placement indices in some model representation than others.

Despite the surge in interest in tensegrity structural systems and their active control capabilities in the last few decades, only few of these structures have actually been realized until present. The next chapter will focus on the design and physical realization of active tensegrity structures.

Chapter 5

PHYSICAL REALIZATION OF TENSEGRITY STRUCTURAL SYSTEMS PART I: PHYSICAL STRUCTURE DESIGN

5.1 Introduction

There has been a surge in interest in tensegrity structural systems and their deployment and control capabilities in the last few decades, however, only a few of these structures have actually been realized in practice until present. Moreover, most of the realized structures only take advantage of the static properties of these structures, although quite recently, some dynamic applications, such as in the three-DOF actuated robots [165], locomotive tensegrity robots [44], [166], tensegrity mobile robot [45], and five-module active tensegrity structure [92] have been realized.

Since tensegrity structures, in general, are broadly regarded as deployable structures [3], for the purpose of this thesis, it is important to make the following distinction: Tensegrity structural systems that are realizable can be classified as either *un-deployed* or *deployed* tensegrity structural systems. On the one hand, the *un-deployed* tensegrity structural systems are tensegrity structural systems that are not designed to be capable of changing their shape significantly; examples of these include tensegrity bridges [24] and cable domes [167]. Moreover, these systems may be equipped with components – for damping or imposing rigidity – to control and restrict the level of vibration by passive or active means. On the other hand, the *deployed* tensegrity structural systems are tensegrity structures that are designed to be capable of changing their shapes significantly and active vibration control are, to a large extent,

inherent in this framework. This chapter and the next deal with the design of the deployed tensegrity structures. The ensuing discussions will focus on practical structural design and optimization issues as well as the implementation of the software and the control system architecture. Importantly, it will bring together novel concepts that have not been investigated in the available literature on this subject hitherto.

Deployed tensegrity structures are capable of significant shape change from arbitrary structural configurations – which may or may not be tensegrity configurations/structures – to tensegrity structural systems with predefined structural shapes. For this class of tensegrity structures, an open-loop control strategy may generally be used for their deployments; examples of these are given in [168] and [165]. The application of an open-loop control technique for the deployment and reconfiguration of a class-2 of tensegrity tower has been demonstrated in [168], for example. In this example, the lengths of the bars – assumed rigid – are fixed and the controller ensures that the cable rest lengths are maintained at predefined cable lengths or set-points. These predefined set-points are obtained using a form-finding method that involves finding the solution to the equations of static equilibrium of tensegrity structure for which the overall structure is pre-stressed and this solution is not a unique set. Moreover, the transformation – by deployment – from one set of tension coefficients to another is considered a structural *reconfiguration*.

Furthermore, several techniques for the deployment of tensegrity structure have been devised and, with few exceptions such as those presented in [165] and [92] where the bar lengths are the control variables, most considered the rest lengths of the cables as the sole control variables. On the one hand, the advantage given for the use of cable rest length control is the possibility of the cables to provide for force sensing and geometry measuring functions while, at the same time, acting as structural members [169]. The disadvantage of the cable rest length control, however, is the potential for the number of candidate sensing elements to be too large since cables make up most of the structural elements of tensegrity structures although it is possible – using optimal actuator and sensor placement techniques of classical structural dynamics (as presented in Chapter 4 or, for instance, in [148], [157], [170]) – to determine the optimal choices of candidate cable for force/geometry sensing when given that the number of sensing elements is few and fixed. On the other hand, bar-length control approach (see, for example, [165]) is especially favourable since the number of bars is significantly less

than that of the cables in tensegrity structural systems. Moreover, bars can also be adapted to serve as force and geometry sensors. However, since the bars are fewer, the overall structural system has limited structural displacement necessary for significant shape change. A significant contribution of this project is the introduction of a new technique that combines the control of the cable and bar lengths simultaneously, thereby combining the advantages of both bar control and cable control techniques. Also, the approach used for the control of cables is significantly different from the techniques used for cable rest length control presented so far in the literature.

The design method and physical realization of tensegrity structures proposed in this thesis are covered in two chapters. Thus, the aim of this chapter and the next are to demonstrate the feasibility of realizing tensegrity structure using a given set of structural members and a predetermined initial structural configuration. In particular, the tensegrity configuration to be considered is the configuration of the simplest form of tensegrity structures, commonly called the simplex. Within the framework of this project, an experimental simplex deployed tensegrity structure was designed, assembled and tested. This experimental prototype is available in the Intelligent Systems Laboratory of the Department of Automatic Control and Systems Engineering of the University of Sheffield. The physical realization of the multi-stable tensegrity structure is an important step and a unique contribution of this present work in the design of tensegrity structural systems. The approach that made this practical realization possible is through varying the stiffness of some of the structural members. In this chapter, the design of the tension and compression structural members and the techniques for form-finding and deployment of a simple mono-stable and a more complex multi-stable tensegrity structures are given and a demonstration of how the multi-stable structure can be used to carry out translation along the three Cartesian axes – x , y and z – as well as rotations about these three axes will be shown. In addition, a collision avoidance technique that may be employed for the simplex tensegrity structure will be described. The next chapter focuses on details of the hardware, hardware configuration, serial communication protocol using the Universal Serial Bus (USB) interface and the employed control techniques.

5.2 Tensegrity Prisms and their Regularity, Minimality and Design Approaches

The definition of *tensegrity prisms* and their regularity and minimality, following the nomenclature given in [2], are given as follows: A three-dimensional single stage tensegrity structure that consists of p number of bars, p number of side cables and $2p$ number of cables that make up the *top* and *bottom* p -sided top and bottom polygons, respectively, is called a tensegrity prism. A tensegrity prism is said to be *regular* if the top and bottom polygons are parallel and equilateral (note that the circumradii of the top and bottom polygons, r_t and r_b , respectively, for the structure need not be the same). Moreover, the tensegrity prism is said to be *minimal* if stability of the prism is as a result of the smallest number of cables. Figure 5.1 shows three different 3-bar minimal tensegrity prisms.

The characteristic angle of any regular polygon is given by $\frac{2\pi}{p}$ and the *twist angle* of any tensegrity prism (regular or irregular) is the angle formed by the bottom polygon and the polygon formed by the projection of the top polygon unto the plane of the bottom polygon (such that the bottom polygon and the projected top polygon are concentric). Figure 5.2 shows the circumradius r , the characteristic angle \emptyset of the bottom polygon and the twist angle α of a 4-bar regular minimal tensegrity prism. In the absence of external forces, the twist angle of any p -bar regular minimal tensegrity prism is given as follows [27], [113]:

$$\alpha = \frac{\pi}{2} - \frac{\pi}{p} \quad (5.1)$$

Also, if the tension coefficients of the cables of the top and bottom polygons are denoted as q_t and q_b , respectively, and the tension coefficients of the vertical cables and bars as q_{vc} and q_{vb} , respectively, in the absence of external forces, the values of q_t , q_b , q_{vc} and q_{vb} for a regular minimal tensegrity prisms are given as follows [2]:

$$\begin{aligned} q_t &= \gamma \cdot \frac{1}{2\sigma \left(\sin\left(\frac{\pi}{p}\right)\right)} \\ q_b &= \gamma \cdot \frac{\sigma}{2 \sin\left(\frac{\pi}{p}\right)} \\ q_{vc} &= \gamma \\ q_{vb} &= -\gamma \end{aligned} \quad (5.2)$$

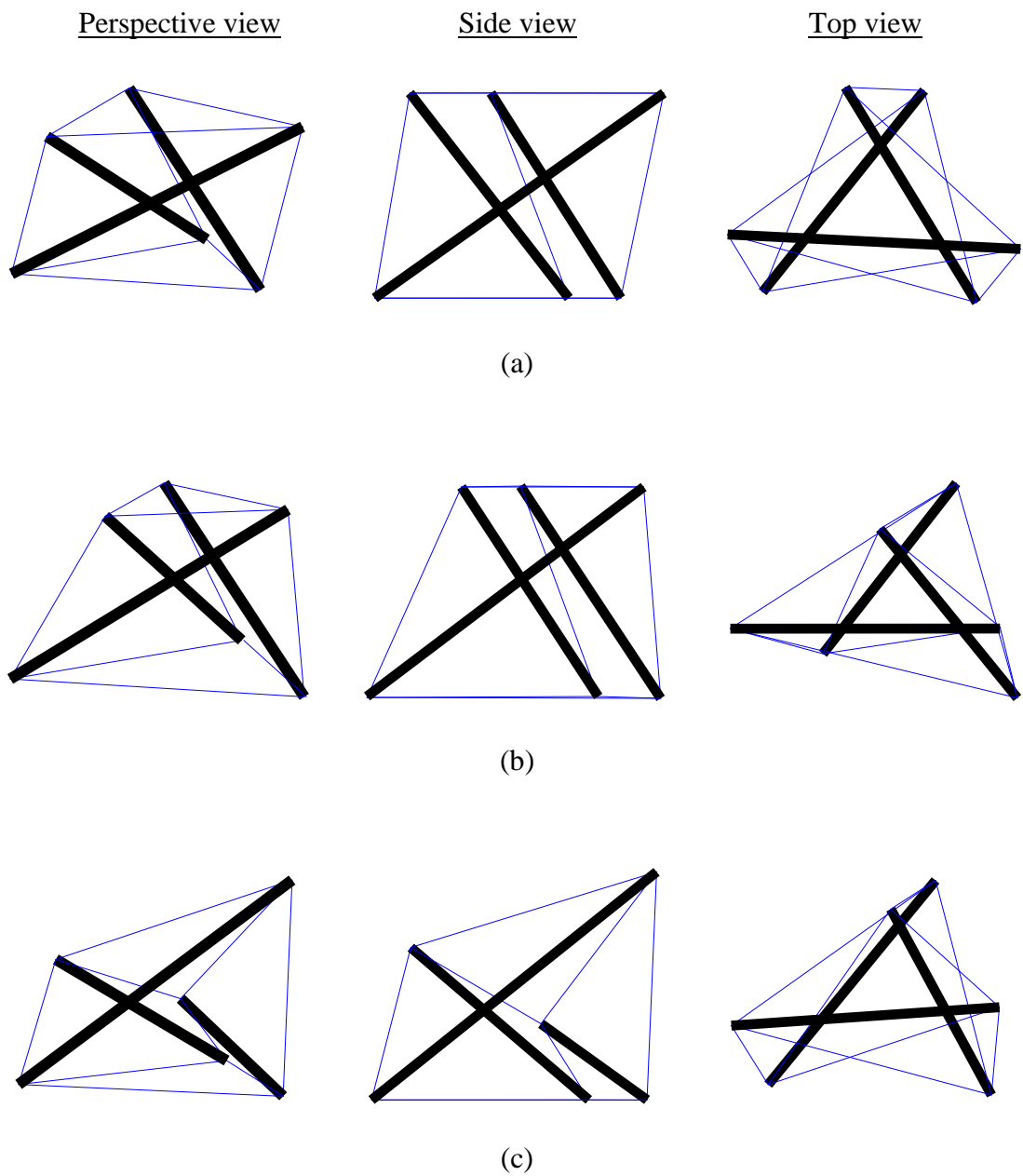


Figure 5.1: Examples of 3-bar minimal tensegrity prisms: (a) A regular minimal tensegrity prism with $r_t = r_b$; (b) A regular minimal tensegrity prism with $r_t < r_b$; and (c) An irregular minimal tensegrity prism with $r_t = r_b$.

where $\sigma := \frac{r_t}{r_b}$ is the ratio of the circumradius of the top polygon to that of the bottom polygon, and $\gamma > 0$ is a scaling factor which can be chosen arbitrarily without affecting the equilibrium of the structure. The level of pre-stress in the structure increases with γ and the first two expressions in (5.2) lead to the relation $q_b = \gamma^2 q_t$. Moreover, just as in the preceding chapters, the expression in (5.2) assumes that the forces (therefore,

tension coefficients) of the cables are positive – denoting that the cables are in tension – while the forces in the bars are negative – denoting that the bars are in compression.

Deployed tensegrity prisms are those tensegrity prisms that fall into the category of deployed tensegrity structures defined in the preceding section. Two design approaches may be used in the realization of a deployed tensegrity prism. The first approach involves a design in which the shape change that can be realized with a tensegrity configuration can only be a regular tensegrity prism; the tensegrity structure realized using this approach is called a *mono-stable* tensegrity prism. The second approach involves a design in which the tensegrity configuration can be used to realize both regular and irregular tensegrity prisms; the tensegrity structure realized using this approach is called a *multi-stable* tensegrity prism.

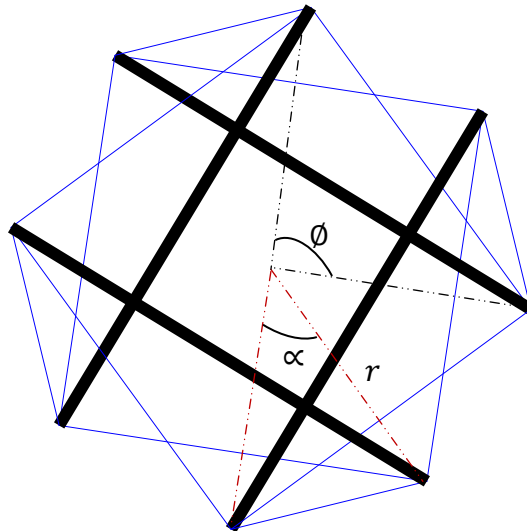


Figure 5.2: Top view of a 4-bar regular minimal tensegrity prism with $r = r_t = r_b$.

5.3 Designs of Compressive and Tensile Structural Members

As mentioned earlier, the most basic issue in the design of tensegrity structures is the form-finding process which involves the selection and definition of their optimal structural forms by searching for all shapes for which the structural configuration is pre-stressed and in a state of static equilibrium in the absence of external forces. The algorithm of the constrained optimisation approach to form-finding developed in Chapter 2 can be found in Table 2.9.

It is worth noting that the form-finding algorithm of Table 2.9 does not take into consideration the type of materials that is used as tensile and compressive structural members. It is obvious that tensile members are more mass efficient than compressive members. Therefore, an improvement in the strength and reduction in weight of a tensegrity may be gained if the use of long compressive members is minimized while the use of tensile members is maximized [2]. The process of continuously replacing the compressive members by another tensegrity structure with shorter compressive members until the required mechanical properties are achieved is called *self-similar tensegrity* [171], and if the iteration process continues infinitely, it is called *tensegrity fractal* [2]. Thus, at microscopic scale ($< 10^{-6}$ m), the process becomes a material design process and at larger scale (for example, $> 10^{-3}$ m), it becomes a structural design process. Hence, there is no difference in material and structural design of tensegrity structures mathematically [2]. Therefore, the constrained optimization form-finding algorithm presented in Chapter 2 is applicable to micro- and large-scale material or structural designs as the case may be. In this chapter however, the emphasis is on the design of tensegrity structural system at a scale between approximately 10^{-3} m to 1 m. Moreover, if there were no restrictions due to manufacturing related issues, yield constraints on the cables and buckling constraints on the bars may be included in the form-finding process to avoid structural failure (such as, the yielding of cable or the buckling of the bars). However, manufacturing of the bars is beyond the scope of this project. Nonetheless, the discussion on the factors that influenced the choice of structural components used for the physical realization of the tensegrity structure that is to be designed will be presented.

To begin the design process of a tensegrity structure, the constrained optimization form-finding technique is used as a starting point. The engineering problem is to design a deployable 3-bar regular minimal tensegrity prism with $r_t = r_b$ and, at equilibrium due to pre-stress and in the absence of external forces, the length of each bar should be equal to 60 cm. Henceforth, the tensegrity structure with this specification will be termed the ‘initial 3-bar tensegrity prism’. Also, the initial 3-bar tensegrity prism should be capable of undergoing structural transformation into a 3-bar irregular minimal tensegrity prism by reconfiguration. Figure 5.3 shows the tensegrity structure obtained from the form-finding process when the length of cable 1 is constrained to 40.875 cm and with no constraints on the set of tension coefficients. (It should be noted that the value of 45.875cm was obtained by scaling the vector

$l = [0.6813 \ 0.6813 \ 0.6813 \ 0.6813 \ 0.6813 \ 0.6813 \ 0.6813 \ 0.6813 \ 0.6813 \ 1 \ 1 \ 1]^T$

by the factor of 60; element of this vector are the lengths of the structural members and are obtained using the constrained form-finding technique with the constraints that all bars are of unit lengths and the cables are of equal lengths). Table 5.1 shows the numerical results when the value of the length constraint is varied in the form-finding process. Furthermore, by varying the length constraint on cable 1 (that is, the length of cable 1 is varied between 32 cm and 49 cm) for instance, the lengths and compressive forces of the bars varies approximately between 46.97 cm to 72 cm and between -209.45 N and -320.73 N, respectively (see Table 5.1; l , f and q denotes the length, force and tension coefficient of a structure member, respectively, and $\|A \cdot \mathbb{q}\|_2$ is the norm of the vector of residual nodal forces as defined in Chapter 2). Thus, for the deployed 3-bar regular minimal tensegrity structure to be designed, it would be desirable that the ‘extensible’ bars have lengths that can cover at least the range from 46.97 cm to 72 cm and can withstand at least 320.73 N of compression of compressive force. Likewise, it can be deduced from Table 5.1 that the cables, in general, should be able to withstand at least 218.50 N – the maximum force that cables are subjected to if the bar lengths are kept within 46.97 cm and 72 cm – assuming all the cables have the same material properties. It is worth noting that the choice of centimetre and Newton scales from the lengths and forces, respectively, in structural members resulting from the form-finding process is rather arbitrary but consistent with the earlier assertion from the previous section (see equation (5.2)), and also in Chapter 2, that the scaling factor can be chosen arbitrarily without affecting the equilibrium of the structure.

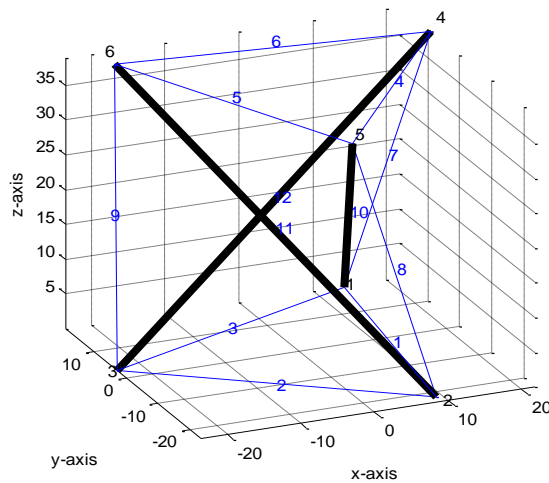


Figure 5.3: The initial 3-bar tensegrity prism (the length of each bar equals to 60 cm and $r_t = r_b$)

Table 5.1: Structural parameters of the initial 3-bar tensegrity prism with the following constraints: $l_1 = l_2 = l_3 = l_4 = l_5 = l_6$, $l_7 = l_8 = l_9$ and $l_{10} = l_{11} = l_{12}$

Structural Member	Constraint: $l_1 = 40.875$ (Structure of Figure 5.3)			Constraint: $l_1 = 32$			Constraint: $l_1 = 49$		
	l (cm)	f (N)	q (N/cm)	l (cm)	f (N)	q (N/cm)	l (cm)	f (N)	q (N/cm)
1	40.8750	105.2308	2.5745	32.0000	82.3825	2.5745	49.0000	126.1482	2.5745
2	40.8750	105.2308	2.5745	32.0000	82.3825	2.5745	49.0000	126.1482	2.5745
3	40.8750	105.2308	2.5745	32.0000	82.3825	2.5745	49.0000	126.1482	2.5745
4	40.8750	105.2308	2.5745	32.0000	82.3825	2.5745	49.0000	126.1482	2.5745
5	40.8750	105.2308	2.5745	32.0000	82.3825	2.5745	49.0000	126.1482	2.5745
6	40.8750	105.2308	2.5745	32.0000	82.3825	2.5745	49.0000	126.1482	2.5745
7	40.8750	182.2650	4.4591	32.0000	142.6907	4.4591	49.0000	218.4951	4.4591
8	40.8750	182.2650	4.4591	32.0000	142.6907	4.4591	49.0000	218.4951	4.4591
9	40.8750	182.2650	4.4591	32.0000	142.6907	4.4591	49.0000	218.4951	4.4591
10	60.0000	-267.5450	-4.4591	46.9725	-209.4542	-4.4591	71.9266	-320.7267	-4.4591
11	60.0000	-267.5450	-4.4591	46.9725	-209.4542	-4.4591	71.9266	-320.7267	-4.4591
12	60.0000	-267.5450	-4.4591	46.9725	-209.4542	-4.4591	71.9266	-320.7267	-4.4591
$\ A \cdot q\ _2$	8.2870×10^{-6}			2.6102×10^{-6}			3.4760×10^{-6}		

5.3.1 Selection of Extensible Bars

As it is beyond the scope of this project to manufacture extensible (telescopic) bars to achieve large longitudinal displacement of bars, the following is an outline of the factors that influenced the selection of the extensible bars used for this project:

- **Physical length:** As a starting point, original lengths of the extensible bars (commonly referred to as telescopic actuators) should be approximately within 40 cm to 75 cm (a conservative bound to cover at least the required 46.97 cm to 72 cm lower and upper bounds, respectively) and, at least, the bars should be able to extend to the 60 cm length – the length of each of the bars of the initial 3-bar tensegrity prism. Thus, if the original (retracted length) of the extensible bar is 45 cm, for instance, the stroke length (the difference between maximum possible bar length and its retracted length) should be 27 cm when the maximum bar length required is 72 cm.
- **Force:** Since the bars of tensegrity structures are only allowed to be subjected to compressive forces alone, the extensible bar must be able to withstand at least 320.7267 N of compressive force.
- **Joint type:** The use of the ideal extensible bar should make it is easy for the structural assembly of the initial tensegrity prism to approximate a pin-jointed structural assembly.
- **Weight:** If it were possible to design the extensible bar, the problem of finding the minimum (optimal) weight for the extensible bar for the maximum expected

stress (or any other failure criteria, for example, flexural, buckling, etc.) can be formulated as an optimization problem since, for an ideal extensible bar with uniform cross-sectional area, the weight can be expressed as [172]:

$$W = \rho Al = \rho \left(\frac{f}{\sigma} \right) l = \frac{fl}{\sigma/\rho} \quad (5.3)$$

where ρ , A , l , f and σ are the mass density, cross-sectional area, length, force and elastic stress of the extensible bar, respectively. However, given the limited scope of this project, it will be ensured that the extensible bar to be used, in addition to being as light weight as possible, satisfies the conditions of the other factors outlined in this section.

- **Sensor:** It will be advantageous to have the extensible bar equipped with force sensing and/or geometry measuring functionality. This will aid the design of an efficient structural control system required during deployment.
- **Powering and gearing:** If the tensegrity structural system is powered during the deployment process to a particular valid tensegrity structure, it will be required that the extensible bars ‘rigidify’ by holding on their current positions after the deployment process when power supply is discontinued; this can be achieved by appropriate choice of the gears located inside the telescopic actuator. This power saving strategy also minimizes the likelihood of total structural collapse (and may be very important for critical applications) in the event of a power failure.

In consideration of these factors, the 12” stroke linear actuator with feedback – one of the Light Duty (LD) series of actuators manufactured by Concentric International [173] – has been chosen for this project. The actuator consists of small and large cylindrical bars; the small cylindrical bar protrudes from the large one during the process of extension. This actuator, pictured in Figure 5.4, is equipped with a potentiometer for measuring position and for use in a feedback system. Also, the linear actuator uses a worm drive gear arrangement which ensures that the drive will hold its position even when unpowered. Table 5.2 presents the technical details related to the linear actuator.



Figure 5.4: A picture of the 12” stroke linear actuator with feedback (LD series actuator) manufactured by Concentric International [173]

Table 5.2: Technical Specification of the 12” stroke linear actuator with feedback [173]

Feature	Specification
Original length:	44.958 cm (± 0.3048 cm)
Stroke length:	30.48 cm
Max. Extended length:	Original length + Stroke length
Weight:	1.5876 Kg
Gear Ratio:	20:1
Free-run current measured at 12 V:	0.5 A
Stall current measured at 12 V:	10 A
Linear Speed measured at 12 V:	1.3 cm/sec
Dynamic Linear force measure at 12 V:	50 Kilogram-force
Static Linear Force (i.e. force it can withstand when not running):	250 Kilogram-force (where 1 Kilogram-force := 9.80665 N)

Furthermore, it should be recalled that the equilibrium position of each of the three bars of the initial 3-bar tensegrity prism is 60 cm and the norm of the vector of nodal residual forces ($\|\mathbb{A} \cdot \mathbb{q}\|_2$) is 8.287×10^{-5} for this configuration. In addition, each of the linear actuators has an original length (that is, retracted length) and a stroke length of approximately 45 cm and 30 cm, respectively. This means that there is the freedom of varying the length of each of the three bars of the tensegrity prism between 45 cm and 75 cm. However, not all possible configurations (that can be obtained by varying all the three bar lengths) are likely to form a three-dimensional pre-stressed and statically stable (valid 3-bar regular/irregular minimal tensegrity) structure. Thus, it will be useful to obtain the region, defined by the length of each bar [45 cm, 75 cm], for which the 3-bar minimal tensegrity configuration results in a valid tensegrity structure. This stability region will be the equilibrium space of the 3-bar irregular minimal tensegrity prism of which the equilibrium space of the regular counterparts (all other possible 3-bar regular minimal tensegrity prisms for this configuration) is a sub-space.

The limits on the lengths of the bars due to the minimum and maximum lengths achievable with the linear actuators require that additional length constraints are included in the form-finding algorithm. These limits also impose restrictions on the value of forces in other structural members (thereby, restrictions on the tension coefficients and, consequently, on the stiffness of the overall structural system). Thus, the following upper and lower bounds are deduced from Table 5.1:

1) The bounds of the tension coefficient of the vertical cables as follows:

The expected maximum force in cables of the structural assembly:	218.50 N
The expected minimum force in cables of the structural assembly:	142.69 N
The expected maximum length of cables of the structural assembly:	49.00 cm
The expected minimum length of cables of the structural assembly:	32.00 cm

Thus, the upper and lower bounds of the constraints on the tension coefficients on the vertical cables for the form-finding algorithm can be deduced as follows:

$$\text{Lower bound } lb_i = \min \left\{ \frac{142.69}{32.00}, \frac{142.69}{49.00} \right\} = 2.91 \text{ N/cm}$$

$$\text{Upper bound } ub_i = \max \left\{ \frac{218.50}{32.00}, \frac{218.50}{49.00} \right\} = 6.828 \text{ N/cm}$$

These bounds lead to the following constraint on the tension coefficient of the i^{th} structural members:

$$2.91 \leq \mathbb{Q}_i \leq 6.828 \quad \text{for } i = 7, 8, 9 \quad (5.4)$$

From the constraint of (5.4), a more conservative bound (this will be explained later in Section 5.3.3) can be written as follows:

$$2.91 \leq \mathbb{Q}_i \leq 6.6888 \quad \text{for } i = 7, 8, 9 \quad (5.5)$$

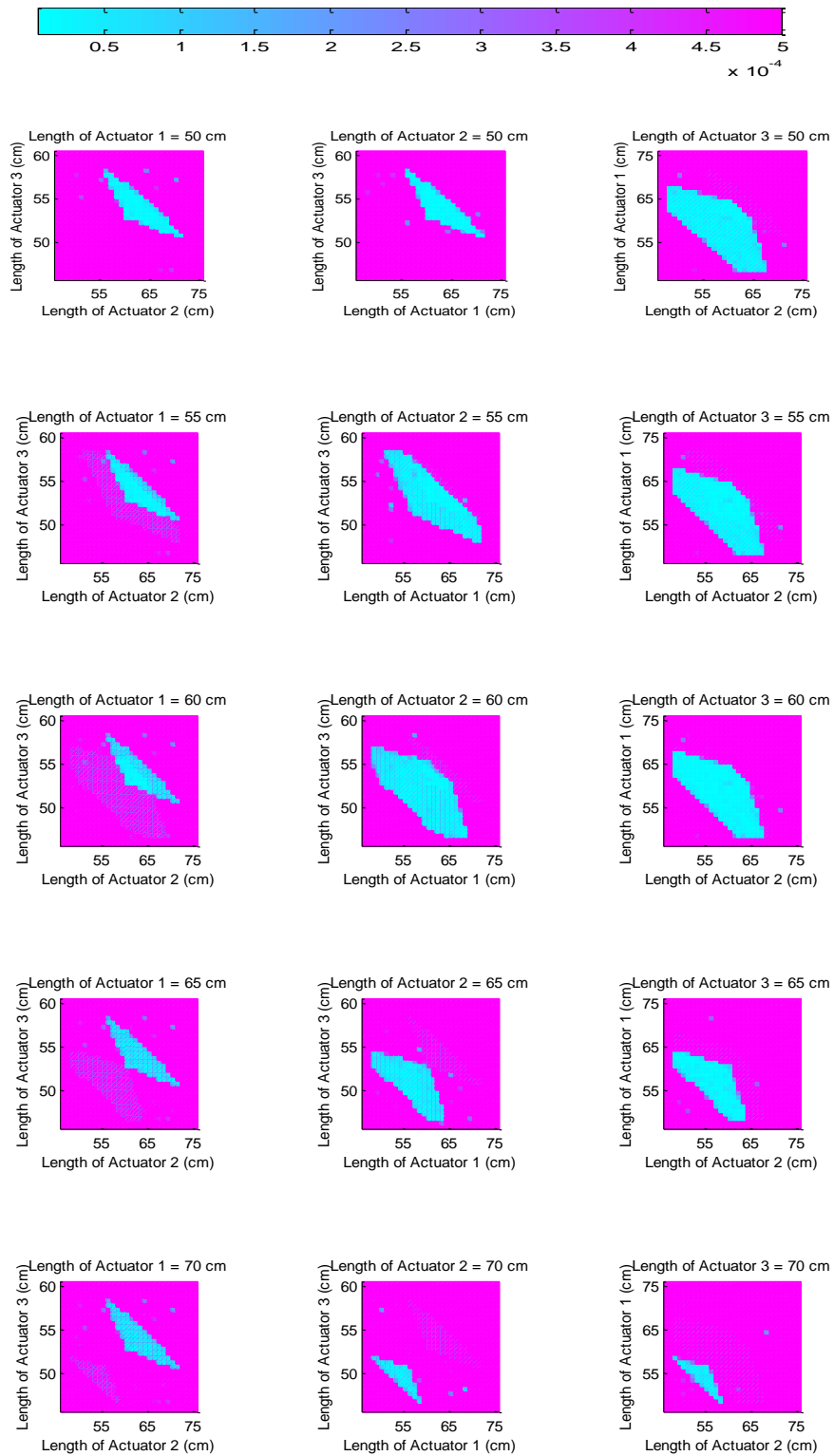
2) The bounds on length of the i^{th} structural member are as follows:

$$l_i = 40.875 \quad \text{for } i = 1, 2, 3 \text{ (the bottom-horizontal cables)} \quad (5.6)$$

$$32.891 < l_i < 42.6502 \quad \text{for } i = 7, 8, 9 \text{ (the vertical cables)} \quad (5.7)$$

$$46.958 < l_i < 70.958 \quad \text{for } i = 10, 11, 12 \text{ (the linear actuators)} \quad (5.8)$$

The explanation on the equality constraint (5.6) and the choice of the lower and upper bounds on the length constraints in (5.7) and (5.8) are differed to Section 5.3.3. It is very important, however, to note that there is no constraint (similarity or otherwise) on the top-horizontal cables. With the set of constraints in (5.5-5.8), the constrained optimization form-finding algorithm can be employed to find the degrees of stability of all tensegrity structures that can be obtained by varying the lengths of each of the three linear actuators l_i (for $i = 10, 11, 12$) from 45 cm to 75 cm. Figure 5.5 shows colour-based plots of the degree of stability (measured by the norm of the nodal residual forces) versus the bar lengths of the 3-bar minimal tensegrity prism in two-dimension. The figure covers the region [45 cm, 75 cm] for each of the bars. Also, Figure 5.6 depicts the same figure in three-dimension using a few number of slices. With these figures, it is concluded that the stability region of the 3-bar irregular minimal tensegrity prism, that is the region in which the multistable tensegrity prism forms valid tensegrity structures, with an initial stable configuration corresponding to the initial 3-bar tensegrity prism obtained using the constrained optimization form-finding technique approximates a geometric shape best described as a circle (of approximately 35 cm in diameter with centre at [60, 60, 60] cm) when viewed from one direction (View A) and a plano-convex lens (of approximately 15 cm in width) when viewed from an orthogonal direction (view B). Moreover, Figure 5.7 shows the SolidWorks® dimensional drawing of the initial 3-bar tensegrity prism that is built with the 12” stroke linear actuator of Figure 5.4.



(a)

(b)

(c)

Figure 5.5: Plots of the degree of stability (measured by the norm of the nodal residual forces) versus the bar lengths of the 3-bar minimal tensegrity prism in two-dimension

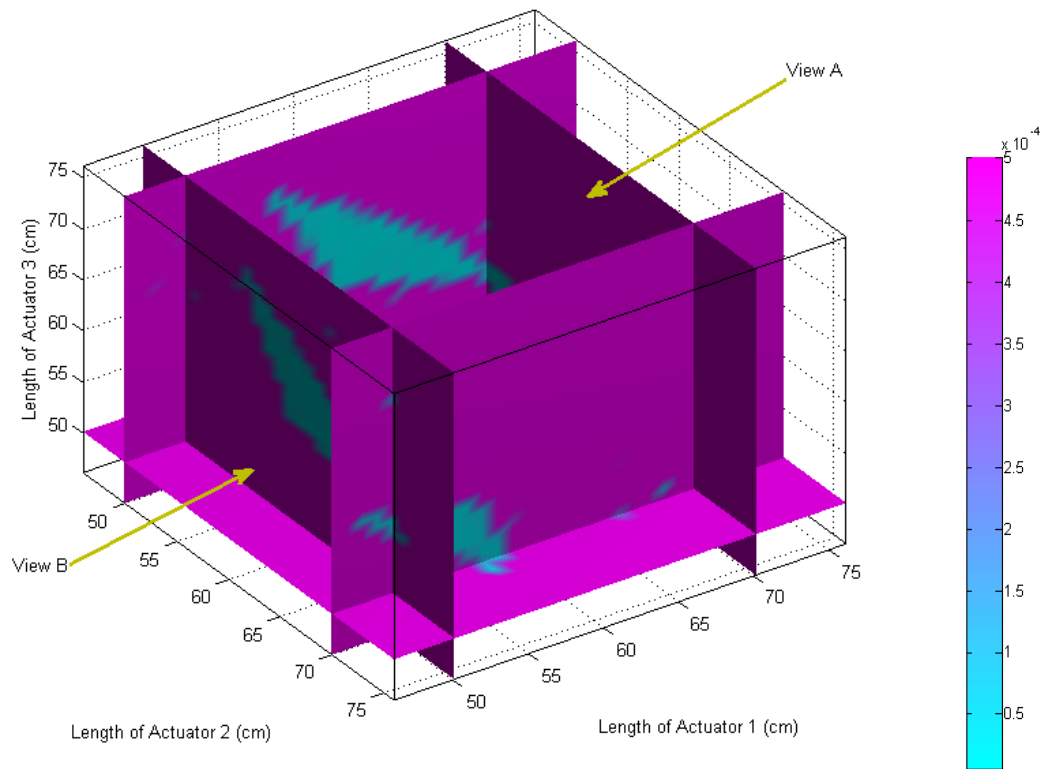


Figure 5.6: A depiction of the stability region of the 3-bar minimal tensegrity prism in three-dimension using a small number of slices

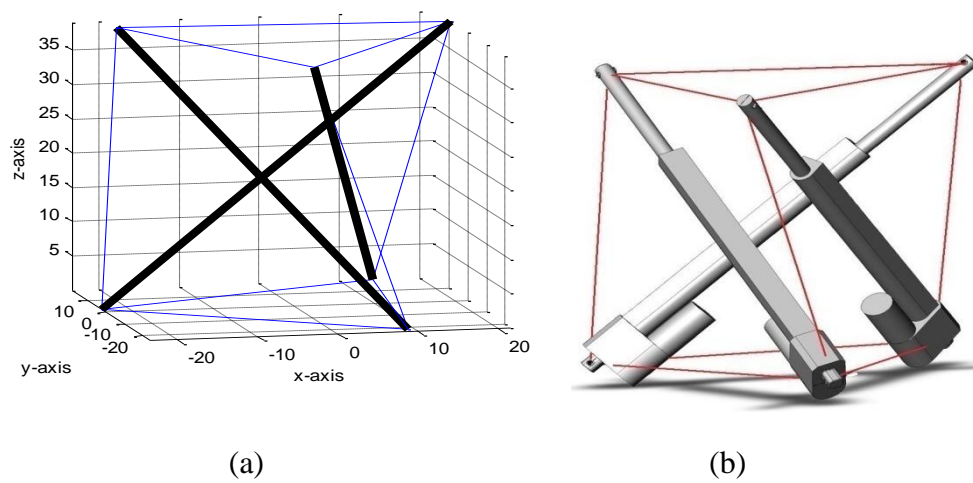


Figure 5.7: (a) The initial 3-bar tensegrity prism; (b) SolidWorks® dimensional drawing of the 3-bar tensegrity prism

5.3.2 Design of Cables

The next stage of the realization process is the design of cables. Here, it will be assumed that the cables are linearly elastic and, as such, can be approximated by linear springs (that will only be subjected to stresses below the yield strength) with fixed stiffness constants and the errors associated with linear approximations will be neglected. The desired structural configuration is shown in Figure 5.8. It is worth noting that the three bottom nodes of this structural system are to be rigidly attached to the base, therefore, eliminated when the boundary conditions are applied. Thus, the need for the bottom springs is removed and the 12-member structural system has 9 DOFs (that is, each of the three top nodes can move in three-dimensional Euclidean space). For the initial 3-bar tensegrity prism, at bar-lengths of 60 cm (length of each of the three bars), each of the six cables (the three top horizontal and the three vertical cables) has a length of 40.8750 cm. The corresponding tensile forces in each of the three top-horizontal and three vertical cables are 105.2308 N and 182.2650 N, respectively, as given in Table 5.1. Assuming that all the linear springs have the same spring constants k , which is 38.15 N/cm, the initial spring lengths can be obtained (from Hooke's law) as follows:

(a) For the vertical spring:

$$\text{Tensile force} \div k = \text{Extension} = \frac{182.2650 \text{ N}}{38.15 \text{ N/cm}} = 4.78 \text{ cm}$$

$$\text{Original length} = \text{Final length} - \text{Extension} = (40.857 - 4.78) \text{ cm} = 36.0974 \text{ cm}$$

(b) For the horizontal spring:

$$\text{Tensile force} \div k = \text{Extension} = \frac{105.2308 \text{ N}}{38.15 \text{ N/cm}} = 2.7583 \text{ cm}$$

$$\therefore \text{Original length} = (40.857 - 2.7583) \text{ cm} = 38.1167 \text{ cm}$$

The spring constant is dependent on the spring material (shear modulus) and geometry (number of active coils) and, in practice, springs are commonly designed using the parameters of the shear modulus and number of active coils as follows [174]:

$$k = \frac{Gd^4}{8nD^3} \quad (5.10)$$

where G , D , d and n are the shear modulus, mean spring diameter, wire diameter and the number of active coils, respectively. Figure 5.9 shows the picture of the spring fabricated for this project to serve as a top-horizontal cable; the spring has the following specifications: G of carbon steel = 79300 Nmm⁻², D = 12.365 mm, d = 2.95 mm and n =

104; thus, the spring constant k is approximately 38.18 N/cm with a tolerance of $\pm 6\%$. The original length of the spring is 37.67 cm which is short of the 38.12 cm required by 0.45 cm. The remaining 0.45 cm corresponds to the length of the inactive part of the spring (the total distance of the inactive parts due to each of the two end connectors) and, thus, on a load (pull force) of 105.23 N, the distance between the midpoints of the end connectors will be approximately equal to 40.875 cm as required.



Figure 5.8: SolidWorks® dimensional drawing of the 3-bar tensegrity prism with cables approximated by elastic springs and the three bottom nodes rigidly attached to the base

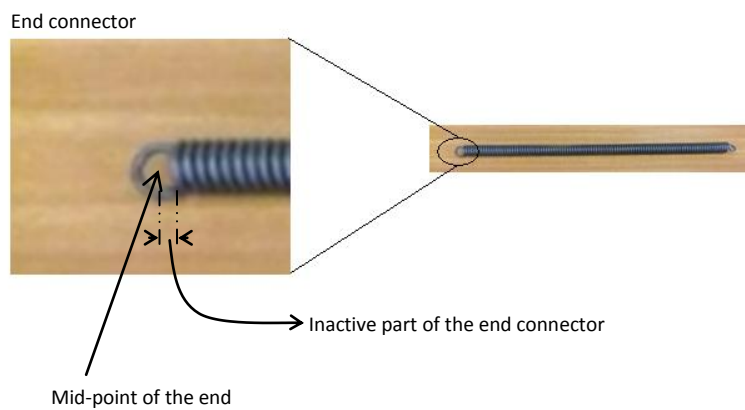


Figure 5.9: Picture of the spring fabricated to approximate the linear cable of the initial 3-bar tensegrity prism

Figure 5.10 shows the results of a SolidWorks® simulation of the 3-bar tensegrity prism of Figure 5.8 with a forced oscillatory motion of an actuator's arm by a force that would drive the arm through a distance of 13 cm while the two other actuators (bars) are restricted to their current lengths of 60 cm. The simulation assumes that the springs are connected to the joints in a pin-jointed fashion. The results reflect the variation of forces in the six springs as the linear actuator oscillates. Importantly, the simulation confirms the correctness of the results of the form-finding algorithm presented in Chapter 2 in that the forces in the top horizontal springs and the vertical springs oscillate around the values of 105.2308 N and 182.2650 N, respectively, which are the nominal values of the corresponding forces obtained from the form-finding process.

The design of the 3-bar regular minimal tensegrity prism just considered is monostable in that, the only tensegrity structure it can realize are regular tensegrity prisms. Thus, since r_b and α are constants (that is, bottom nodes are rigid and the twist angle of regular tensegrity structures are unique), the only other configuration for which the initial 3-bar tensegrity prism will obtain a valid tensegrity structure is by varying the circumradius of the top polygon r_t , thereby changing the height of the tensegrity prism by simultaneously increasing or decreasing the lengths of each of the three vertical bars equally. This particular case of varying the height of the 3-bar regular minimal tensegrity prism was also adopted in [165]. Figure 5.11 shows the degree of stability of the initial 3-bar tensegrity prism (measured by the natural log of the norm of the nodal residual forces) as its height is varied by simultaneously increasing the lengths of the bars equally from 45 cm to 75 cm. It can be seen that the valid tensegrity structures can only be truly realized if the lengths of the bars are roughly within 55 cm and 62.5 cm range. Using the well-known formula of computing the circumradius of a regular polygon (circumradius = $\frac{\text{side length}}{2 \sin(\frac{180^\circ}{\text{no.of sides}})}$), the 55 cm to 62.5 cm range correspond to $31.75 \text{ cm} < r_t < 36.08 \text{ cm}$. The hindrance to the possibility of having better shape control of the structural assembly (through obtaining more valid tensegrity prism) is due to the passive nature of the cables or linear springs that are used. This is illustrated by considering the example that follows.

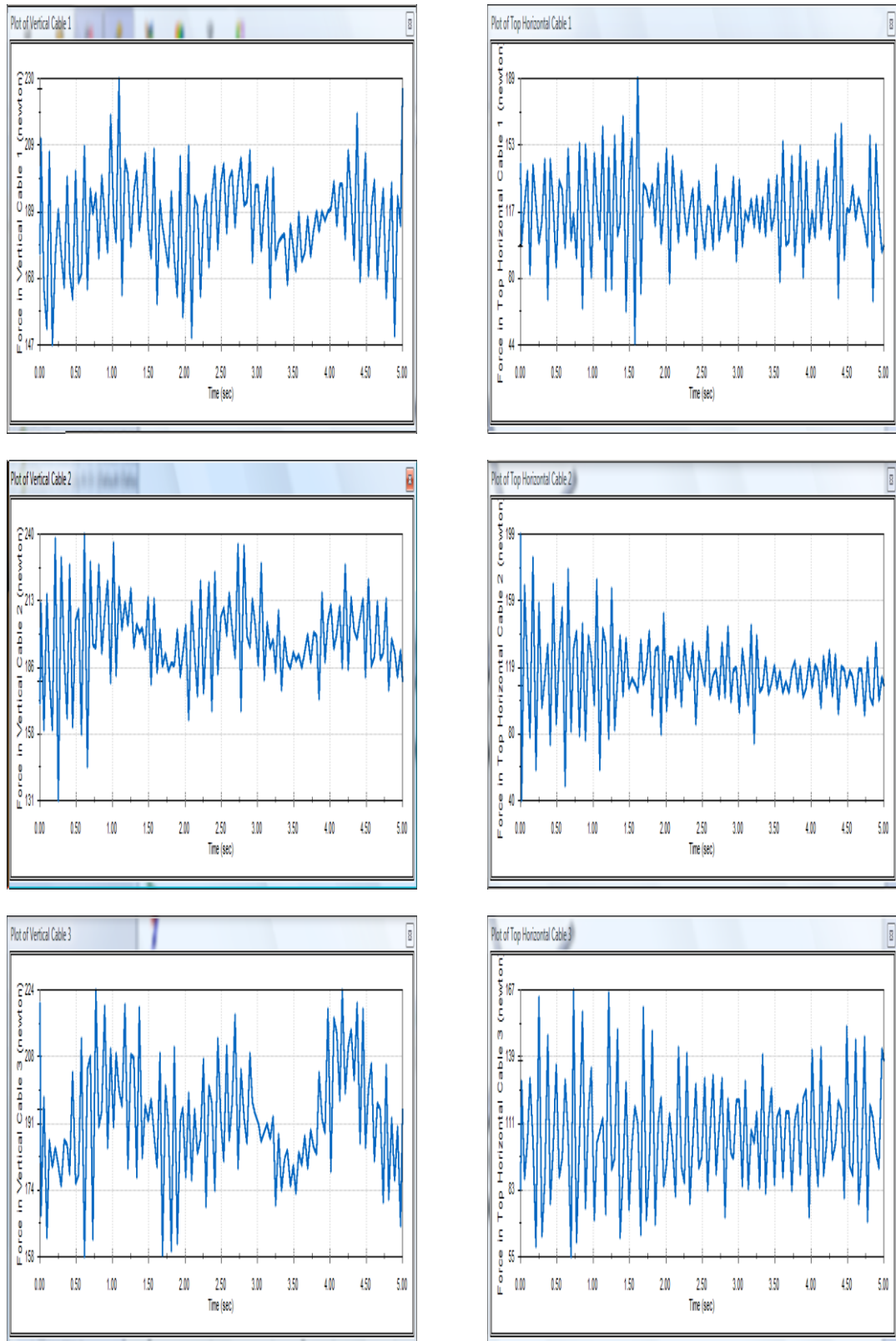


Figure 5.10: The variation of forces in the six springs as a linear actuator is driven (a forced oscillatory motion) through a distance of 13 cm

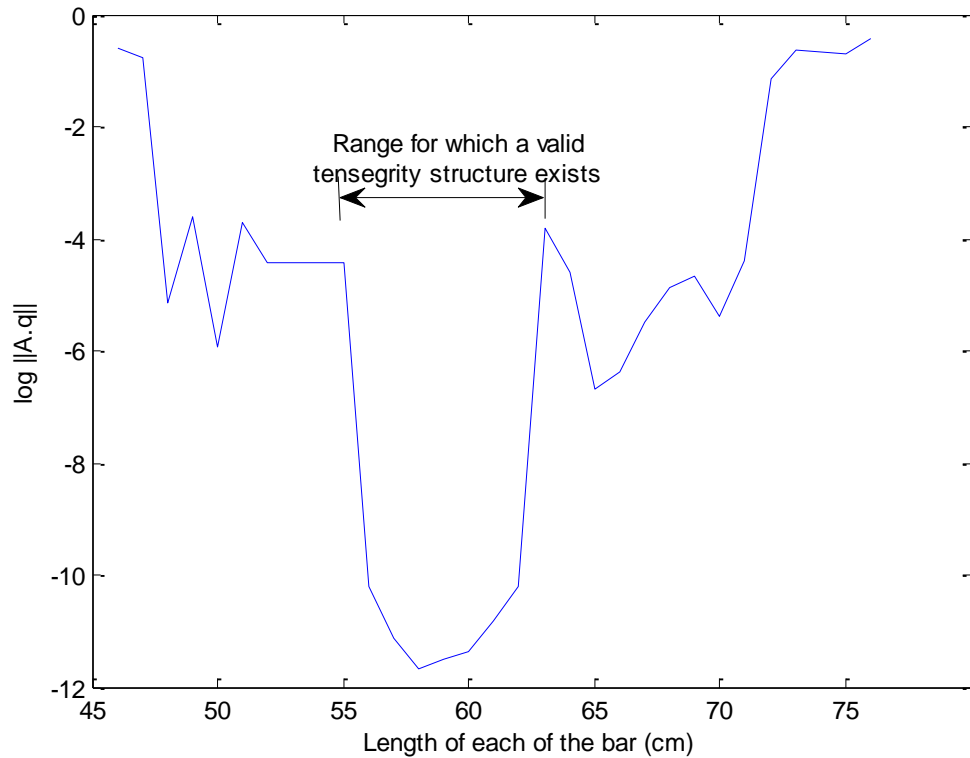


Figure 5.11: The degree of stability of the initial 3-bar tensegrity prism (measured by the natural log of the norm of the nodal residual forces, $\|A \cdot q\|_2$) as its height is varied by increasing the lengths of the bars equally from 45 cm to 75 cm

Consider the three tensegrity structures shown in Figure 5.12, the first structure, (a), is the initial 3-bar tensegrity prism and has the original lengths of the top and vertical springs equal to 36.0974 cm and 38.1167 cm, respectively. This makes the required stiffness constant for all the springs equal to 38.15 N/cm. Now, if the structure is to be transformed by deployment into Figure 5.12 (b) – which is also a valid tensegrity structure with $r_t = r_b$ – the required original lengths of the vertical spring must be altered if the stiffness constant for all the springs used must remain the same. In particular, for the structure in Figure 5.12 (b), the final lengths of the vertical spring are 41.9863 cm, 37.5095 cm and 45.2774 cm and the corresponding forces for these structural members are 186.8189 N, 167.2580 N and 201.8956 N, respectively; assuming a linear spring model with a spring constant of 38.15 N/cm, the extensions of these members are, using Hooke’s law, 4.8970 cm, 4.3842 cm and 5.2922 cm, respectively, and thus, the required original lengths of the vertical springs are 36.9993 cm, 33.1253 cm and 39.985 cm, respectively. Likewise, if the tensegrity structure of

Figure 5.12 (a) is to be transformed to the valid tensegrity prism of Figure 5.12 (c), the original lengths of the three vertical springs must have the values of 29.6309 cm, 25.5764 cm and 32.9691 cm. Thus, the problem of structural transformation of the tensegrity prism may be looked at as the problem of varying the initial length of the tensile structural members by active means rather than passive.

Therefore, to have better shape control of the structural assembly as well as to increase the range of r_t for which valid tensegrity structures can be obtained using the initial 3-bar tensegrity prism, it is pertinent to employ a multistable design approach by incorporating active tensile structural members to function as *active cables* into the structural assembly. Fulfilling this need will mean that, the control variable for achieving shape change that gives valid tensegrity structure will not be limited to circumradius of the top polygon alone (that is, the equality constraint of $l_{10} = l_{11} = l_{12}$ on the three bars). As such, a new approach towards the design of active cables for realizing a multistable tensegrity prism is proposed in the next section.

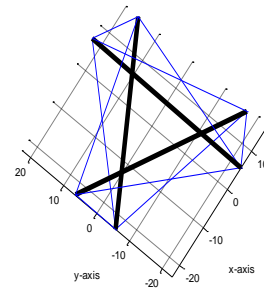
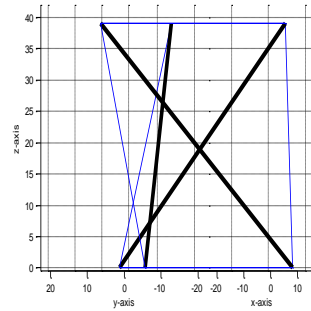
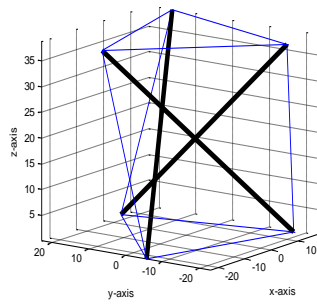
5.3.3 Design of Active Cables

In the preceding section, it was shown that varying the original lengths of the three vertical springs of the initial 3-bar tensegrity prism can be used as a means of better shape control of this tensegrity structure. By combining the control of the original lengths of these vertical springs with the control of the bar lengths, a cable-and-bar length controlled tensegrity structure is realized. In general, this control scheme combines the advantages of cable length and bar length controlled tensegrity structural systems together. On the one hand, optimal actuator and sensor placement techniques can be employed to determine, in an optimal sense, the best bar and cable candidates – to be actuated and/or to serve as sensors – for control. This expands the search domain since optimal actuator and sensor locations are no longer restricted to bar locations alone or cable locations alone. On the other hand, when cable and bar lengths can be controlled simultaneously, the magnitudes of the possible structural displacements which are necessary for significant shape change increase.

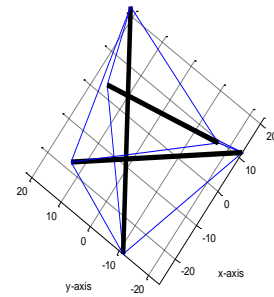
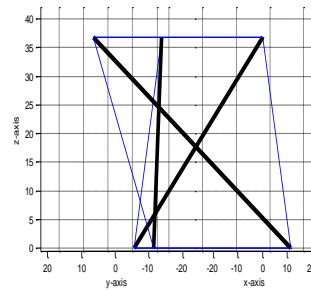
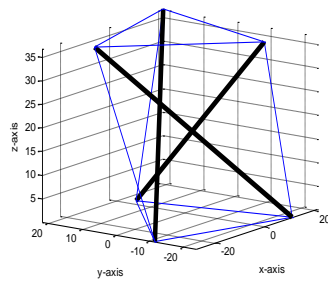
Perspective view

Side view

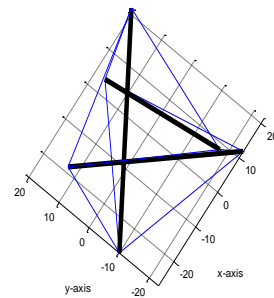
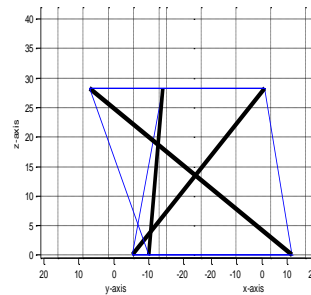
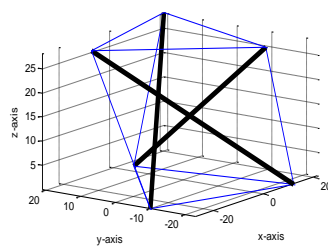
Top view



(a) $l_7 = l_8 = l_9 = 40.8750, l_{10} = l_{11} = l_{12} = 60.0$



(b) $l_7 = 41.8963, l_8 = 37.5095, l_9 = 45.2774, l_{10} = 50.0, l_{11} = 60.0, l_{12} = 70.0$



(c) $l_7 = 33.5526, l_8 = 28.9621, l_9 = 37.3326, l_{10} = 45.0, l_{11} = 55.0, l_{12} = 64.0$

Figure 5.12: Examples of three regular 3-bar minimal tensegrity prisms (with $r_t = r_b$, $l_1 = l_2 = l_3 = l_4 = l_5 = l_6 = 40.8750$ cm, $q_1 = q_2 = q_3 = q_4 = q_5 = q_6 = 2.5745$ N/cm, $q_7 = q_8 = q_9 = 4.4591$ N/cm, and $q_{10} = q_{11} = q_{12} = -4.4591$ N/cm in the three structures)

From a practical point of view, it is not convenient to design and install a new spring with a new original length each time a tensegrity structure is required to perform a structural transformation. Thus, a possible alternative scheme for accomplishing the task of getting the correct lengths and forces in the tensile structural members can be to introduce, in the form of very small actuators, electromechanical or active material-based components (such as shape memory alloys or piezoelectric devices). These components can easily be embedded into the tensegrity system as shown in Figure 5.13 to provide an additional increase or a decrease in length to the tensile structural members as may be required with minimum additional weight and space requirements as possible. The electromechanical or active material-based actuator can be positioned at the middle or at the end of a tensile component (which, of course, must be in tension at all times) as shown in Figure 5.14 (a) and (b), respectively. From the example of the previous section related to the transformation of Figure 5.12 (a) to Figure 5.12 (b) where, assuming a spring constant of $k = 38.15 \text{ Ncm}^{-1}$, the required lengths of the vertical springs of Figure 5.12 (b) are 41.9863 cm, 37.5095 cm and 45.2774 cm and the corresponding forces are 186.8189 N, 167.2580 N and 201.8956 N, respectively, the stroke length that an electromechanical actuator that forms part of the vertical tensile structural member of Figure 5.14 (b), for example, will be required to provide can be computed using the following equations:

$$l_e = L - (l_{ao} + l_o + F/k) \quad (5.11)$$

where L , F , l_{ao} and l_o are the length of the tensile structural member, the force in the tensile structural member, the retracted length of the electromechanical actuator inline with the tensile structural member and the original length of the spring of the tensile structural member, respectively. The spring constant k for each of the springs is 38.15 N/cm. Let l_{ao} and l_o of each of the vertical tensile structural member be 21.558 cm and 11.00 cm, respectively; thus, using Equation (5.10), the extended length l_e for the electromechanical actuators for Figure 5.12 (a – c) are as given in Table 5.3.

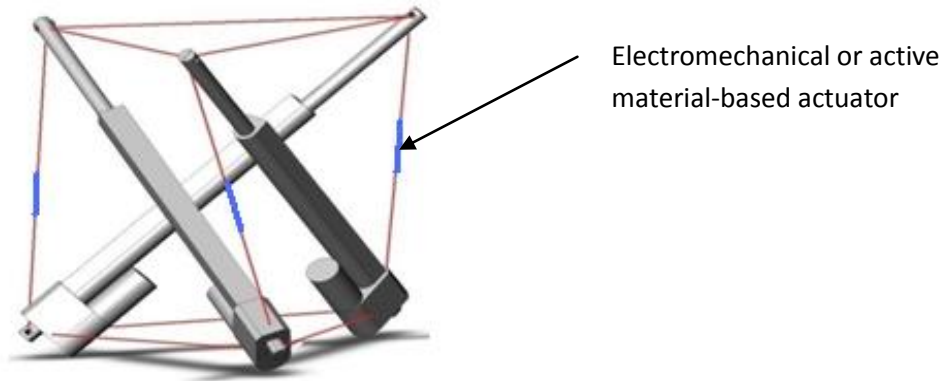


Figure 5.13: The 3-bar tensegrity prism with electromechanical or active material based actuator embedded in-line with the tensile structural members

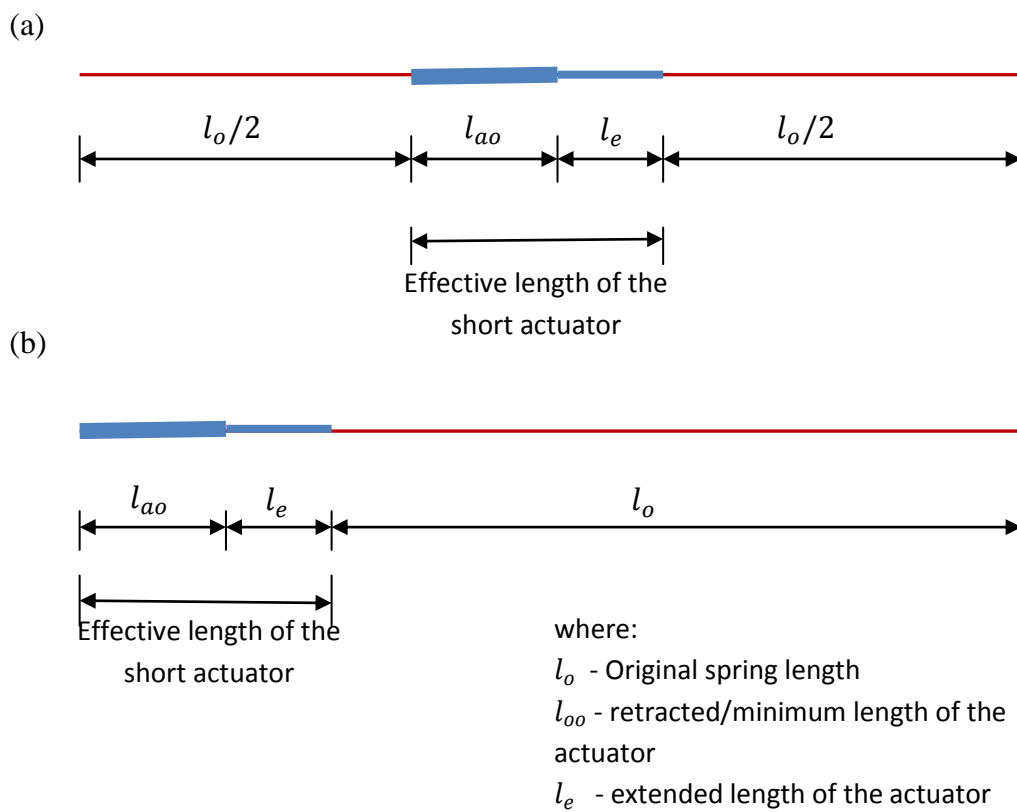


Figure 5.14: (a) and (b) are tensile structural members with electromechanical actuator positioned in-line at the middle and at the end of cable, respectively

Table 5.3: The extended length l_e for the electromechanical actuators of Figure 5.12 (a-c)

Structural Member	Structures of Figure 5.12		
	(a) l_e (cm)	(b) l_e (cm)	(c) l_e (cm)
7	3.5394	4.4413	-2.9272
8	3.5394	0.5673	-6.9811
9	3.5394	7.4272	0.4111

Thus, it can be seen that the transformation from Figure 5.12 (a) to Figure 5.12 (b) requires that the extended length l_e of the electromechanical actuator of structural member 7 changes from 3.5394 cm to 4.4413 cm, that of structural member 8 changes from 3.5394 cm to 0.5673 cm and that of structural member 9 changes from 3.5394 cm to 7.4272 cm. Likewise, the transformation from Figure 5.12 (a) to Figure 5.12 (c) requires that l_e of the electromechanical actuator of structural member 7 changes from 3.5394 cm to -2.9272, that of structural member 8 changes from 3.5394 cm to -6.9811 cm and that of structural member 9 changes from 3.5394 cm to 0.4111 cm. In this latter case, the negative signs show that the effective length of two of the vertical tensile structural members (structural members 7 and 8) should be smaller than the retracted length of the electromechanical actuators. As it is physically not possible for the electromechanical actuators to retract below l_{ao} and, moreover, there is a limit on the maximum extended length l_e that can be achieved with the in-line actuators, and the springs of the tensile members have constant original length l_o ; it is important to include all these length constraints into the form-finding algorithm and this leads to the following considerations:

1. The three bottom nodes of the structural assembly are to be rigidly fixed to a base as explained in Section 5.3.2; this corresponds to the following constraint on the structural members 1, 2, and 3 in the form-finding algorithm:

$$l_i = 40.875 \quad \text{for } i = 1, 2, 3 \quad (5.12)$$

2. The three linear actuators that form the bars of the structural assembly have limited stroke lengths (retracted length of actuator = 44.958 cm, stroke length of actuator = 30.48 cm). Moreover, for an applied set-point voltage of 0 – 5 V corresponding to 0 – 30.48 cm of the extended (stroke) length of the linear actuator, the LD series linear actuator was experimentally found to respond linearly if its extended length is kept approximately within 2 cm and 26 cm. Thus, the lengths of the linear actuators are

restricted to a minimum value of $[44.958 + 2]$ cm and a maximum value of $[44.958 + 26]$ cm; this leads to the following constraints on the structural members 10, 11 and 12 in the form-finding algorithm:

$$46.958 < l_i < 70.958 \quad \text{for } i = 10, 11, 12 \quad (5.13)$$

3. The length of the vertical tensile structural member must be greater than $l_{ao} + l_o$ since tensile structural member must be in tension at all times. It is assumed that the in-line electromechanical actuator has a retracted length of $l_{ao} = 21.558$ cm, a stroke length of 5 cm and a linear response with an input voltage of 0 - 5 V (corresponding to 0 - 5 cm of the extended length) if the set-point of the stroke length is kept within 0.333 - 4.333 cm. Also, the original length of the in-line spring that forms part of the vertical tensile structural member l_o is 11.00 cm. Thus, the length of the tensile structural member must not be below $[l_{ao} + l_o + 0.333]$ cm and must not exceed $[l_{ao} + l_o + 4.333 + \text{'maximum allowable spring extension'}]$ cm. Suppose the maximum allowable force on the vertical tensile structural member is 220 N, the maximum allowable spring extension is $(220 \div 38.15) 5.7667$ cm. These leads to the following constraints on the tensile structural members 7, 8 and 9 in the form-finding algorithm:

$$32.891 < l_i < 42.6502 \quad \text{for } i = 7, 8, 9 \quad (5.14)$$

The constraints (5.12 - 5.14) presented here correspond to the constraints (5.6 - 5.8) included in the constrained optimization form-finding algorithm in Section 5.3.1. Also, as explained in Section 5.3.1, the length constraints impose restrictions on the value of forces in the vertical structural member. If the minimum and maximum forces allowed in the vertical structural members are 142.69 N and 220 N, respectively, the upper and lower bound on the associated tension coefficients are as follows:

$$\text{Lower bound } lb_i = \min \left\{ \frac{142.69}{32.891}, \frac{142.69}{42.65} \right\} = 2.91 \text{ N/cm} \quad (5.15)$$

$$\text{Upper bound } ub_i = \max \left\{ \frac{220}{32.891}, \frac{220}{42.65} \right\} = 6.6888 \text{ N/cm} \quad (5.16)$$

Equations (5.15) and (5.16) lead to the following constraints on the tension coefficients on the vertical tensile structural members:

$$2.91 \leq q_i \leq 6.6888 \quad \text{for } i = 7, 8, 9 \quad (5.17)$$

Thus, the constraints of (5.4) and (5.17) may simply be written as given (5.17) since the satisfaction of (5.17) implies that (5.4) is already satisfied but the opposite is

not true (that is, $\min\{6.828, 6.6888\} = 6.6888$); thus, the appropriate constraint on the tension coefficient, as given in (5.17), has been previously expressed in (5.5).

In relation to the design of a multistable tensegrity prism, the fabrication or design of the in-line electromechanical or piezoelectric actuators is beyond the scope of this project. However, to demonstrate the feasibility and usage of the design and practical realization issues presented thus far, a small version of the linear actuators employed for the bars, shown in Table 5.4 with its technical details, will be used to serve as the electromechanical actuators that form part of the vertical tensile structural members. Indeed, the retracted length of this short actuator is 19.558 cm. If the end connector of 2 cm in length is taken into account, the effective retracted length l_{ao} equals 21.558 cm. Furthermore, Figure 5.15 shows the picture of the short springs fabricated to form part of the vertical tensile structural member. The spring is made of carbon steel (shear modulus $G = 79300 \text{ N/mm}^2$) and has mean spring diameter $D = 19.63 \text{ mm}$, wire diameter $d = 2.95 \text{ mm}$ and number of active coils $n = 26$. Thus, the spring constant of the short spring is 38.17 N/cm which is approximately equivalent to that of the long springs that made up the top-horizontal cables of the tensegrity prism.

Table 5.4: A picture and technical details of the 2” stroke linear actuator with feedback (LD series actuator) manufactured by Concentric International [173]

Picture	Feature	Specification
	Original length: Stroke length: Weight: Gear Ratio: Free-run current measured at 12 V: Stall current measured at 12 V: Linear Speed measured at 12 V: Dynamic Linear force measure at 12 V: Static Linear Force:	19.558 cm ($\pm 0.3048 \text{ cm}$) 4.826 cm 1.1623 Kg 20:1 0.5 A 10 A 1.3 cm/sec 50 Kilogram-force 227 Kilogram-force



Figure 5.15: Picture of the short spring fabricated to form part of the vertical tensile structural member

5.4 Collision avoidance, detection and related issues

For a tensegrity structure that is capable of significant shape change, or the deployed tensegrity structure, it is possible for structural members to come into contact – during the deployment process – with either other structural members of the same structure or with the components of the environment that the structure is operating in; these two forms of collisions are termed internal (or self) and external collision, respectively [175], [176]. Depending on the intended application, either, both or none of these forms of collision may be desirable. The strategies for avoiding contact (collision avoidance) or discovering contact (collision detection) between structural members of tensegrity structures or between the tensegrity structure and its operating environment have only been recently investigated in the literature.

Generally, there are two methods in which collision avoidance and detection strategies may be implemented. In the first method (see, for example, [177]), additional constraints are included in the form-finding optimization algorithm. These constraints specify the minimum distance allowed among the bars of the structural assembly as well as the minimum distance allowed among the nodes to avoid internal collision. If an external collision avoidance scheme is also included in this method, the minimum distance allowed between the structural assembly and the external object is also included as a constraint in the algorithm. Moreover, to serve as collision detectors or indicators, the distances among the various constituents of the structural assembly (bars, nodes, etc) or the external object are compared with predefined values of distances which, for bars and nodes, correspond to the minimum distances between the bars and nodes of a tensegrity structure. This collision avoidance method of including constraints in the form-finding algorithm may better be described as a collision prevention strategy since the form-finding algorithm can only give solutions in which collisions are not present at all in the first place. As such, the method offers no strategy for dealing with collision if it is to occur during the shape changing, or transition, phase. Nonetheless, the method can be used as a first step for developing path-planning algorithm for tensegrity-based deployable structures [177].

The second method of collision avoidance operates during the structural transition phase (see, for example, [178]). It involves including the constraints outline in the first method in the optimisation model used for computing the control law for the actuated structural members. The objective function of the optimization problem is not a form-

finding problem but, depending on what is desirable during the shape transition process, could be related to the control effort, element forces, vibration suppression, and so on. Model Predictive Control (MPC) technique – famous for its ability to handle system’s input and output constraints – has been used in [175] for computing the future behaviour of the tensegrity structural system and to choose the control input(s) at each instant of time such that collisions are avoided up until the prediction horizon. To use MPC techniques for this collision avoidance scheme effectively, however, will require that a back-up control law be provided for cases where there are no feasible control input. Also, as the number of structural elements increase, it becomes harder to solve the control optimization problem since the number of constraints increase quadratically with an increase in the number of structural elements [175]. In addition, just as in the first method, the second method has only so far been proved to be useful if the tensegrity configuration does not change during the structural transition process. It is important to emphasize that none of the methods presented in the literature so far offers a general approach to solving the collision avoidance problem and, as yet, they have only been demonstrated to work with small scale structural systems with very simple node connectivity. Beside, none of the methods proposed is capable of dealing with structural transition process involving structural reconfiguration.

In the remainder of this section, discussions on how the characteristics of a tensegrity prism can be explored for the purpose of including collision avoidance and detection strategies (that is, the first method as introduced earlier in this section) in the form-finding optimization algorithm will be covered. Since the nodes of practically realizable tensegrity structure are made of joints that are likely to have a fixed range of angular motions, the discussion will also be extended to the process of including these joint constraints into the form-finding algorithm.

Consider the two structural members shown in Figure 5.16. Since each structural member is made up of two nodes, the parametric equation of the line describing each of the members is the coordinate of a node and a vector in the direction of the second node; this may be written as follows:

$$\text{Member A:} \quad A(e) = A1 + e(A2 - A1) \quad 0 \leq e \leq 1 \quad (5.18)$$

$$\text{Member B:} \quad B(f) = B1 + f(B2 - B1) \quad 0 \leq f \leq 1 \quad (5.19)$$

where $A1$ and $A2$ are the coordinates of the nodes of member A such that $A(0) = A1$ and $A(1) = A2$; $B1$ and $B2$ are the coordinates of the nodes of member B such that $B(0) = B1$ and $B(1) = B2$; thus, e and f are real numbers. The optimization problem to find minimum distance between member A and B may be written as follows:

$$\min_{\substack{0 \leq e \leq 1 \\ 0 \leq f \leq 1}} g$$

where the vector between points on the two lines can be expressed as $g(e, f) = A(e) - B(f)$. At minimum distance, $g_m = g(e_m, f_m) = A(e_m) - B(f_m)$. Therefore, the minimum distance d between $A(e)$ and $B(f)$ can be written as follows:

$$d = \|g_m\| \quad (5.20)$$

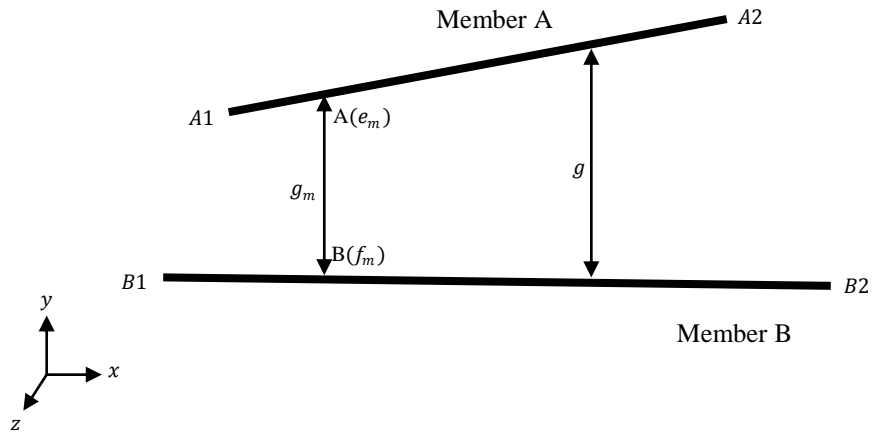


Figure 5.16: Two structural members with each member made up of two nodes

Let $A2 - A1 = \bar{A}$, $B2 - B1 = \bar{B}$ and $A1 - B1 = \bar{C}$. Also, $\bar{A} \cdot \bar{A} = a$, $\bar{B} \cdot \bar{B} = b$, $\bar{C} \cdot \bar{C} = c$, $\bar{A} \cdot \bar{C} = h$ and $\bar{B} \cdot \bar{C} = j$, where ‘ \cdot ’ denotes the scalar (dot) product operator, the analytical solution to the above optimization problem can be found as follows:

Of all vectors g for which $0 \leq e \leq 1$ and $0 \leq f \leq 1$, the vector g_m is the only vector perpendicular to both $A(e)$ and $B(f)$ [179]. This implies that $g_m \cdot \bar{A} = 0$ and $g_m \cdot \bar{B} = 0$. Thus, at minimum distance, the following equations are satisfied:

$$g_m = A(e_m) - B(f_m) = \bar{C} + e_m \bar{A} - f_m \bar{B} \quad (5.21)$$

$$g_m \cdot \bar{A} = [\bar{C} + e_m \bar{A} - f_m \bar{B}] \cdot \bar{A} = 0 \quad (5.22)$$

$$g_m \cdot \bar{B} = [\bar{C} + e_m \bar{A} - f_m \bar{B}] \cdot \bar{B} = 0 \quad (5.23)$$

Re-arranging (5.22) and (5.23), and solving the resulting two simultaneous linear equations for the two unknowns, e_m and f_m , the following equations are obtained:

$$e_m = \frac{jc-bh}{ba-c^2} \quad , \quad f_m = \frac{ja-ch}{ba-c^2} \quad (5.24)$$

Substituting $\bar{C} = A1 - B1$ and equation (5.24) into equation (5.21) gives the following equation:

$$g_m = (A1 - B1) + \frac{(jc-bh)\bar{A} - (ja-ch)\bar{B}}{ba-c^2} \quad (5.25)$$

where $ba - c^2 \geq 0$. The case of $ba - c^2 = 0$ indicates that the two lines $A(e)$ and $B(f)$ are parallel; in this case, if $f_m = 0$, equations (5.24) and (5.25) can respectively be written as follows:

$$e_m = -\frac{h}{a} = -\frac{j}{c} \quad (5.26)$$

$$g_m = (A1 - B1) + e_m\bar{A} = (A1 - B1) - \frac{h}{a}\bar{A} \quad (5.27)$$

In general, g_m can be computed as follows:

$$g_m = \begin{cases} (A1 - B1) + \frac{(jc-bh)\bar{A} - (ja-ch)\bar{B}}{ba-c^2} & , \quad \text{if } ba - c^2 > 0 \\ (A1 - B1) - \frac{h}{a}\bar{A} & , \quad \text{if } ba - c^2 = 0 \end{cases} \quad (5.28)$$

Thus, the shortest distance d between the two lines $A(e)$ and $B(f)$ can be computed by substituting (5.28) into (5.20). For the initial 3-bar tensegrity prism under consideration, the shortest distances between Bar 1 and Bar 2, Bar 1 and Bar 3, and Bar 2 and Bar 3, are shown in Figure 5.17 as L, M and N, respectively. The coordinates of the corresponding points on Bar 1, 2 and 3 are as follows:

- Shortest distance between Bar 1 ($A(e)_{Bar\ 1}$) and Bar 2 ($B(f)_{Bar\ 2}$) = length of L:

$$e_m = 0.5591 \quad , \quad f_m = 0.4409$$

$$A(e_m)_{Bar\ 1} = [6.3113, -2.5604, 1.6044] \quad , \quad B(f_m)_{Bar\ 2} = [-0.4337, -6.4026, -3.2091]$$

$$\text{Length of L, } d_L = \|g_m\|_{Bar\ 1-Bar\ 2} = \|A(e_m)_{Bar\ 1} - B(f_m)_{Bar\ 2}\| = 9.1339 \text{ cm}$$

- Shortest distance between Bar 1 ($A(e)_{Bar\ 1}$) and Bar 3 ($B(f)_{Bar\ 3}$) = length of M:

$$e_m = 0.4409 \quad , \quad f_m = 0.5591$$

$$A(e_m)_{Bar\ 1} = [5.8812, 3.2512, -2.4318] \quad , \quad B(f_m)_{Bar\ 3} = [-1.0066, 6.3209, 2.7220]$$

$$\text{Length of M, } d_M = \|g_m\|_{Bar\ 1-Bar\ 3} = \|A(e_m)_{Bar\ 1} - B(f_m)_{Bar\ 3}\| = 9.1339 \text{ cm}$$

- Shortest distance between Bar 2 ($A(e)_{Bar\ 2}$) and Bar 3 ($B(f)_{Bar\ 3}$) = length of N:
 $e_m = 0.5591$, $f_m = 0.4409$
 $A(e_m)_{Bar\ 2} = [-5.0937, -4.4521, 1.7639]$, $B(f_m)_{Bar\ 3} = [-5.6582, 3.8427, -2.0185]$
 Length of N, $d_N = \|g_m\|_{Bar\ 2-Bar\ 3} = \|A(e_m)_{Bar\ 2} - B(f_m)_{Bar\ 3}\| = 9.1339$ cm

Thus, the shortest distance d between any two bars of the initial 3-bar tensegrity prism is 9.1339 cm. If the j^{th} bar is now considered a circular cylinder of radius r_j , then the extra constraints to be added to the form-finding algorithm to prevent collision of the bars can be written as follows:

$$r_j < d \text{ for } j = 1, 2, 3. \quad (5.29)$$

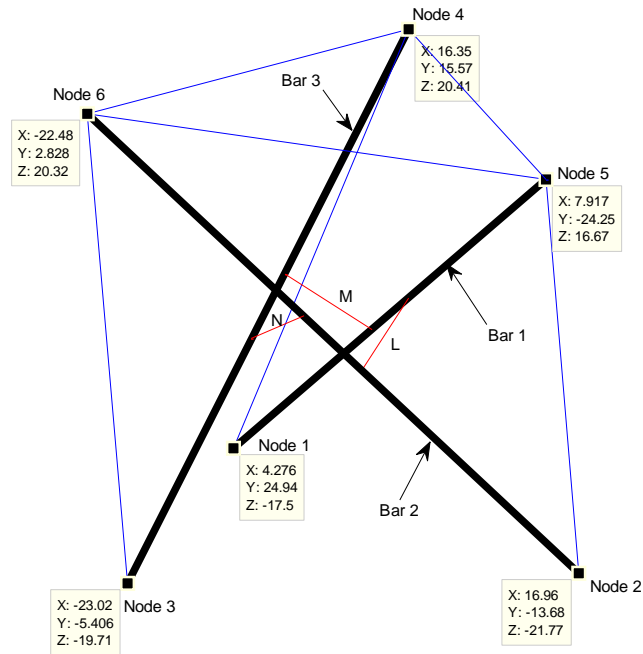


Figure 5.17: An illustration of the shortest distance between any two bars of the initial 3-bar tensegrity prism

The radius of the small and large cylindrical bars that made up the telescopic linear actuator shown in Figure 5.4 are approximately 0.991 cm and 2.389 cm, respectively; while r_j is taken as the largest of these two values as a conservative measure, d is obtained from (5.20) and computed using (5.21 – 5.28). When the

collision avoidance constraint (5.29) is included in the form-finding algorithm for obtaining the initial 3-bar tensegrity prism or its multistable counterpart, it is found that the constraint is always inactive for any point in the feasible region. This is because the 12-member structural system has a few DOF (9 DOFs – having constrained the other 9 DOFs of the possible total 18 DOFs of the initial 3-bar tensegrity prism). Therefore, the constraint (5.29) can be dropped since the form-finding algorithm ignores the inactive constraints anyway. Nonetheless, this approach which consists of including a collision avoidance strategy can be useful and employed for larger structures with larger number of flexible DOFs. Moreover, the constraint (5.29) can be employed for collision detection. Given an optimal solution from the form-finding algorithm, the collision detection algorithm can have the following structure, for instance:

Given an optimal solution from a form-finding algorithm, check if $r_j < d$ is satisfied for $j = 1, 2, 3$:

- *If the constraint $r_j < d$ is inactive (that is, $r_j < d$), there is no collision*
- *If the constraint $r_j < d$ is active (that is, $r_j = d$), there is a collision*
- *If the constraint $r_j < d$ is violated (that is, $r_j > d$), the shape change is infeasible as it requires the physical structural members to cross into each other.*

Furthermore, it should be noted that the collision avoidance constraint in (5.29) is an internal collision avoidance strategy that involves only the distances between the bars. The consideration of the bars only is justified in that internal collisions with the cables is not possible for this structural configuration except if the constraint $r_j < d$ is violated since cables are at the outside of the structure. More so, it should be noticed that internal collision avoidance between the nodes is inherent in the form-finding algorithm itself (by definition of the tensegrity configuration and the constraint requirement that none of the structural members can have zero length). If it were not, it would mean that one or more cables have been eliminated from the tensegrity structure since cables, which are of none zero lengths, must be in tension at all times.

Also, for the initial 3-bar tensegrity prism shown in Figure 5.17, it may be desirable to know the angles that each of the vertical structural members makes with the bottom horizontal plane (that is, the plane containing nodes 1,2 3). As will be shown next, these angles can be used to include joint (angular) constraints in the form-finding algorithm to take into account the limited range of angular motion that the nodal joints are capable of. In addition, they can also be used for optimal joint trajectory planning

and, also, for including joint constraint for computing the control law for structures that are controlled during the transition phases. From geometry, a plane can be described completely by a normal vector n perpendicular to the plane and any point p on the plane. For the structural member of Figure 5.18, let the coordinates of the three bottom nodes be P_1 , P_2 and P_3 , the normal vector can be computed as follows:

$$n = (P_2 - P_1) \times (P_3 - P_1) \quad (5.30)$$

where ‘ \times ’ denotes the cross (vector) product operator. The point p may be chosen as P_1 , P_2 or P_3 . Any structural member i with nodes b_1 and b_2 can be uniquely described by the Euclidean vector \bar{b}_i as follows:

$$\bar{b}_i = b_2 - b_1 \quad (5.31)$$

where the magnitude of \bar{b}_i , $\|\bar{b}_i\|$, gives the length of that structural member. If ξ denotes the angle between vectors n and \bar{b}_i , the value of ξ can be computed as follows:

$$\xi = \cos^{-1} \left[\frac{n \cdot \bar{b}_i}{|n| |\bar{b}_i|} \right] \quad (5.32)$$

The angle between the i^{th} structural member and the plane, denoted θ , is therefore given as follows:

$$\theta(\text{rad}) = \pi/2 - \xi \quad (5.33)$$

Using equation (5.33) for the initial 3-bar tensegrity prism, the angles between each of the bars and the plane and each of the vertical cables and the plane are 40.5503° and 72.6110° , respectively. Therefore, if each of the three bottom joints of the linear actuators (the bars) is a two-axis joint that allows each actuator to travel $0^\circ - 360^\circ$ (unrestricted) about the vertical axis as shown in Figure 5.18 and each actuator to make the angle θ with the bottom horizontal plane such that $\theta_l^\circ < \theta(\text{deg}) < \theta_r^\circ$, then the constraint to be included in the form-finding algorithm is written as follows:

$$\theta_l^\circ < \theta < \theta_r^\circ \quad (5.34)$$

where θ is computed using (5.33) and converted to degrees.

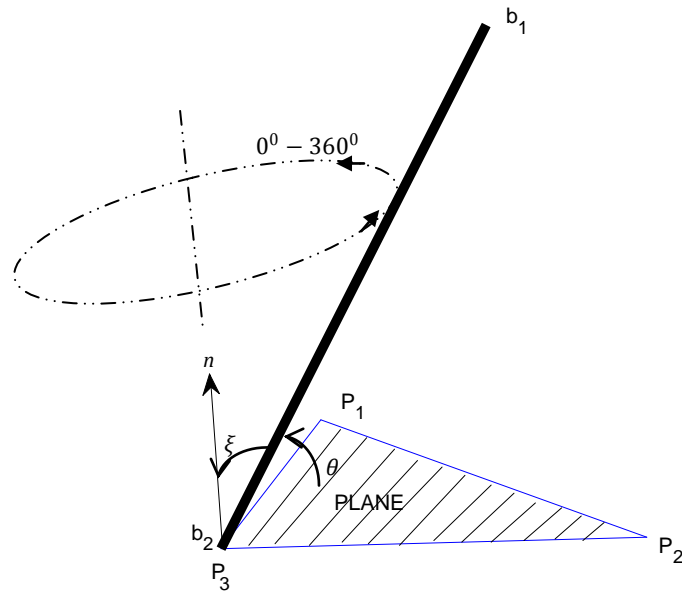


Figure 5.18: An illustration of a structural member that makes an angle of θ with the plane containing nodal points P_1 , P_2 and P_3 .

5.5 Motion of Tensegrity Structures

If tensegrity structures must be used in applications requiring large displacements, the development of computationally efficient techniques for performing useful movements is necessary. The complexities of computation arise as a result of many factors including the additional devices (such electromechanical or piezoelectric actuators) that may have been introduced to provide adjustable stiffness (for shape changing, vibration suppression and robustness to external loads and disturbances) as well as the requirement to avoid internal structural collisions and to have a desired final structural shape that is still a valid tensegrity structure, for example.

In this section, the process of achieving well-defined movement of tensegrity prisms will be discussed. Although the focus is on the initial 3-bar tensegrity prism, the discussion extends to tensegrity prisms in general. The triangle formed by the three top horizontal cables of the initial 3-bar tensegrity prism and the plane containing these cables will be called the top triangle and the triangular plane, respectively. The motion of the top triangle whose corners (vertices) are the three top nodes of the initial 3-bar

tensegrity prism, in three dimensional Euclidean space, can be characterized by translation in the three axes – x , y and z – and rotation about these three axes as shown in Figure 5.19. The focus will be to understand whether or not translational and rotational movements of the top triangle will give another valid tensegrity structure and, if they do, over what range of translational or rotational variations? If they do not, then is the problem peculiar to this structural configuration or extends to tensegrity structures in general?

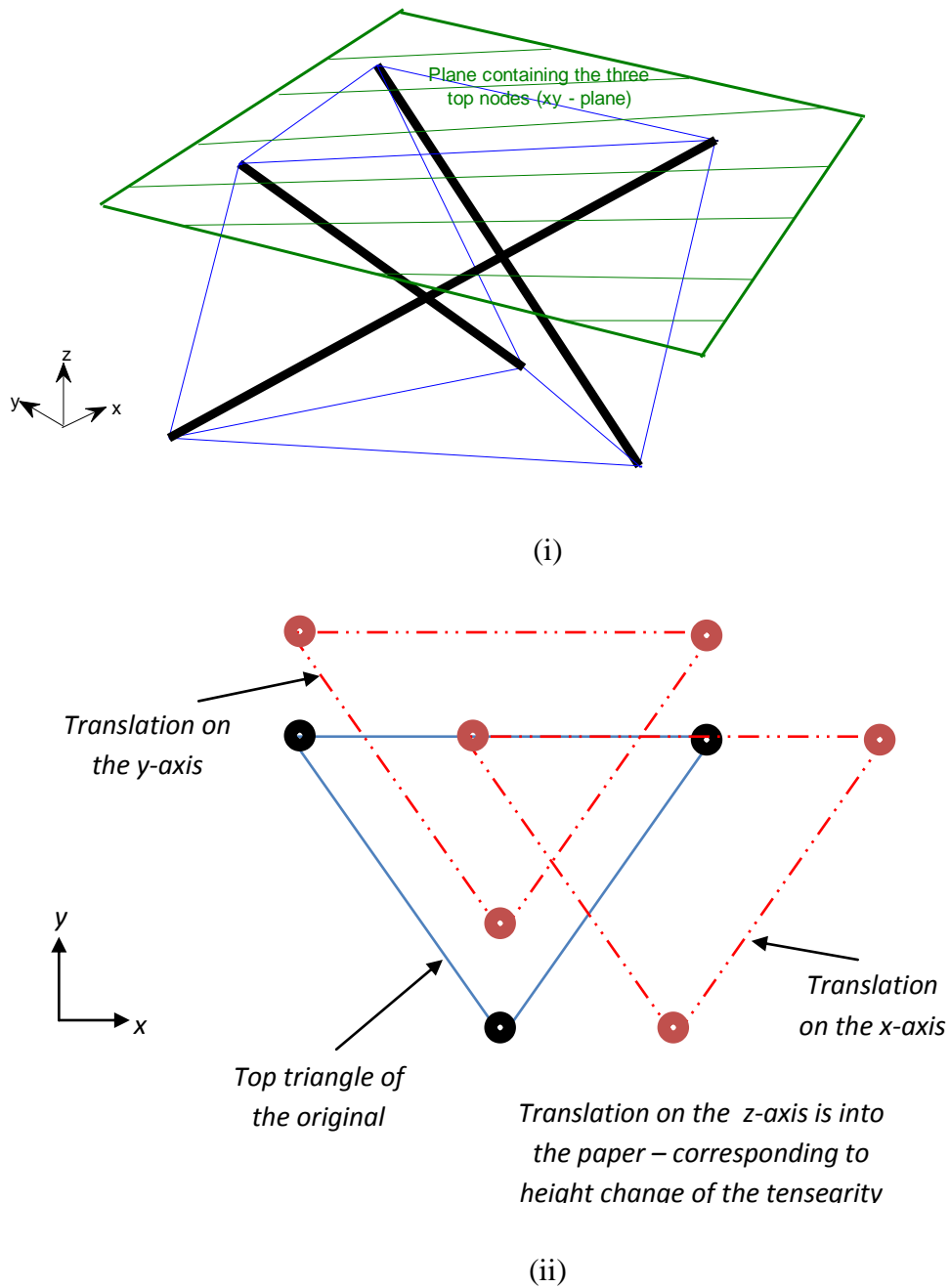


Figure 5.19 (a): (i) and (ii) are the plane containing the three top nodes and the translation of the top triangle in the x - y plane, respectively.

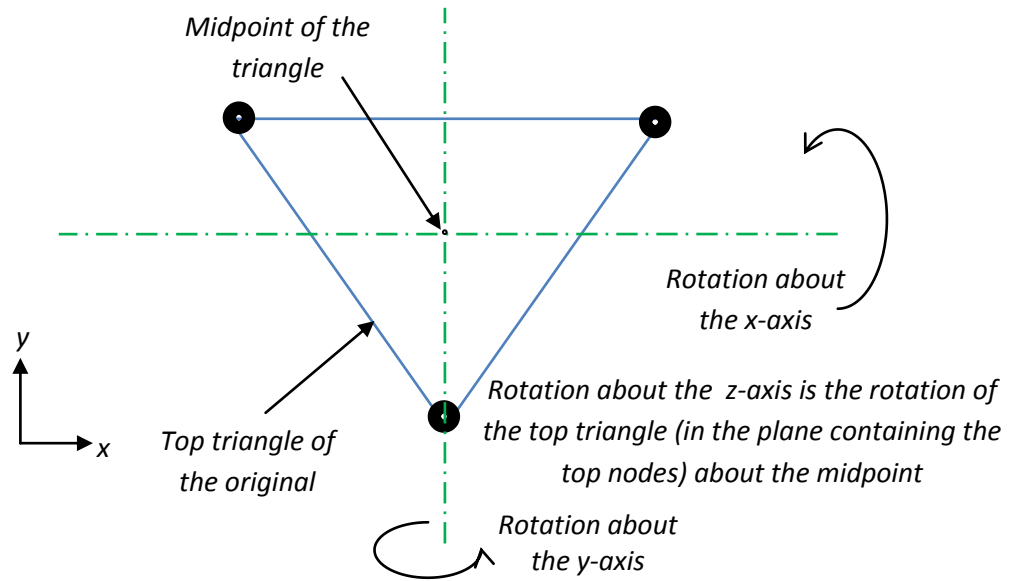


Figure 5.19 (b): Rotation of the top triangle about the x and y axes.

5.5.1 Translation of the Tensegrity Prisms

In this section, the engineering problem is to achieve translation in the direction of the x , y and z axes of the top triangle (whose corners are the three top nodes – nodes 4, 5 and 6) of the initial 3-bar tensegrity prism using the constrained optimization form-finding algorithm presented in Chapter 2. (The nodal coordinates of this structure are already given in Figure 5.17.) This problem is solved by including the following constraints in the form-finding algorithm:

1. The three bottom nodes are rigidly attached to the base; the associated equality constraints being:

$$\begin{aligned}
 \text{Node 1: } & x_1 = 4.2761, \quad y_1 = 24.9402, \quad z_1 = -17.4954 \\
 \text{Node 2: } & x_2 = 16.9575, \quad y_2 = -13.6822, \quad z_2 = -21.7685 \\
 \text{Node 3: } & x_3 = -23.0179, \quad y_3 = -5.4061, \quad z_3 = -19.7103
 \end{aligned} \tag{5.35}$$

2. The translation of the three top nodes ($i = 4, 5, 6$) due to the translation vector $(\Delta x, \Delta y, \Delta z)$ results to the final nodal coordinate vector of the i^{th} node $(x_{f_i}, y_{f_i}, z_{f_i})$; x_{f_i} , y_{f_i} and z_{f_i} are computed as follows:

$$x_{f_i} = x_i + \Delta x, \quad y_{f_i} = y_i + \Delta y, \quad z_{f_i} = z_i + \Delta z \tag{5.36}$$

where, for the initial 3-bar tensegrity prism, the nodal coordinates of the top nodes are as follows:

$$\begin{aligned}
\text{Node 4: } x_4 &= 16.3531, \quad y_4 = 15.5697, \quad z_4 = 20.4138 \\
\text{Node 5: } x_5 &= 7.9165, \quad y_5 = -24.2494, \quad z_5 = 16.6680 \\
\text{Node 6: } x_6 &= -22.4850, \quad y_6 = 2.8275, \quad z_6 = 20.3234
\end{aligned} \tag{5.37}$$

3. If it is required that the area of top triangle (which is an equilateral triangle) remain the same after translation, this requirement can be expressed as the following equality constraint:

$$A_{top_f} = A_{top} \tag{5.38}$$

where $A_{top} = 723.4627 \text{cm}^2$ and A_{top_f} denote the area of the triangle before and after translation; A_{top} is computed using the well-known Heron's formula for computing the area of a triangle which is expressed as follows:

$$Area = \sqrt{s(s - l_4)(s - l_5)(s - l_6)} \tag{5.39}$$

where l_i is the length of the i^{th} structural member and $s = \frac{1}{2}(l_4 + l_5 + l_6)$. It should be noted that the equality constraint (5.38) may not be necessary to obtain a valid tensegrity prism after the rotation, but, without it, the results of the form-finding may not necessarily satisfy the constraint of (5.38). Also, it should be observed that this constraint also constrains the lengths of the three top cables.

4. The three linear actuators that form the bars of the structural assembly have limited stroke lengths and ranges in which the input-output relationship is linear ($2 \text{ cm} \leq l_e \leq 26 \text{ cm}$); as discussed in relation to the constraint of Equation (5.13), this limitation corresponds to the inequality constraint as follows:

$$46.958 < l_i < 70.958 \quad \text{for } i = 10, 11, 12 \tag{5.40}$$

5. Constraints due to additional devices (in the current case, in the form of short (in-line) electromechanical actuators) to provide adjustable stiffness to the vertical cables and in view of the linear range in which these devices work ($0.333 \text{ cm} \leq l_e \leq 4.333 \text{ cm}$), as expressed in relation to the constraint given in (5.14), are as follows:

$$32.891 < l_i < 42.6502 \quad \text{for } i = 7, 8, 9 \tag{5.41}$$

6. The nodal constraints (which also imply length constraints) in (5.35), as mentioned in relation to the constraint given in (5.17), also imposes the following constraints on the tension coefficients of the structure:

$$2.91 \leq \mathbb{Q}_i \leq 6.6888 \quad \text{for } i = 7, 8, 9 \quad (5.42)$$

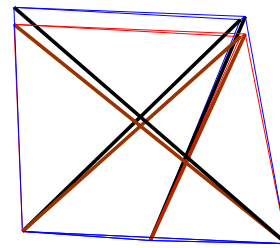
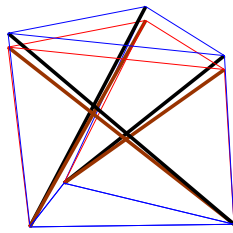
Figure 5.20 shows the translations of the initial 3-bar tensegrity prism as a result of the preceding six constraints. The values of $\|\mathbb{A} \cdot \mathbb{Q}\|_2$ of the final structure (after translation) are given in each case. It should be noted that all the final structures in this figure due to the translation vector specified for each structure are valid tensegrity structures and they all satisfy all the conditions of the constraints included in the form-finding algorithm. Also, it is important to observe that if the cables are described by direction vectors, the angles between the cables 1 and 4, cables 2 and 5, and cables 3 and 6 are the same for all these valid tensegrity structures and they are equal to the twist angle ($\alpha = \frac{\pi}{2} - \frac{\pi}{3} = 30^\circ$) of the initial 3-bar tensegrity prism. This confirms that, just as the vector of tension of coefficients is unique for any tensegrity prism (for any tensegrity structure for that matter), the twist angle of any tensegrity prism is also unique and it is independent of translation of the top polygon as long as the final structure is a valid tensegrity structure. In other words, the twist-angle is unique for any given p -bar tensegrity prism – regular or irregular.

It has not been possible to find an expression describing the range over which translations in the direction of the x , y and z axes of the top triangle of the initial 3-bar tensegrity prism will give a valid tensegrity structure. However, the following results (obtained after several simulations) are examples of valid ranges for pure translations in the z -axis direction:

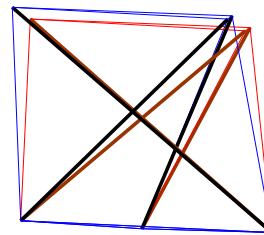
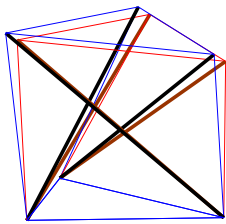
- Translation in the direction of the z -axis with $\Delta x = 0$ and $\Delta y = 0$ results in a valid tensegrity structure for $-4.8\text{cm} < \Delta z < 0$ cm
- Translation in the direction of the z -axis with $\Delta x = 1$ and $\Delta y = 1$ results in a valid tensegrity structure for $-4.8\text{cm} < \Delta z < -0.65$ cm
- Translation in the direction of the z -axis with $\Delta x = 2$ and $\Delta y = 2$ results in a valid tensegrity structure for $-4.0\text{cm} < \Delta z < -1.0$ cm

Perspective view

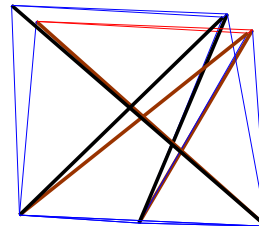
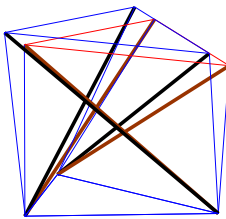
Side view



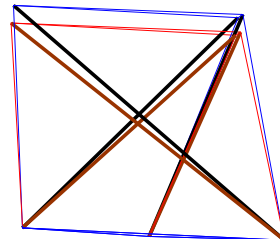
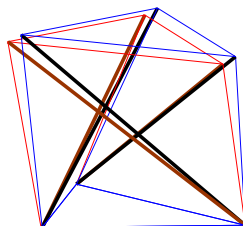
(a) $\Delta x = 0, \Delta y = 0, \Delta z = -3, \|\mathbb{A} \cdot \mathbb{q}\|_2 = 2.4268 \times 10^{-4}$



(b) $\Delta x = 3.2, \Delta y = 1, \Delta z = -2, \|\mathbb{A} \cdot \mathbb{q}\|_2 = 2.6756 \times 10^{-4}$



(c) $\Delta x = 4, \Delta y = -1, \Delta z = -3, \|\mathbb{A} \cdot \mathbb{q}\|_2 = 2.3501 \times 10^{-4}$



(d) $\Delta x = 1, \Delta y = 6, \Delta z = -2.5, \|\mathbb{A} \cdot \mathbb{q}\|_2 = 8.8396 \times 10^{-5}$

Figure 5.20: The translation of the initial 3-bar tensegrity prism (Before translation: cable = blue, bar = black; after translation: cable = red, bar = brown)

5.5.2 Rotation of the Tensegrity Prisms

In the introduction of this chapter, it has been mentioned that the design of a regular tensegrity prism can be approached as a monostable or multistable design. Thus, on the one hand, if the design of the initial 3-bar tensegrity prism is considered to be monostable, it will be impossible to rotate the top triangular to obtain another valid tensegrity prism. On the other hand, if the multistable design approach is adopted, since the vertical cables are now equipped with mechanisms to vary their stiffness, it is possible to rotate the top triangle and obtain a valid tensegrity prisms. All of these different valid tensegrity prisms have a twist angle that is the same as that of the monostable system and it is impossible to rotate the top polygon (triangle, in the current case) of any valid tensegrity prism about the triangle centre and on the plane containing the triangle vertices to find another valid tensegrity structure. Nonetheless, the rotations of the top triangle about the x , y and z axes that can possibility be achieved with the multistable tensegrity structure that has been considered so far in this chapter will be considered in this section to understand the variation of the norm of the residual forces as the rotations are being carried-out.

A general rotation of the top triangle about the x , y and z axes by θ_x , θ_y and θ_z , respectively, with the bottom nodes rigidly fixed, is as follows:

$$\begin{bmatrix} x_{f_4} & y_{f_4} & z_{f_4} \\ x_{f_5} & y_{f_5} & z_{f_4} \\ x_{f_6} & y_{f_6} & z_{f_4} \end{bmatrix} = R \cdot \begin{bmatrix} x_4 & y_4 & z_4 \\ x_5 & y_5 & z_5 \\ x_6 & y_6 & z_6 \end{bmatrix} \quad (5.43)$$

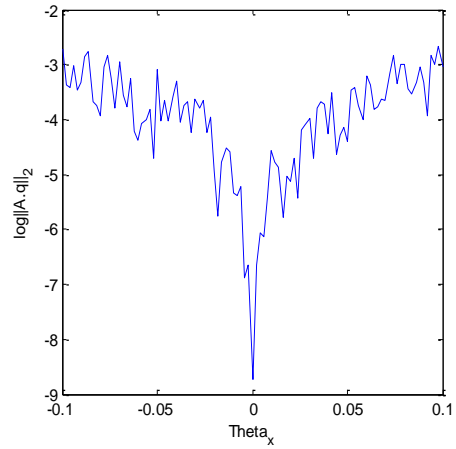
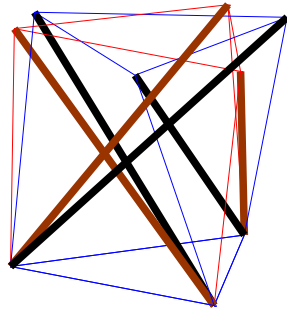
where $R = R_x \cdot R_y \cdot R_z$ and R_x , R_y and R_z are defined as follows:

$$R_x = \begin{bmatrix} 1 & 0 & 0 \\ 0 & \cos \theta_x & \sin \theta_x \\ 0 & -\sin \theta_x & \cos \theta_x \end{bmatrix}, R_y = \begin{bmatrix} \cos \theta_y & 0 & -\sin \theta_y \\ 0 & 1 & 0 \\ \sin \theta_y & 0 & \cos \theta_y \end{bmatrix}, R_z = \begin{bmatrix} \cos \theta_z & \sin \theta_z & 0 \\ -\sin \theta_z & \cos \theta_z & 0 \\ 0 & 0 & 1 \end{bmatrix} \quad (5.44)$$

Also, the vector $(x_{f_i}, y_{f_i}, z_{f_i})$ denotes the nodal coordinates of node i after the rotation from an initial position (x_i, y_i, z_i) . Figure 5.21 shows the rotation of the top triangle of the initial 3-bar tensegrity prism about its z axis ($\theta_x = 0$, $\theta_y = 0$). This figure also shows the variation of the norm of the residual force vector ($\|\mathbb{A} \cdot \mathbb{q}\|_2$) as the structure rotates about the x , y and z axes. Generally, the rotation of the initial 3-bar tensegrity prism is possible in the following cases:

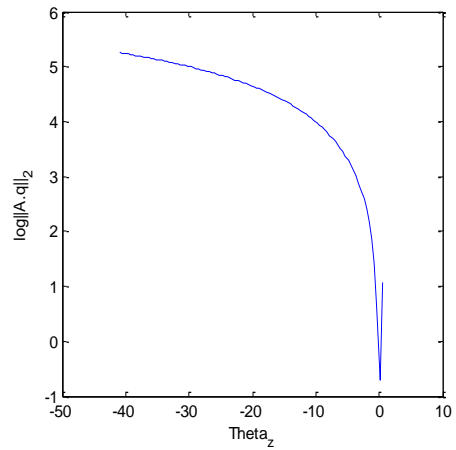
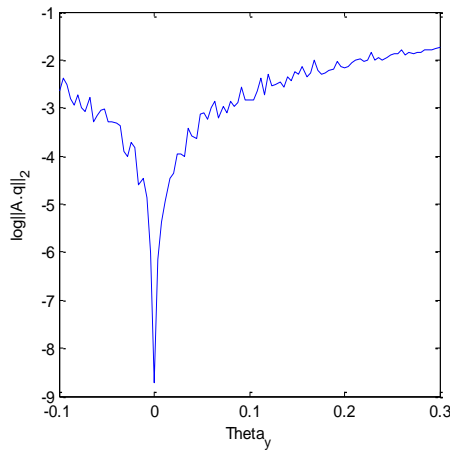
- Rotation about the x -axis ($\theta_y = 0, \theta_z = 0$): $-0.17^\circ < \theta_x < 0.1^\circ$
- Rotation about the y -axis ($\theta_x = 0, \theta_z = 0$): $-0.12^\circ < \theta_y < 0.29^\circ$
- Rotation about the z -axis ($\theta_x = 0, \theta_y = 0$): $-40^\circ < \theta_z < 0^\circ$

More so, Figure 5.22 combines the translation and rotation processes together; it shows the rotation of the top triangle of the tensegrity prisms of Figure 5.20 (b), (c) and (d), and – as stated before – the outcome of rotation is not a tensegrity structure but a tensegrity configuration.



(a) $\theta_x = 0, \theta_y = 0, \theta_z = -40^\circ$

(b) $\theta_y = 0, \theta_z = 0, -0.17^\circ < \theta_x < 0.1^\circ$



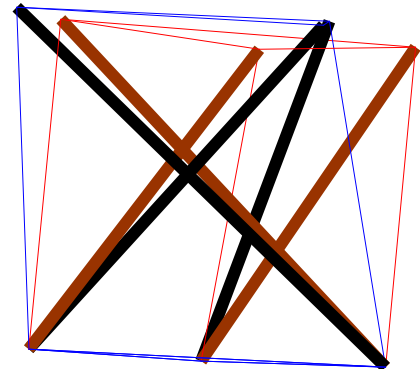
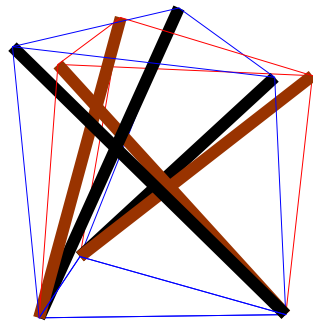
(c) $\theta_x = 0, \theta_z = 0, -0.12^\circ < \theta_y < 0.29^\circ$

(d) $\theta_x = 0, \theta_y = 0, -40^\circ < \theta_z < 0^\circ$

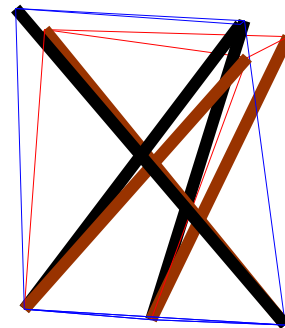
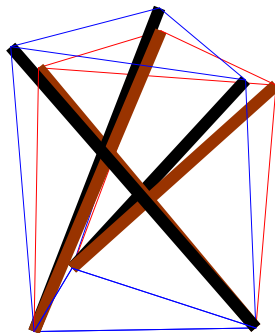
Figure 5.21: (a) Rotation of the top-triangle of the initial 3-bar tensegrity prism about the z -axis; (b), (c) and (d) are the variation of the norm of the nodal residual forces as rotation of the top triangle is carried-out about the x , y and z axes, respectively.

Perspective view

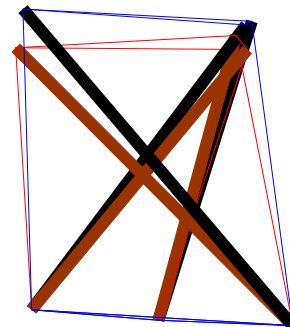
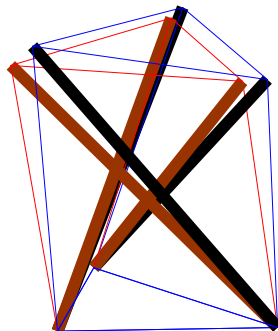
Side view



(a) $\Delta x = 3.2, \Delta y = 1, \Delta z = -2, \theta_x = 0, \theta_y = 0, \theta_z = -25^\circ, \|\mathbf{A} \cdot \mathbf{q}\|_2 = 125.7888$



(b) $\Delta x = 4, \Delta y = -1, \Delta z = -3, \theta_x = 3, \theta_y = 0, \theta_z = -8^\circ, \|\mathbf{A} \cdot \mathbf{q}\|_2 = 43.0677$



(c) $\Delta x = 1, \Delta y = 6, \Delta z = -2.5, \theta_x = 3, \theta_y = 3, \theta_z = 4^\circ, \|\mathbf{A} \cdot \mathbf{q}\|_2 = 24.3739$

Figure 5.22: The translation and rotation of the initial 3-bar tensegrity prism (Before translation: cable = blue, bar = black; after translation: cable = red, bar = brown)

5.6 Discussions

The translation and rotation of the top triangle of the multistable initial 3-bar tensegrity prism is an example of a mechanical design that potentially has wide area of applications. Additional flexibility (that may be required for precision control applications) can be added by increasing the number of active structural members. Importantly, the significance of the translation and rotation exercises of the preceding sections, from an application perspective, is that the equilibrium of a tensegrity structure can be modified to achieve a desired shape (to suite a shape morphing application, for instance) without requiring power to hold this new shape. Moreover, the translation and rotation of the top triangle gives the structural system that has just been considered a six-DOF of movement similar to the motion of the popular Stewart platform[180]. The Stewart platform has gained popularity mainly as a positioning tool for wide range of applications including flight simulators, satellite dish positioning, and machine tools [181]. Generally, the practical usage of the Stewart platform has been in applications requiring low speed and large payload conditions [182]. A 2-stage 3-order class 1 tensegrity structure has been proposed in [48] as a six-DOF motion simulator that, unlike the classical Stewart platform, eliminates the need for telescopic actuators and the problems associated with using them. However, while telescopic actuators has been used for the realization of the multistable 3-bar tensegrity prism in this project, the two important differences between this structural system and the classical Stewart platform are as follows:

1. For the 3-bar tensegrity prism used for 6-DOF position control system, there is the extra requirement that the bars (‘telescopic actuators’) must be in compression and the cables (whose stiffness is adjustable) must be in tension at all times. These requirements are not present in Stewart platform used for position control applications.

2. In the 3-bar tensegrity prism, the top triangle (called the ‘platform’ in the standard Stewart platform) consists of cables that are in tension. This implies that the forces of the structural members that connect the top nodes are tensile. Moreover, the platform of the Stewart platform is a rigid body.

Thus, in view of the features of tensegrity structural systems, an approach that would combine the structural optimization (to obtain valid tensegrity structures) as well as the required control strategy (for deployment and position control) opens many

potential applications. The following area, for instance, is an example of a potential application:

A unique feature of wind energy generation that has made it both technologically and economically viable, as against other major energy generation systems, is the possibility of generating energy on a large-scale without the consequence of having serious environmental pollution. The cost of building wind turbines may be relatively small but the wind field from which wind turbines generate power is also the source of large fatigue loads on the wind turbine. This causes a significant increase in maintenance costs and also a decrease in the operational lifetime of the turbines [183].

To address this problem, many techniques that attempt to reduce fatigue loads on the turbines while the turbines still generate sufficient power exist. These techniques use methods involving controlling the blade pitch [183–185]. However, future turbine designs will likely be stability-driven since it is not likely that performance can be enhanced significantly without influencing structural stability and vibration characteristics. Moreover, recent research has also shown that the blade geometry may be optimised to gain performance, loads, and stability benefits [186]. This possibility creates more flexible designs such as the possibility to realize torsionally-flexible rotor blades. However, the approach introduces problems related to material and geometric couplings. Also to be dealt with are multidisciplinary problems related to blade elasticity, aerodynamics, dynamics, and control. Finding solutions to these problems must be approached from a multidisciplinary viewpoint [91], [166] and tensegrity structures provide possible platform for solving these difficult tasks – primarily due to their light weight, ability to form complex variable geometry and stiffness, and the possibility of modelling these structures easily. Large wind turbine blades capture more wind energy but are more susceptible to fatigue stresses at high winds in particular. On the other hand, small blades capture less wind but are less susceptible to structural fatigue. Using the concept of multistable tensegrity structures, turbine blades can be made flexible – making it possible to control their shapes depending on the loading conditions to avoid structural fatigue while the efficiency of energy conversion is not at risk and the system weight is kept to the minimum. A flexible wind turbine blade loaded with tensegrity prisms is shown in Figure 5.23 as a demonstration of this concept. The morphing capability of the turbine blades relies on controlled deformation of the blade's shape under the action of tensegrity prisms located inside the blade box.

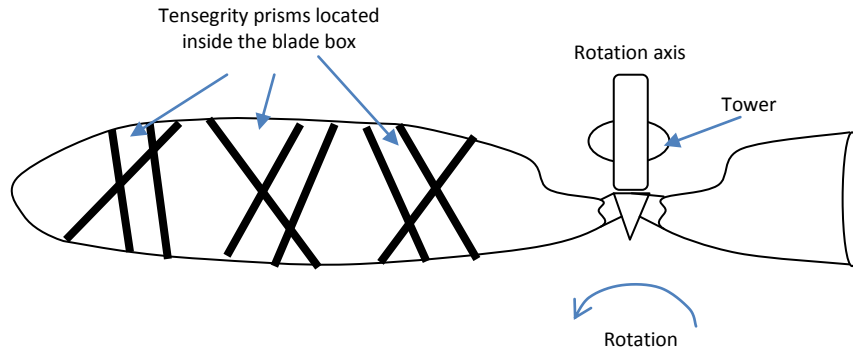


Figure 5.23: A sectional-view of a flexible (morphing) wing turbine blade loaded with tensegrity prisms

5.7 Summary

This chapter deals with the design of the deployed tensegrity structures which are tensegrity structural systems that are designed to be capable of changing their shapes significantly. The discussion has focused on practical structural design and optimization issues and brings together many novel concepts. In particular, it introduced a new physical realization approach that makes it possible to combine the control of the cable and bar lengths simultaneously, thereby combining the advantages of both bar control and cable control techniques of tensegrity structural systems together. Importantly, the approach that made this practical realization possible is by varying the stiffness of the cable structural members. Also, the technique used for the control of cables is significantly different from the techniques used for cable rest length control presented so far in the literature.

This chapter also includes the design of the tension and compression structural members and the techniques for form-finding and deployment of a simple mono-stable and a more complex multi-stable tensegrity structures and a demonstration of how the multi-stable structure can be used to carry out translation along the three Cartesian axes – x , y and z – as well as rotations about these three axes was shown. In addition, a collision avoidance technique that may be employed for the simplex tensegrity structure has been described. The chapter concludes by suggesting that shape-change capability

of wind turbine blades which relies on controlled deformation of the blade's shape is possible under the action of tensegrity prisms located inside the blade box.

The next chapter focuses on details of the hardware, hardware configuration, serial communication protocol using the Universal Serial Bus (USB) interface and the implementation of the software and the control system architecture for the initial 3-bar multistable tensegrity prism designed in this chapter. The next chapter will also include mathematical modelling and structural analyses of the mono- and multi-stable tensegrity structures covered in this chapter using realistic structural parameters.

Chapter 6

PHYSICAL REALIZATION OF TENSEGRITY STRUCTURAL SYSTEMS PART II: HARDWARE ARCHITECTURE AND A DECENTRALIZED CONTROL SCHEME

6.1 Introduction

The aim of this chapter and the preceding one has been to demonstrate the feasibility of realizing a tensegrity structure using a given set of structural members and a predetermined initial structural configuration. The block diagram showing the various components of a computer controlled tensegrity structural system is presented in Figure 6.1. There are three main tasks involved in this project for the realization of this system: the first task entails the structural optimization and related design issues of the 3-bar initial tensegrity prism covered in the preceding chapter. The second task involves the configuration of the hardware and the control architecture, and the third task is associated with the design of application software user interface and the implementation of the control algorithm. These last two tasks are the focus of this chapter. The components of the computer controlled tensegrity structure are discussed briefly. The chapter concludes by the development of the mathematical models and the carrying-out of the structural analyses of the mono- and multi-stable tensegrity structures designed in the preceding chapter using realistic structural parameters.

6.2 Hardware Architecture and Components and the Serial Communication Protocol using the USB interface

The block diagram of the setup of the computer controlled tensegrity structural system in Figure 6.1 consists of three main components: the personal computer (PC), the interface board, and the tensegrity structure. The block diagram shows the relationship and information flow among the constituent components of the system.

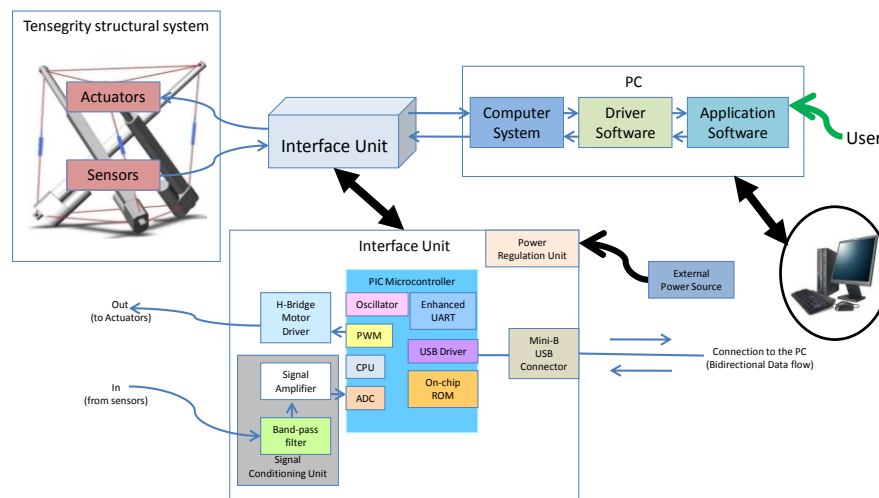


Figure 6.1: A setup for a computer control system of a tensegrity structure showing the relation among the various constituent components

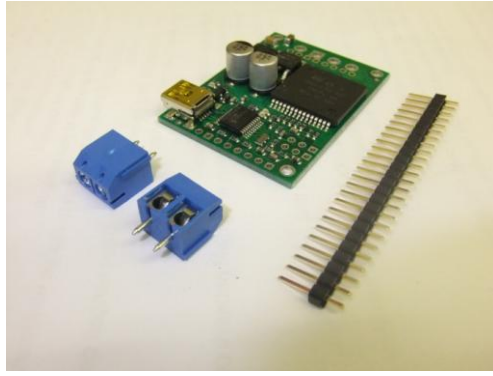
The PC is composed of two elements: the computer and the software. The computer provides the processor that, in addition to carrying out the arithmetic and logical operations, regulates: the data flow; the system clock, which determines the time-information of the data transfer; the bus, along which data are transferred; and, the memory and disk space, which allow for the data to be stored during or after processing. The software facilitates communication between the computer and the control board and there are two types: the driver software and the application software. On the one hand, the driver software allows the set-up of configuration information, such as sampling rate and other parameters of the data acquisition and signal conditioning hardware, to be sent

to these hardware. Also, it allows the sending and receiving of information, such as data, status and error messages from these hardware. The data acquisition hardware access to the computer resources such as the system memory and processor interrupts through the driver software. On the other hand, the application software facilitates data analyses and numerical computations for computing control signals to be sent back, through the computer, to the connected hardware. It is also involved in the storage of data in the system memory for further processing or in the system disk space for safe-keeping. It is the application software that provides the interface with which a user communicates, through the data acquisition hardware, with the system being controlled.

For this project, the specification of the PC used to implement this hardware configuration is a standard PC, running a 64-bit Microsoft[®] Corporation Windows 7 Professional (2009) Operating System (OS) with a 16 GB of RAM and Intel(R) Core(TM) i7-2600 3.40 GHz CPU; the application software is MATLAB 7.12.0.635 (R2011a); the interface unit, or board, is the Pololu Jrk 12v12 USB Motor Controller with Feedback manufactured by Pololu[®] Corporation (see product details in [187]); and the driver software is provided by the manufacturer of the interface board as a free utility that allows easy calibration and configuration through the USB port. In the following sections, elaborate description of the interface board, the serial protocol adopted for information exchange between the board and the user application, and the development of the MATLAB-based user interface will be presented.

6.2.1 The Interface Board

The interface board used for this project is the Pololu Jrk 12v12 USB motor controller with feedback, abbreviated henceforth, as the ‘PJ board’. This product is a highly configurable general-purpose simple motor controller designed for the bidirectional control of a brushed direct current (DC) motor and can support a variety of interfaces including the Universal Serial Bus (USB). The PJ board is shown in Figure 6.2 and its technical specifications are given in Table 6.1. Other features of the motor controller can be found in [187].



(a)



(b)

Figure 6.2: (a) The PJ board with a 14×1 straight 0.1” male header strip and two 2-pin 3.5 mm terminal blocks; (b) The PJ board with the header strip and terminals soldered unto the board.

Table 6.1: Technical Specification of the PJ board [187]

Feature	Specification
No. of motor that can be controlled bi-directionally be each board [Motor Channel]:	1
Minimum Operating Voltage Range:	6 V – 16 V
Continuous Output Current to Motor Channel :	12 A
Peak Output Current to Motor Channel :	30 A
Current Sensing:	0.149 mA per unit (on a unit scale of 0 – 255)
Available PWM Frequencies:	20 KHz, 5 KHz
Minimum Logic Voltage:	4V
Maximum Logic Voltage:	5V
Auto-detect baud rate range:	300 – 115,200 bps
Available fixed baud rates:	300 – 115,200 bps

The interface board consists of five main components: the mini-B USB connector, the Microchip PIC18F14K50 which is a 20-pin USB Flash microcontroller, the VNH2SP30-E H-bridge motor driver manufactured by STMicroelectronics[®], the power regulation unit and the signal conditioning unit. The PIC18F14K50 serves as the data acquisition unit which is the ‘heart’ of any data acquisition hardware. Its main function is to convert (filtered and amplified) analog signals to digital signals and vice-versa. The H-bridge is a common electronic circuit configuration that allows a voltage to be applied across a load in any of the two possible directions. It is commonly used to drive DC motors in the forward and backward directions. The layout block diagram of the five main components of the interface board and their relationship with one another and the rest of the system are shown in Figure 6.1. Moreover, Figure 6.3 is a labelled top-view picture of the interface board. In the discussion that follows regarding this

interface board, the manufacturer's data sheet [188] will be used as the main source of reference.

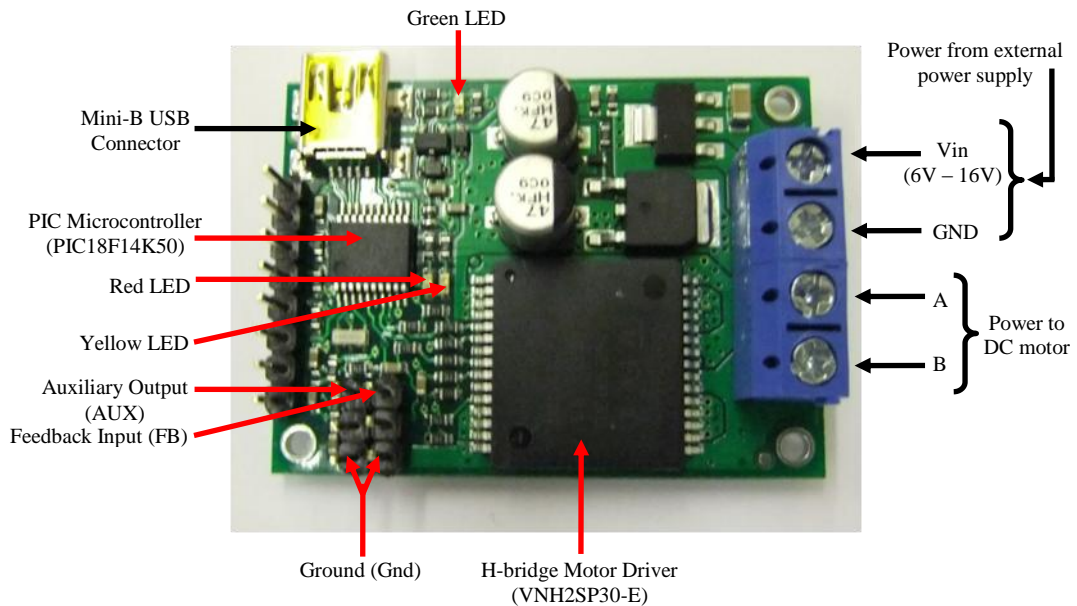


Figure 6.3: A labelled top-view picture of the PJ board

The mini-B connector of the interface board connects to the PC's USB connector through the USB A to mini-B cable. Thus, the mini-B connector provides an interface through which the motor controller is configured and through which it communicates with the PC. If the interface board is required to provide power for the motor it drives, power for the interface board must be supplied by an external power source through its voltage input (V_{in}) and ground (GND) pins. The external power supply will power the electrical circuitry of the board and supply the current (between 12 A and 30 A) to drive the motor through pins A and B that are shown in Figure 6.3. The controller board has a reverse power protection on the motor lines so that it is not damaged when motor is accidentally switched on. If an external power source is not provided to the board, the board will draw power from PC's USB port for its electrical circuitry but will not drive the connected motor. The external power supply unit employed in this project is the XP Power's 90 Watts VEH series (VEH90PS12), with output voltage, output current and efficiency of 12.0 V, 7.50 A and 88%, respectively, when the mains' input voltage and frequency ranges are between 90-264 VAC and 47-63 Hz, respectively [189].

The voltage regulation unit of the interface board converts the voltage input of 12.0 V from the V_{in} to a 5V supply for powering internal circuitry of the control board and excess power are dissipated as heat. The board also has three indicator light emitting diodes (LEDs); the green LED when ON indicates that the driver software is installed correctly; the red LED when ON indicates that there is an error stopping the connected motor from moving; and the yellow LED indicates the status of the connected motor – it is normally OFF when the red LED is ON, flashes when the control board is waiting for the signal, and stays ON when the motor is ON or has reached the desired target state.

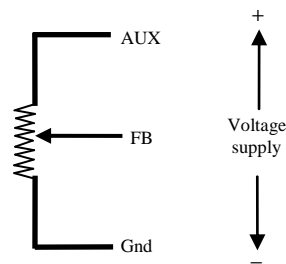


Figure 6.4: A configuration of a potentiometer used as a sensor

The signal conditioning unit consists of a set of passive two-terminal electrical components on the interface board that are responsible for making the sensor signal compatible with the data acquisition unit (the PIC18F14K50). The unit consists of signal amplifiers, which amplify the signals from the sensor by a given fraction, and the band-pass filtering unit, which removes the noise from the signals before they are digitized. The signal conditioning unit is connected to the external sensor through the auxiliary output (AUX), the feedback input (FB) and the ground (Gnd) pins that are shown in Figure 6.3. Consider that the sensor is a potentiometer with three terminals as shown in Figure 6.4, the Gnd and AUX corresponds to the zero and the maximum voltages supplied to the sensor by the controller board, and FB corresponds to the feedback analog voltage connecting the sensor to the control board; the value of the sensor voltage varies between zero and the maximum of the supply. Thus, the interface board uses the AUX pin to detect if a sensor is connected to the board or not and the FB pin measures the analog output of the sensor on a scale between the minimum (determined by the Gnd voltage) and the maximum (determined by the AUX voltage)

voltages. Other pins of this versatile control board have not been used for this project but details of their functions can be found in [187]. Figure 6.5 shows the physical wiring of the PJ board for this project.

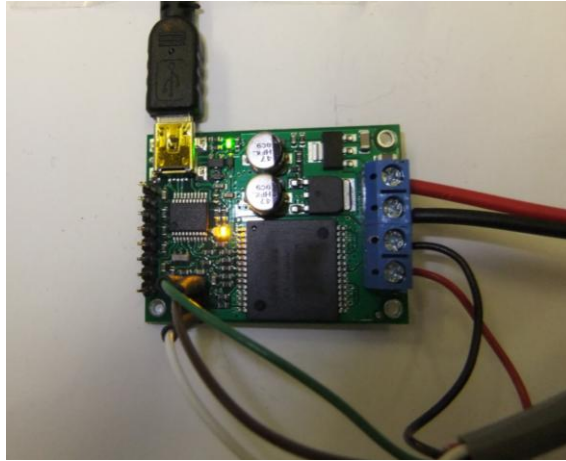


Figure 6.5: The wiring of the PJ board

6.2.2 Configuration of the Interface Board

The PJ board connects to the USB port on the PC running a Microsoft® Windows OS via the USB A to mini-B cable. On connecting the interface board to the computer, and after installing the driver software provided by its manufacturer, the interface board appears as two serial ports which are referred to as COM ports by the PC. To be able to communicate with the interface board through an application software such as MATLAB, the COM Port numbers associated with each device connected to the PC through the PJ board must be known. This can be determined by viewing each of the devices from the PC's Device Manager. For each device, the first of the two COM ports is the 'Command Port' which establishes a communication line between the PC and the interface board. The second of these is the 'TTL Port' which, when in use, allows the PC to communicate directly with any other serial device(s) that may be connected to the interface board.

The installation of the driver software of the PJ board also provides a user interface for setting configuration and control parameters of the interface board. Figure 6.6 shows this configuration utility dialog box. Alternatively, the settings of the five

tabs on the dialog box (Input, Feedback, PID, Motor and Error tabs) can be set using the Notepad text editor of Microsoft® Windows. In this case, the settings on the Notepad are loaded through the file menu on the dialog box and the settings are applied by clicking the ‘Apply settings to device’ button on the dialog box.

6.2.3 The Serial Port Interface and the ‘Pololu’ Communication Protocol

The serial port of the PC provides a means through which devices connected to the PC can communicate with it using low-level protocol by transmitting data one bit at a time over a communication link or bus. This sequential data transfer process is often referred to as serial communication [190]. The serial ports, also referred to as COM ports, created by each PJ board connected to the PC through the USB cable, allows MATLAB to access the controller using any of the serial port interface standards such as the RS-232, RS-422 and RS-485 [191]. These standards differ, from the technical viewpoint, mainly in their serial port characteristics such as: their maximum bit transfer rates and cable lengths; the names, electrical characteristics, and functions of signals; and the mechanical connections and pin assignments [190]. The serial interface of PJ board uses the RS-232 serial communication standard which is one of the standards supported by MATLAB serial port interface. To communicate with the interface board - just as with any other serial device - through the serial port interface in MATLAB involves the following steps [191]:

Step 1: Create a serial port object.

Step 2: Configure the serial port properties of the object created. (In practice, this step can be performed immediately after Step 1 and before, during, or after steps 3 and 4.)

Step 3: Connect to the serial port device.

Step 4: Write and/or read data to the device.

Step 5: Clean-ups: Disconnect device, delete the serial port object, and clear variable from MATLAB workspace.

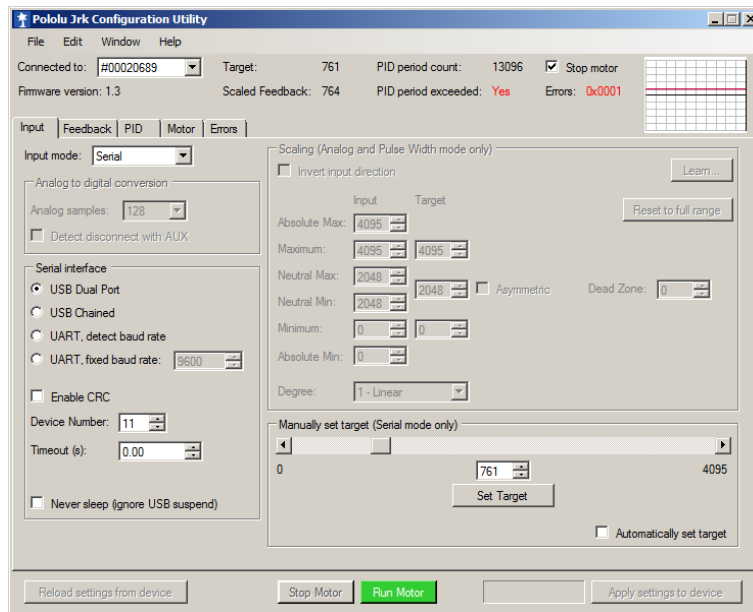


Figure 6.6: The PJ board configuration utility dialog box.

The workflow of the MATLAB implementation of the above steps developed for this project is shown in Figure 6.7. The instructions in the single-sided rectangular processing steps, labelled A to E, are implemented using standard commands in MATLAB. The ‘COM5’ shown in the processing step A is the ‘COMMAND Port’ number associated with the first PJ board connected to the PC. The processing step B shows some of the available properties of the serial port that can be configured in MATLAB. These properties include: the baud rate (rate at which bits are transmitted); the byte order (specifies the order that a device stores the first or last byte in the first memory location, e.g. the byte order ‘little endian’ means that the first byte is stored in the first memory address); sizes of the buffers (the input /output buffer represents the total number of bytes that can be stored in the input/output buffer during a read/write operation); the number of the data bits (the number of bits that represent actual data byte – excluding the framing bits – in the serial data format); the stop bit (indicates when the data byte has been transferred); the parity bit (a bit used for error-checking transmitted data); and the time out (the maximum waiting time in seconds allowed for a read or write operation to complete).

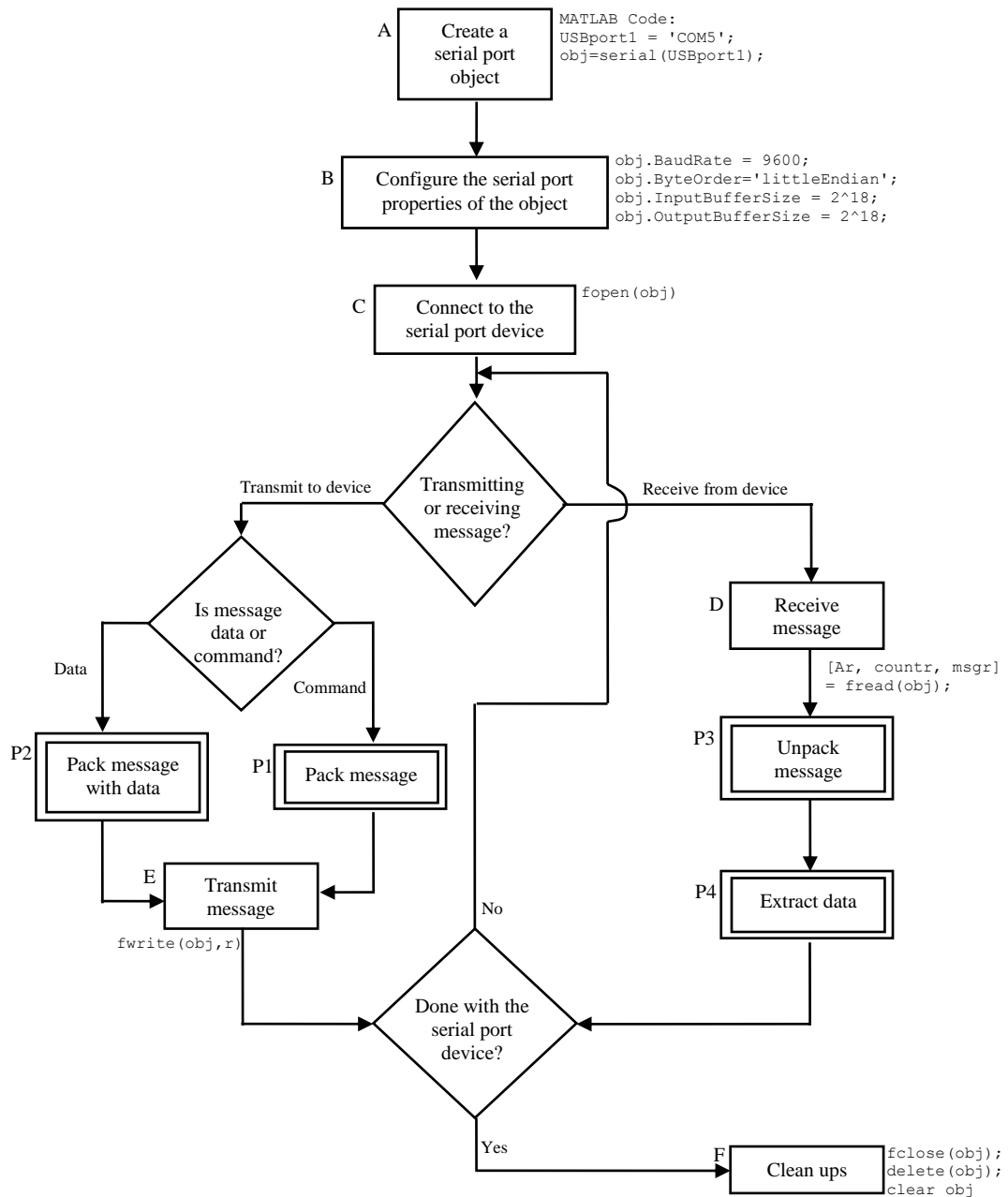


Figure 6.7: The workflow for executing serial port communication in MATLAB

Furthermore, the MATLAB implementation of the double-sided rectangular processing steps in the flowchart of Figure 6.7, labelled P1, P2, P3 and P4, were achieved using the interface board manufacturer’s so-called ‘Pololu’ serial communication protocol [187]. Communication between MATLAB and the interface board, using the Pololu protocol, was achieved by sending a set of data packets which are written in specific formats and arranged following particular rules. Thus, the processing steps P1, P2, P3 and P4 involve the following data packets:

- P1: Message packing process (with no data byte)

Detect baud rate byte	Device number byte	Command byte with MSB cleared
-----------------------	--------------------	-------------------------------

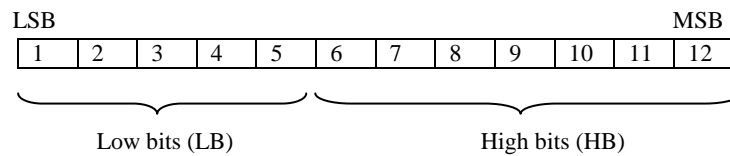
- P2: Message packing process (with data byte)

General case:

Detect baud rate byte	Device number byte	Command byte with MSB cleared	Data byte
-----------------------	--------------------	-------------------------------	-----------

High resolution 'set target' command case:

Data bits: 12 bits with LSB in the first column and MSB in the last column

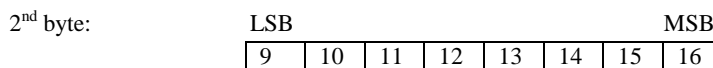
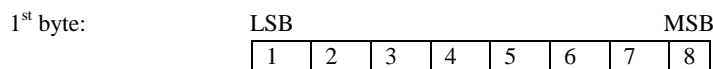
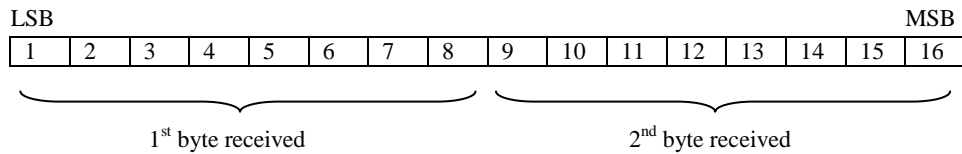


Data packet:

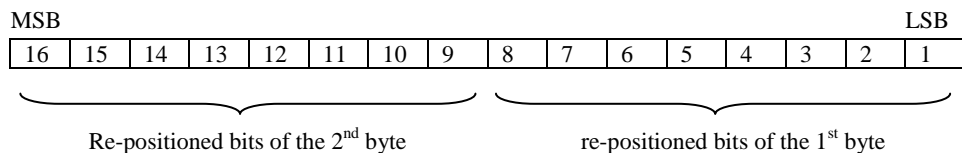
Detect baud rate byte	Device number byte	'Set target' Command byte with MSB cleared 'plus' LB	HB
-----------------------	--------------------	--	----

- P3: Message unpacking process

Data bits: 16 bits (2 bytes) in little endian format



- P4: Data extraction process



where MSB, LSB, LB, HB denote most significant bit, least significant bit, low bits, high bits, respectively

Assume that the interface board is used for a position control feedback application in which a linear actuator is equipped with a motor and a position sensor, then there will be two types of commands that are involved when the workflow diagram of Figure 6.7 is implemented which are as follows:

1) Commands that require no response from the interface board: To stop the running motor of the linear actuator or to set the position of the linear actuator to a particular value, for instance, requires no response from the interface board. On the one hand, the ‘Stop Motor’ command requires no ‘data’ byte, therefore, implements the processing step P1 (of Figure 6.7) using the following MATLAB code, for instance:

```
SERIAL_MODE_UART_DETECT_BAUD_RATE_BIT = 'aa'; % in hexadecimal format
SERIAL_MODE_DEVICE_NUMBER = '0b'; % in hexadecimal format
% 1st and 2nd Command bytes:
r1 = hex2dec(SERIAL_MODE_UART_DETECT_BAUD_RATE_BIT); % in decimal format
r2 = hex2dec(SERIAL_MODE_DEVICE_NUMBER); % in decimal format
% 3rd byte of the Stop Motor Command:
STOPCOMMAND = '7f'; % Stop command
s3 = hex2dec(STOPCOMMAND); % in decimal format
r = [r1,r2,s3]; % Packets to be transmitted
```

The ‘set target-position’ command, on the other hand, requires ‘data’ byte containing information regarding the desired target-position; therefore, the processing step P2 (of Figure 6.7) is implemented using the following MATLAB code, for instance:

```
% 'variable' is the desired target position
% 1st and 2nd Command bytes:
r1 = hex2dec(SERIAL_MODE_UART_DETECT_BAUD_RATE_BIT); % in decimal format
r2 = hex2dec(SERIAL_MODE_DEVICE_NUMBER); % in decimal format
% 3rd and 4th bytes of Pololu Protocol:
[r3, r4] = High_res(variable); % r3 & r4 are in decimal format
% High_res is a self-made function that obtains third and fourth bytes in
% Pololu protocol format given the 'variable'
r = [r1,r2,r3,r4]; % Packets to be transmitted
```

Figure 6.8 shows the workflow diagram involving the implementation of the ‘Stop Motor’ and the ‘set target-position’ commands

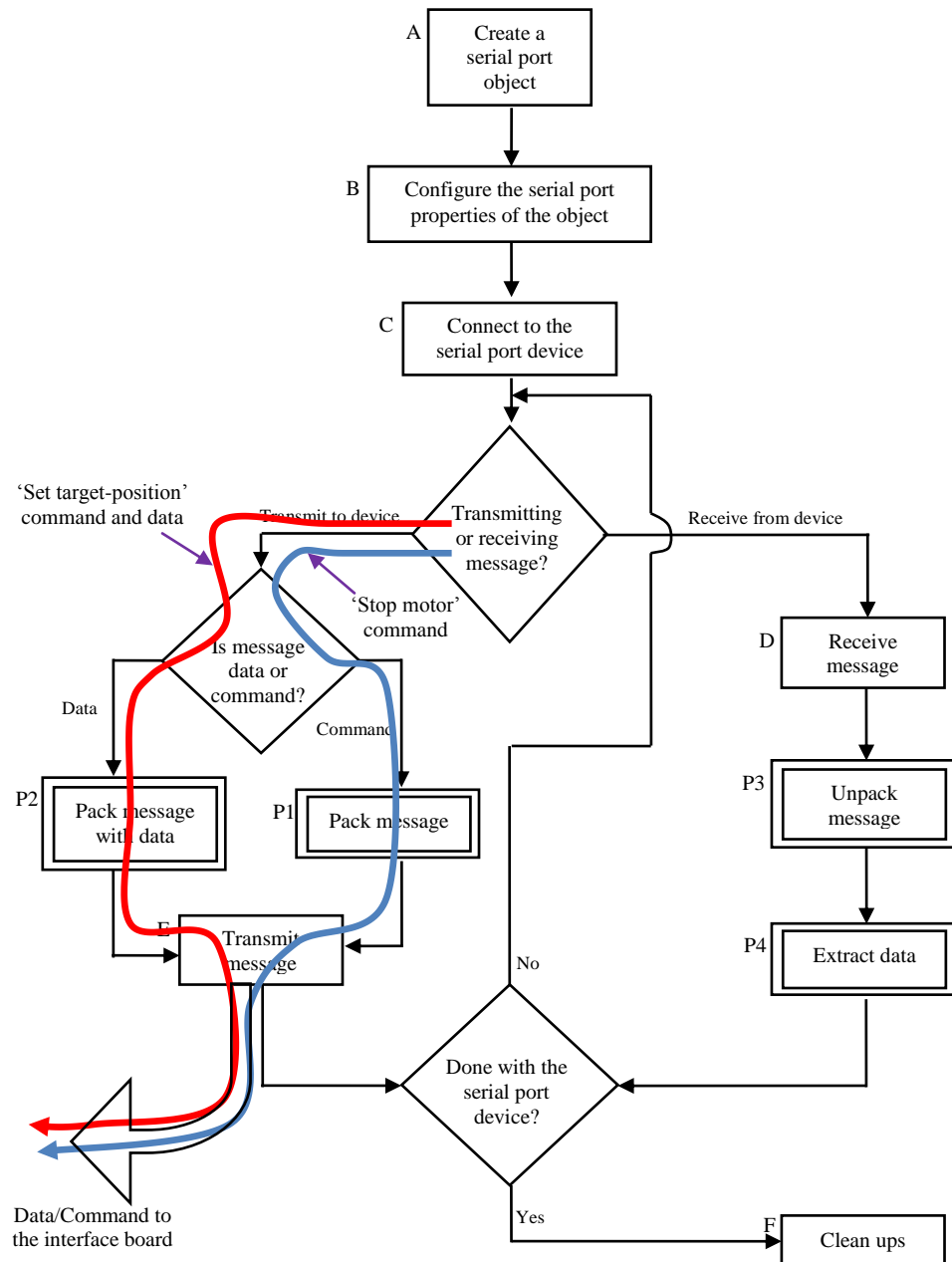


Figure 6.8: The workflow involving the implementation of the 'stop motor' and the 'set target-position' commands

2) Commands that require response from the interface board: To read the current position from the sensor of the linear feedback actuator, for instance, requires that a 'read feedback sensor' command must first be sent to the interface board. With this, the interface board collects the current position of the linear actuator from the attached

sensor. A second ‘send me feedback reading’ command will now be sent again to the interface board from MATLAB (this is the function of the processing step D in the workflow diagram); the interface board then transmit the sensory readings in the form of data packets to MATLAB. The MATLAB codes associated with the ‘read feedback sensor’ command data packet, for instance, are as follows:

```

FEEDBACK          = 'a5'; % in hexadecimal format
% 1st and 2nd Command bytes:
r1 = hex2dec(SERIAL_MODE_UART_DETECT_BAUD_RATE_BIT); % in decimal format
r2 = hex2dec(SERIAL_MODE_DEVICE_NUMBER); % in decimal format
% 3rd byte of the Read Command:
r3 = hex2dec(FEEDBACK); % FEEDBACK = The 'read feedback sensor' command
[vr3] = remove_msb(r3); % Implement the Pololu Protocol: Removing the MSB
% remove_msb is a self-made function that removes MSB in the third bytes in-
line with the Pololu protocol
r = [r1,r2,vr3]; % Packets to be transmitted

```

Figure 6.9 shows the workflow diagram involving the implementation of the ‘read feedback sensor’ and ‘send me feedback reading’ commands.

6.2.4 Control Parameters and Algorithm of the Interface Board

The PJ board is designed to be part of a feedback control system. In particular, it implements the Proportional Integral Derivative (PID) control algorithm – which is the most common form of feedback controller [192] – for the control of motor speed or position. The structure of the implementation of PID control algorithm of the PJ board is shown in Figure 6.10. The PJ board allows its sampling rate to be set to as low as 1ms and the PID algorithm is implemented at every sampling intervals. For motor position control application, the reference input is a target value from 0 to 4095. The reference input is specified using the ‘set target-position’ command from the previous section. The feedback sensor reads a voltage value that represents motor position that falls between 0 to 5 V. The reading is scaled by a constant K_f for conversion into 0 – 4095 scale. Accordingly, each nominal unit on the 0 – 4095 scale represent $5/4095 = 1.2$ mV; therefore, the value of K_f is 819. A second feedback sensor reads the current through the motor as a unit number that falls between 0 and 255 and a calibration value k_{mA} converts this reading to actual current in Amps. From the manufacturer’s manual [187], each normal unit on the 0 – 4095 scale on the PJ board represents a current of 149 mA in the motor.

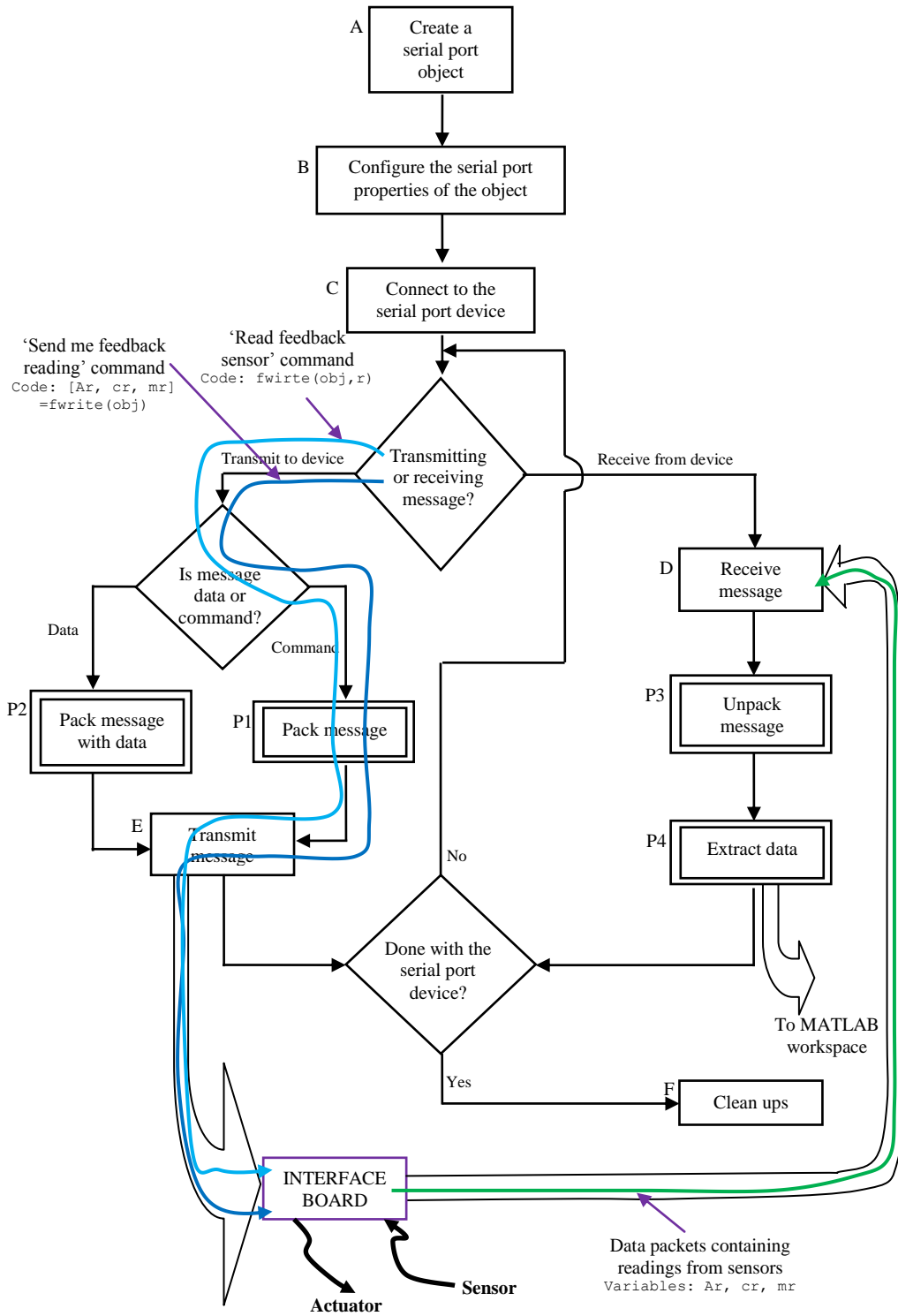


Figure 6.9: The workflow involving the implementation of the 'read feedback sensor' and 'send me feedback reading' commands

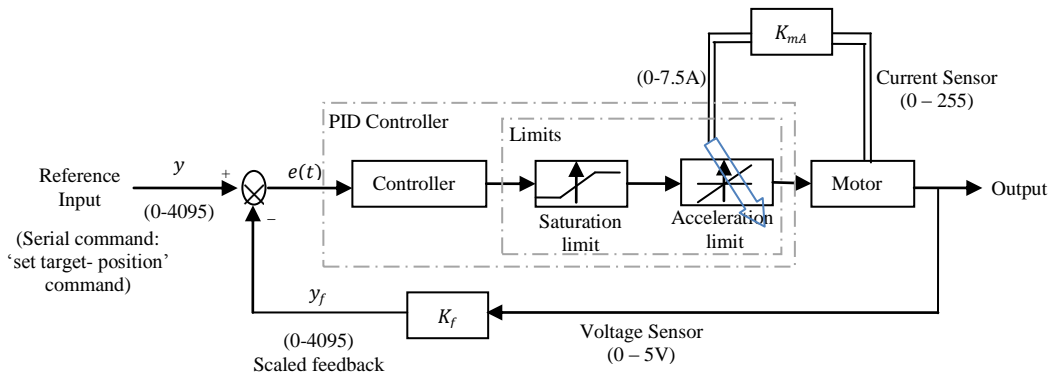


Figure 6.10: The structure of the implementation of PID control algorithm of the PJ board [187]

The input of the PID controller is the error $e(t)$ – which designates the difference between the reference input and the scaled output of the feedback sensor. The PID controller uses the error to compute the duty cycle of the Pulse Width Modulation (PWM) signal that is applied to the motor. The value of the duty cycle ranges from -600 to +600. Therefore, a 100% duty cycle in the forward direction represents a value of +600; a 100 % duty cycle in the backward direction represents a value of -600; and a duty cycle of 0% represents a value of 0 – that is, motor is in ‘off’ condition. Allowable switching frequencies of the PWM for the PJ board are 5 KHz and 20 KHz. The 20 KHz PWM frequency is typically desirable since – being ultrasonic – it eliminates audible motor humming, but this is at the expense of greater power loss as a result of switching [187].

The mathematical representation of a typical PID controller is as follows [192]:

$$u(t) = K(e(t) + \frac{1}{T_i} \int_0^t e(\tau) d\tau + T_d \frac{de(t)}{dt}) \quad (6.1)$$

where the output of the PID controller $u(t)$ (which serves as the input to the motor plant) is the sum of three terms: the proportional term $Ke(t)$, the integral term $\frac{K}{T_i} \int_0^t e(\tau) d\tau$ and the derivative term $KT_d \frac{de(t)}{dt}$. There are many variations of the structure of the PID controller; for instance, two other possible representations are as follows [192]:

$$u(t) = K(1 + \frac{1}{T_i} \int_0^t e(\tau) d\tau)(1 + T_d \frac{de(t)}{dt}) \quad (6.2)$$

$$u(t) = K_p e(t) + K_i \int_0^t e(\tau) d\tau + K_d \frac{de(t)}{dt} \quad (6.3)$$

The parametrized PID controller represented by equation (6.3) involves only three constants: K_p – the proportional coefficient, K_i – the integral coefficient, and K_d – the derivative coefficient. In general, different PID controller structures have different parameters although some of the structures are equivalent (for instance, equations (6.1) and (6.3) are equivalent).

Furthermore, to avoid poor performance, the practical implementation of a PID controller requires that techniques to deal with nonlinear effects be introduced. Particularly, in the PID controller implemented in the PJ board for motor position control that is being considered, a phenomenon which involves the integral term of the PID controller not being able to keep the error $e(t)$ small as a result of the motor's saturation (due to its inability to move the connected load beyond 'the maximum' position) is encountered. This well-known phenomenon, commonly called the windup phenomenon, may also be caused by large disturbances or malfunctioning of the control system. Different manufacturers have invented different techniques, commonly called anti-windup techniques, of dealing with these nonlinear effects but the techniques they employ are commonly kept as trade secrets [192]. The anti-windup technique employed in the PJ board involves limiting the 'integral wind-up' by setting a limit to the magnitude of the integral, or resetting the integral to 0 when the proportional terms exceeds the maximum duty cycle, or by fixing an amount – called the feedback dead zone value – below which if the magnitude of the error falls, will reset the duty cycle target and the integral to zeros [187]. A limit is also imposed on the maximum acceleration of the duty cycle so as to limit the amount in which it can change in any given sampling period. The duty cycle is also adjusted so that the current through the motor does not exceed the maximum current allowable. As indicated in Figure 6.10, the 'acceleration limit' block adjusts the duty cycle based on the values of maximum acceleration of the duty cycle and the maximum allowable current in the motor. However, the use of limiters frequently leads to conservative bounds and consequently poor system performance [192].

Tuning a PID controller is the process of adjusting its parameters until the response of the control system is satisfactory in view of the load disturbances, process

uncertainties, reference signals and sensor noise that affect the system. The possibility of having a satisfactory controller from less plant information (such as unavailability or incomplete mathematical model), simplicity of tuning and ease of understanding the tuning process are some of the factors that made PID controllers popular in the industry. In addition, these controllers are commonly used at lower-level control loops for (coupled and uncoupled) multivariable system that use sophisticated control strategies such as model predictive control [192]. The popularity of the PID controller has led to the development of many tuning techniques such as the Ziegler-Nichols, Coohen-Coon, and optimization-based techniques [193].

The manufacturer of the PJ board suggested the use of a trial-and-error method for the determination (tuning) of the three PID parameters until satisfactory system performance is realized. In this project however, attempt is made to find the three PID controller parameters by posing the problem of finding these parameters as an optimization problem. Before presenting the optimization-based approach that was employed, the details on the PJ board that made finding the solution of the optimization problem particularly difficult should be kept in mind. As there are many structures for implementing a PID control algorithm, the particular structure used by the PJ board is not given in the manufacturer's manual. Furthermore, once the three parameters are chosen, they are programmed onto the EEPROM of the PJ board – therefore, changing these parameters requires updating the EEPROM with the new values. In other words, parameter changes cannot be done online – making the application of an online or adaptive tuning technique impractical. Also, in addition to the three PID controller parameters, various other parameters have effect on the overall performance of the motor position control system – for instance, the nonlinear effects as a result of the introduction of limiters used as anti-windup strategy.

In the absence of knowledge on the structure of the PID, the impracticality of online tuning of the PID parameters, and the lack of information on the implementation of the limiting techniques adopted as the anti-windup strategy, the optimisation problem of finding the optimal values of the three PID parameters may be formulated as the problem of minimizing the Integral of Squared Error (ISE) for all time steps from 0 until the time the system responses settles reasonably to its final value. In other words, some initial values of the three PID controller parameters (K_p , K_i , and K_d) are chosen and a simulation of the system is ran for a fixed period of time t_f with predefined set-

points. Next, the value of the ISE for this simulation is calculated. The values of the PID controller parameters to be used for the next simulation so that the value of the ISE will be reduced are determined. This iterative process is repeated until the ISE is within a specified bound. For the motor position control application using the PJ board, error is the difference between the reference input and the scaled feedback of the output. The ISE is given by the following equation:

$$\text{Integral of Squared Error (ISE)} = \sum_{i=1}^p (e_i)^2 \quad (6.4)$$

With the sampling time set to 1 ms, the set-point is increased by 137 unit every 2 seconds from the initial set-point of 410 to the final set-point of 2740 for a total simulation time of 36 sec. It should be recalled that the reference input is a target value from 0 to 4095; however, the range of target values within which the behaviour of the system is linear is found to be roughly between 400 and 3600. Also, the values of 0 – 4095 set-point corresponds to the positions of 0 – 30 cm of the actuator arm. The set-point values of 137, 410 and 2740 therefore correspond to approximated values of 1 cm, 3 cm, and 20 cm, respectively. Thus, by predefining set-point range of 3 cm to 20 cm with 1 cm increment after every 2 sec starting from 3 cm, the search of the PID controller parameters takes into account the likelihood of set-point of the control system to have any value within the linear range and the possibility that the set-point can change from one value to another within this range. As such, the search problem has been written as the following optimization problem:

$$\min_x f(x) \quad (6.5)$$

where $x = [K_p \ K_i \ K_d]^T$ and $f(x) = \sum_{i=1}^p (e_i)^2$; e_i is the error at the i^{th} sampling instant and p is the total number of samples at the final time of simulation. To solve this problem, the steepest descent [105] unconstrained optimization technique is employed. The flow chart of this technique is shown in Figure 6.11 and the descriptions of the implementation of the algorithm for the determination of the PID controller parameters for the PJ board are as follows:

Step 1: Specify the values of the sampling time, the maximum duty cycle, the maximum value of motor current, and the frequency of the PWM signal; in this exercise, these values have been set as 1 ms, 100% duty cycle, 7.45 A and 20 KHz, respectively. The maximum motor current has been set to 7.45 A since 7.5 A is the maximum current that can be supplied to the interface board by the power supply unit. The starting values of

the PID controller parameters, for instance, are $K_p = 5.1$, $K_i = 1$, and $K_d = 6.6$, respectively.

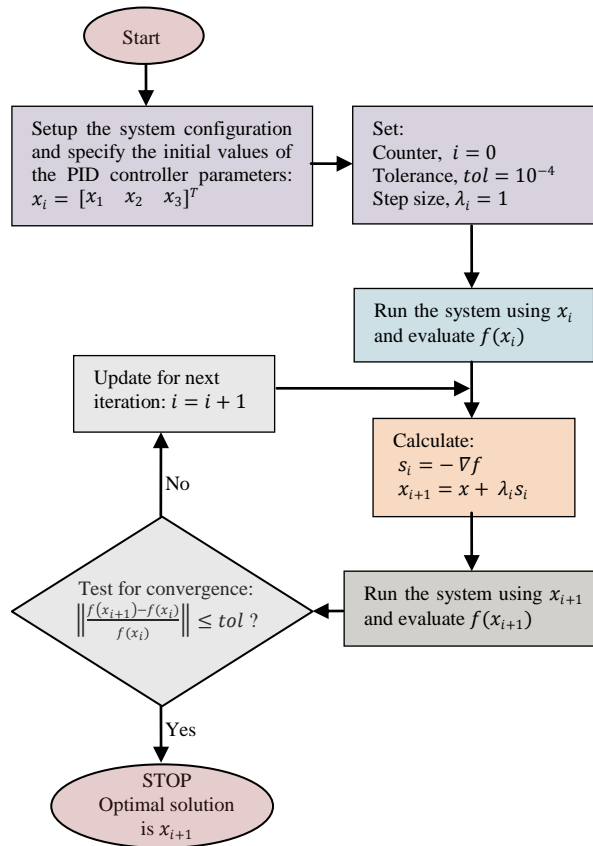


Figure 6.11: Flow chart for the determination of the PID controller parameters for the PJ board

Step 2: Run the simulation of the system using the parameters set in Step 1 using reference set-point range of 3 cm to 20 cm with 1 cm increment and a running period of 2 seconds at each set-point. The initial motor position is 0 cm. This results to a total running time of 36 seconds. Calculate the value of the objective function $f(x_i)$ using equation (6.5).

Step 3: Calculate the direction of steepest descent s_i given by the negative of the gradient vector ∇f ; this is expressed as follows:

$$s_i = -\nabla f \quad (6.6)$$

The gradient ∇f is evaluated by computing the partial derivatives $\frac{\partial f}{\partial x_i^j}$, $j = 1, 2, 3$ using the backward difference formula. That is, the approximate partial derivative at the i^{th} time instant is computed as follows:

$$\frac{\partial f}{\partial x_i^j} = \frac{f(x_i) - f(x_{i-1})}{\Delta x_i^j}, \quad j = 1, 2, 3 \quad (6.7)$$

where $\Delta x_i^j = x_i^j - x_{i-1}^j$. Also, define the step length $0 \leq \lambda_i \leq 1$. There are algorithms to determine the optimal step length (see, for instance, [105]); however, for simplicity, $\lambda_i = 1$ has been used in the initial start of algorithm and the step length has been computed using $\lambda_{i+1} = 0.9\lambda_i$ for subsequent iterations. Thus, the next run of the system is prepared by updating the PID controller parameters as follows:

$$x_{i+1} = x_i + \lambda_i s_i \quad (6.8)$$

Step 4: Run the simulation of the system again as in Step 2 but with the new controller parameters x_{i+1} . Next, obtain the value of the objective function $f(x_{i+1})$ using equation (6.5).

Step 5: The criterion used to terminate the iterative process is when the absolute value of the relative change in the values of the objective function in two consecutive iterations is small relative to a predefined value of tolerance value tol (for instance, $tol = 10^{-4}$). This convergence criterion is expressed as follows:

$$\left| \frac{f(x_{i+1}) - f(x_i)}{f(x_i)} \right| \leq tol \quad (6.9)$$

If the inequality in equation (6.9) is satisfied, the iterative process stops and x_{i+1} is taken as the optimal PID controller parameters; otherwise, the algorithm prepares for the next iteration and the next iteration begins from Step 3 after the next sampling instant.

The results of the algorithm just described applied to the process of determining the optimal PID parameters for the PJ board parameters are as follows:

Iteration Number	(K_p) x1	(K_i) x2	(K_d) x3
1	5.1000	1.0000	6.6000
2	5.7981	1.5766	7.2981
3	5.8324	1.6182	7.3324
4	5.8401	1.6245	7.3401
5	5.9244	1.7276	7.4244
6	5.9255	1.7358	7.4255
7	5.9848	1.7682	7.4857
8	5.9850	2.0000	7.4861

Optimization terminated: the specified termination condition is satisfied

It shows that the optimal parameters are $K_p = 5.985$, $K_i = 2.00$, and $K_d = 7.4861$. However, it is worth noting that the method of steepest descent direction in optimization is a local property [105]. But given the difficulties associated with the use of the PJ board mentioned earlier, the results of the approach used has been found to be satisfactory. Figure 6.12 shows the system responses at the beginning of the iteration process (with $K_p = 5.1$, $K_i = 1$, and $K_d = 6.6$) and at the end of the iteration process (with $K_p = 5.985$, $K_i = 2.00$, and $K_d = 7.4861$).

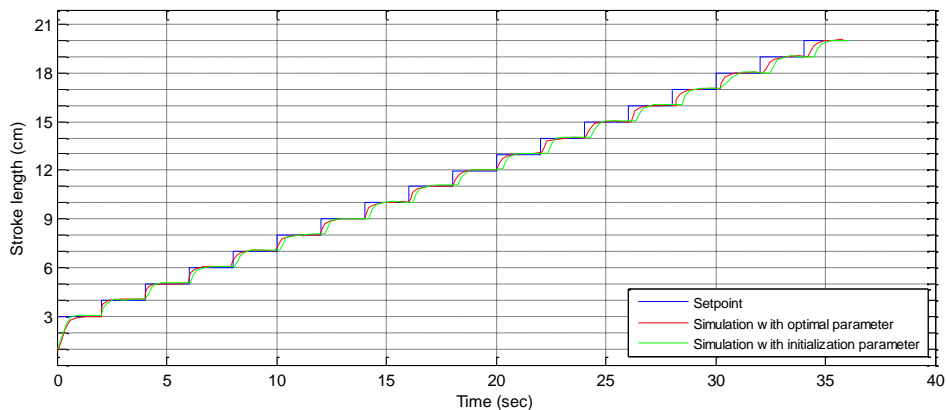


Figure 6.12: System responses at the beginning and at the end of the iteration process

6.3 Control Strategy, Design Characteristics and Setbacks

In Section 6.2.4, the feedback control system for the control of a linear actuator with the PJ board in the form of a motor position control system was presented. Linear actuators are used as bars in the initial 3-bar tensegrity prism. For demonstrating the usefulness of the concepts presented in this project, the use of short linear actuators to vary the stiffness of the vertical cables in the multistable design approach of the tensegrity prism

has been used. For the long linear actuator (the bars) and the short linear actuators (the inline actuators of the vertical cables), the stroke lengths are 0 – 30 cm and 0 – 5 cm, respectively; the linear ranges of 3 – 26 cm and 0.333 – 4.333 cm of stroke lengths for the bars and inline actuators, respectively, will be worked with in this project. The block diagram for the PID control algorithm used for position control of each actuator of the bars and inline actuators (as detailed in Section 6.2.4) is shown in Figure 6.13.

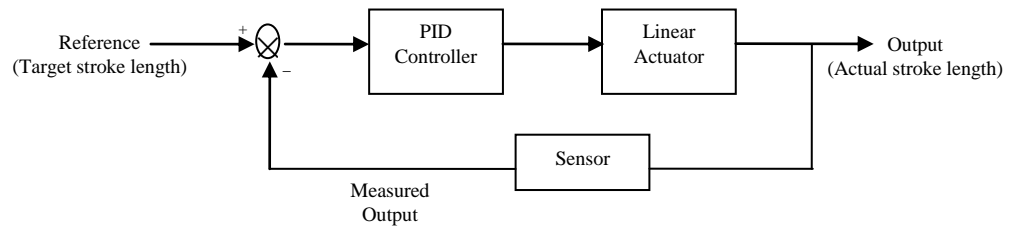


Figure 6.13: Block diagram of the control system for each actuator

The general block diagram for the control of the tensegrity structure that employs the proposed multistable design approach (where bars are actuated and stiffness of the vertical cables are controlled) is shown in Figure 6.14. As the figure shows, the actuators and sensors are highly integral (inseparable) parts of the structural system. Four sets of structural components can be identified in the figure: structural components A are those structural components that are actuated and sensed (for example, the linear actuators are equipped with position sensors and serve as bars of the tensegrity structure); structural components B are those structural components that are actuated but not sensed (for example, the vertical cables – the forces in them are not measured but they are actuated by the movement of the electromechanical parts); structural components C are those structural components that are not directly actuated but sensed (for example, the top horizontal cables of the structure may not be directly actuated but it may be necessary to sense their tensile forces to guarantee structural stability); and structural member D are those structural components that are neither directly actuated nor sensed (for example, the joints – they are idealistically assumed to be pin-jointed and friction loss is neglected). It should be observed that all these components (A, B, C and D) have their parameters affected to some degree by the effect of actuation, external load and/or disturbances, and the effectiveness of the control systems will depend on the magnitude and level of interaction between all these components.

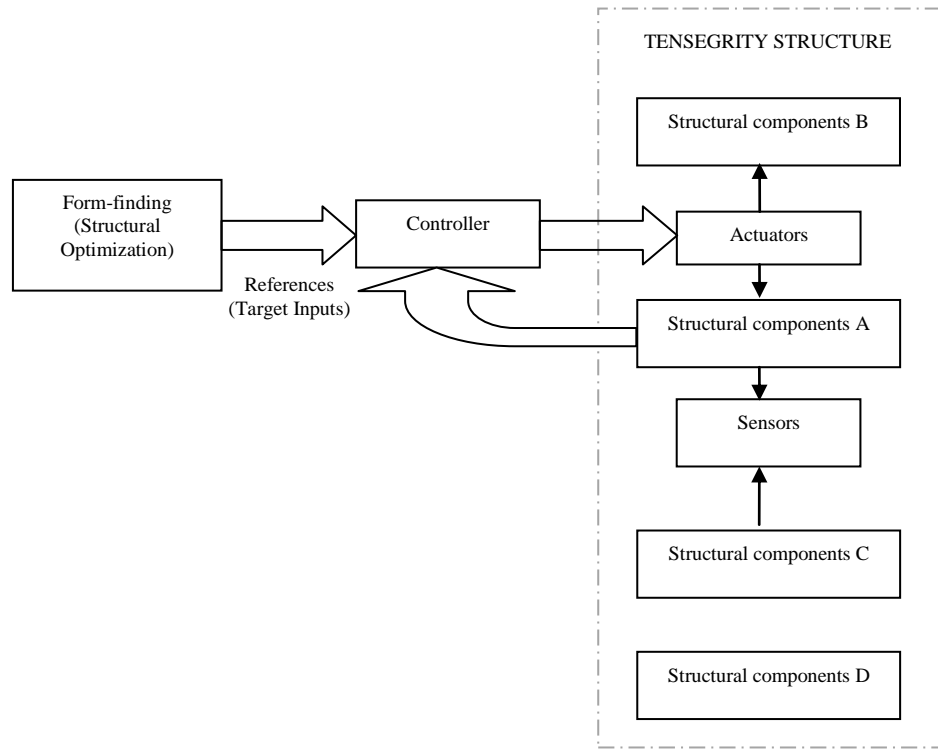


Figure 6.14: A general block diagram for the control of the tensegrity structure that uses the proposed multistable design approach

The control strategies developed for the monostable and multistable 3-bar tensegrity prism are shown in Figure 6.15 and Figure 6.16, respectively; these figures are 3-loop and 6-loop single-input single-output (SISO) systems, respectively. In both, the primary sources of disturbance to the actively controlled structural members 10, 11 and 12 (the bars) are due to the forces in structural members 5-6-9, 4-5-7 and 4-6-8, respectively; in addition to these disturbances, for Figure 6.16, other primary sources of disturbance to the actively controlled structural members 7, 8 and 9 are due to the forces in structural members 4-5-11, 4-6-12 and 5-6-10, respectively. In relation to Figures 5.15 and 6.16, $k_0 = 45$ cm is the retracted length of the linear actuator, k_1 is the sum of the retracted lengths ($l_{ao} = 21.558$ cm) of the electromechanically actuated component of the vertical cable and the original length ($l_o = 11$ cm) of the spring component of the vertical cable, and l_i is the length of the i^{th} structural member. The fundamental characteristic of these control strategies are that they attempt to control a highly coupled (integrated) structural system using a decentralized (independent) multiple SISO control systems. The decentralized control architecture of Figure 6.16 has been used for the

control of the multistable tensegrity prism. Figure 6.17 shows the picture of the set-up for the calibration of the 6 electromechanical actuators while Figure 6.18 shows the picture of the final structure after assemblage of all the constituent components. Also, the nodes of the structure, as should be noticed in Figure 6.18 (d) in particular, contain sensors for measuring nodal vibration. The control strategy of Figure 6.16 assumes that the primary disturbances are independent inputs. The outputs of the form-finding algorithm are used to compute the reference inputs for each of the six independent SISO control systems. This architecture is a form of static decoupling architecture [194] since the reference signals from the algorithm are constants. Details on the anti-windup technique which is necessary for the implementation of each PID controller of each SISO system of this architecture has been presented in Section 6.2.4.

For the multistable 3-bar tensegrity structural system, the control strategy is suitable for any of the following control objectives:

- 1) To change the shape of the structure from an arbitrary tensegrity configuration to a valid tensegrity structure (deployment);
- 2) To change the shape of the structure from a valid tensegrity structure to another valid tensegrity structure (transformation from one structure to another); and
- 3) To change the shape of the structure from a valid tensegrity structure to another structure that is not tensegrity structure but a tensegrity configuration (for example, the rotation of the top polygon of the tensegrity prism while the bottom polygon is rigidly fixed to the base).

Associated with each of these objectives, of course, is the desire for acceptable disturbance rejection characteristics of the system in the presence of model uncertainties. Under the assumptions that the magnitudes of the disturbance and the level of interaction among the six independent SISO systems are small, the springs designed in Sections 5.3.2 and 5.3.3 have exactly the specified stiffness constants, the frictional force at the joints are negligible and the geometric configuration of the structural assembly is correct to at least 10^{-4} m, the control architecture of Figure 6.16 leads to acceptable results. Clearly, these assumptions are very stringent demands and impossible to achieve in practice. Moreover, as in classical control, there is the need to pair the input and outputs (for instance, using relative gain array [195]) to implement a complete decentralized control architecture. Thus, for the implementation of a

decentralized control scheme, this thesis should be considered a first attempt and a solid foundation for future work. Beside, an alternative control technique for the control of tensegrity structures in general is presented in the next chapter. Meanwhile, the dynamic model of the 3-bar tensegrity prism will be presented in the remainder of this chapter.

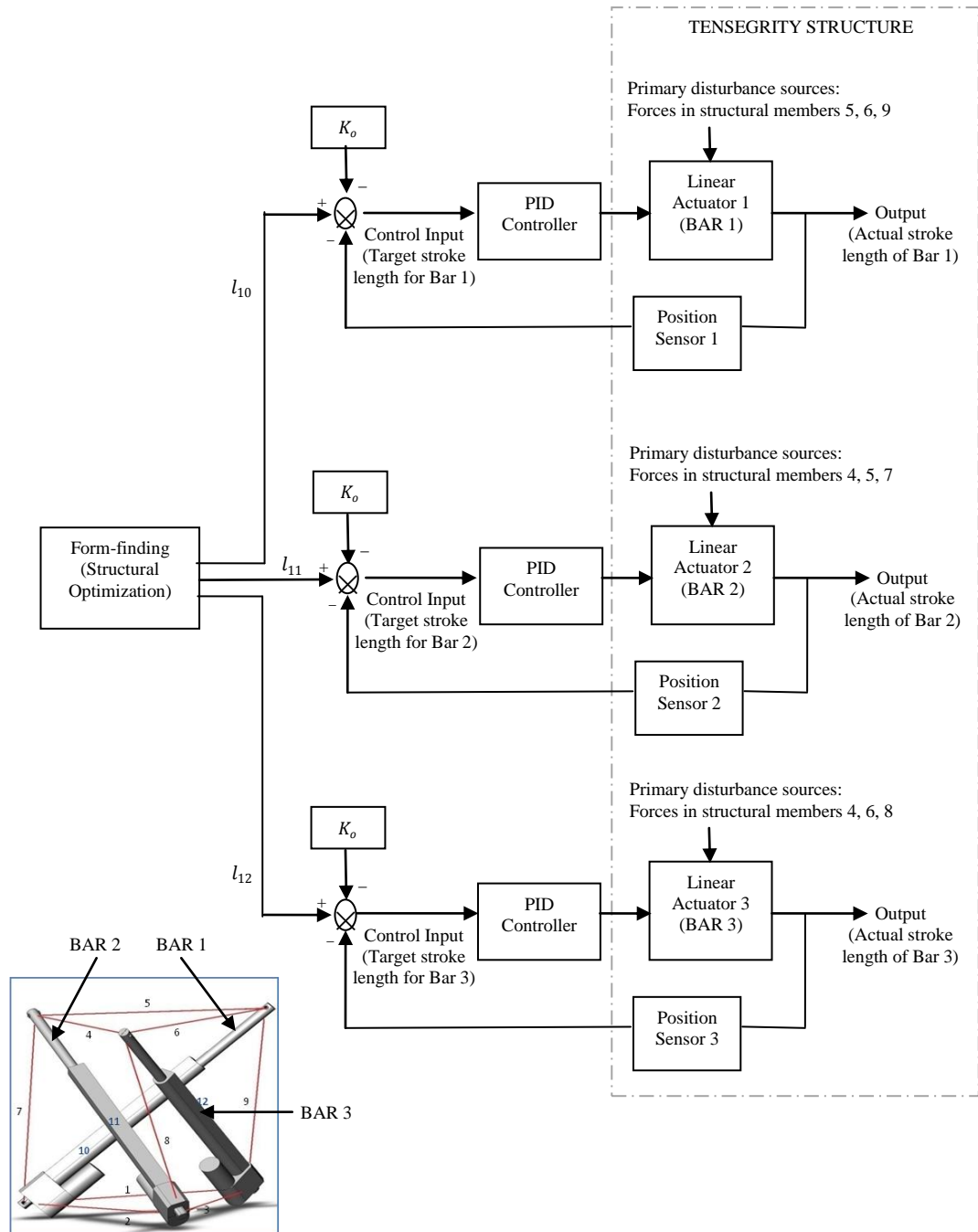


Figure 6.15: Control strategy for the monostable 3-bar tensegrity prism involving multiple SISO control loops (the bottom nodes are rigidly attached to the base)

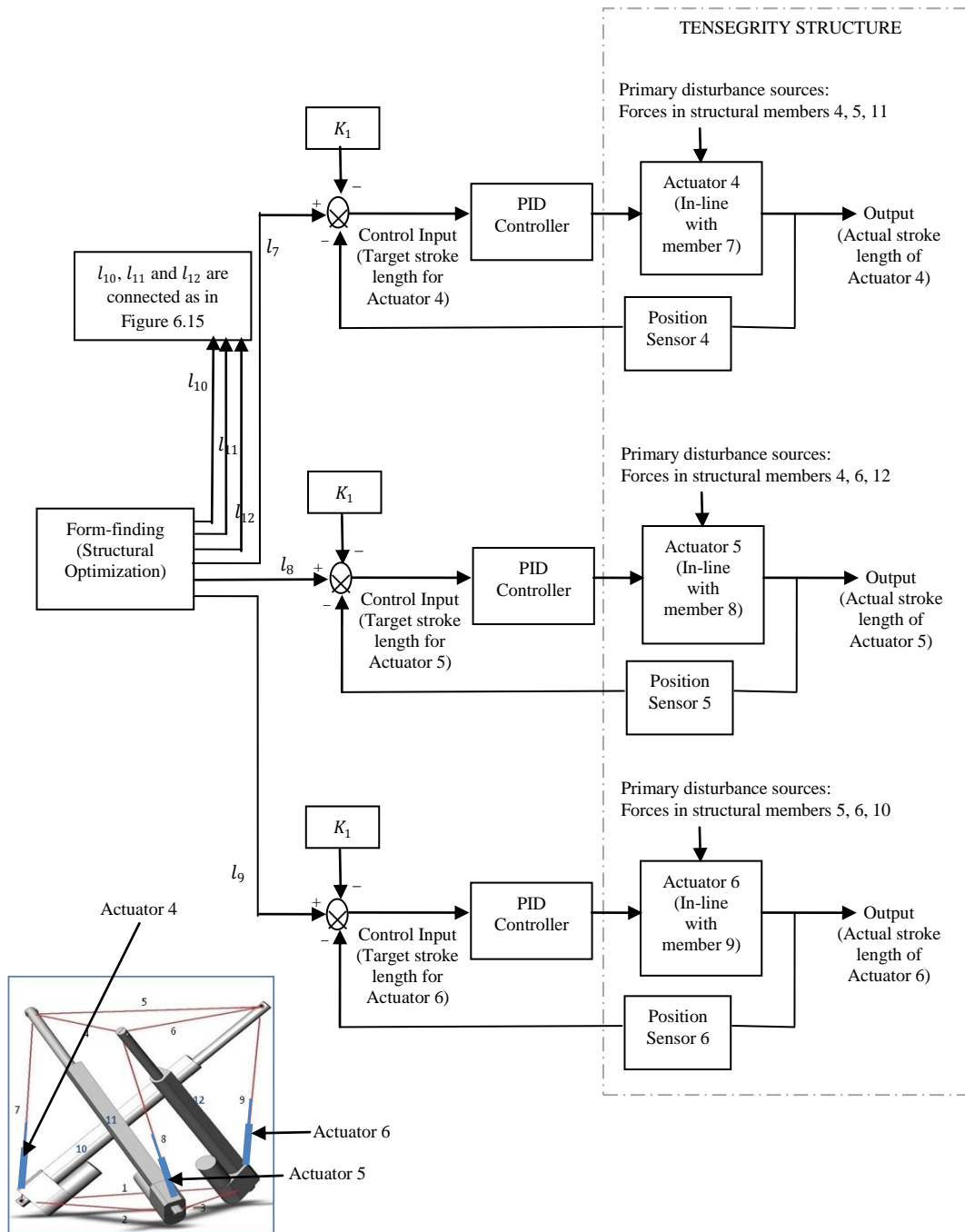


Figure 6.16: Control strategy for the multistable 3-bar tensegrity prism involving multiple SISO control loops (the bottom nodes are rigidly attached to the base)

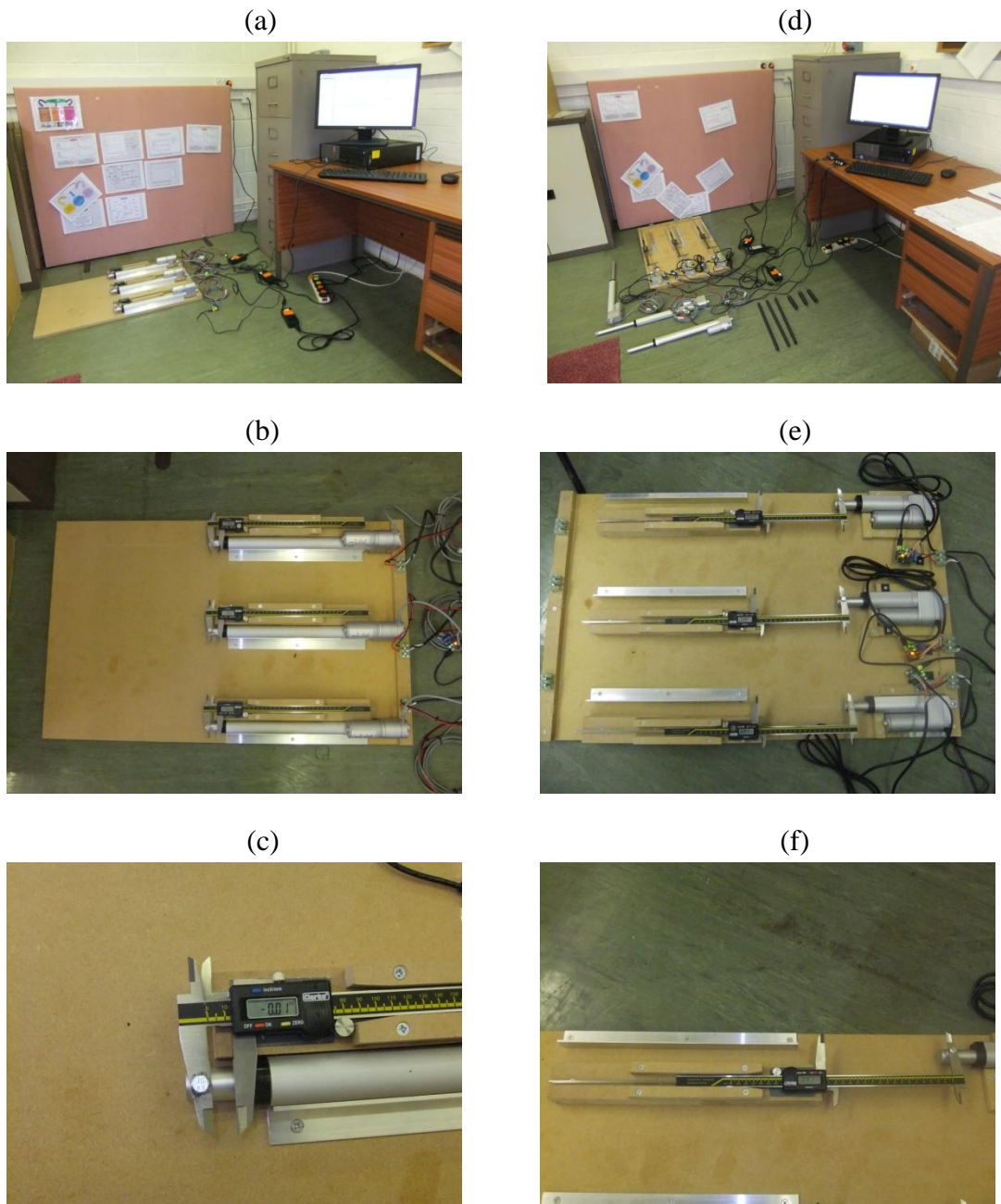


Figure 6.17: Pictures of the set-up for the calibration of the 6 electromechanical actuators

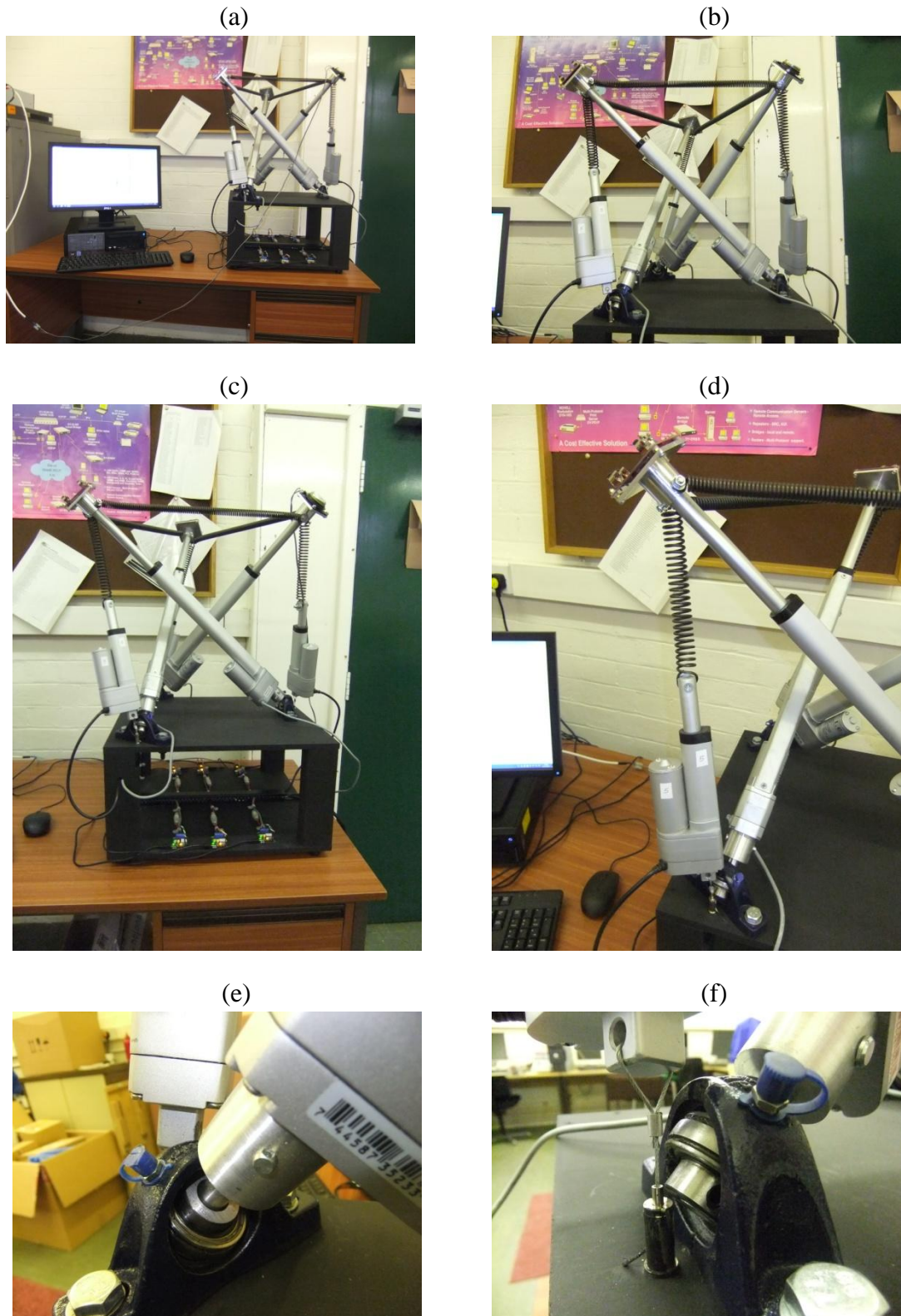


Figure 6.18: Pictures of the final structure after assemblage of all the constituent components

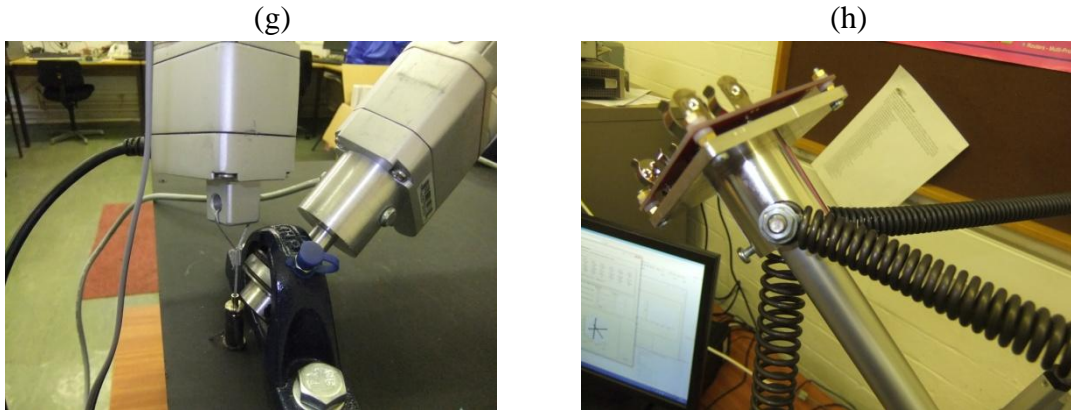


Figure 6.18 (continue): Pictures of the final structure after assemblage of all the constituent components

As should be obvious from Figures 6.15 and 6.16, the main sources of interaction between each SISO system are the forces acting between the structural members that link these SISO systems together. Thus, the fundamental assumption that disturbances (primarily, forces due to the links) for each SISO system are independent inputs of the SISO systems is, strictly speaking, not very accurate. And also, the major drawback of the architecture is the absence of the force feedback. The advantage of the architecture lies in the ease to design, implement and maintain the computer controlled structural system in a straight forward manner. It is also a good place to start controller design before introducing a multivariable control system approach of the next chapter.

Figures 6.19 (a) and (b) show the plots of the stroke length of the six actuators versus time as the physical 3-bar tensegrity structural system changes its shape through tensegrity structures of Figure 5.20 (a-d) and Figure 5.22 (a-c), respectively. Figures 6.20 (a) and (b) show the graphical user interface (GUI) developed as part of this project using MATLAB graphical user interface development environment (GUIDE) for the deployment and the six-DOF position control systems of the multistable 3- bar tensegrity structural system, respectively.

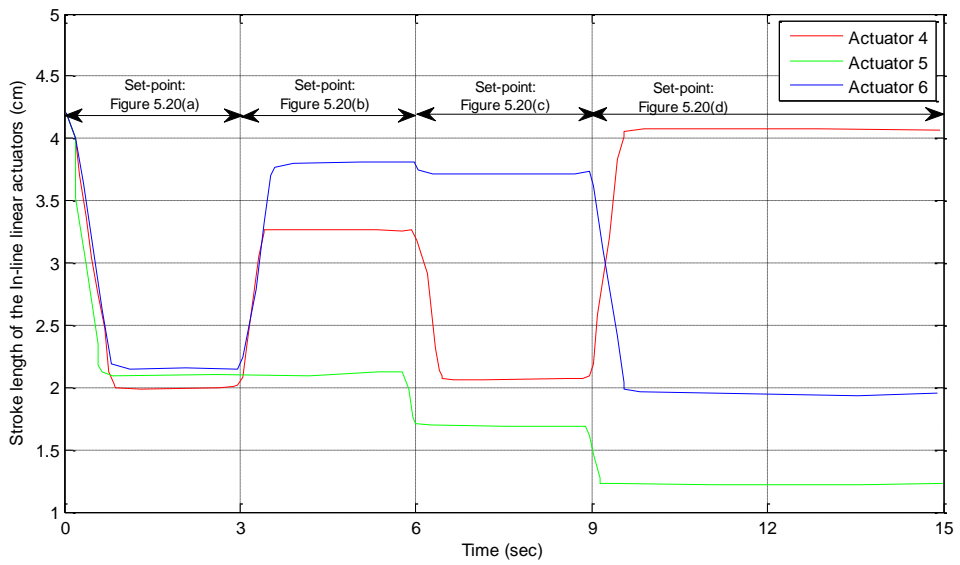
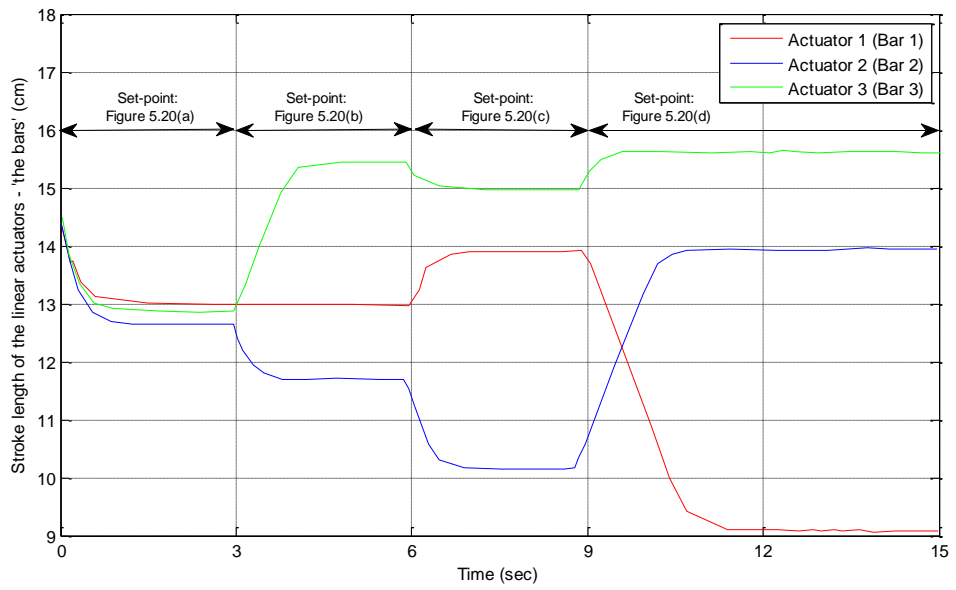


Figure 6.19 (a): The plots of the stroke lengths versus time as the multistage 3-bar tensegrity structural system changes its shapes through tensegrity structures 5.20 (a), (b), (c) and (d).

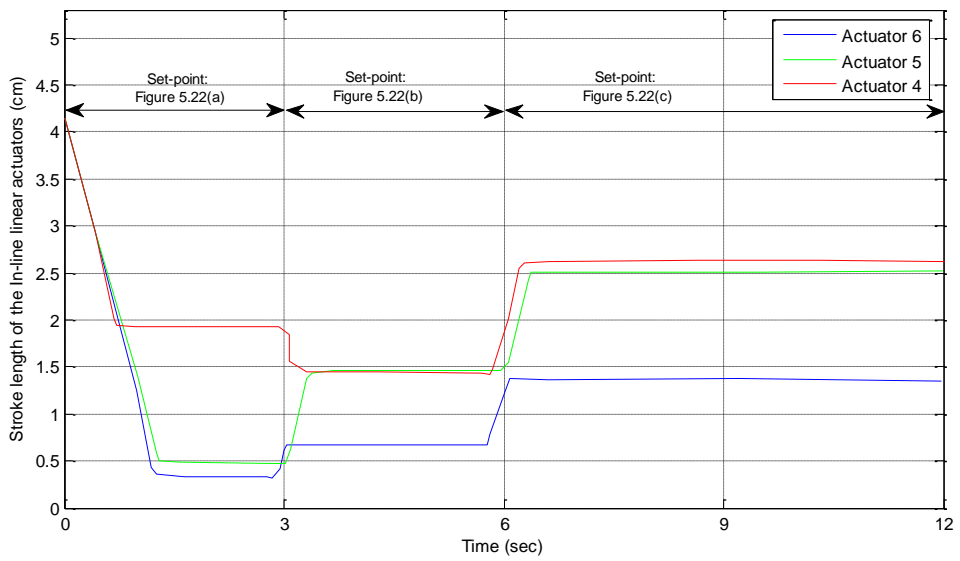
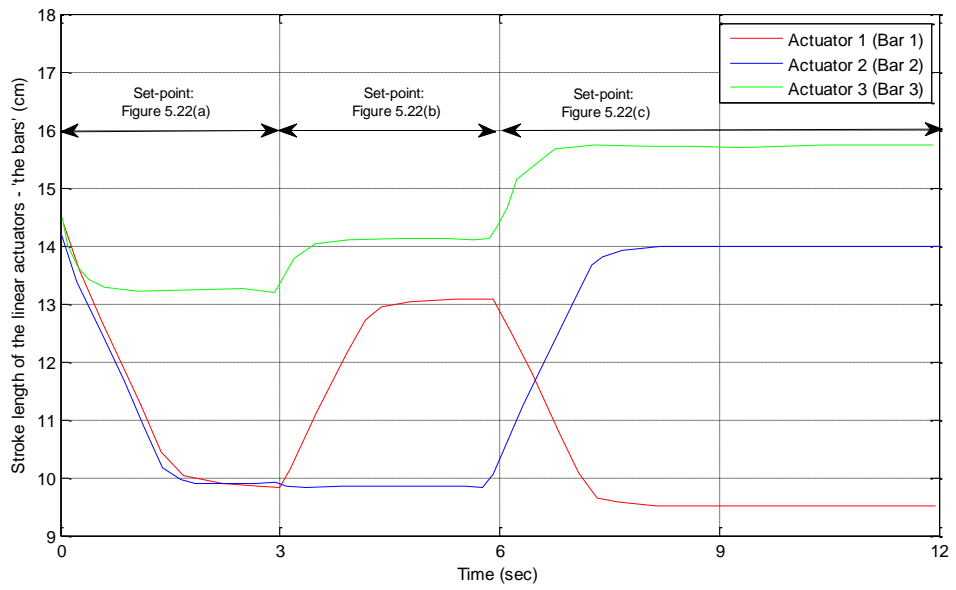
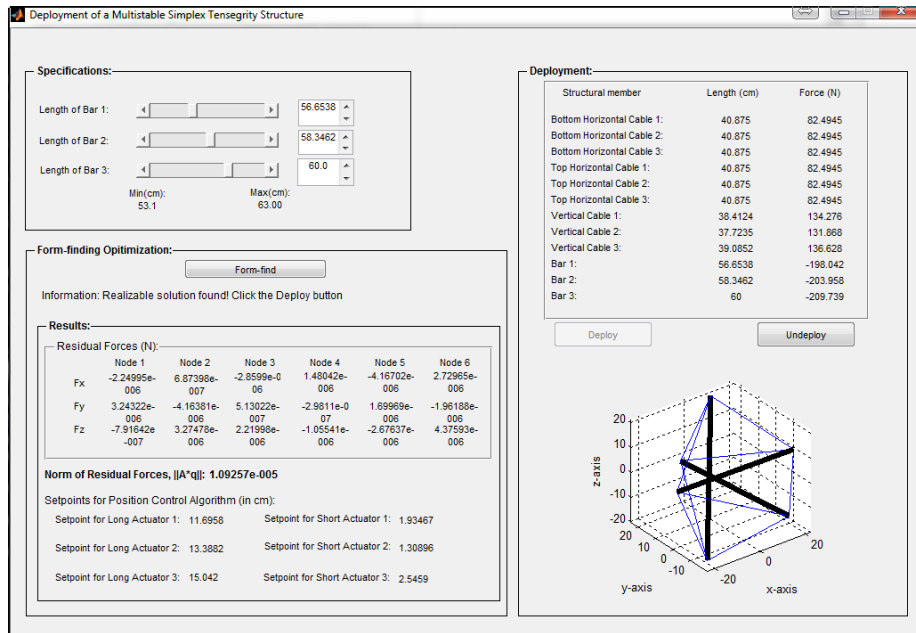
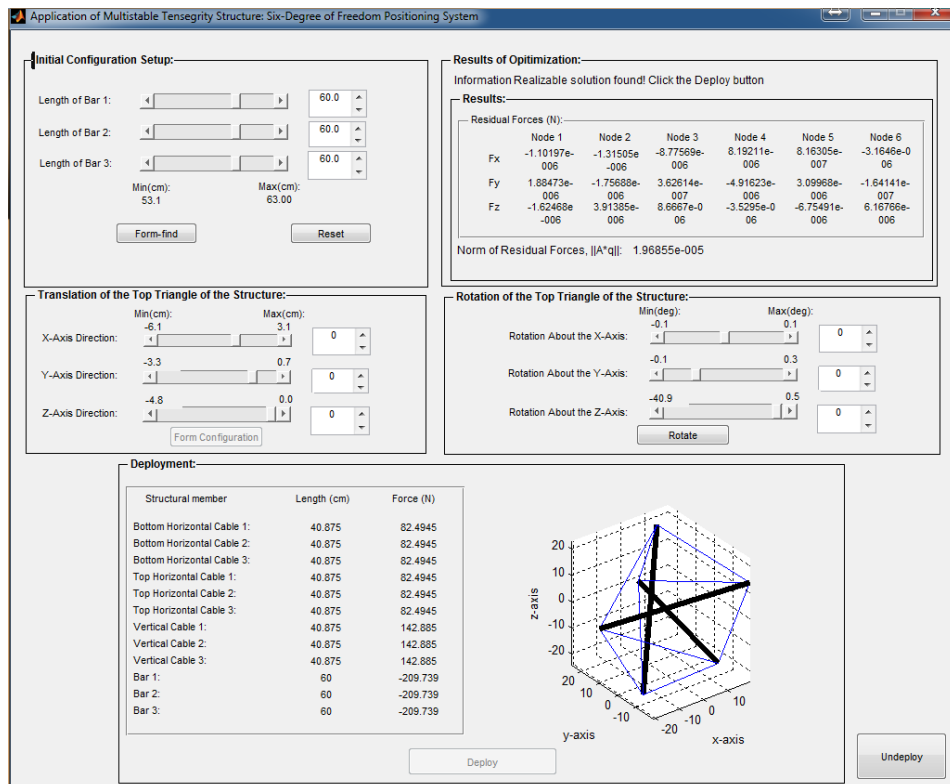


Figure 6.19 (b): The plots of the stroke lengths versus time as the multistage 3-bar tensegrity structural system changes its shapes through tensegrity structures 5.22 (a), (b) and (c).



Figures 6.20 (a): A graphical user interface developed using MATLAB graphical user interface development environment (GUIDE) for deployment of the 3-bar tensegrity prism



Figures 6.20 (b): A graphical user interface developed using MATLAB graphical user interface development environment (GUIDE) for the six-DOF position control system of the 3-bar tensegrity prism

6.4 Modelling and Simulation of the 3-bar Tensegrity Structural System

In this section, the dynamic models and analyses of the three 3-bar tensegrity structures (a), (b) and (c) shown in Figure 6.21 will be presented. Figure 6.21 (a) shows a standard tensegrity structure whose cables and bars are made with copper wires and hollow steel bars, respectively; Figure 6.21 (b) is the monostable 3-bar tensegrity prism considered in Section 5.3.2; and Figure 6.21 (c) is the multistable 3-bar tensegrity prism considered in Section 5.3.3. These three structures have the same geometries and tension coefficients as those of the initial 3-bar tensegrity prism introduced in Chapter 5 and, for the current analysis, the three bottom nodes of each of these structures are rigidly attached to the base. The material and physical properties of these structures are also given in Figure 6.21. It will be assumed that the structural members are connected at the nodes in pin-jointed manner. The lumped mass matrix of the i^{th} structural member with length l_i , cross-sectional area A_i , and mass density ρ_i , in local coordinate system for the three structures in Figure 6.21 are as follows:

- Structure (a):
$$m_i = \frac{\rho_i A_i l_i}{2} \begin{bmatrix} 1 & 0 \\ 0 & 1 \end{bmatrix} \quad (6.10)$$

- Structures (b) and (c):
$$m_i = \frac{\bar{m}_i}{2} \begin{bmatrix} 1 & 0 \\ 0 & 1 \end{bmatrix} \quad (6.11)$$

The transformation of Equations (6.10) and (6.11) to the global coordinate system to obtain the global mass matrix M of the FEM is computed using Equations (3.42) and (3.43).

Furthermore, assuming structural members undergo only linear elastic axial deformation, the global stiffness matrix K is computed using Equations (3.24-3.26). For the three tensegrity prisms of Figure 6.21, the values of the parameter π_i'' in Equations (3.26) are computed using the following equations:

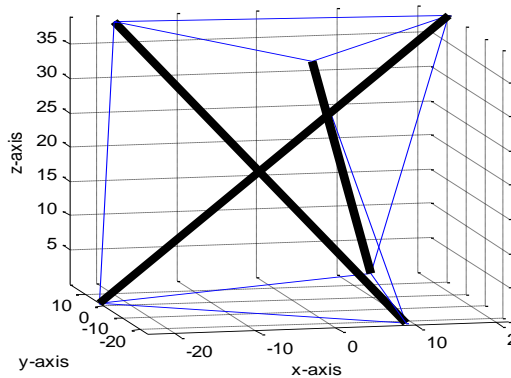
- Structure (a):

$$\pi_i'' = \frac{A_i E_i}{l_i} \quad (6.12)$$

- Structures (b) and (c):

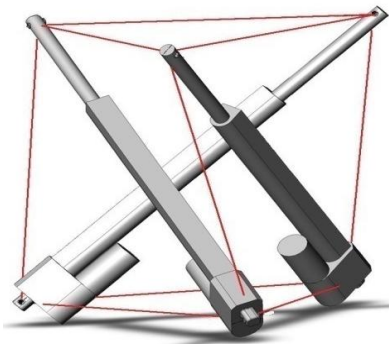
$$\pi_i'' = 38.155 \text{ N/cm for } i = 1, 2, \dots, 9; \quad \pi_i'' = \frac{A_i E_i}{l_i} \quad \text{for } i = 10, 11, 12 \quad (6.13)$$

(a) A standard 3-bar tensegrity prism



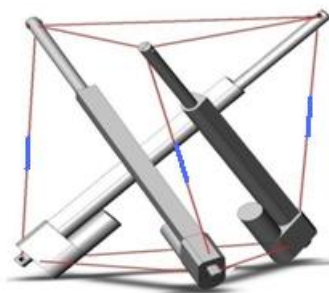
Structural Member	Cables (1 - 9)	Bars (10 - 12)
Area, A (m^2)	1.5×10^{-6}	6×10^{-6}
Young's Modulus, E (N/m^2)	117×10^9	200×10^9
Mass density, ρ (Kg/m^3)	8920×10^{-2}	7850×10^{-2}

(b) The monostable 3-bar tensegrity prism



Structural Member	Cables (1 - 6)	Cables (7 - 9)	Bars (10 - 12)
Area, A (m^2)	-	-	6×10^{-6}
Young's Modulus, E (N/m^2)	-	-	200×10^9
Stiffness Constant (N/cm)	38.115	38.115	-
Mass (Kg)	0.1984	0.1879	1.5876

(c) The multistable 3-bar tensegrity prism



Structural Member	Cables (1 - 6)	Cables (7 - 9)	Bars (10 - 12)
Area, A (m^2)	-	-	6×10^{-6}
Young's Modulus, E (N/m^2)	-	-	200×10^9
Stiffness Constant (N/cm)	38.115	38.115	-
Mass (Kg)	0.1984	$0.0573 + 1.1623 = 1.2203$ (spring + inline actuator)	1.5876

Figure 6.21: A standard, a monostable and a multistable 3-bar tensegrity structures

From Section 3.2.2, the dynamic model of each of the three structural systems is written in the modal form as given in Equation (3.55). Assuming that the damping constant for each mode is $\zeta_j = 0.02$ for $j = 1 - 9$ (having applied the boundary conditions) and $\zeta = \text{diag}(\zeta_j)$ and choosing the generalized (modal) displacements and velocities as the state variables ($x_1 = \Phi(t)$ and $x_2 = \dot{\Phi}(t)$) for each of these structural systems, the representation of Equation (3.55) is written in the state differential form as given in (3.76). If the measured outputs of the structural systems are displacements, the modal and nodal displacements are respectively computed using the following equations:

$$y = \eta = [I \ 0] x \quad , \quad \Phi(t) = \bar{\Phi} y \quad (6.14)$$

Figure 6.22 shows the plots of nodal displacements versus time for the three structures in Figure 6.21 when three vertically downward loads, each of 100 N, are suddenly placed at nodes 4, 5, and 6 at time, $t = 0$ sec with zero initial nodal displacements. The simulations of Figure 6.22 show marked differences among the dynamic responses of the three structural systems. In particular, the difference in the dynamic behaviours of the monostable (Figure 6.21 (b)) and the multistable (Figure 6.21 (c)) tensegrity prisms is due to the additional weight that the electromechanical actuators added to the vertical cables of the multistable tensegrity prism. It is important to note that the linearised models of the three structural systems were obtained at the same equilibrium point of 60 cm – 60 cm – 60 cm bar lengths (that is, the length of each of the three bars is 60 cm) of the initial 3-bar tensegrity prism. Also, the frequency response plots of the three structures of Figure 6.21 are shown in Figure 6.23.

Consider the linear models of the four structures of Figure 5.20 (a), (b), (c) and (d) which are all valid tensegrity structures obtained by carrying out translation operations (as explained in Section 5.5) for the top triangle of the multistable tensegrity prism of Figure 6.21 (c), to obtain the linear models of these four structures, the structure of Figure 6.21 (c) is linearised around the equilibrium points of bar lengths 58.344 cm – 57.9348 cm – 58.0368 cm, 8.3396 cm – 56.8108 cm – 61.2264 cm, 59.5695 cm – 54.9991 cm – 60.4836 cm, and 53.7535 cm – 59.5989 cm – 61.4254 cm, respectively, the simulations of the responses of these four linear models to the same loading and initial conditions as those of the models used for the simulations in Figure 6.22 are shown in Figure 6.24.

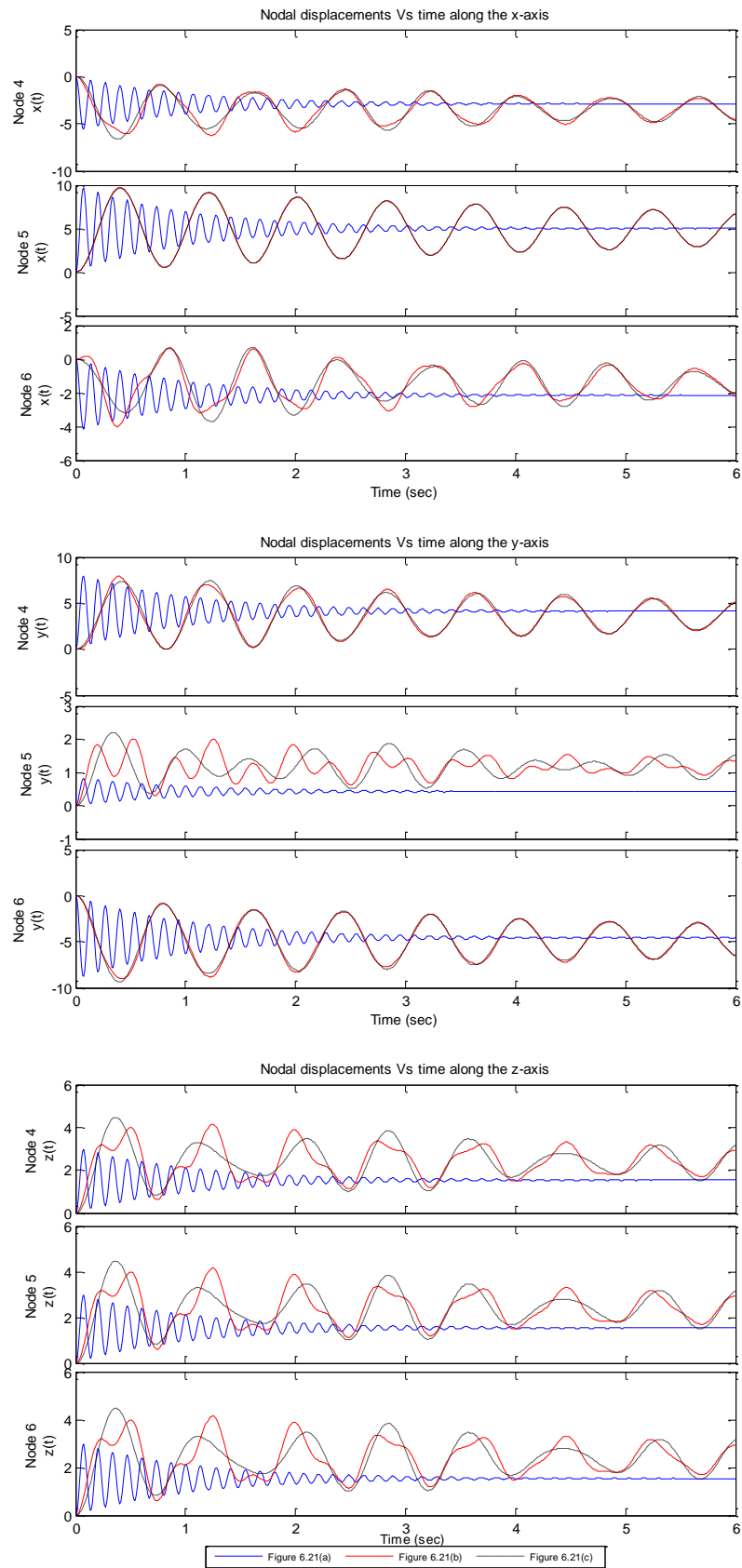


Figure 6.22: Dynamic response plots: The plots of nodal displacements (cm) Vs time (sec) of the structures of Figure 6.21 (a), (b) and (c)

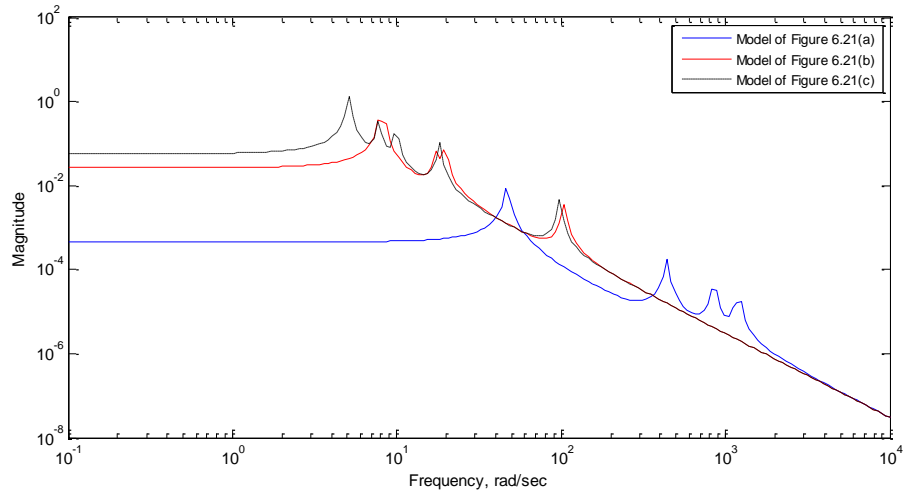


Figure 6.23: Frequency response plots of the structures of Figure 6.21 (a), (b) and (c)

6.5 Discussions

The preceding section completes the design and physical realization (began in the preceding chapter) of the prototype 3-bar multistable tensegrity structural system proposed in this thesis. The control algorithm implemented in this chapter has been used under the assumptions that the magnitudes of the disturbance and the level of interaction among the six independent SISO systems are small, the springs designed in Sections 5.3.2 and 5.3.3 have exactly the specified stiffness constants, the frictional force at the joints are negligible and the geometric configuration of the structural assembly is correct to at least 10^{-4} m. Clearly, these assumptions are very stringent. In particular, the structural model of a tensegrity structure is also a function of member forces, and thus, it is indispensable to have a force-feedback (or an estimation of the member forces from the measured geometric parameters) to ensure the accurate control of the tensegrity structural system by compensating for, firstly, the inaccuracies in the spring designs, and secondly, the non-negligible high level of coupling among the six independent SISO controllers which is due to the forces acting between the structural members linking these SISO systems together.

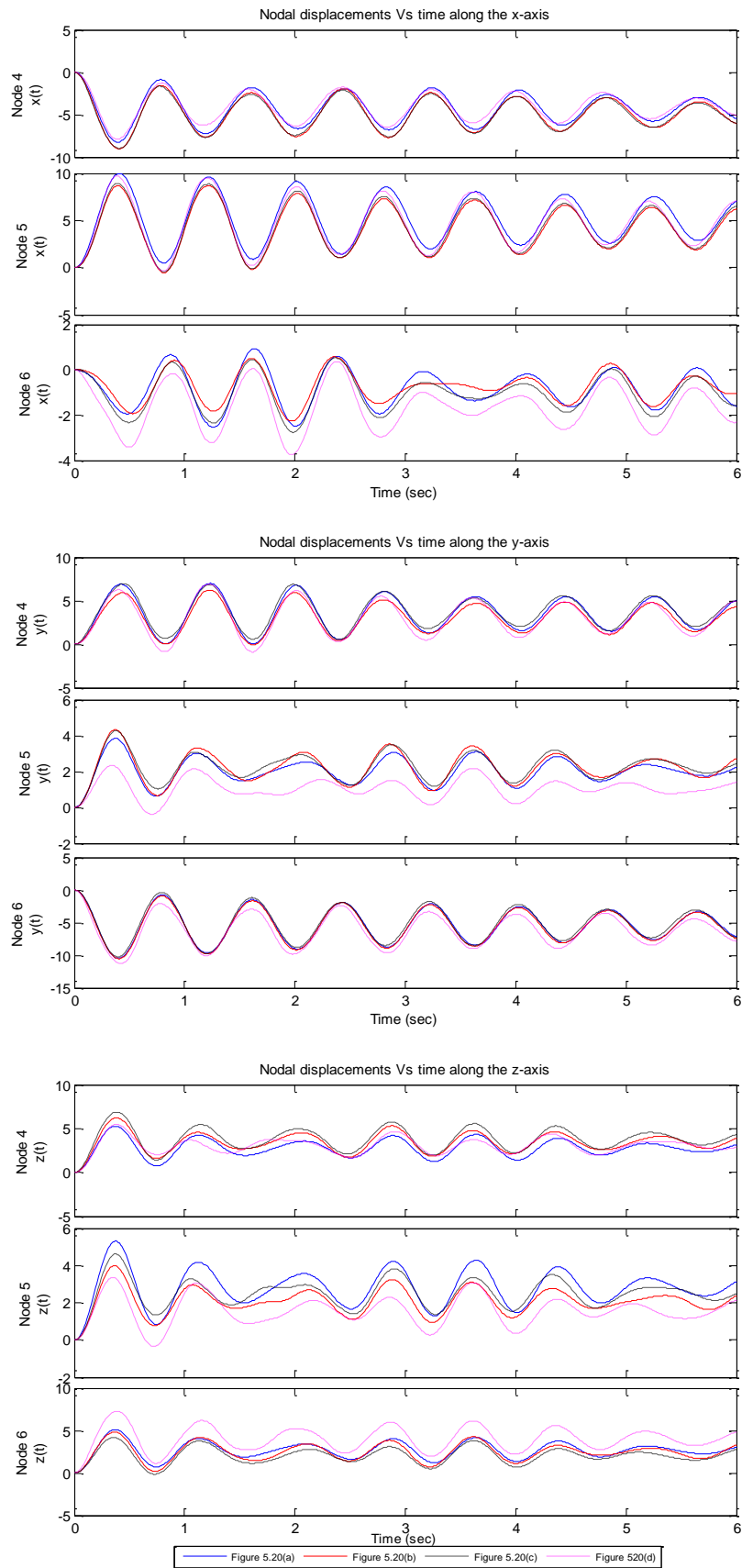


Figure 6.24: Dynamic response plots: The plots of nodal displacements (cm) Vs time (sec) of the structures of Figure 5.20 (a), (b), (c) and (d)

6.6 Summary

In this chapter and the preceding one, the feasibility of realizing a tensegrity structure using a given set of structural members and a predetermined initial structural configuration has been demonstrated. There are three main tasks involved in the realization process. The first task entails the components design and structural optimization of the 3-bar initial tensegrity prism; this was covered in the preceding chapter. The second task involves the configuration of the hardware and the control architecture, and the third task is associated with the implementation of the control algorithm and the design of application software user interfaces. These last two tasks have been presented in this chapter. Details of the hardware, the hardware configuration, the serial communication protocol using the USB interface and the implementations of the control system architecture and algorithm for the initial 3-bar multistable tensegrity structural system designed was given. This chapter concludes by developing the mathematical models and carrying-out the structural analyses of the mono- and multi-stable tensegrity structures designed using realistic structural parameters. The next chapter will introduce a multivariable control scheme for the control of tensegrity structures in general.

Chapter 7

CONTROL SYSTEM DESIGN FOR TENSEGRITY STRUCTURES

7.1 Introduction

In this chapter, the active control of tensegrity structures is presented in a multivariable and centralized control context unlike in the preceding chapter where the primary concern was the control of the 3-bar multi-stable tensegrity structure which was achieved through decentralized (independent) multiple SISO control systems.

In the field of control of active structures, the choice of the measured output divides active structural systems into two: collocated and non-collocated systems. Collocated control systems are those in which actuators and sensors are paired together for the suppression of vibration requiring low amount of force typically. Non-collocated control systems are commonly used as high-authority controllers which, in addition to providing damping forces, are capable of making structural systems undergo significant movement (shape change) often requiring the use of powerful actuators to provide significant amount of force. Consequently, the control system design in this chapter is divided into these two classes of controllers.

In relation to the collocated controller, a new method is presented in the determination of the feedback gain to reduce the control effort as much as possible while the closed-loop stability of the system is unconditionally guaranteed. For the non-collocated control systems, the most successful controller design used in the field of active structures, the LQG (Linear system, Quadratic cost, Gaussian noise) controllers [129], which are suitable for both collocated and non-collocated control systems is applied to actively control tensegrity structural systems for vibration

suppression (low-authority controllers) and precise positioning or tracking (high-authority controllers). The chapter concludes with a detailed discussion on the findings in this chapter and their relationships with the other chapters of this thesis and other previous work on active control of flexible structures, in general, and tensegrity structures, in particular.

7.2 Collocated Control of Tensegrity Structures

Let the system (A, B, C, D) be the linear time-invariant model of a structural system and consider a simple feedback control system with a constant feedback gain K as shown in Figure 7.1, the control problem for this system is to find the value of K for which the performance of the system is enhanced. Performance here denotes the stabilization of the system (if the system is unstable) and/or improvement of its stability to ensure that transient phenomenon dies down sufficiently fast. The control law for the system in Figure 7.1 can be written as follows:

$$u = -Ky + r \quad (7.1)$$

where y is the measured output of the system, r is the reference input and z is the controlled output. Also relating to Figure 7.1, depending on whether displacement or velocity is the controlled variable, H is equal to $[I \ 0]$ or $[0 \ I]$, respectively (I is the identity matrix), and many other choices of H are possible.

In the field of control of active structures, the choice of y divides active structural systems into two: collocated and non-collocated systems. On the one hand, collocated control systems are those in which actuators and sensors are paired together (making it easy for a single structural member to act as an actuator and a sensor simultaneously) and are characterized by having alternating poles and zeros along the imaginary axis [129]. Collocated controllers form a class of low-authority controllers that are used for active damping to suppress vibration of a structural system with typically low amount of force [133]. On the other hand, non-collocated control systems are those systems in which sensors and actuators need not to be paired together and may be placed at different locations, making it possible to position sensors (actuators) at the best possible location that will enhance system performance given that the actuator (sensor) locations are fixed [196]. Due to the high degree of flexibility in choosing sensor/actuator

locations in non-collocated systems, they are commonly used as high-authority controllers which, in addition to providing damping forces, are capable of making structural systems undergo significant movement (shape change) often requiring the use of powerful actuators to provide significant amount of force; as a result, these controller are better suited for applications where the structural system is required to track a given reference [133].

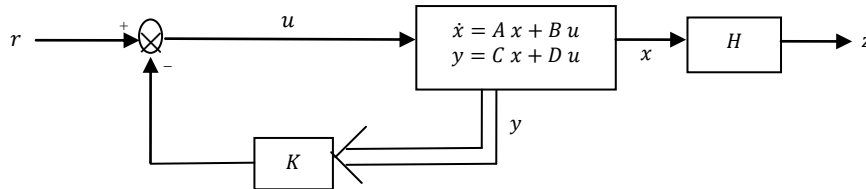


Figure 7.1: Assumed structural system for controller design

The transfer functions of flexible structures (such as tensegrity structures) are known to be positive real [197]. It should be noted that the term positive real denotes the dissipative nature of the structural system and the terms dissipative, passive, hyper stable and positive real are synonymous [133], [198]. As such, the controllability and observability grammians of these structural systems are nonsingular. The algebraic criterion for a matrix of transfer function of the system (A, B, C, D) to be positive real can be written as follows [199]:

$$A^T P + PA = -Q^T Q \quad (7.2a)$$

$$B^T P = C - W^T Q \quad (7.2b)$$

$$D + D^T = -W^T W \quad (7.2c)$$

where Q and W are real matrices and P is a real symmetric positive definite matrix. For the case where the feed-forward matrix D equals zero, $W^T = W = 0$; therefore, Equation (7.2) can be written as:

$$A^T P + PA = -Q^T Q \quad (7.3a)$$

$$B^T P = C \quad (7.3b)$$

To obtain the control law for a low-authority controller with zero reference input ($r = 0$) using (7.1), the measured output matrix C needs to be determined first. The measured output is obtained as follows:

$$y = Cx \quad (7.4)$$

Consider the following three cases of choosing the matrix C :

Case 1: Let $Q = C$; substituting this value of Q in Equation (7.3a) and comparing the resulting equation with Equation (4.10) gives the following expression:

$$P = W_o \quad (7.5)$$

where W_o , as in Chapter 4, is the observability grammian. Thus, equations (7.3b) and (7.1) can respectively be written as follows:

$$C = B^T W_o \quad (7.6)$$

$$u = -KB^T W_o x \quad (7.7)$$

Moreover, the choice of $Q = C$ signifies that, once the actuators are chosen, the sensory outputs (measured outputs) are a weighted sum of the row vectors of $B^T W_o$. It should be noted that since the computation of W_o requires the availability of matrix C (see Equation (4.6), for instance), matrix C is taken to be equal to matrix H for computing W_o ; subsequently, this value of W_o is then used to compute C using Equation (7.6).

Case 2: Let $Q = (PB)^T$; substituting this value of Q in Equation (7.3a), and noting that $P = P^T$, and comparing the resulting equation with Equation (4.9) gives the following equation:

$$P = (W_c)^{-1} \quad (7.8)$$

where W_c is the controllability grammian. Thus, in this case, equations (7.3b) and (7.1) can respectively be written as follows:

$$C = B^T (W_c)^{-1} \quad (7.9)$$

$$u = -KB^T (W_c)^{-1} x \quad (7.10)$$

The choice of $(PB)^T$ signifies that, once the outputs to be measured (sensor locations) are chosen, the actuator forces are a weighted sum of the row vectors of $B^T (W_c)^{-1}$.

Case 3: Let $Q = (-A - A^T)^{1/2}$; substituting this value of Q in Equation (7.3a) gives the following expression:

$$A^T P + PA = A + A^T \quad (7.11)$$

From (7.11), the value of P can be expressed as follows:

$$P = I \quad (7.12)$$

In this case, equations (7.3b) and (7.1) can respectively be written as follows:

$$C = B^T \quad (7.13)$$

$$u = -KB^T x \quad (7.14)$$

The third case (Case 3) is the most commonly used closed-loop configuration for collocated systems [133]. Moreover, the sensor outputs are a weighted sum of the row vectors of B^T . In particular, the choice of $C = B^T$ in Equation (7.13) signifies that the stability of the closed-loop system is strictly positive real [200], [201]. However, as noted in [202], stability does not imply good performance.

The task of determining the control law for each of the preceding three cases is now reduced to determining the value of the constant state-feedback gain K ; it should be noted that if K is diagonal, the constant is a proportional state-feedback gain. The equations for the closed-loop systems given by the three cases just considered are as follows:

$$\text{Case 1: } \dot{x} = (A - BKB^T W_o)x \quad (7.15a)$$

$$y = B^T W_o x \quad (7.15b)$$

$$\text{Case 2: } \dot{x} = (A - BKB^T W_c^{-1})x \quad (7.16a)$$

$$y = B^T W_c^{-1} x \quad (7.16b)$$

$$\text{Case 3: } \dot{x} = (A - BKB^T)x \quad (7.17a)$$

$$y = B^T x \quad (7.17b)$$

From equations (7.15-7.17), there are two issues to be considered: The first issue relates to the pairing of the measured outputs and the forces applied by the actuators; for example, given the choice between using displacement or velocity sensors, which of these sensors is the most suitable with force actuators placed at fixed locations? The second issue relates to the use of the properties of the closed-loop dynamics for

obtaining the value of K that will enhance the performance of the system; these closed-loop dynamics for the three cases are defined by the following matrices, respectively:

$$A_{c1} = A - BK B^T W_o \quad (7.18a)$$

$$A_{c2} = A - BK B^T W_c^{-1} \quad (7.18b)$$

$$A_{c3} = A - BK B^T \quad (7.18c)$$

More so, the output matrices of the three cases can be deduced from equations (7.15-7.17) as follows:

$$C_{c1} = B^T W_o \quad (7.19)$$

$$C_{c2} = B^T W_c^{-1} \quad (7.20)$$

$$C_{c3} = B^T \quad (7.21)$$

It should be noted that the upper-half of the partition of the input matrix B of the state-space model of a structural system, given by equations (3.68 – 3.71) or (3.75 – 3.77) for example, is equal to zero. Consequently, the actuator forces are effectively located only at the lower-half partition of the input matrix B and, as a result, the left-half of the output matrix of the velocity measurement representation (given by equation (3.73) or (3.79)) is zero while its right-half partition is non-zero; this right-half partition is the location of the velocity measurements. Thus, it is most convenient that the non-zero lower-half partition of B and the non-zero right-half partition be paired, or ‘collocated’, together; this means, actuator forces and velocity sensors should be paired together for the design of a collocated controller in this case. In other words, in this pairing arrangement, the right-half partition (where the velocity measurements are located) of the matrices C_{c2} and C_{c3} will generally be non-zero while the left-half partition of these matrices will be equal to zero (that is, for cases 2 and 3).

As for Case 1, it should be observed that the computation of C_{c1} requires the availability of the input matrix B and the observability grammian W_o ; W_o in turn is dependent on the output matrix C (see equations (4.6), (4.8) and (4.10)). This implies that the sensor location and actuator locations are simultaneously known and available. Moreover, if velocity sensors are used, the velocity measurements is collocated with the actuator forces as in Cases 2 and 3 since the left-half partition of C_{c1} will be zero and the right-half partition will contain the velocity measurement. However, if displacement sensors are used, both the left- and right-half partitions of C_{c1} are generally non-zero.

Thus, it is not possible to make a general statement about collocation requirements in this case of displacement sensors for Case 1. As for both cases 2 and 3, the displacement sensors results in zero left-half partition and non-zero right-half partitions of C_{c2} and C_{c3} .

Next, the value of K can be determined by any suitable pole-placement technique; this involves the placement of the closed-loop poles (that is, the characteristic values of the closed-loop matrices) of Equation (7.18) at desirable locations in order to stabilize the closed-loop system, shape the transient response, enhance the robustness of the closed-loop system and/or minimize the norm of the feedback gain that was due to the pole-placement [203–205]. Pole assignment is one of the central problems in control systems design and there are numerous pole-placement techniques that have been proposed in the literature covering both the theoretical viewpoint (for example, [149], [200], [206]) and the computational perspective (for example, [207–211]) of pole-placement; see [212] for a brief account of some of these techniques, for example. In relation to collocated and other low-authority active flexible structural systems where robustness is difficult to achieve primarily due to many closely-spaced low-frequency lightly damped modes [213], pole-placement techniques are used to design constant gain controllers that will ensure that the transient phenomenon of the structure dies down sufficiently fast. In the likely event of un-modelled dynamics and parametric uncertainties, the strictly passive collocated controllers achievable with pole-placement algorithms guarantees robust stability [200], [214], [215]. However, the prices to be paid (quantified by the amount of control effort) for using these pole-placement techniques for designing collocated controllers have not received much attention so far in the literature. Nonetheless, the issue of reducing the control effort as much as possible is of great importance since, as it is well-known, the further one moves the poles, the greater the gain (and, as such, the control effort) required.

In what follows, the problem of finding the value of K for which the control input are minimum while the closed-loop system response will approximate the response of a system whose closed-loop poles are at pre-defined locations in the complex plane will be addressed. For example, given that a closed-loop system \mathbb{P}_1 , with closed-loop dynamics $(A - BL)$ where L is the constant gain matrix, has the desired closed-loop poles at p_o (where p_o is chosen so that the closed-loop system is asymptotically stable; p_o is a vector whose elements are the individual poles), the task is to find the values of

K , if they exist, for the closed-loop systems \mathbb{P}_2 and \mathbb{P}_3 whose closed-loop matrices are given by the closed-loop matrices $(A - BKB^TW_c^{-1})$ and $(A - BKB^T)$ of cases 2 and 3, respectively. The optimal values of K in both cases should result in the minimum control inputs for systems \mathbb{P}_2 and \mathbb{P}_3 while, at the same time, ensure that the closed-loop responses of \mathbb{P}_2 and \mathbb{P}_3 match that of \mathbb{P}_1 as close as possible. Obviously, the system matrices A and B must be the same for the systems \mathbb{P}_1 , \mathbb{P}_2 and \mathbb{P}_3 for the solution to make any sense. It should be noted that, in order for stability to be unconditionally guaranteed (despite modelling error), the symmetric part of the constant feedback gain K must be positive semidefinite [207], [214], [215]. For a constant feedback gain satisfying $K = K^T$, for example, this positive semi-definiteness condition may be written as follows:

$$K \geq 0 \quad (7.22)$$

For convenience, let K be a diagonal matrix (that is, a constant proportional state-feedback gain) in the subsequent analysis. Thus, the problem of finding K may be written as the following optimisation problem:

$$\begin{aligned} & \text{minimize}_{k_i} \quad \text{Trace}(S) \\ & \text{such that} \quad K \geq 0 \end{aligned} \quad (7.23)$$

where $K = \text{diag}(k_i)$; it should be recalled that the closed-loop poles are the values of s such that $\det[sI - (A - BKC)] = 0$, and as such, S is a measure of the total system energy and it is a diagonal matrix of singular values of the closed-loop matrix \mathfrak{X} defined as follows:

$$\mathfrak{X} = \Sigma - (A - BKC) \quad (7.24)$$

where Σ is a diagonal matrix whose diagonal entries are the entries of vector p_o (that is, $\Sigma = \text{diag}(p_{o_i})$); C is the output matrix, which for cases 1, 2 and 3, is equal to C_{c1} , C_{c2} and C_{c3} (defined by equations (7.19), (7.20) and (7.21)), respectively; and S is obtained from \mathfrak{X} by singular value decomposition (SVD) that can be written in the following form:

$$\mathfrak{X} = \mathcal{E} S \mathcal{Z}^T \quad (7.25)$$

where \mathcal{E} and \mathcal{Z} are the left and right orthonormal matrices, respectively. More details on SVD can be found in Chapter 2 of this thesis. Thus, the optimization problem posed in

(7.23) attempts to minimize the total energy of the closed-loop system, thereby the control effort, by the relocation of the poles specified in vector p_o in the complex plane. Also, as in Chapter 2, the solution to the optimization problem can be computed using the interior-point method of solving linear and nonlinear convex optimisation problems. The effectiveness of employing the proposed optimization approach for computing K is demonstrated using the three structural systems of Figure 6.21 as examples. In each of these examples, the poles of the closed-loop matrix $(A - BL)$ specified in vector p_o is determined using the following principles [151], [216]: To reduce the control effort as much as possible, the low frequency modes (poles) are chosen so that the desired system behaviour (fast settling time, minimal steady-state error, etc) is achieved; each of the remaining poles is selected by increasing the damping σ_i while holding the frequency ω_i constant (where $s_i = \sigma_i + j\omega_i$ denotes the i^{th} pole location in the complex plane). Importantly, it should be noted that the example structural systems are completely controllable and observable – a condition necessary for the closed-loop poles of the LTI systems to be arbitrary assigned to any location in the complex plane (of course, with the restriction that complex poles appear in conjugate pairs) [151].

Hence, for each of the collocated structural systems of Figure 6.21, the velocity sensors are paired with force sensors as in Case 3. Thus, the output matrix for each of these systems is computed as follows:

$$C = B^T \quad (7.26)$$

Table 7.1 gives the eigenvalues of the open-loop structural systems, the entries of the vector p_o defined by the eigenvalues of $(A - BL)$, and the eigenvalues of the optimized closed-loop system $(A - BKC)$ obtained by finding solution to the optimization problem of (7.23).

Figure 7.2 shows the plots of the eigenvalues of A , $(A - BL)$ and $(A - BKC)$ in the complex plane. It should be noted that, while $K = \text{diag}(k_i)$ is computed by finding the solution of (7.23), L is obtained by a well-known pole-assignment algorithm given in [205]; in MATLAB[®], given A , B and p_o , the value of L can be obtained using the ‘place’ function. Thus, the values of the constant feedback gain K for the structural systems of Figure 6.21 (a), (b) and (c) obtained using the nodal models of these structural systems are respectively as follows:

Structure 6.21(a):

$$K = \text{diag}[0.0081 \quad 0.0000 \quad 0.0000 \quad 0.0001 \quad 0.0002 \quad 0.0000 \quad 0.0000 \quad 0.0069 \quad 0.0000]$$

Structure 6.21(b):

$$K = \text{diag}[0.0004 \quad 0.0695 \quad 0.1248 \quad 0.1776 \quad 1.2381 \quad 0.0000 \quad 0.4669 \quad 0.0000 \quad 0.3490]$$

Structure 6.21(c):

$$K = \text{diag}[0.0006 \quad 0.0081 \quad 0.1624 \quad 0.0000 \quad 1.7230 \quad 0.2810 \quad 0.3375 \quad 0.0000 \quad 0.6223]$$

Table 7.1: Poles of the open-loop and closed-loop structural systems for $C = B^T$

Structural System of Figure 6.21(a)

Open-loop eigenvalues: $\text{eig}(A)$ ($\times 10^{-3}$)	Entries of p_o : $\text{eig}(A - BL)$ ($\times 10^{-3}$)	Eigenvalues of the optimized closed-loop system: $\text{eig}(A - BKC)$ ($\times 10^{-3}$)
-0.0229 ± 1.1453i	-0.0300 ± 1.1453i	-0.2823 ± 1.1304i
-0.0009 ± 0.0468i	-1.0100 ± 0.4376i	-0.0674 ± 1.1864i
-0.0245 ± 1.2235i	-1.0100 ± 0.4376i	-0.0484 ± 1.1521i
-0.0245 ± 1.2235i	-1.0100 ± 0.0000i	-0.5353
-0.0088 ± 0.4376i	-0.0200 ± 0.8541i	-0.0052
-0.0088 ± 0.4376i	-0.0300 ± 1.2235i	-0.0390 ± 0.4047i
-0.0171 ± 0.8541i	-0.0300 ± 1.2235i	-0.0860 ± 0.4427i
-0.0171 ± 0.8549i	-0.0200 ± 0.8549i	-0.0175 ± 0.8557i
-0.0171 ± 0.8549i	-0.0200 ± 0.8549i	-0.0168 ± 0.8539i
		-0.0176 ± 0.8544i

Structural System of Figure 6.21(b)

Open-loop eigenvalues: $\text{eig}(A)$ ($\times 10^{-2}$)	Entries of p_o : $\text{eig}(A - BL)$ ($\times 10^{-2}$)	Eigenvalues of the optimized closed-loop system: $\text{eig}(A - BKC)$ ($\times 10^{-2}$)
-0.0209 ± 1.0453i	-0.0300 ± 1.0453i	-0.0195 ± 1.0453i
-0.0209 ± 1.0448i	-0.0250 ± 1.0448i	-0.0233 ± 1.0446i
-0.0209 ± 1.0448i	-0.0250 ± 1.0448i	-0.0218 ± 1.0449i
-0.0035 ± 0.1752i	-0.0400 ± 0.1752i	-0.0522 ± 0.1851i
-0.0039 ± 0.1970i	-0.1999	-0.0503 ± 0.1747i
-0.0039 ± 0.1970i	-0.1889	-0.0348 ± 0.1569i
-0.0016 ± 0.0778i	-0.1111	-0.1342
-0.0017 ± 0.0836i	-0.0450 ± 0.1970i	-0.0395 ± 0.0744i
-0.0017 ± 0.0836i	-0.0450 ± 0.1970i	-0.0526 ± 0.0688i
	-0.1001	-0.0607
	-0.1000	
	-0.1000	

Structural System of Figure 6.21(c)

Open-loop eigenvalues: $\text{eig}(A)$	Entries of p_o : $\text{eig}(A - BL)$	Eigenvalues of the optimized closed-loop system: $\text{eig}(A - BKC)$
-1.9585 ± 97.9035i	-2.0000 ± 97.9035i	-2.0026 ± 97.6372i
-1.9528 ± 97.6195i	-2.2000 ± 97.6195i	-2.0583 ± 97.7888i
-1.9528 ± 97.6195i	-2.2000 ± 97.6195i	-2.5841 ± 97.6608i
-0.1556 ± 7.7760i	-3.0000 ± 9.8868i	-2.3481 ± 17.7995i
-0.1978 ± 9.8868i	-5.1050	-4.4041 ± 16.2578i
-0.3632 ± 18.1567i	-6.8405	-0.6955 ± 9.6162i
-0.3632 ± 18.1567i	-8.2621	-4.2427 ± 7.3639i
-0.1026 ± 5.1311i	-2.0000 ± 18.1567i	-1.4898 ± 5.0262i
-0.1026 ± 5.1311i	-2.0000 ± 18.1567i	-0.7056 ± 5.0965i
	-9.9976	
	-10.1026	
	-10.1026	

It should be noted that the fact that some diagonal entries of K are zeros or small relative to others (given that K is a diagonal matrix) signifies the relative importance of the corresponding outputs (states) compared to other outputs. In other words, just as deduced from the results of Chapter 4 on modal reduction and actuator/sensor placement, some outputs measurements (sensor) and applied forces (actuators) that are of least importance can be eliminated from the structural system (without adversely affecting the effectiveness of the control system) to improve computation efficiency and reduce the overall cost of the control system (as a result of the reduced number of sensors and actuators that are now used).

The simulation results of the structural systems of Figure 6.21 (a), (b) and (c) for initial nodal velocities of $[0.5 \ 0.2 \ -0.4 \ 0.5 \ 0.2 \ -0.4 \ 0.5 \ 0.2 \ -0.4] \text{ cm}^2/\text{s}$ using the collocated controllers are shown in Figure 7.3. The actuator and sensor dynamics are assumed to be negligible in these simulations, and it should be recalled that these structural systems have nine degrees-of-freedom as previously noted in Chapter 6.

Furthermore, let the velocity sensors be collocated with the actuator forces as in Case 2, then the output matrix C is computed as follows:

$$C = B^T W_c^{-1} \quad (7.27)$$

For the value C in (7.27), Table 7.2 gives the eigenvalues of the open-loop structural systems, the entries of the vector p_o defined by the eigenvalues of $(A - BL)$, and the eigenvalues of the optimized closed-loop system $(A - BKC)$ obtained by finding solution to the optimization problem of (7.23) for the collocated structural systems of Figures 6.21 (a), (b) and (c). For these systems, Figure 7.4 shows the plots of the eigenvalues of A , $(A - BL)$ and $(A - BKC)$ in the complex plane. Thus, the values of the constant feedback gain K for the structural systems of Figure 6.21 (a), (b) and (c) obtained using the nodal models of these structural systems are as follows:

Structure 6.21(a):

$$K = \text{diag}[0.0000 \ 48.4046 \ 38.0578 \ 40.4674 \ 3.3089 \ 26.1115 \ 59.6831 \ 28.1385 \ 17.7762]$$

Structure 6.21(b):

$$K = \text{diag}[60.0921 \ 30.2421 \ 27.6791 \ 27.2953 \ 3.9270 \ 0.0000 \ 29.8015 \ 52.3344 \ 18.0592]$$

Structure 6.21(c):

$$K = \text{diag}[10.8886 \ 5.7095 \ 42.8892 \ 0.0003 \ 2.4016 \ 8.9294 \ 9.5676 \ 16.5308 \ 51.8550]$$

Also, Figure 7.5 shows the simulation results of the structural systems of Figure 6.21 (a), (b) and (c) with the same initial conditions (nodal velocities) and model parameters and assumptions as in Figure 7.3.

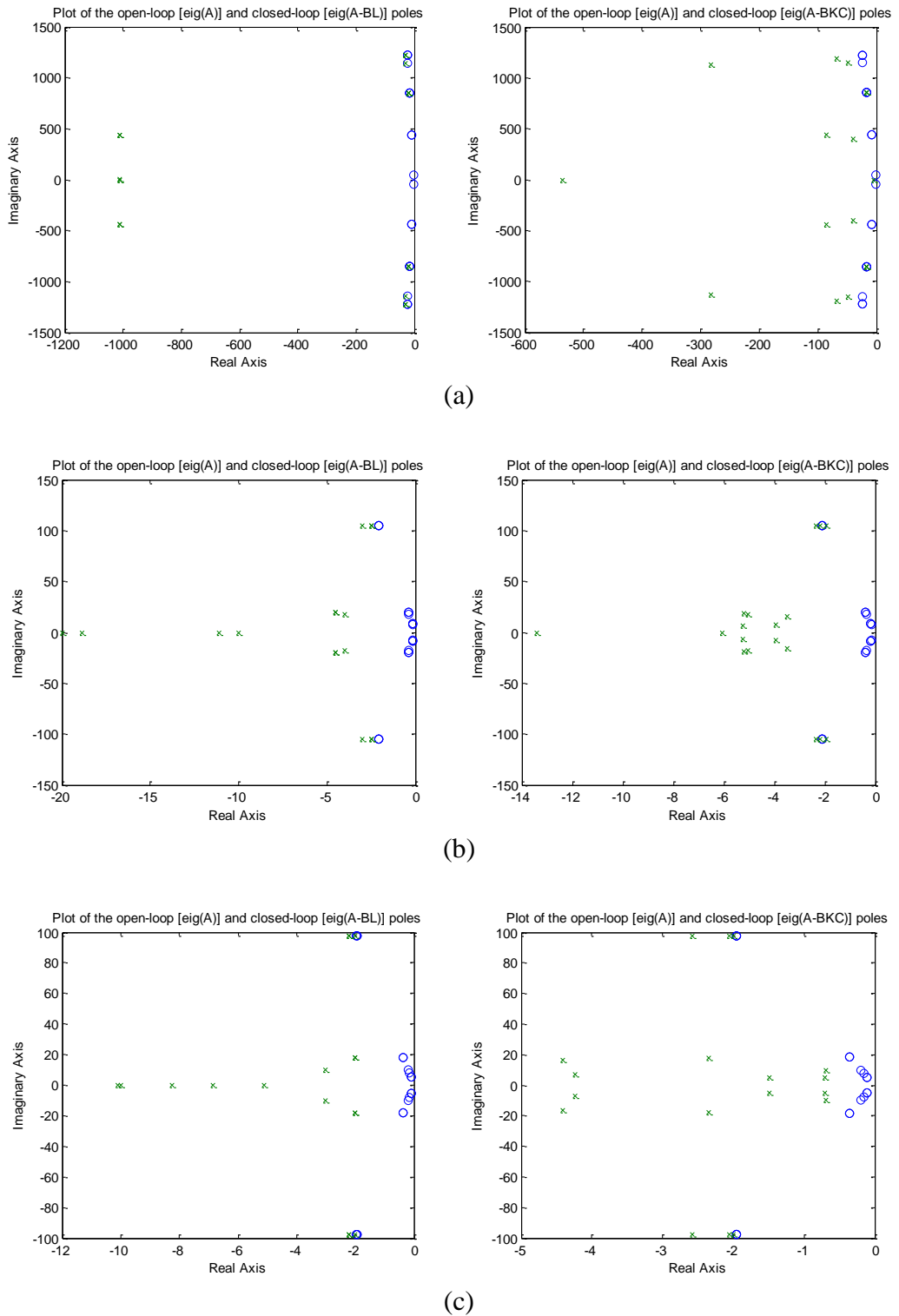


Figure 7.2: (a), (b) and (c) are the plots of the open- and closed-loop poles of the structural systems of Figure 6.21 (a), (b) and (c), respectively, in the complex plane for the output matrix $C = B^T$ ('o' – open-loop poles; 'x' – closed-loop poles).

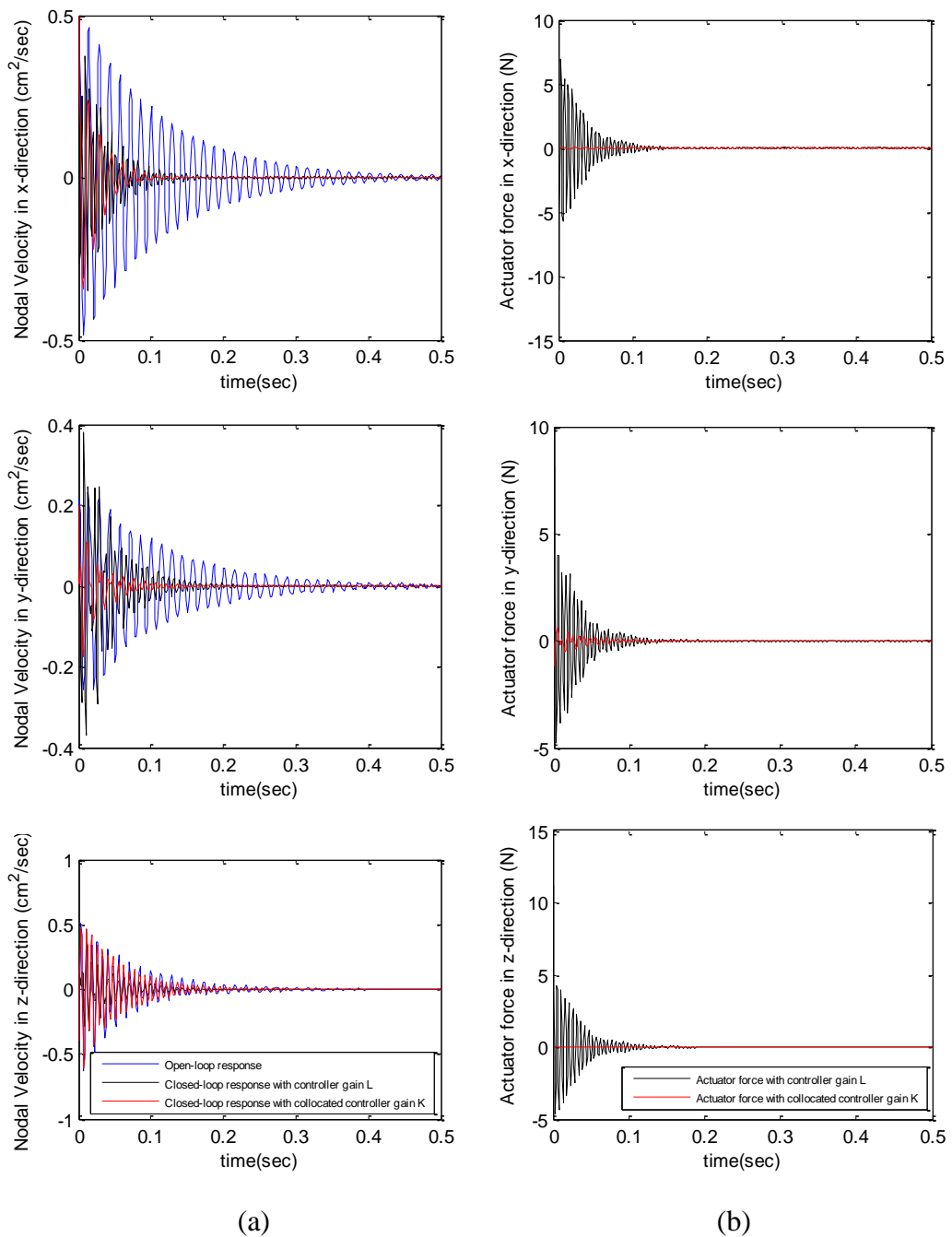


Figure 7.3 (a): (a) and (b) are the plots of the dynamic responses (nodal velocities [cm^2/s] Vs time [sec]) and the control efforts (actuator forces [N] Vs time [sec]) at Node 6 in the structural system of Figure 6.21 (a), respectively, for the output matrix $C = B^T$.

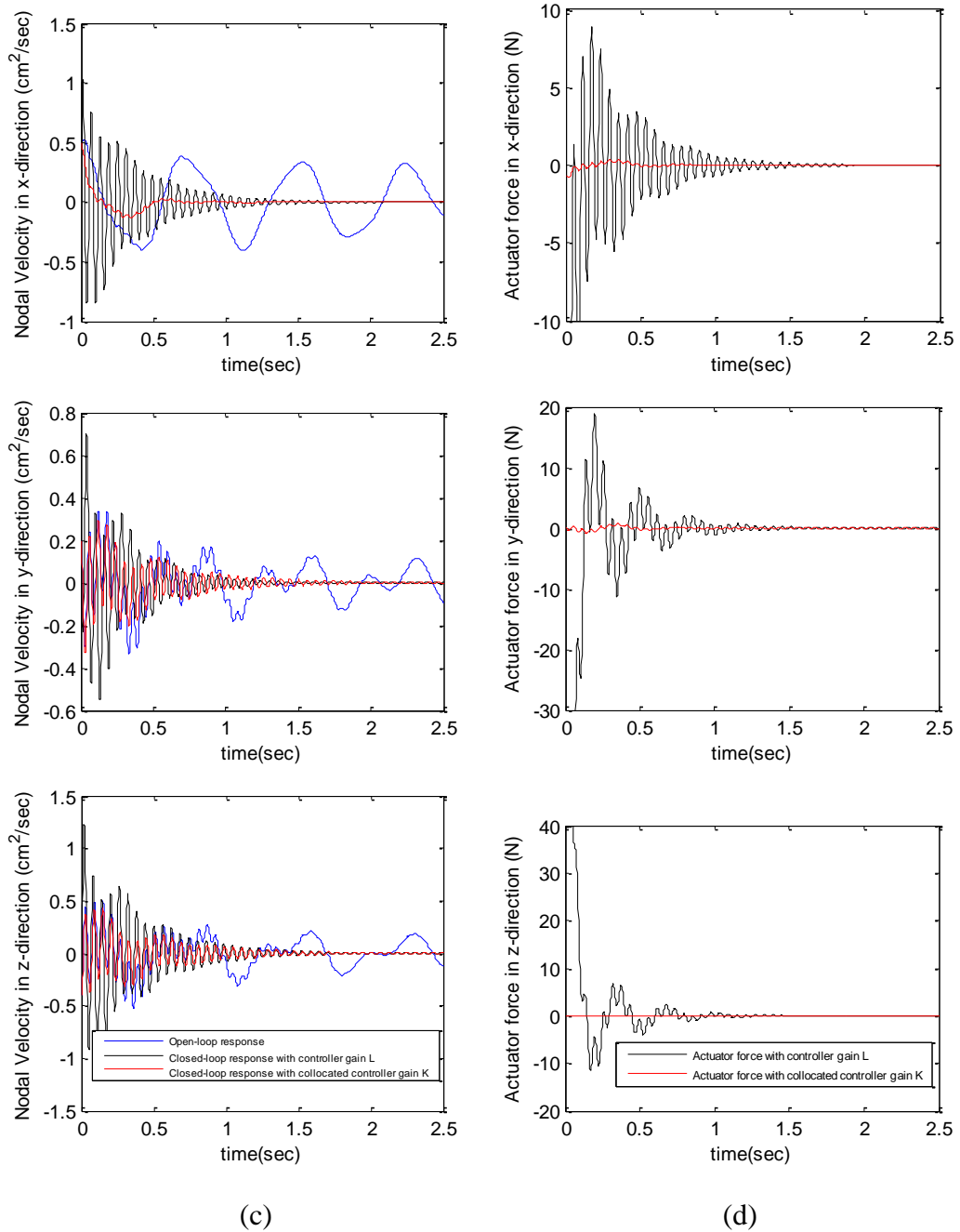


Figure 7.3 (b): (c) and (d) are the plots of the dynamic responses (nodal velocities [cm^2/s] Vs time [sec]) and the control efforts (actuator forces [N] Vs time [sec]) at Node 5 in the structural system of Figure 6.21 (b), respectively, for the output matrix $C = B^T$.

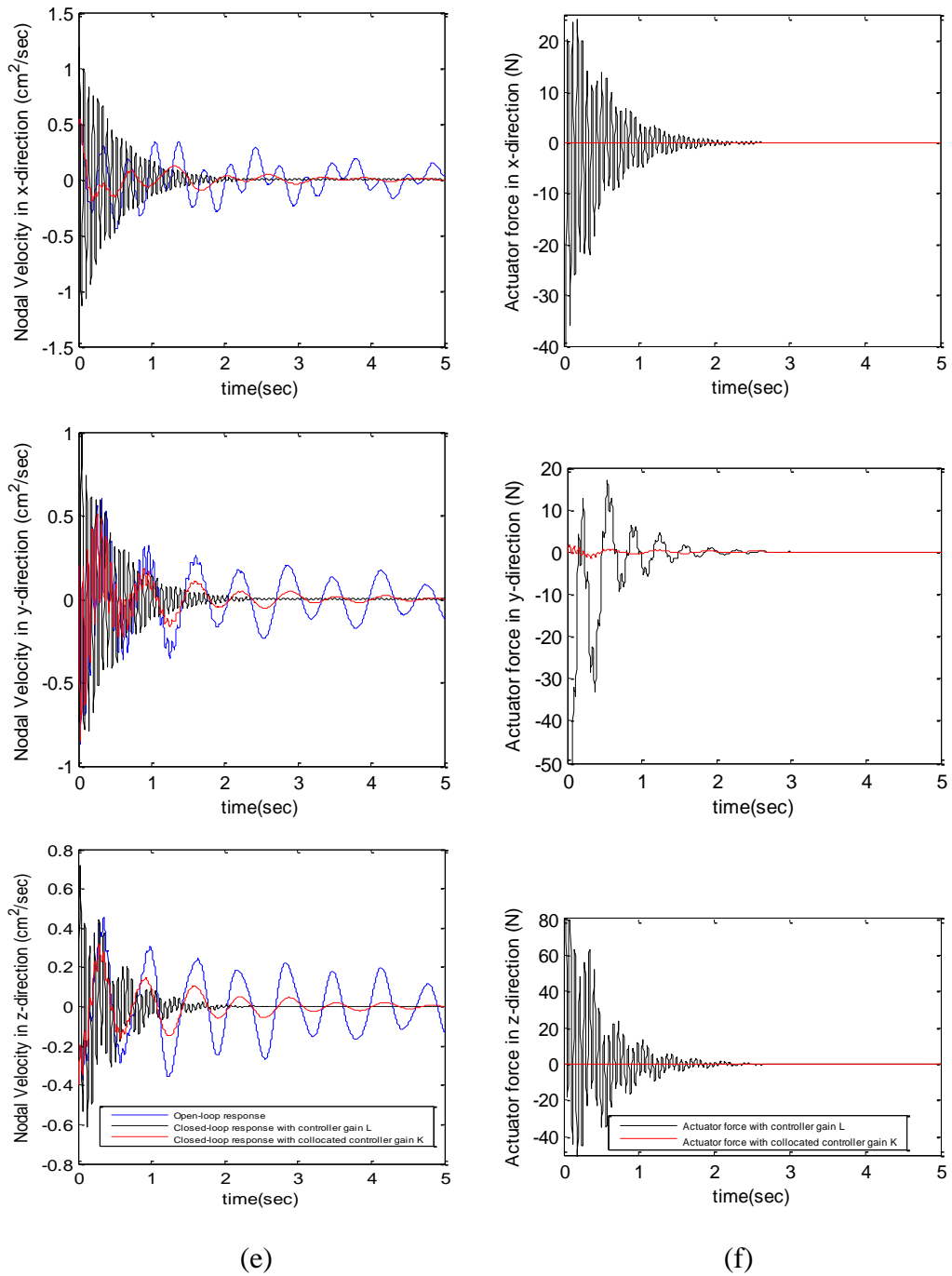


Figure 7.3 (c): (e) and (f) are the dynamic responses (nodal velocities [cm^2/s] Vs time [sec]) and the control efforts (actuator forces [N] Vs time [sec]) at Node 5 in the structural system of Figure 6.21 (c), respectively, for the output matrix $C = B^T$.

Table 7.2: Poles of the open-loop and closed-loop structural systems for $C = B^T W_c^{-1}$

Structural System of Figure 6.21(a)

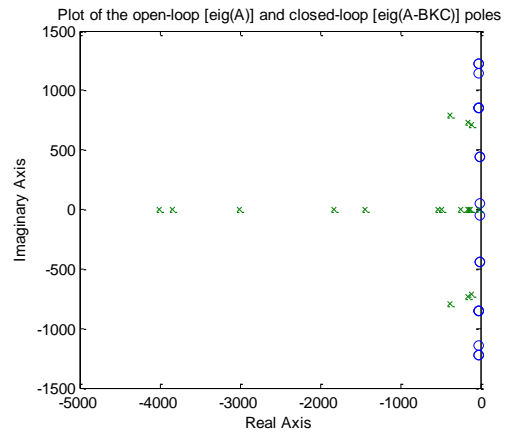
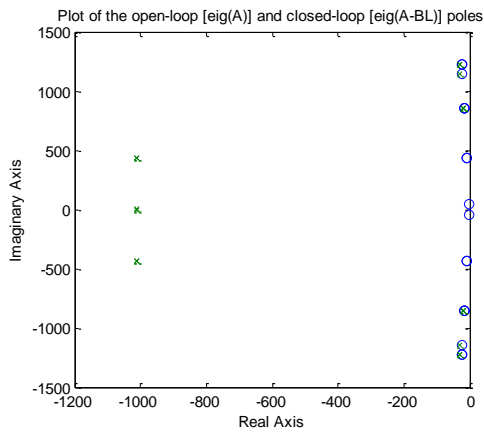
Open-loop eigenvalues: $eig(A)$ ($\times 10^{-3}$)	Entries of $p_o: eig(A - BL)$ ($\times 10^{-3}$)	Eigenvalues of the optimized closed-loop system: $eig(A - BKC)$ ($\times 10^{-3}$)
-0.0229 ± 1.1453i -0.0009 ± 0.0468i -0.0245 ± 1.2235i -0.0245 ± 1.2235i -0.0088 ± 0.4376i -0.0088 ± 0.4376i -0.0171 ± 0.8541i -0.0171 ± 0.8549i -0.0171 ± 0.8549i	-0.0300 ± 1.1453i -1.0100 ± 0.4376i -1.0100 ± 0.4376i -1.0100 ± 0.0000i -0.0200 ± 0.8541i -0.0300 ± 1.2235i -0.0300 ± 1.2235i -0.0200 ± 0.8549i -0.0200 ± 0.8549i	-4.0074 -3.8467 -3.0097 -1.8236 -1.4458 -0.3759 ± 0.7954i -0.1552 ± 0.7348i -0.1079 ± 0.7080i -0.5372 -0.4792 -0.0193 -0.2533 -0.1578 -0.1398 -0.1279

Structural System of Figure 6.21(b)

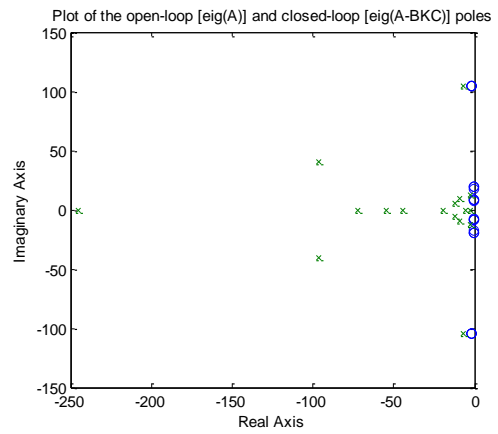
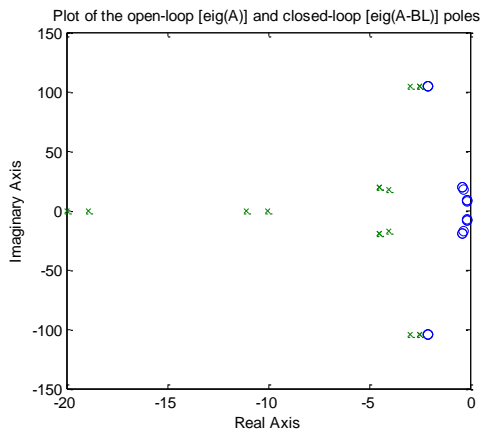
Open-loop eigenvalues: $eig(A)$ ($\times 10^{-2}$)	Entries of $p_o: eig(A - BL)$ ($\times 10^{-2}$)	Eigenvalues of the optimized closed-loop system: $eig(A - BKC)$ ($\times 10^{-2}$)
-0.0209 ± 1.0453i -0.0209 ± 1.0448i -0.0209 ± 1.0448i -0.0035 ± 0.1752i -0.0039 ± 0.1970i -0.0039 ± 0.1970i -0.0016 ± 0.0778i -0.0017 ± 0.0836i -0.0017 ± 0.0836i	-0.0300 ± 1.0453i -0.0250 ± 1.0448i -0.0250 ± 1.0448i -0.0400 ± 0.1752i -0.1999 -0.1889 -0.1111 -0.0450 ± 0.1970i -0.0450 ± 0.1970i -0.1001 -0.1000 -0.1000	-2.4517 -0.0697 ± 1.0413i -0.9641 ± 0.4007i -0.7228 -0.5439 -0.4458 -0.0220 ± 0.1231i -0.1910 -0.0894 ± 0.0968i -0.1195 ± 0.0587i -0.0579 -0.0224 -0.0293

Structural System of Figure 6.21(c)

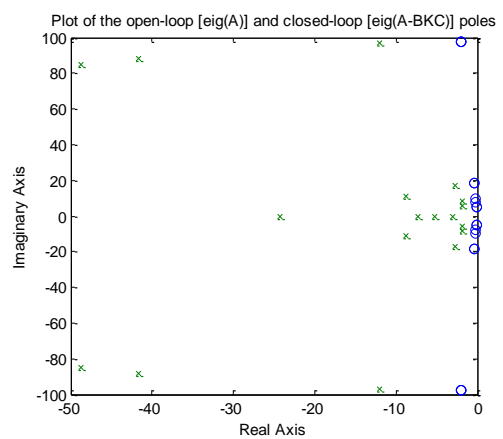
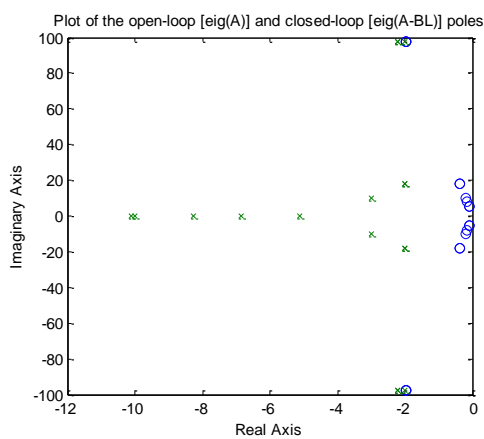
Open-loop eigenvalues: $eig(A)$	Entries of $p_o: eig(A - BL)$	Eigenvalues of the optimized closed-loop system: $eig(A - BKC)$
-1.9585 ± 97.9035i -1.9528 ± 97.6195i -1.9528 ± 97.6195i -0.1556 ± 7.7760i -0.1978 ± 9.8868i -0.3632 ± 18.1567i -0.3632 ± 18.1567i -0.1026 ± 5.1311i -0.1026 ± 5.1311i	-2.0000 ± 97.9035i -2.2000 ± 97.6195i -2.2000 ± 97.6195i -3.0000 ± 9.8868i -5.1050 -6.8405 -8.2621 -2.0000 ± 18.1567i -2.0000 ± 18.1567i -9.9976 -10.1026 -10.1026	-12.0309 ± 96.9639i -41.6238 ± 88.4039i -48.7880 ± 84.6600i -24.3009 -2.6935 ± 16.9586i -8.8005 ± 10.7510i -1.9012 ± 8.4815i -1.8485 ± 5.7263i -7.3587 -5.2155 -3.0829



(a)



(b)



(c)

Figure 7.4: (a), (b) and (c) are the plots of the open- and closed-loop poles of the structural systems of Figure 6.21 (a), (b) and (c), respectively, in the complex plane for the output matrix $C = B^T W_c^{-1}$ ('o' – open-loop poles; 'x' – closed-loop poles).

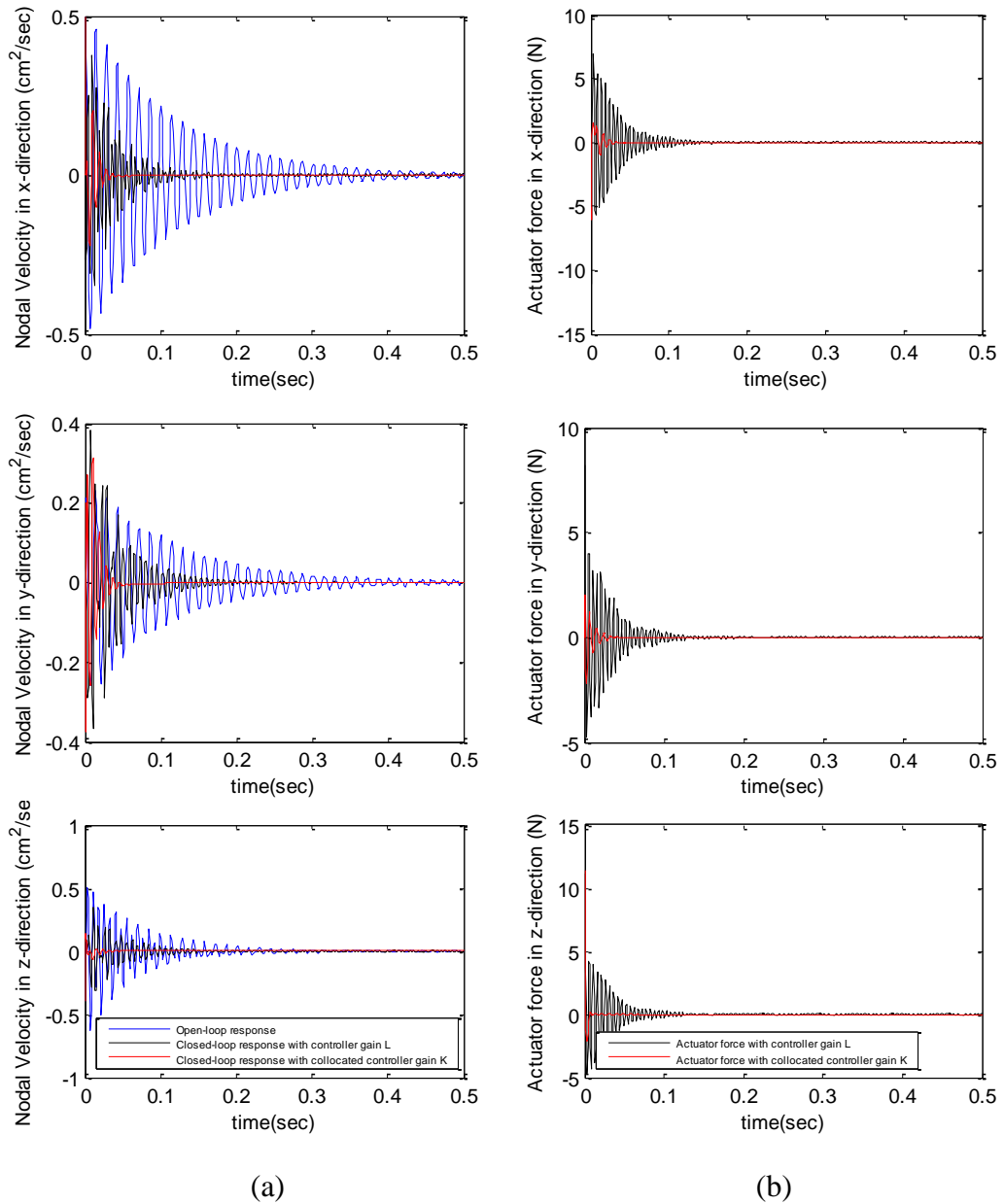


Figure 7.5 (a): (a) and (b) are the dynamic responses (nodal velocities [cm^2/s] Vs time [sec]) and the control efforts (actuator forces [N] Vs time [sec]) at Node 6 in the structural system of Figure 6.21 (a), respectively, for the output matrix $C = B^T W_c^{-1}$.

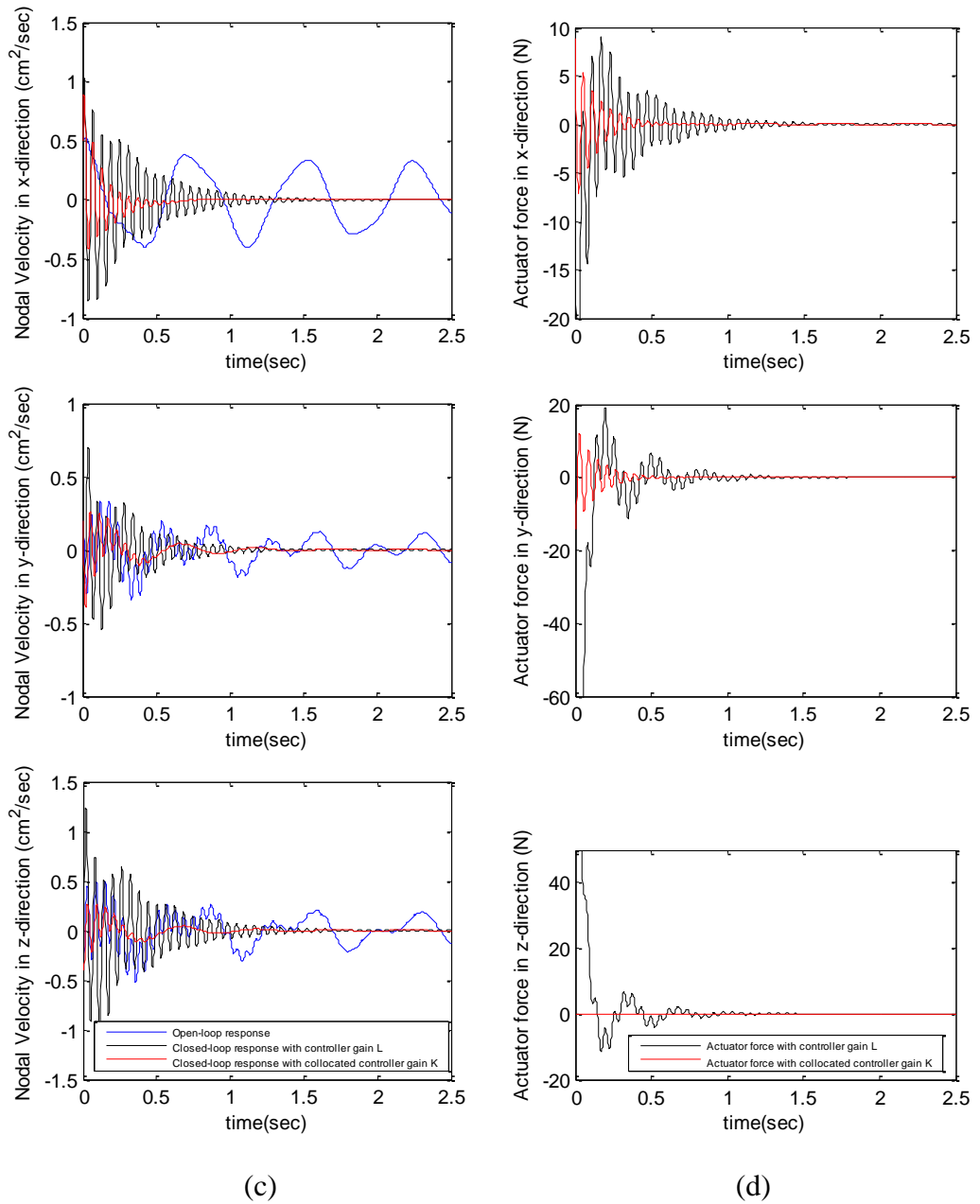


Figure 7.5 (b): (c) and (d) are the dynamic responses (nodal velocities [cm^2/s] Vs time [sec]) and the control efforts (actuator forces [N] Vs time [sec]) at Node 5 in the structural system of Figure 6.21 (b), respectively, for the output matrix $C = B^T W_c^{-1}$.

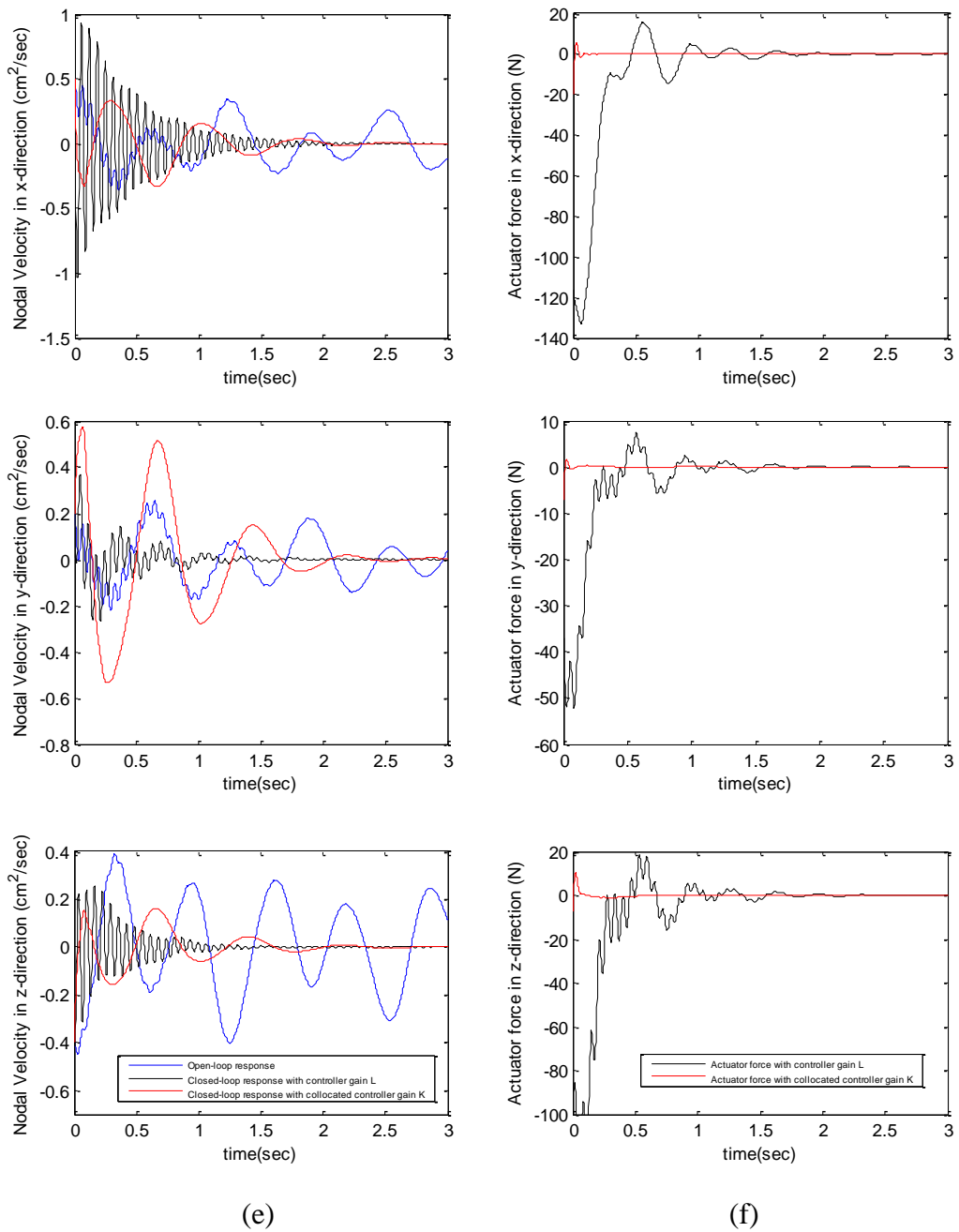


Figure 7.5 (c): (e) and (f) are the dynamic responses (nodal velocities [cm^2/s] Vs time [sec]) and the control efforts (actuator forces [N] Vs time [sec]) at Node 4 in the structural system of Figure 6.21 (c), respectively, for the output matrix $C = B^T W_c^{-1}$.

It can be seen from these results that the optimal value of K obtained by solving the optimization problem of (7.23) does indeed reduce the control efforts significantly compared to using the pole-assignment algorithm directly for computing the gain matrix L . Moreover, it should be noted that the proposed optimization method of obtaining the constant gain K by this pole-relocation approach is applicable to nodal, modal, balanced and reduced-model of any structural system; this is unlike many of the common methods of obtaining K (such as methods given in [133], [217]) which require that the structural model be in a specific format.

Furthermore, the design of the collocated control scheme for the active structural systems presented in this section is applicable to low-authority controller. For many practical structural applications (such as tethered satellite systems [218] and shape morphing of aircraft wings [219], for instance), high authority controllers (where the structural systems are required to track reference signals within the controller bandwidth and within the disturbance bandwidth) are the most suitable. The most successful controller design used in the field of active structures is the LQG (Linear system, Quadratic cost, Gaussian noise) controllers [129]. These controllers are suitable for both collocated and non-collocated control systems. Moreover, they can be made to inculcate features such as estimator designs (full- and reduced-order), disturbance rejection, robust tracking, etc. The LQG controller design is the subject of the next section.

7.3 Linear Optimal Control of Tensegrity Structures

The field of optimal control theory has attained considerable maturity that has enhanced its widespread applications since its inception in the 1950's. In this section, the results of some of the most fundamental optimal control problems (the linear quadratic control problems, in particular) will be applied to tensegrity structural systems for vibration suppression (low-authority controllers) and precise positioning or tracking (high-authority controllers). Many literatures that cover the analysis and design of linear quadratic controllers are available (such as [151], [153], [154], [157], [216]); the main results that are needed for the current study on active tensegrity structures are presented in the Appendix and [151], [216] are used as the main sources of reference. The sections that follow are dedicated to applying these results to tensegrity structural systems in particular. It is worth noting that the sections, equations and figures that are given in the

Appendix and that are being referred to in the subsequent sections are prefixed with the letter “A”.

7.3.1 Collocated Control with Linear Optimal State-feedback Regulator

A linear state-feedback regulator can be used for vibration suppression of an active tensegrity structure. This effectively makes the controller a low-authority controller since it is not designed to be used for reference tracking. In this section, the design of a linear state-feedback regulator for a collocated tensegrity structural system will be considered by applying the results of the deterministic linear optimal regulator given in Section A.1. The block diagram of the control system equipped with this linear optimal regulator is given in Figure A.1 (a). Consider the linear control law of the optimal linear state-feedback regulator given by Equation (A.5), the optimal regulator gain K^o is computed using the following expression:

$$K^o = R_2^{-1}B^T P \quad (7.28)$$

where P is obtained by solving the algebraic Riccati equation of (A.8) which, by substituting (A.4) in (A.8), can be expressed as follows:

$$R_1 - PBR_2^{-1}B^T P + A^T P + PA = 0 \quad (7.29)$$

Given R_1 , Equation (7.29) is easily solved for P using the algorithm presented in [220], for instance. Thus, for equations (7.28) and (7.29), the value of the optimal linear regulator gain K^o is determined by the two matrices, namely, R_1 and R_2 . In general, $P \neq I$ in this case.

Alternatively, consider the positive real criterion expressed in Equation (7.3), the case where $Q = (-A - A^T)^{1/2}$ such that Equation (7.11) is valid gives the value of P as $P = I$ for a collocated structural system (refer to Case 3 of Section 7.2). In this case, the value of K^o is determined as follows:

$$K^o = R_2^{-1}B^T \quad (7.30)$$

Equation (7.30) is obtained by substituting $P = I$ in Equation (7.29); hence, R_1 is defined as follows:

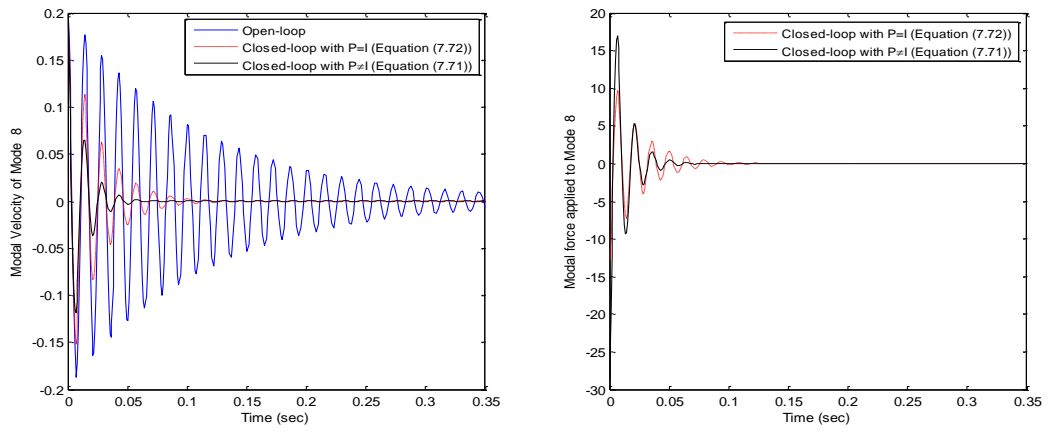
$$R_1 = BR_2^{-1}B^T \quad (7.31)$$

Thus, Equation (7.30) is a special case of Equation (7.28). In this context, only one weighting matrix (R_2) is needed for computing K^o using (7.30) whereas two weighting matrices (R_1 and R_2) are needed for computing K^o using (7.28); consequently, in the computation of K^o using (7.28), there is the extra freedom in manipulating the stability and transient phenomenon by choosing R_2 appropriately.

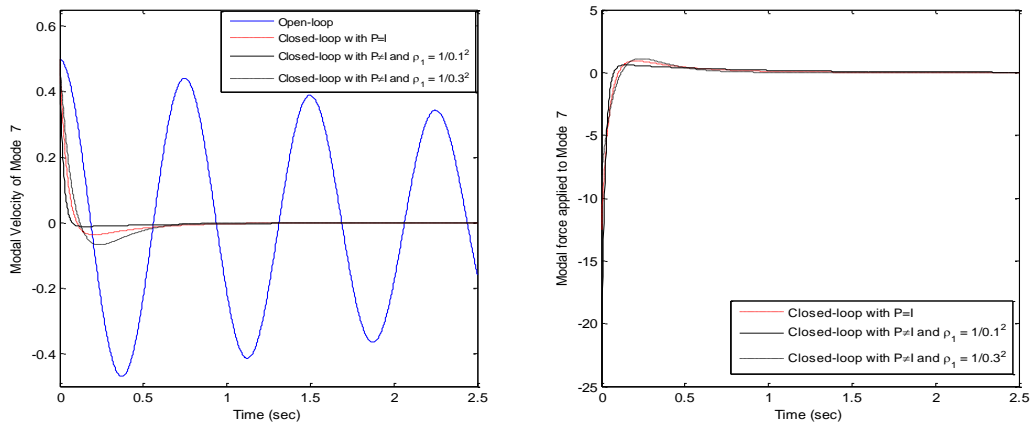
The simulation results for the case where P is computed with (7.29) and the case where it is computed with $P = I$ to obtain the value of K^o for the tensegrity structures of Figure 6.21(a–c) are shown in Figure 7.6. Moreover, the modal models of these structures are used for this simulation and the figure shows the results of only a few number of modes. Also, it should be observed that the modal velocities and modal forces are paired (collocated) together. The initial modal velocities for the modes shown in Figure 7.6 (a), (b) and (c) are 0.2, 0.5 and -0.4 , respectively. Let $R_1 = \rho_1 I_{mb}$ and $R_2 = \rho_2 I_{mb}$ where I is the identity matrix and its subscript ‘ mb ’ denotes the number of columns of matrix B ; for the simulation results in Figure 7.6 (a), (b) and (c), the values of ρ_2 for computing R_2 are $\frac{1}{8^2}$, $\frac{1}{5^2}$ and $\frac{1}{3^2}$, respectively; the values of ρ_1 used for computing R_1 are indicated in Figure 7.6 for the various simulation results.

7.3.2 Non-collocated Control with Linear Optimal Output-feedback Controller

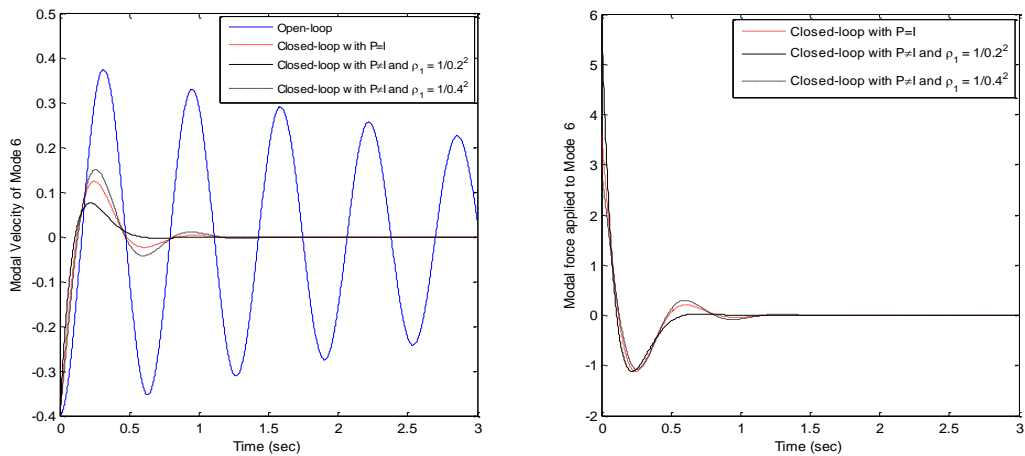
In the preceding section, the design of linear optimal state-feedback regulators for collocated control of tensegrity structural systems was presented. In this section, the task is to design linear output-feedback controllers for non-collocated control of the structural systems. The block diagram of a control system equipped with the linear output-feedback controller is shown in figures (A.3) and (A.4). The problem of vibration suppression of tensegrity structural systems will be considered in this section just as in the preceding one; the problem of robust tracking for non-collocated control is dealt with in the next section.



(a) Tensegrity Structure of Figure 6.21(a)



(b) Tensegrity Structure of Figure 6.21(b)



(c) Tensegrity Structure of Figure 6.21(c)

Figure 7.6: Simulation results for the cases of $P \neq I$ and $P = I$ computed with (7.28 – 7.29) and (7.30), respectively, for the tensegrity structures of Figure 6.21(a–c).

The design of an output-feedback controller can be approached using the separation principle (refer to Section A.3 for details). This design involves finding the estimator and the regulator gains. This can be approached either by pole-placement or by obtaining optimal solution to a quadratic criterion provided the associated restrictions on the use of either methods is respected. Consider the state-space model of the multistable 3-bar tensegrity structural system of Figure 6.21(c) with 18 number of states and with (nodal/modal) displacements and forces as the measured variable and control input, respectively (that is, the active tensegrity structure is non-collocated), the reduced model of this state model with 8 number of states has been obtained using the truncation method described in Section 4.3.1; the reduced model is the system $(A_{8 \times 8}, B_{8 \times 4}, C_{4 \times 8}, D_{4 \times 4})$. Of the 8 states that can be selected as output variables of the reduced model, only four are measured (that is, $y_{4 \times 1} = C_{4 \times 8}x_{8 \times 1}$); the other four variables (that are unmeasured) are the least significant (least affected by the control input) and are essentially zero irrespective of the system input. The design of an output-feedback controller for this system using the pole-placement and optimization methods follows.

Output-feedback Controller Design by Pole-placement: The open-loop poles and the poles of the closed-loop system obtained by pole-placement for the linear regulator are shown in Table 7.3. Also, the estimator poles are chosen so that the estimator dynamics $(A - LC)$ is four times faster than the regulator dynamics $(A - BK)$.

Table 7.3: Open-loop and closed-loop poles of the reduced-model of the structural system (non-collocated case) of Figure 6.21(c)

Open-loop poles: $eig(A)$	Closed-loop poles: $eig(A - BK)$
$-1.9585 \pm 97.9035i$	$-5.9340 \pm 2.9660i$
$-0.1026 \pm 5.1311i$	$-4.6680 \pm 2.3328i$
$-0.1026 \pm 5.1311i$	$-2.7780 \pm 1.5393i$
$-0.1556 \pm 7.7760i$	$-3.0780 \pm 1.5393i$

Output-feedback Controller Design by Optimization of Quadratic Criterion: The gain of the linear optimal regulator is computed using (A.6) where R_1 and R_2 are $25I_{na}$ and $\frac{1}{32}I_{mb}$ ('na' and 'mb' are the number of states and the number of columns of B , respectively). Also, the gain of the linear optimal estimator is computed using Equation

(A.22) where V_1 and V_2 are taken as $4I_{nc}$ and $\frac{1}{40^2}I_{nc}$, respectively (' nc ' is the number of rows of C), and the disturbance and measured noises are assumed to be uncorrelated.

The simulation results using the output-feedback controller designed with the two methods (pole-placement and optimization) for the reduced model of the non-collocated active structural systems of Figure 6.21(c) are shown in Figure 7.7; the initial condition of the state variables is $[0.5 \ 0.2 \ -0.4 \ 0.5 \ 0.5 \ 0.2 \ -0.4 \ 0.5]^T$.

7.3.3 Robust Tracking System for Active Tensegrity Structures

In this section, the task involves the design of a robust tracking controller for an active tensegrity structure. The block diagram for the robust tracking control system is given in Figure A.7. Furthermore, the reduced model (of non-collocated active structural system) of the multistable 3-bar tensegrity structure given in the preceding section is also used in this section as the example structural system and the linear tracking control system design technique of Section A.4 is directly applied. Moreover, in relation to the discussions in Section A.4, \underline{K} (which can also be obtained by pole-placement) is computed here by solving the optimal linear regulator problem described in Section A.1 using the augmented system model of Equation (A.38); the matrices R_2 , R_3 and R_I required to minimize (A.39) are defined, for the example structural system, as follows: $R_2 = \frac{1}{40^2}I_{mb}$; $R_3 = \frac{1}{6^2}I_{na}$; and $R_I = \frac{1}{4^2}I_{nc}$. Thus, the regulator gain K and the integral gain K_I are deduced by partitioning \underline{K} . Also, matrices M and \bar{N} are obtained using equations (A.28 – A.34).

In addition, the estimator gain L can be computed using pole-placement or by computing the optimal estimator gain given by Equation (A.22); using the pole-placement method for the example active structural system, L is obtained so that the closed-loop dynamics of the estimator ($A - LC$) is four times faster than the closed-loop poles of ($A - BK$) where K is the left-hand side partition of \underline{K} ; for the optimization method, the optimal linear estimator gain L^o is computed by assuming that $V_1 = 4I_{nc}$, $V_2 = \frac{1}{40^2}I_{nc}$, and the disturbance and measurement noises are uncorrelated. Both methods of obtaining L are used for the simulation of the robust tracking system of the active structural system of Figure 6.21(c). The simulation results are shown in Figure 7.8. The initial condition of the state variables is $[0.5 \ 0.2 \ -0.4 \ 0.5 \ 0.5 \ 0.2 \ -0.4 \ 0.5]^T$ and the reference vector is $[-3 \ -2 \ 1 \ 2]^T$.

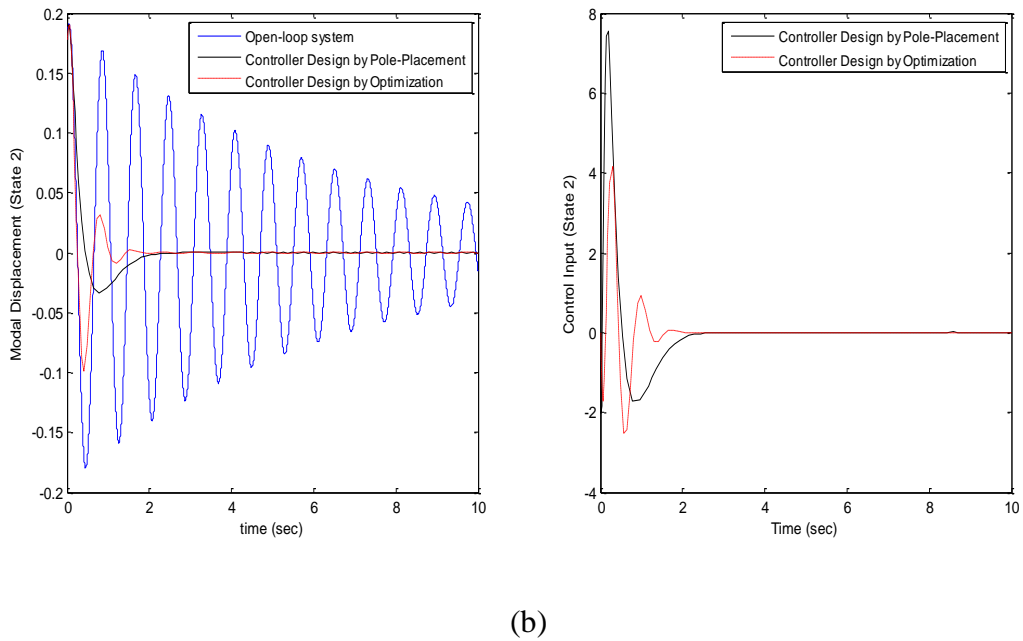
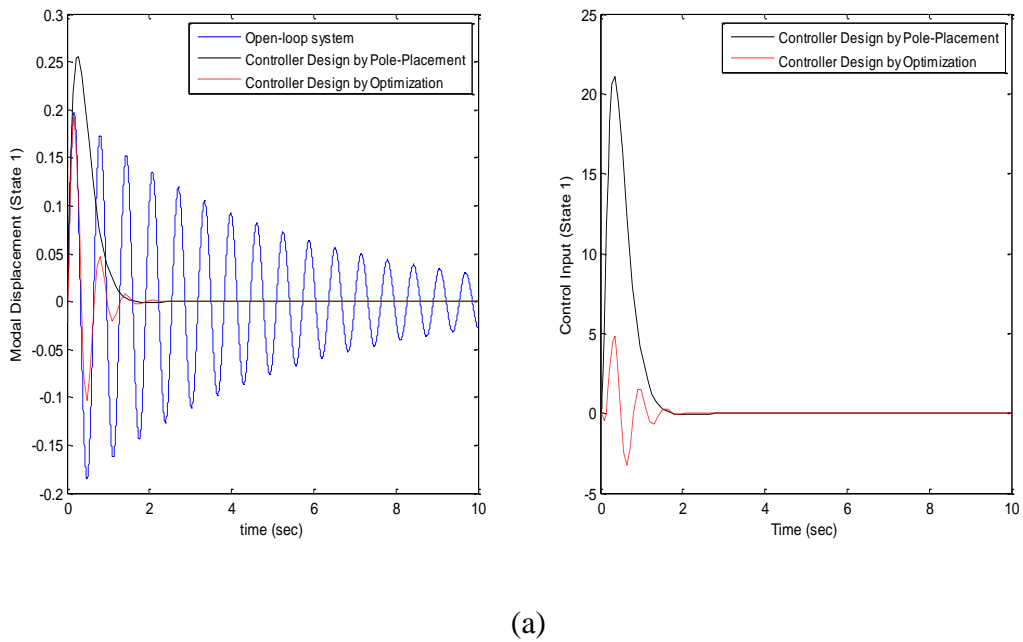
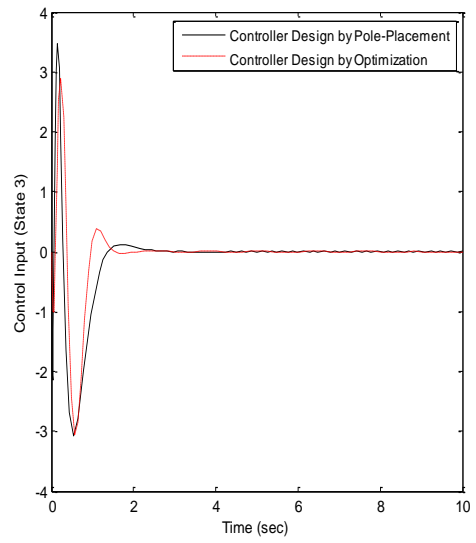
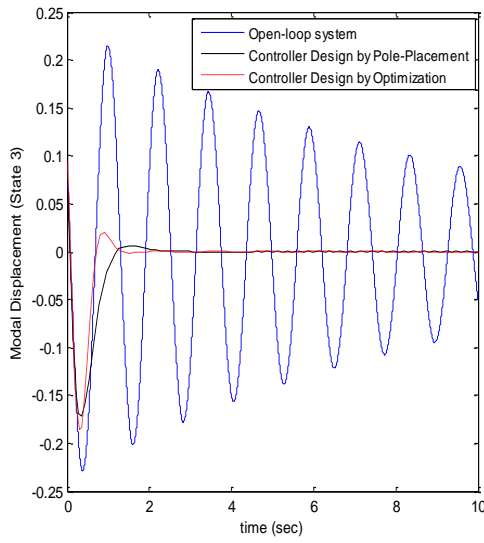
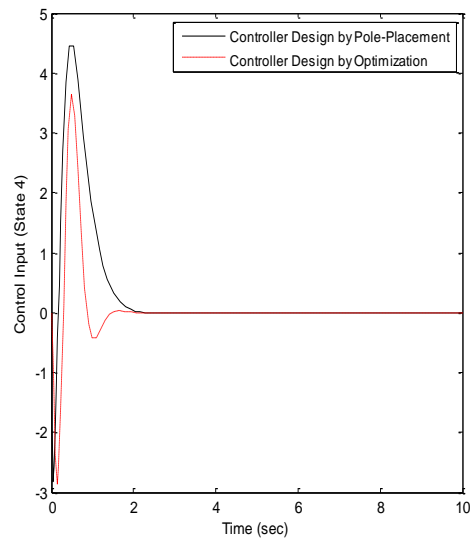
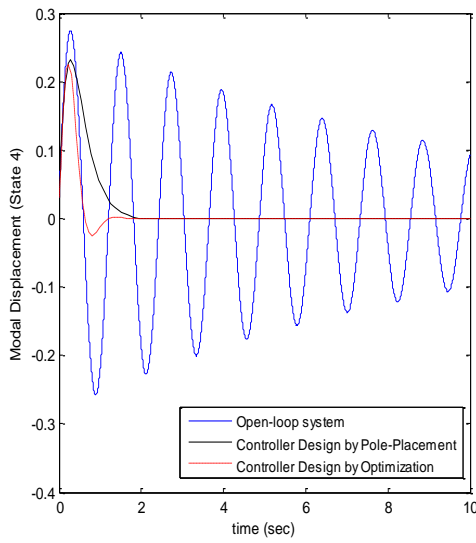


Figure 7.7: Simulation results for the (non-collocated) tensegrity structural system of Figure 6.21(c) using output-feedback controllers designed with pole-placement and optimization approaches.

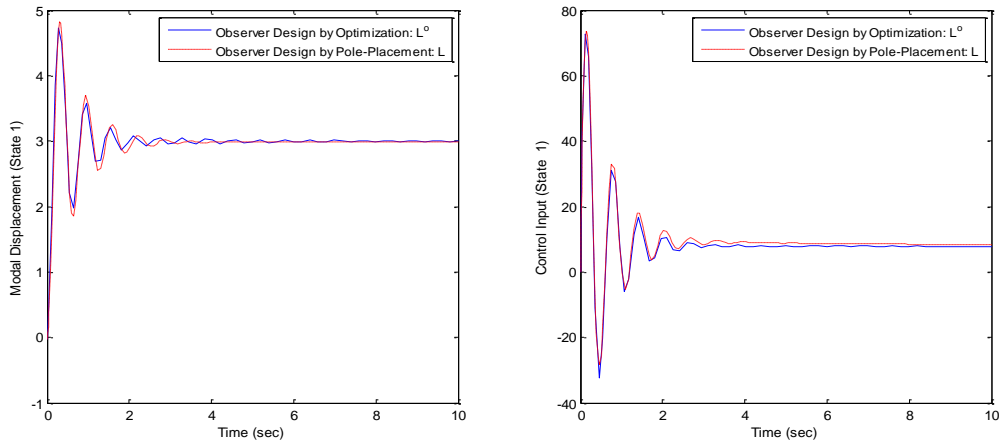


(c)

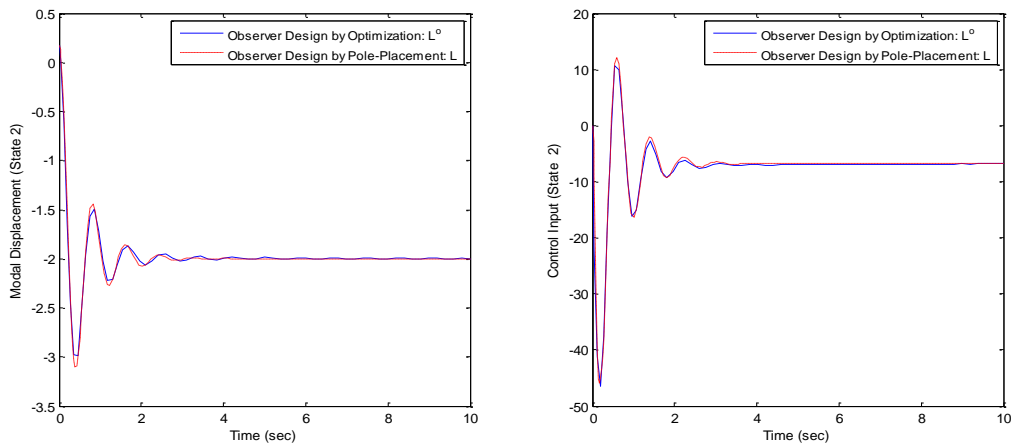


(d)

Figure 7.7 (continued): Simulation results for the (non-collocated) tensegrity structural system of Figure 6.21(c) using output-feedback controllers designed with pole-placement and optimization approaches.

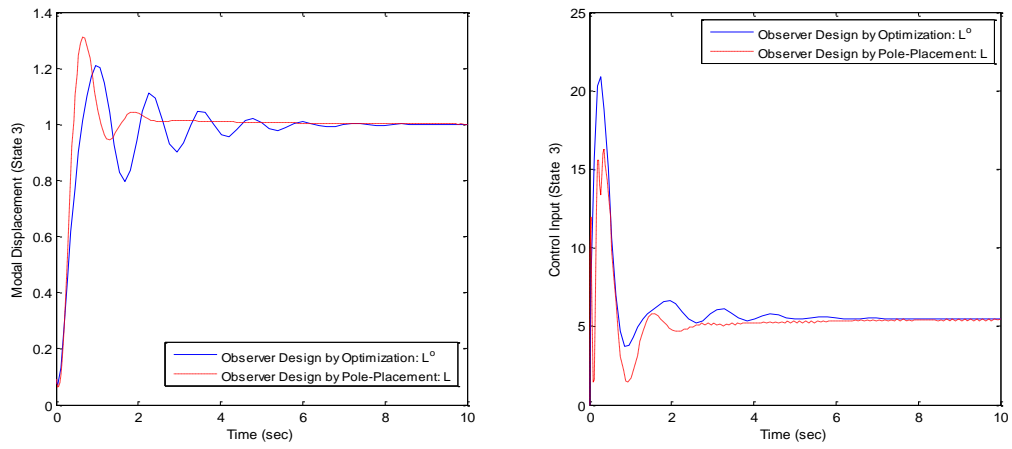


(a)

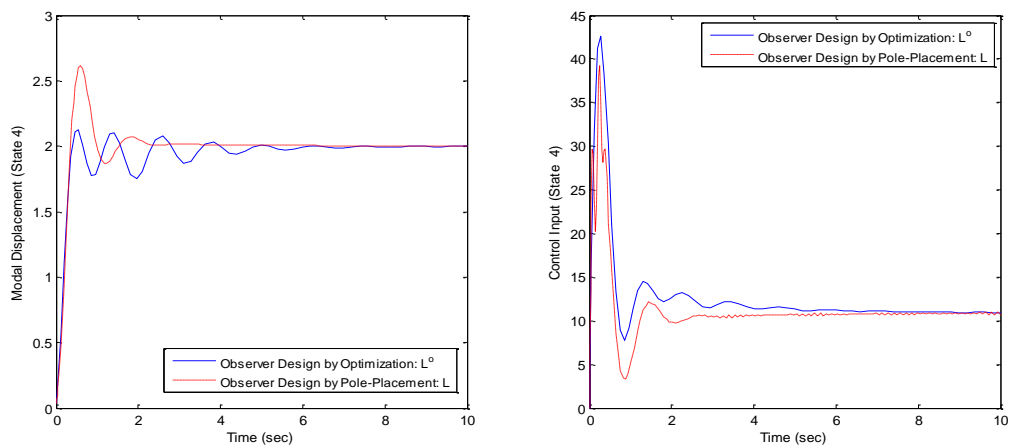


(b)

Figure 7.8: Simulation results for the robust tracking control for the (non-collocated) tensegrity structural system of Figure 6.21(c) using linear observer designed with pole-placement and optimization approaches.



(c)



(d)

Figure 7.8 (continued): Simulation results for the robust tracking control for the (non-collocated) tensegrity structural system of Figure 6.21(c) using linear observer designed with pole-placement and optimization approaches.

7.4 Discussions

Unlike in the previous chapter where the shape control of the multistable 3-bar tensegrity structure is achieved through independent multiple PID control systems, the framework for the shape control of tensegrity structures presented in this chapter is based on centralized linear quadratic control architecture (that is, the LQG controller). It should be recalled that, the fundamental assumption that the sources of disturbance (primarily, due to the un-modelled member forces that link the SISO systems together) for each independent PID control system are independent of each other is not accurate. For the LQG controller, since the control law is computed using the information of the systems states, a highly coupled tensegrity structural system is effectively controlled taking into account, not only the level of interaction between the states but also, the presence of model uncertainties due to the dimensional and material imperfections of the cables and bars, the lack of the precise knowledge on the frictional force at the joints, and the inaccuracies as a result of geometrical configuration of the structure.

It is well-known that centralized controllers are able to obtain solutions that are the globally optimal solutions while decentralized controllers are better suited for large-scaled system but solutions are local optimal solutions at best. Hence, on the one hand, in large structural systems consisting of several active tensegrity modules, the linear optimal control system design, as described in this chapter (that is, the LQG controller), will be suitable for obtaining a local optimal solution for each of the local tensegrity modules. On the other hand, for tensegrity structures consisting of only few structural members, the linear optimal control system design will be suitable for obtaining global optimal solution since the number of variables for the structural system involved in this case are few, and as a result, can be computed fast.

Furthermore, the reference variables of the linear state/output-feedback or robust tracking control systems of the linear optimal control system design presented in this chapter are determined from the results of form-finding (structural optimisation), and the form-finding algorithm presented in Chapter 2 can be used, for instance, to compute these reference variables just as was the case in Chapter 6. Moreover, vibration suppression feature is an important characteristic of the low- and high-authority controllers designed in this chapter, making the controllers suitable for the control of both the un-deployed and the deployed tensegrity structural systems discussed in Chapter 5. Aircrafts that have the ability to change the shape of their wings to improve

fuel efficiency [219], [221] and biological inspired surgical robots that can perform complex computations required for skilful movement [222], [223] are, for example, potential applications of these reference robust tracking controllers.

In addition, while the models of tensegrity structures are nonlinear and difficult to describe by simple mathematical functions, these structures are pre-stress stable (that is, they are in a state of static equilibrium due to pre-stress; see, for example, Chapter 2 for more detail). Thus, the use of linearised model (obtained from the Finite Element Modelling of Chapter 3, for instance) for the control system design described in this chapter, given that the actual structural system is nonlinear, is justified in the light of the fact that for a controller designed for a linearised model of a stable or an unstable nonlinear plant for which the closed-loop system is asymptotically stable, the actual nonlinear plant with this controller is also asymptotically stable for small deviations from the equilibrium state [151].

More so, in the example structural system considered in Sections 7.3.2 and 7.3.3, the controllers were designed for the model of the active structural system of Figure 6.21(c). This, in essence, makes the controller in Section 7.3.2 a linear output-feedback controller of reduced dimension and that in Section 7.3.3 a linear tracking controller of reduced dimension. These controllers, as demonstrated by the simulation results of the two sections, render quite satisfactory system performances although the ‘linear optimal’ control law is obviously not optimal for the full model (the linear optimal controller is only optimal for the reduced-order linear model that was considered). As a result of model reduction in which only few dominant low-frequency modes are taken into account, it is possible that the un-modelled (residual) high-frequency modes are excited – though in the rare cases, such as in the space environment; the observer designed for the reduced-order model will not model response to these high-frequency inputs which may be capable of destabilising an otherwise stable closed-loop system. Many literature on how to tackle this situation, often called spillover, exist; reference [129], for instance, contains a simple way of dealing with spillover for flexible structures.

Also, the linear optimal state-feedback regulator discussed in Section A.1 (and applied to tensegrity structural system in Section 7.3.1) has guaranteed stability margins (Gain Margin = $\frac{1}{2}$ to ∞ and Phase Margin $> 60^\circ$) for each mode [129]. The introduction of an observer in the state-feedback control-loop may adversely affect this robust

stability feature [224], [225]. As such, the estimator design presented in Section A.2 is commonly modified so that this robust stability feature is recovered to some extent; the associated observer modification procedure is commonly called the Loop Transfer Recovery (LTR) [216], [226]. However, the LTR procedure is usually at the expense of having, for example, a worse sensor noise sensitivity properties and the design to achieve an acceptable trade-off between these conflicting criteria depends on the problem at hand [216]. Procedures for LTR can be found in [226], [227] and details on the limits of achievable performance can be found in [228], for instance.

The model of tensegrity structures that has been used throughout this thesis has been obtained using the Finite Element Modelling (FEM) technique presented in Chapter 3. The outcome of this modelling exercise is a system model in the nodal coordinate format and, for further analyses, the nodal model has been expressed in nodal, modal, balanced and reduced state-space model representations (see Chapters 3 and 4). Although the results of these analyses are not comprised, it should be noted however that for shape control (in addition to vibration suppression) of flexible structural systems in which structural members acts as sensors and actuators, the outcome of the FEM and its state-space representation counterpart can be alternatively expressed in slightly different formats that will make them much more easily interpretable and accessible for the control of both statically determinate and indeterminate structures. In particular, consider the 2-stage 3-order active tensegrity structure of Figure 7.9, for instance, the control input and output (measurement) variables of this and similar structure can be expressed in terms of the member length changes due to the actuators (referred to as the stroke lengths in Chapter 5) and the member axial forces, respectively, instead of expressing them in terms of nodal forces and velocities (or displacements), respectively, as has been the case in most part of this thesis. Moreover, it will be sometimes necessary (depending on the actuators and sensors selection) to convert the models in terms of nodal forces and velocities (or displacements) back to those in stroke lengths and axial forces for shape control of active tensegrity structures due to their static indeterminate nature and the high degree of integration amongst the structural members, actuators, sensors and geometric configurations. To achieve this conversion, consider the model of the discretized elastic structural system expressed in Equation (3.44), re-written here as follows:

$$M\ddot{\Phi}(t) + C\dot{\Phi}(t) + K\Phi(t) = P(t) \quad (7.32)$$

where the parameters in this equation are already defined in Section 3.2.3.

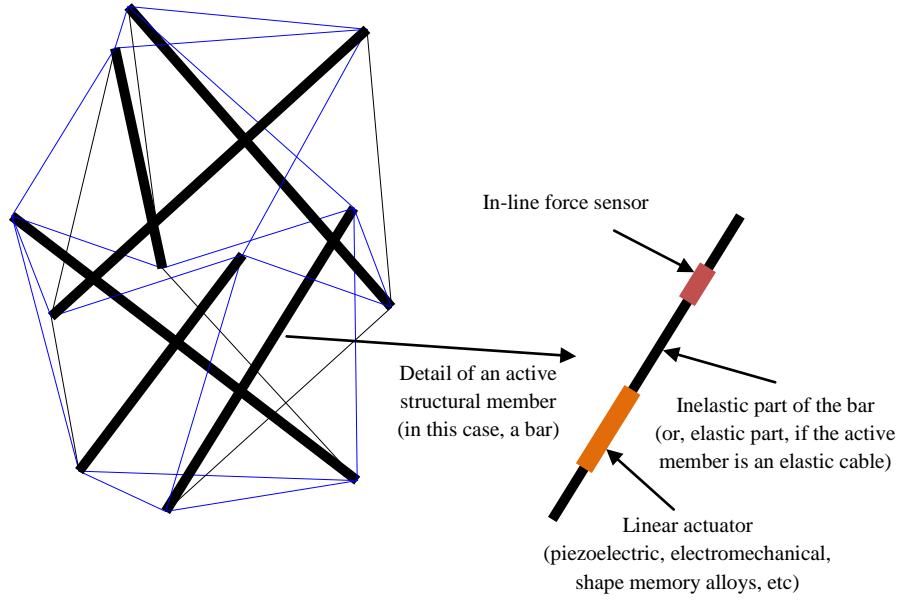


Figure 7.9: A 2-stage 3-order active tensegrity structure

Let s and l represent the vectors of member axial forces and member lengths, respectively, the equation of nodal force equilibrium in (2.4) can then be expressed as follows:

$$A \cdot q = p \quad (7.33a)$$

$$(A\mathbb{L}^{-1}) \cdot s = p \quad (7.33b)$$

$$J \cdot s = p \quad (7.33c)$$

where $J = A\mathbb{L}^{-1}$ is an influence matrix of direction cosines and $\mathbb{L} = \text{diag}(l)$; substituting (7.33c) in (7.32) gives the following equation:

$$M\ddot{\Phi}(t) + C\dot{\Phi}(t) + K\Phi(t) = J s \quad (7.34)$$

s in Equation (7.34) now represents the active control forces (axial of structural member) of the structural system. Also, s , from the generalized Hooke's law (the constitutive equations), is a product of a stiffness matrix $\mathbb{K} = \text{diag}(\mathbb{k}^i)$ – where \mathbb{k}^i represents the stiffness of the i^{th} structural member – and member elongation vector e_e ; e_e is a vector of member length changes due to elastic deformation, or simply, $s = \mathbb{K} e_e$. The total element length changes e_t is the sum of the element length changes due

to elastic deformations e_e and the element length changes due to actuators e_a ; that is, $e_t = e_e + e_a$. The geometric compatibility equation can be expressed as $J^T \Phi = e_t$ [229]. The foregoing expressions lead to the following set of equations:

$$s = \mathbb{K} e_e \quad (7.35a)$$

$$e_t = e_e + e_a \quad (7.35b)$$

$$J^T \Phi = e_t \quad (7.35c)$$

Substituting Equation (7.35) in Equation (7.34) and rearranging the result leads to the following expression:

$$M \ddot{\Phi}(t) + C \dot{\Phi}(t) + \bar{K} \Phi(t) = \bar{B} e_a \quad (7.36)$$

where $\bar{K} = K - J\mathbb{K}J^T$ and $\bar{B} = -J\mathbb{K}$. It should be recalled that tensegrity structures are statistically indeterminate structures (see, for example, Chapters 2 and 3 for details); thus, the stiffness matrix K is the sum of elastic stiffness matrix K_e and geometric (pre-stress) stiffness matrix K_q (see equations (3.24-3.26)). Therefore, there is a significant geometrical modification of the structure during a shape change (due to shape control, for instance) as a result of changes in K_q . Moreover, Equation (7.36) establishes the desired relationship amongst the stroke length of actuators through e_a , axial forces of structural members through s (which is a function of \mathbb{K}), and the nodal coordinates Φ through the geometric compatibility equations. Additional supplementary notes on matrix representations and analysis for active control of flexible structures can be found in, for example, [229–232]. Meanwhile, it is clear that since K and \mathbb{K} are functions of varying length of structural members (matrix \mathbb{L} , which in turn is a function of e_a), \bar{K} and \bar{B} are both nonlinear time-varying matrices; for the same reason, matrices M and C are nonlinear and time-varying in a more general sense. In general, the nonlinear model of an active tensegrity structure can be approximated by a linear time-varying model (as with other flexible structural systems [233]); analyses of the resulting equations are left for future work.

Besides, the control system design covered in this chapter used for controlling tensegrity structures modelled as LTI systems has been restricted to the application of fundamental concepts of linear optimal control theory (such as linear quadratic regulators, observers, robust tracking and integral control) which has proven to be very successful in the field of active control of flexible structures [129], future work should,

therefore, consider the usefulness of more advance concepts (such as H_2 and H_∞ in robust control, for instance, which are frequency-domain approaches to controller design) that are well-known to be better in dealing with robustness issues [156].

It should be remembered that, when subjected to rigid body displacements, the dynamic behaviour of tensegrity structures presents a coupling between rigid body displacements and flexible modes and, as such, can become highly nonlinear or even unstable (consider that K in the expression $\bar{K} = K - J\mathbb{K}J^T$ of Equation (7.36) is given by $K = K_e + K_q$ (see equations (3.24-2-26)); should K_q become $K_q = 0$, the system becomes unstable and the tensegrity structure collapses). Consequently, linear controllers are, therefore, often unsuitable for this class of problems [233]; several approaches have been proposed to enable their use in the control of statically indeterminate flexible structural systems (that are similar to tensegrity structures) but these are difficult to apply in practice [233–235]. In the general case, it might be convenient to use several linear controllers together so that elastic and rigid body modes are controlled independently [236], [237]. However, it would be useful to investigate the performance of adaptive controllers (for example, such as optimal control for linear time-varying systems [238] and time-varying optimal control for nonlinear systems [239]) that will be capable of taking into account the geometrical modifications of the structure when shape control algorithms are implemented.

As a further remark, consider once again the equations of motion in (7.32), it should be recalled that the control input u , from Section 3.2.3, is given by $u = P$. Assuming that the structural system is collocated by pairing the nodal velocities and the applied forces (measured output and control input, respectively) together, the control law can be written as $u = -G_1\dot{\Phi}$, where $G_1 > 0$ unconditionally guarantees closed-loop stability (refer to Equation (7.22)), Equation (7.32) can therefore be expressed as follows:

$$M\ddot{\Phi}(t) + (C + G_1)\dot{\Phi}(t) + K\Phi(t) = 0 \quad (7.37)$$

Similarly, for the non-collocated system, when the nodal displacements are paired with the applied forces (with control law $u = -G_2\Phi$ with $G_2 > 0$) or when the nodal accelerations are paired with the applied forces (with control law $u = -G_3\ddot{\Phi}$ with $G_3 > 0$), Equation (7.32) can respectively be written as follows:

$$M\ddot{\Phi}(t) + C\dot{\Phi}(t) + (K + G_2)\Phi(t) = 0 \quad (7.38)$$

$$(M + G_3)\ddot{\Phi}(t) + C\dot{\Phi}(t) + K\Phi(t) = 0 \quad (7.39)$$

It is easily seen that in equations (7.37), (7.38) and (7.39), the controller gains G_1 , G_2 and G_3 appear as damping, stiffness and mass matrices, respectively; consequently, these control approaches can be considered damping control, stiffness control and mass control, respectively. While the damping control and the stiffness control are directly linked to the collocated control (as presented in Sections 7.2 and 7.3.1) and non-collocated control (as presented in Section 7.3.2) strategies, the mass control with acceleration feedback is achievable since velocity feedback is obtained by integrating the acceleration measurements, thereby, obtaining a damping effect such as in Equation (7.37). Acceleration measurement is particularly easier than displacement and velocity measurements for stiff structures [129]. Numerous literature on active mass damping control systems relating to active structural systems exist; references for these can be found in [91], for instance.

Lastly, previous work on active control of tensegrity structures from the control community includes, for example, [2], [71], [85–87], [90], [95], [240–242]; all these, however, have considered the control of tensegrity structures from the viewpoint of multibody dynamical systems that are limited to the control of few structural members. This thesis is the first, to the best of the author’s knowledge, to present the control of tensegrity structures from the viewpoints of structural and topology optimization and design for small and large structures (Chapters 2 and 5), on the one hand, and structural dynamics and active control (Chapters 3, 4 and this chapter), on the other – making the presented control design approach suitable for structural systems with a large number of active members. This viewpoint is motivated by the need to present a platform for integrated design of optimal structures and optimal control system.

7.5 Summary

The active control of tensegrity structures is presented in this chapter. The chapter presents a new method in the determination of the feedback gain for the design of collocated tensegrity structural systems. Also, the LQG control techniques which are suitable as controllers for both collocated and non-collocated flexible structural systems are applied to design controllers for active tensegrity structural systems to suppress

vibration and for shape control. The chapter concludes by discussing the findings in this chapter and their relationships with the other chapters of this thesis and other previous work on active control of flexible structures in general and tensegrity structures in particular. The next chapter summarizes the main findings of this thesis and presents a platform for future research.

Chapter 8

CONCLUSIONS AND FUTURE WORK

8.1 Conclusions

The overall objective of the present work is to contribute to the scientific research and technological development by investigating tensegrity structures' related problems across a wide spectrum of engineering disciplines from a control systems perspective. Moreover, it can be viewed as a contribution in the process of meeting the needs of design challenges for the physical realization of tensegrity structures given that it highlights some of the most important aspects of system design that must be considered for the design of these structures. Potential application areas are also proposed. The accomplishments of this thesis are recapitulated in the paragraphs that follow.

A new algorithm for the form-finding of tensegrity structures has been presented. The use of computational techniques, which is inevitable for large structures, is adopted in general. As such, the new method is based on the interior point constrained optimisation technique and the efficacy of the method is demonstrated with several examples. The use of the four fundamental spaces of the static equilibrium matrices in conjunction with the new constrained optimization approach for form-finding of large tensegrity structures with a complex connectivity of members was also described. Moreover, the new method offers control of both forces and lengths of structural members and this was also illustrated via several examples. However, as with other form finding methods, the proposed method is not without its disadvantages. The main disadvantage of the method is the requirement that feasible initial nodal coordinates must be defined for the initial tensegrity configuration. This shortcoming can be overcome by pre-processing the initial parameters to obtain initial feasible nodal coordinates.

Very useful systems can only be built with the right set of tools and with the correct set of theories. Thus, the dynamic model of tensegrity structures was derived using the powerful engineering design tool, the Finite Element Method (FEM), and the static and dynamic analyses of these structures were carried-out using representation of the state-space theory. The analyses exercises reveal a number of theoretical and numerical results. For instance, the study of the pseudo-static analysis reveals the following: i) for a given load, as the tension coefficients of the tensegrity structure is increased, the nodal displacements reduces in a nonlinear manner; ii) for a given pre-stress level, the displacements are proportional to the nodal point loads; and iii) for a given load, the nodal displacements of the tensegrity structure increases linearly with the scale of the structure. The implication of these particular set of results in the design of tensegrity structural systems is that, although tensegrity structures are scalable, the tension coefficient has to be increased as the scale of the tensegrity structure increases to maintain same level of rigidity and vice versa.

Furthermore, the effect of including additional structural members (than strictly necessary) on the dynamics of n-stage tensegrity structures was also examined. It was concluded that additional structural members' cause increase in the stiffness of these structural assemblies. It was demonstrated that a tensegrity structure with a highly complex configuration can be made to change its geometric properties in the event of structural failure through self-diagnosis and self-repair.

Also investigated were the procedures for model reduction and optimal placement of actuators and sensors for tensegrity structures to facilitate further analysis and design of control systems. These procedures have the potential of minimizing the control efforts and determining the credibility of the output feedback signals. The applicability of these procedures was demonstrated with several examples.

The design strategy adopted for the physical realization of tensegrity structures proposed in this thesis involves three main tasks which are as follow: i) the structural optimization and related design issues; ii) the configuration of the hardware and the control architecture; and iii) the design of application software user interface and the implementation of the control algorithm. These stages of design were presented in details and the mathematical models and dynamic behaviour of the tensegrity structures designed were obtained. Moreover, the control of one these tensegrity structures, the

initial 3-bar multi-stable tensegrity structure, was achieved through decentralized multiple SISO control systems.

Lastly, the active control of tensegrity structures in a multivariable and centralized control context is presented for the design of collocated and non-collocated control systems. A new method is presented in the determination of the feedback gain for collocated controllers to reduce the control effort as much as possible while the closed-loop stability of the system is unconditionally guaranteed. In addition, the LQG controllers which are suitable for both collocated and non-collocated control systems was applied to actively control tensegrity structural systems for vibration suppression (low-authority controllers) and precise positioning or tracking (high-authority controllers).

8.2 Future Work

Engineering research in tensegrity structures is still an emerging field and there are still many open problems. The main focus of future research, based on the findings of this thesis, is summarized in the paragraphs that follow.

Techniques to obtain a set of different geometric configuration of tensegrity structures with the same number of structural members need further investigation. Close examination of the different form-finding techniques and their possible combination is still required to be able to explore the subsets of a given tensegrity structure to determine the possibility of structural transformation from one subset to another with and/or without the introduction of redundant structural members. Thus, the key factors that should determine the efficacy of any new form-finding algorithm that tackles this particular challenge are: (i) computational cost of obtaining one structure from another by varying one or more parameters of the initial structure; (ii) the number of optimization parameters (such as material properties, geometry, structural configuration, etc.) and constraints that can possibly be included or varied in the optimisation algorithm; and (iii) the possibility of re-configurability: obtaining one structure from another of different configuration.

Mathematical modelling techniques for practical and active tensegrity structures are available (see Chapter 3 of this thesis, for instance). However, in most

mathematical models, some fundamental assumptions have been made to simplify the complex mathematics involved in the theoretical derivations. These include, for instance, the assumptions that members are connected at the nodes in pin-jointed manner (the joints can only transmit forces and are affected by kinetic friction and offer no resistance to rotation) and the influences of external force fields (e.g. self-weight due to gravity, pre-stress due to temperature variation, etc.) are negligible. If tensegrity technology would be used for many practical control engineering applications and in a multi-objective optimization scenario, it is necessary to include practical considerations into the mathematical models. Data-driven parameter estimation methods may also be used for modelling purposes instead. Moreover, damping parameters of the structure can only actually be approximated by data-driven models.

Further research is still required in order to design hybrid controllers for tensegrity structures that will combine structural optimisation and systems engineering techniques to determine, in addition to control outputs in the form of actuator forces/stroke lengths, the optimal structural geometry and the optimal path to follow in transforming from one structural shape to another. The computational complexities of this problem arise due many factors including the computation of the geometric modifications as a result of the additional devices (such electromechanical or piezoelectric actuators) that may have to be introduced to provide adjustable stiffness and the requirement to avoid internal structural collisions and to have a desired final structural shape.

Finally, to obtain useful hybrid controllers, multi-objective criteria encompassing conflicting demands on active tensegrity structures such as performance enhancement, vibratory response, and load reduction subject to multidisciplinary constraints such as structural stability, system weight and other material and/or physical structural properties, actuator and sensor locations, and structural topology, must be used. Thus, advanced search techniques must be developed to determine an optimally directed set of control actions, relative to the performance goals and their priorities since local minima will be present in the search space.

REFERENCES

- [1] H. Lalvani, “Origins of tensegrity: views of Emmerich, Fuller and Snelson,” *International Journal of Space Structures*, no. 11, pp. 27–55, 1996.
- [2] R. E. Skelton and M. C. Oliveira, *Tensegrity Systems*. Springer, 2009.
- [3] G. Tibert, “Deployable Tensegrity Structures for Space Applications,” Royal Institute of Technology, Stockholm, 2002.
- [4] W. J. Lewis, *Tension Structures: Form and Behaviour*. Thomas Telford Ltd, 2003.
- [5] F. Otto, “The Aesthetic,” Institute of Lightweight Structures (IL), 1979.
- [6] K. D. Snelson, “Continuous Tension, discontinuous compression structures: US patent 3,169,611,” 1965.
- [7] A. Pugh, *An Introduction to Tensegrity*. University of California Press, 1976.
- [8] R. Motro, *Tensegrity: Structural Systems for the Future*. London and Sterling: Kogan Page Science, 2003.
- [9] R. Motro, “Tensegrity Systems: The State of the Art,” *International Journal of Space Structures*, vol. 7, no. 2, pp. 75–84, 1992.
- [10] R. E. Skelton, J. W. Helton, R. Adhikari, J.-P. Pinaud, and W. Chan, “An Introduction to the Mechanics of Tensegrity Structures,” in *The Mechanical Systems Design Handbook: Modeling, Measurement, and Control*, Y. Hurmuzlu and O. D. I. Nwokah, Eds. CRC Press, 2002.
- [11] Y. Nishimura and H. Murakami, “Initial shape-finding and modal analyses of cyclic frustum tensegrity modules,” *Computer Methods in applied mechanics and engineering*, vol. 190, pp. 5795 – 5818, 2001.
- [12] H. C. Tran and J. Lee, “Advanced form-finding of tensegrity structures,” *Computers and Structures*, no. 88, pp. 237–246, 2010.
- [13] A. Hanaor, “Preliminary Investigation of Double-Layer Tensegrities,” *Proceedings of International Conference on the Design and Construction of Non-conventional Structures*, vol. 2, 1987.

- [14] R. B. Fuller, "Tensile integrity structures," U.S. Patent 3,063,521/1959.
- [15] D. G. Emmerich, "Construction de Reseaux Autotendants," U.S. Patent 1,377,290/1964.
- [16] M. Gough, "In the Laboratory of Constructivism: Karl Ioganson's Cold Structures," *JSTOR*, vol. 84, pp. 90–117, 1998.
- [17] K. Snelson, "Letter from Kenneth Snelson to Maria Gough on Karl Ioganson," *June 17, 2003*. [Online]. Available: http://bobwb.tripod.com/synergetics/photos/snelson_gough.html. [Accessed: 25-Dec-2012].
- [18] D. G. Emmerich, *Structures Tendues et Autotendantes*. Paris, France: Ecole d'Architecture de Paris la Villette, 1988.
- [19] F. Fu, "Study on the new prestressed tensegrity structure," Beijing University of Technology, 2000.
- [20] F. Fu, "Structural behavior and design methods of tensegrity domes," *Journal of Constructional Steel Research*, vol. 61, no. 1, pp. 23–35, 2005.
- [21] M. Kawaguchi, I. Tatemichi, and P. Chen, "Optimum shapes of a cable dome structure. Engineering Structures," *Engineering Structures*, vol. 21, no. 8, pp. 719–725, 1999.
- [22] P. Gossen, D. Chen, and E. Mikhlin, "The first rigidly clad 'tensegrity' type dome," The Crown Coliseum, Fayetteville, North Carolina, 2005.
- [23] C. Wilkinson, "Tensegrity bridge," Wilkinson Eyre Report, Washington D.C., USA, 2010.
- [24] L. Rhode-Barbarigos, N. Bel Hadj Ali, R. Motro, and I. F. C. Smith, "Designing tensegrity modules for pedestrian bridges," *Engineering Structures*, vol. 32, no. 4, pp. 1158–1167, 2010.
- [25] H. Klimke and S. Stephan, "The making of a tensegrity tower," Würzburg, Germany, 2003.
- [26] C. Sultan and R. Skelton, "Deployment of tensegrity structures," *International Journal of Solids and Structures*, no. 40, pp. 4637–4657, 2003.
- [27] R. Connelly and A. Back, "Mathematics and tensegrity," *American Scientist*, vol. 86, no. 2, pp. 142–151, 1998.
- [28] D. E. Ingber, "Commentary Cellular tensegrity: defining new rules of biological design that govern the cytoskeleton," *Journal of Cell Science*, no. 104, pp. 613–627, 1993.

- [29] D. E. Ingber, "Tensegrity I. Cell structure and hierarchical systems biology," *Journal of Cell Science*, no. 116, pp. 1157–1173, 2003.
- [30] D. E. Ingber, "Tensegrity II. How structural networks influence cellular information-processing networks," *Journal of Cell Science*, no. 116, pp. 1397 – 1408, 2003.
- [31] S. M. Levin, "The Icosahedron as a biologic support system," in *34th Annual Conference on Engineering in Medicine and Biology*, 1981.
- [32] S.-M. Cretu, "Tensegrity Concept – From Natural Systems to Robots," in *EUCOMES 08*, 2009, pp. 549 – 557.
- [33] T. Liedl, B. Högberg, J. Tytell, D. E. Ingber, and W. M. Shih, "Self-assembly of three-dimensional prestressed tensegrity structures from DNA," *Nature Nanotechnology*, vol. 5, no. 7, pp. 520 – 524, 2010.
- [34] M. Nikkhah, J. S. Strobl, R. De Vita, and M. Agah, "The cytoskeletal organization of breast carcinoma and fibroblast cells inside three dimensional (3-D) isotropic silicon microstructures," *Biomaterials*, vol. 31, no. 16, pp. 4552–4561, 2010.
- [35] D. E. Ingber, "Tensegrity and mechanotransduction," *Journal of Bodywork and Movement Therapies*, vol. 12, no. 3, pp. 198–200, 2008.
- [36] J. Gardiner, J. Marc, and R. Overall, "Cytoskeletal thermal ratchets and cytoskeletal tensegrity: determinants of brain asymmetry and symmetry?," *Frontiers in Bioscience*, no. 13, pp. 4649–4656, 2008.
- [37] K. Y. Volokh, O. Vilnay, and M. Belsky, "Cell cytoskeleton and tensegrity," *Biorheology*, vol. 39, no. 1–2, pp. 63–67, 2002.
- [38] G. J. Morgan, "Virus design, 1955-1962: science meets art," *Phytopathology*, vol. 96, no. 11, pp. 1287–1291, 2006.
- [39] C. Pflüger, "The Meaning of Tensegrity Principles for Osteopathic medicine," Donau University Krems and Vienna School of Osteopathy, 2008.
- [40] H. M. Farrell Jr., E. M. Brown, P. D. Hoagland, and E. L. Malin, "Higher Order Structure Of The Caseins: A Paradox?," in *Advanced Dairy Chemistry*, 3rd ed., vol. 1, P. F. Fox and P. L. H. McSweeney, Eds. 2003, pp. 203–231.
- [41] P. Ganguly, "Molecular geometry from molecular tensegrity: A case study of gas-phase MX₂ Compounds," *Current Science*, vol. 90, no. 9, 2006.
- [42] "Website of Koenig Associates," *Contemporary Furniture*. [Online]. Available: <http://www.koenigdesign.com/>. [Accessed: 25-Dec-2012].

- [43] “Website of Intension Designs,” *Tensegrity Furniture*. [Online]. Available: <http://www.intensiondesigns.com/gallery.html>. [Accessed: 25-Dec-2012].
- [44] M. Shibata and S. Hirai, “Rolling Locomotion of Deformable Tensegrity Structure,” in *12th International Conference on Climbing and Walking Robots and the Support Technologies for Mobile Machines*, 2009, vol. 19, no. 6, pp. 479–486.
- [45] A. G. Rovira and J. M. M. Tur, “Control and simulation of a tensegrity-based mobile robot,” *Robotics and Autonomous Systems*, no. 57, pp. 526–535, May 2009.
- [46] W. B. Carlson, D. Williams, and R. E. Newnham, “Piezotensegritic structures for transducer applications,” *Materials Research Innovations*, vol. 3, no. 3, pp. 175–178, 1999.
- [47] K. W. Moored and H. Bart-Smith, “The Analysis of Tensegrity Structures for the Design of a Morphing Wing,” *Journal of Applied Mechanics*, vol. 74, no. 4, pp. 668–677, 2007.
- [48] C. Sultan and M. Corless, “Tensegrity Flight Simulator,” *Journal of Guidance, Control and Dynamics*, vol. 23, no. 6, pp. 1055–1064, 2000.
- [49] R. Connelly and W. Whiteley, “Second order rigidity and prestress stability for tensegrity frameworks,” *Discrete Mathematics*, vol. 9, no. 3, pp. 453–491, 1996.
- [50] R. Connelly, “Tensegrity Structures: Why are they stable,” in *Rigidity Theory and Applications*, M. F. Thorpe and P. M. Duxbury, Eds. Plenum Press, New York, 1999, pp. 47–54.
- [51] R. Connelly and M. Terrell, “Globally rigid symmetric tensegrities,” *Journal of Structural Topology*, no. 21, pp. 59–78, 1995.
- [52] R. Connelly, “The rigidity of certain cable frameworks and the second order rigidity of arbitrarily triangulated convex surfaces,” *Advances in Mathematics*, no. 37, pp. 272–299, 1980.
- [53] T. F. Havel, “The Role of Tensegrity in Distance Geometry,” in *Rigidity theory and applications*, M. F. Thorpe and P. M. Duxbury, Eds. Kluwer Academic/Plenum Publishers, 1999, pp. 55–68.
- [54] R. Connelly, “Rigidity,” in *Handbook of Convex Geometry*, P. M. Gruber and J. M. Wills, Eds. Elsevier Publishers Ltd, 1993, pp. 223–271.
- [55] R. Connelly, “Rigidity and energy,” *Inventiones Mathematicae*, no. 66, pp. 11–33, 1982.

- [56] B. Roth and W. Whiteley, "Tensegrity frameworks," *Transactions of the American Mathematical Society*, no. 265, pp. 419–446, 1981.
- [57] A. So, M. El-Chammas, and Y. Ye, "A Semidefinite Programming Approach to Tensegrity Theory and Graph Realization," in *6th Annual MOPTA Conference*, 2006.
- [58] C. Calladine, "Buckminster Fuller's 'Tensegrity' structures and Clerk Maxwell's rules for the construction of stiff frames," *International Journal of Solids and Structures*, vol. 14, no. 2, pp. 161–172, 1978.
- [59] S. Pellegrino and C. R. Calladine, "Matrix Analysis of Statically and Kinematically Indeterminate Frameworks," *International Journal of Solids and Structures*, vol. 22, no. 4, pp. 409–428, 1986.
- [60] H. Murakami, "Static and dynamic analyses of tensegrity structures. Part 1. Nonlinear equations of motion," *International Journal of Solids and Structures*, no. 38, pp. 3599–3613, May 2001.
- [61] C. R. Calladine and S. Pellegrino, "First-Order Infinitesimal Mechanisms," *International Journal of Solids and Structures*, vol. 27, no. 4, pp. 505–515, 1991.
- [62] E. N. Kuznetsov, "Letter To The Editor: Discussion of 'First-order infinitesimal mechanisms'," *International Journal of Solids and Structures*, vol. 27, no. 4, pp. 517–519, 1991.
- [63] C. R. Calladine and S. Pellegrino, "Further Remark on First Order Infinitesimal Mechanism," *International Journal of Solids and Structures*, vol. 29, no. 17, pp. 2119–2122, 1992.
- [64] S. Pellegrino, "Structural computations with the singular value decomposition of the equilibrium matrix," *International Journal of Solids and Structures*, vol. 30, no. 21, pp. 3025–3035, 1993.
- [65] S. Pellegrino, "Analysis of prestressed mechanisms," *International Journal of Solids and Structures*, vol. 26, no. 12, pp. 1329–1350, 1990.
- [66] E. Kuznetsov, "Singular configurations of structural systems," *International Journal of Solids and Structures*, vol. 36, no. 6, pp. 885–897, Feb. 1999.
- [67] E. Kuznetsov, "On the evaluation of statical-kinematic stiffness matrix for underconstrained structural systems," *International Journal of Solids and Structures*, vol. 37, no. 15, pp. 2215–2223, Apr. 2000.
- [68] S. Guest, "The stiffness of prestressed frameworks: A unifying approach," *International Journal of Solids and Structures*, no. 43, pp. 842–854, Feb. 2006.

- [69] N. Vassart and R. Motro, "Multiparametered formfinding method: application to tensegrity systems," *International Journal of Space Structures*, vol. 14, no. 2, pp. 147–154, 1999.
- [70] R. M. Masic, E. Skelton, and P. E. Gill, "Algebraic tensegrity form-finding," *International Journal of Solids and Structures*, vol. 42, no. 16–17, pp. 4833–4858, 2005.
- [71] C. Sultan, "Modelling, Design, and Control of Tensegrity Structures with Applications," Purdue University, 1999.
- [72] R. P. Raj and S. D. Guest, "Using Symmetry for Tensegrity Form-Finding," in *IASS-APCS 2006 Symposium: New Olympics – New Shell and Spatial Structures*, 2006.
- [73] M. Pagitz and J. M. Mirats Tur, "Finite element based form-finding algorithm for tensegrity structures," *International Journal of Solids and Structures*, vol. 46, no. 17, pp. 3235–3240, Aug. 2009.
- [74] R. Motro, "Forms and forces in tensegrity systems," in *3rd International Conference on Space Structures*, Elsevier, 1984, pp. 180–185.
- [75] C. Paul, H. Lipson, and F. Cuevas, "Evolutionary form-finding of tensegrity structures," in *The 2005 Conference on Genetic and Evolutionary Computation*, 2005.
- [76] X. Xu and Y. Luo, "Form-finding of nonregular tensegrities using a genetic algorithm," *Mechanics Research Communications*, vol. 37, no. 1, pp. 85–91, Jan. 2010.
- [77] B. Domer, E. Fest, V. Lalit, and I. F. C. Smith, "Combining Dynamic Relaxation Method with Artificial Neural Networks to Enhance Simulation of Tensegrity Structures," *Journal of Structural Engineering*, vol. 129, no. 5, pp. 672–681, 2003.
- [78] M. Masic, R. Skelton, P. Gill, "Optimization of tensegrity structures," *International Journal Solids and Structures*, vol. 43, pp. 4687–4703, 2006.
- [79] F. Bossens, R. A. De Callafon, and R. E. Skelton, "Modal Analysis of a Tensegrity Structure – an experimental study." [Online]. Available: http://maeweb.ucsd.edu/~skelton/publications/bossens_modal_three_stage.pdf. [Accessed: 14-Jan-2013].
- [80] H. Furuya, "Concept of Deployable Tensegrity Structures in Space Applications," *International Journal of Space Structures*, vol. 7, no. 2, pp. 143–151, 1992.

- [81] I. J. Oppenheim and W. O. Williams, "Vibration of an Elastic Tensegrity Structure," *European Journal of Mechanics and Solids*, no. 20, pp. 1023–1031, 2001.
- [82] I. J. Oppenheim and W. O. Williams, "Vibration and Damping in Three-Bar Tensegrity Structure," *Journal of Aerospace Engineering*, no. 14, pp. 85–91, 2001.
- [83] H. Murakami, "Static and dynamic analyses of tensegrity structures. Part II. Quasi-static analysis," *International Journal of Solids and Structures*, no. 38, pp. 3615–3629, May 2001.
- [84] J. M. M. Tur and S. H. Juan, "Tensegrity frameworks: Dynamic analysis review and open problems," *Mechanism and Machine Theory*, no. 44, pp. 1–18, Jan. 2009.
- [85] W. L. Chan, D. Arbelaez, F. Bossens, and R. E. Skelton, "Active vibration control of a three-stage tensegrity structure," in *The SPIE Smart Structures and Materials: Damping and Isolation*, 2004, pp. 340–346.
- [86] B. De Jager, R. E. Skelton, and M. Masic, "Integrated control/ structure design for planar tensegrity models," in *The IEEE International Conference on Control Applications*, 2002, pp. 862–867.
- [87] A. S. Wroldsen, M. C. De Oliveira, and R. E. Skelton, "A discussion on control of tensegrity systems," in *The 45th IEEE Conference on Decision and Control*, 2006, pp. 2307–2313.
- [88] M. Masic and R. E. Skelton, "Path planning and openloop shape control of modular tensegrity structures," *Journal of Guidance, Control, and Dynamics*, vol. 28, no. 3, pp. 421–430, 2005.
- [89] M. Masic and R. E. Skelton, "Selection of prestress for optimal dynamic/control performance of tensegrity structures," *International Journal of Solids And Structures*, vol. 43, no. 7–8, pp. 2110–2125, 2006.
- [90] S. Djouadi, R. Motro, J. C. Pons, and B. Crosnier, "Active control of tensegrity systems," *ASCE Journal of Aerospace Engineering*, vol. 11, no. 2, pp. 37–44, 1998.
- [91] S. Korkmaz, "A review of active structural control: challenges for engineering informatics," *Computers & Structures*, vol. 89, no. 23–24, pp. 2113–2132, Dec. 2011.
- [92] I. F. C. Smith, "From Active to Intelligent Structures," in *7th international Conference on the Application of Artificial Intelligence to Civil and Structural Engineering*, 2003.

- [93] A. H. Chowdhury, M. D. Iwuchukwu, and J. J. Garske, “The past and future of seismic effectiveness of tuned mass dampers,” *Structural Control*, 1985.
- [94] R. E. Skelton, “Structural systems: a marriage of structural engineering and system science,” *Journal of Structural Control*, vol. 9, pp. 113–33, 2002.
- [95] C. Sultan, M. Corless, and R. E. Skelton, “Linear dynamics of tensegrity structures,” *Engineering Structures*, no. 24, pp. 671–685, 2002.
- [96] D. Williamson, R. E. Skelton, and J. Han, “Equilibrium conditions of a tensegrity structure,” *International Journal of Solids and Structures*, no. 40, pp. 6347–6367, 2003.
- [97] R. Motro, “Tensegrity systems—latest developments and perspectives,” in *10 Years of Progress in Shell and Spatial Structures, 30th Anniversary of IASS*, 1989.
- [98] H. Schek, “The force density method for form finding and computation of general networks,” *Computer Methods in Applied Mechanics and Engineering*, no. 3, pp. 115–134, 1974.
- [99] J. H. Argyris, “Recent Advances in Matrix Methods of Structural Analysis,” *Progress in Aeronautical Science*, vol. 4. Pergamon Press, New York, 1964.
- [100] G. Tibert and S. Pellegrino, “Review of Form-Finding Methods for Tensegrity Structures,” *International Journal of Space Structures*, vol. 18, no. 4, pp. 209–223, Dec. 2003.
- [101] G. Strang, *Linear Algebra and its Applications*, Second. Orlando, Florida: Academic Press, Inc, 1980.
- [102] J. Graver, B. Servatius, and H. Servatius, *Combinatorial rigidity*, vol. 2. American Mathematical Society, 1994.
- [103] G. G. Estrada, “Analytical and numerical investigations of form-finding methods for tensegrity structures,” University of Stuttgart, 2007.
- [104] G. Estrada, H. Bungartz, and C. Mohrdieck, “Numerical form-finding of tensegrity structures,” *International Journal of Solids and Structures*, no. 43, pp. 6855–6868, Nov. 2006.
- [105] S. S. Rao, *Engineering Optimization: Theory and Practice*. New York: John Wiley and Sons, Inc, 1996.
- [106] R. H. Byrd, M. E. Hribar, and J. Nocedal, “An Interior Point Algorithm for Large-Scale Nonlinear Programming,” *SIAM Journal on Optimization*, vol. 9, no. 4, pp. 877–900, 1999.

- [107] R. H. Byrd, R. B. Schnabel, and G. A. Shultz, “Approximate Solution of the Trust Region Problem by Minimization over Two-Dimensional Subspaces,” *Mathematical Programming*, vol. 40, pp. 247–263, 1988.
- [108] A. V. Fiacco and G. P. McCormick, “Extensions of SUMT for nonlinear programming: equality constraints and extrapolation,” *Management Science*, vol. 12, pp. 816–828, 1966.
- [109] “MATLAB Optimization Toolbox 5: User’s Guide,” 2010.
- [110] J. E. Dennis and R. B. Schnabel, *Numerical Methods for Unconstrained Optimization and Nonlinear Equations*. Enlewookd Cliffs, New Jersey: Prentice Hall, 1983.
- [111] R. A. Waltz, J. L. Morales, J. Nocedal, and D. Orban, “An interior algorithm for nonlinear optimization that combines line search and trust region steps,” *Mathematical Programming*, vol. 107, no. 3, pp. 391–408, 2006.
- [112] H. Crapo and W. Whiteley, “Statics of frameworks and motions of panel structures, a projective geometric introduction,” *Topologie structurale*, vol. 6, pp. 43–82, 1982.
- [113] H. Kenner, *Geodesic Math and How to Use It*. Berkeley, California: University of California Press, 1976.
- [114] S. Pellegrino, “Mechanics of Kinematically Indeterminate Structures,” *Ph.D. Thesis, University of Cambridge*, 1986.
- [115] R. W. Burkhardt, *A Practical Guide to Tensegrity Design*. Cambridge, USA , 2008.
- [116] S. Juan and J. Miratstur, “Tensegrity frameworks: Static analysis review,” *Mechanism and Machine Theory*, no. 43, pp. 859–881, Jul. 2008.
- [117] S. H. Juan and J. M. M. Tur, “Tensegrity frameworks: Static analysis review,” *Mechanism and Machine Theory*, no. 43, pp. 859–881, 2008.
- [118] H. Nooshin and P. Disney, “Elements of formian,” *Computers & Structures*, vol. 41, no. 6, pp. 1183–1215, 1991.
- [119] S. S. Rao, *The Finite Element Method in Engineering*, Third. Butterworth-Heinemann, 1999.
- [120] O. C. Zienkiewicz and R. L. Taylor, *The Finite Element Method Set: Its Basis and Fundamentals*, 6th ed. Butterworth-Heinemann, 2005.
- [121] K.-J. Bathe and E. L. Wilson, *Numerical Methods in Finite Element Analysis*. Prentice-Hall, 1976.

- [122] G. Pelosi, “The finite-element method, Part I: R. L. Courant,” *Antennas and Propagation Magazine, IEEE*, vol. 49, no. 2, pp. 180–182, 2007.
- [123] H. Neudecker, “Some Theorems on Matrix Differentiation with special reference to Kronecker matrix products,” *Journal of American Statistical Association*, vol. 64, pp. 953–963, 1969.
- [124] P. M. Bentler and S.-Y. Lee, “Matrix Derivates with Chain Rule and Rules for Simple, Hadamard, and Kronecker Products,” *Journal of Mathematical Psychology*, vol. 17, pp. 255–262, 1978.
- [125] M. Ohsaki and J. Zhang, “Stability conditions of prestressed pin-jointed structures,” *International Journal of Non-Linear Mechanics*, vol. 41, pp. 1109–1117, Dec. 2006.
- [126] J. S. Archer, “Consistent Mass Matrix for Distributed Mass Systems,” *Journal of Structural Division*, vol. 89, pp. 161–178, 1963.
- [127] H. Benaroya and M. L. Nagurka, *Mechanical Vibration: Analysis, Uncertainties, and Control*, Third. CRC Press, 2010.
- [128] R. W. Clough and J. Penzien, *Dynamics of Structures*, Second. McGraw-Hill, 1993.
- [129] A. Preumont, *Vibration Control of Active Structures: An Introduction*, Second. Kluwer Academic Publishers, 2002.
- [130] R. J. Guyan, “Reduction of stiffness and mass matrices,” *American Institute of Aeronautics and Astronautics*, vol. 3, no. 2, 1965.
- [131] H. Crapo and W. Whiteley, *The Geometry of Rigid Structures*. Cambridge University Press, 1993.
- [132] R. C. Dorf and R. H. Bishop, *Modern Control Systems*, Eighth. Addison Wesley Longman, Inc., 1998.
- [133] W. K. Gawronski, *Advanced Structural Dynamics and Active Control of Structures*. Springer-Verlag, New York, Inc., 2004.
- [134] J. T. . Yao, “Concept of Structural Control,” *ASCE Journal of the Structural Division*, vol. 98, pp. 1567–1574, 1972.
- [135] J. Spencer, B.F. and M. K. Sain, “Controlling Buildings: A New Frontier in Feedback,” *IEEE Control Systems*, pp. 19–34, 1997.
- [136] G. G. Yen, “Reconfigurable Learning Control in Large Space Structures,” *IEEE Transactions on Control Systems Technology*, vol. 2, no. 4, pp. 362–370, 1997.

- [137] A. Y. T. Leung, "An accurate method of dynamic substructuring with simplified computation," *International Journal of Numerical Methods*, vol. 14, pp. 1241–1256, 1979.
- [138] K. Yae and D. Inman, "Model reduction in a subset of the original states," *Journal of Sound and Vibration*, vol. 155, no. 1, pp. 165–176, May 1992.
- [139] P. Salvini and F. Vivio, "Dynamic reduction strategies to extend modal analysis approach at higher frequencies," *Finite Elements in Analysis and Design*, vol. 43, no. 11–12, pp. 931–940, Aug. 2007.
- [140] D. Hyland and D. Bernstein, "The optimal projection equations for model reduction and the relationships among the methods of Wilson, Skelton, and Moore," *IEEE Transactions on Automatic Control*, vol. 30, no. 12, pp. 1201–1211, Dec. 1985.
- [141] M. Aoki, "Control of large-scale dynamics systems by aggregation," *IEEE Transactions on Automatic Control*, vol. 13, pp. 246–253, 1963.
- [142] W. K. Gawronski and H. G. Natke, "Balancing Linear Systems," *International Journal of Systems Science*, vol. 18, pp. 237–249, 1987.
- [143] W. K. Gawronski and H. G. Natke, "On balancing Linear Symmetric Systems," *International Journal of Systems Science*, vol. 17, pp. 1509–1519, 1986.
- [144] B. Moore, "Principal Component Analysis in Linear Systems: Controllability, Observability, and Model Reduction," *IEEE Transactions on Automatic Control*, vol. AC-26, pp. 17–31, 1981.
- [145] R. E. Skelton and F. Li, "Economic sensor/actuator selection and its application to flexible structures and materials," in *SPIE 5383, Smart Structures and Materials 2004: Modeling, Signal Processing, and Control*, 2004, vol. 5383, pp. 194–201.
- [146] F. Li and R. E. Skelton, "Sensor/actuator selection for tensegrity structures," in *The 45th IEEE Conference on Decision and Control*, 2006, pp. 2332–2337.
- [147] M. Van De Wal and B. De Jager, "A review of methods for input/output selection," *Automatica*, vol. 37, pp. 487–510, Apr. 2001.
- [148] W. K. Gawronski, "Actuator and Sensor Placement for Structural Testing and Control," *Journal of Sound and Vibration*, vol. 208, no. 1, pp. 101–109, Nov. 1997.
- [149] T. Kailath, *Linear Systems*. Englewood Cliffs, New Jersey: Prentice Hall, 1980.
- [150] A. J. Laub, "Computation of Balancing Transformations," *Joint Automatic Control Conference*, vol. 1, no. FA8-E, 1980.

- [151] H. Kwakernaak and R. Sivan, *Linear Optimal Control Systems*. John Wiley and Sons, Inc, 1972.
- [152] A. J. Laub, C. C. Heath, and R. C. Ward, "Computation of System Balancing Transformations and Other Applications of Simultaneous Diagonalization Algorithms," *IEEE Transactions on Automatic Control*, vol. AC-32, pp. 115–122, 1987.
- [153] F. W. Fairman, *Linear Control Theory: The State Space Approach*. Chichester, England: John Wiley and Sons, Inc, 1998.
- [154] A. E. Bryson and Y. C. Ho, *Applied Optimal Control: Optimization, Estimation and Control*. New York: John Wiley and Sons, 1975.
- [155] N. A. Bruisma and M. Steinbuch, "A Fast Algorithm to Compute the H_∞ -Norm of a Transfer Function Matrix," *System Control Letters*, vol. 14, pp. 287–293, 1990.
- [156] S. Skogestad and I. Postlethwaite, *Multivariable Feedback Control: Analysis and Design*. Chichester, England: John Wiley and Sons, Inc, 1996.
- [157] R. E. Skelton, *Dynamic Systems Control: Linear Systems Analysis and Synthesis*. John Wiley and Sons, Inc, 1988.
- [158] K. Glover, "All optimal Hankel-norm approximations of linear multivariable systems and their $L(\infty)$ -error bounds," *International Journal of Control*, vol. 39, no. 6, pp. 1115–1193, 1984.
- [159] K. Zhou, "Frequency-weighted model reduction with L_∞ error bounds," *Systems & Control Letters*, vol. 21, no. 2, pp. 115–125, Aug. 1993.
- [160] M. G. Safonov and R. Y. Chiang, "Model Reduction for Robust Control: A Schur Relative-Error Method," *American Control Conference*, vol. 2, pp. 259–272, 1988.
- [161] W. Gawronski and K. B. Lim, "Balanced actuator and sensor placement for flexible structures," *International Journal of Control*, vol. 65, no. 1, pp. 131–145, Sep. 1996.
- [162] J. Onoda and R. T. Haftka, "An approach to structure/control simultaneous optimization for large flexible spacecraft," *AIAA Journal*, vol. 25, pp. 1133–1138, 1987.
- [163] R. E. Skelton and M. L. Delorenzo, "Space structure control design by variance assignment," *Journal of guidance and control*, vol. 8, pp. 454–462, 1985.

- [164] M. L. Delorenzo, "Sensor and actuator selection for large space structure control," *Journal of Guidance, Control and Dynamics*, vol. 13, pp. 249–257, 1990.
- [165] J. M. Mirats-tur and J. Camps, "A Minimal Tensegrity Configuration," *Robots and Automation Magazine, IEEE*, vol. 18, no. 3, pp. 96–103, 2011.
- [166] C. Paul, F. J. Valero-Cuevas, and H. Lipson, "Design and control of tensegrity robots for locomotion," *IEEE Transactions on Robotics*, vol. 22, no. 5, pp. 944–957, Oct. 2006.
- [167] R. Motro, "Tensegrity systems and geodesic domes," *International Journal of Space Structures*, vol. 5, no. 3–4, pp. 341–351, 1990.
- [168] M. Masic and R. E. Skelton, "Open – Loop Control of Class – 2 Tensegrity Towers," in *SPIE 5383, Smart Structures and Materials 2004: Modeling, Signal Processing, and Control*, 2004, no. 1, pp. 298–891.
- [169] C. Sultan, "A force and torque tensegrity sensor," *Sensors and Actuators A: Physical*, vol. 112, no. 2–3, pp. 220–231, May 2004.
- [170] B. de Jager and R. E. Skelton, "Input-output selection for planar tensegrity models," *IEEE Transactions on Control Systems Technology*, vol. 13, no. 5, pp. 778–785, Sep-2005.
- [171] W. Chan and R. E. Skelton, "Equilibria and stiffness of planar tensegrity structures," in *AAS/AIAA Space Flight Mechanics Meeting*, 2002.
- [172] D. Rees, *Mechanics of Optimal Structural Design: Minimum Weight Structures*. John Wiley and Sons, Inc, 2009.
- [173] "Light Duty Series Actuators," *Concentric International*. [Online]. Available: <http://www.concentricintl.com/products/electrical-control/linear-actuators/ld-series/>. [Accessed: 14-Jan-2013].
- [174] R. D. Cook and W. C. Young, *Advanced Mechanics of Materials*. New York, NY: Macmillan Publishing Co., 1985.
- [175] S. H. Juan, R. E. Skelton, and J. M. M. Tur, "Dynamically Stable Collision Avoidance for Tensegrity Based Robots," in *International Conference on Reconfigurable Mechanisms and Robots*, 2009, pp. 315–322.
- [176] M. Cefalo and J. M. Mirats Tur, "Real-time self-collision detection algorithms for tensegrity systems," *International Journal of Solids and Structures*, vol. 47, no. 13, pp. 1711–1722, Jun. 2010.

- [177] S. Hernandez Juan and J. M. M. Tur, "A method to generate stable, collision free configurations for tensegrity based robots," in *International Conference on Intelligent Robotics and Systems*, 2008.
- [178] J. van e Widdeven and B. De Jager, "Shape Change of Tensegrity Structures: Design and Control," in *American Control Conference*, 2005, pp. 2522–2527.
- [179] H. Zhang and A. J. Hanson, "Physically interacting with four dimensions," in *Advances in Visual Computing*, 2006 Proce., Springer Berlin Heidelberg, 2009, pp. 232–242.
- [180] D. Stewart, "A Platform with Six Diegrees of Freedom," *The Institution of Mechanical Engineers (UK)*, vol. 1, no. 15, pp. 371–376, 1965.
- [181] H. Tari, H.-J. Su, and J. D. Hauenstein, "Classification and complete solution of the kinetostatics of a compliant Stewart–Gough platform," *Mechanism and Machine Theory*, vol. 49, pp. 177–186, Mar. 2012.
- [182] C. Hsu and I. Fong, "Motion control of a hydraulic Stewart platform with computed force feedback," *Journal of the Chinese Institute of Engineers*, vol. 24, no. 6, pp. 709–721, Sep. 2001.
- [183] B. Biegel and A. Description, "Wind Turbine Pitch Optimization," in *IEEE International Conference on Control Applications*, 2011, pp. 1327–1334.
- [184] S. Nourdine, H. Camblong, I. Vechiu, and G. Tapia, "Comparison of wind turbine LQG controllers using Individual Pitch Control to alleviate fatigue loads," *18th Mediterranean Conference on Control and Automation, MED'10*, pp. 1591–1596, Jun. 2010.
- [185] Y. Xingjia, W. Xiaodong, X. Zuoxia, L. Yingming, and L. Jun, "Individual pitch control for variable speed turbine blade load mitigation," *IEEE International Conference on Sustainable Energy Technologies*, pp. 769–772, Nov. 2008.
- [186] P. Veers, G. Bir, and D. Lobitz, "Aeroelastic Tailoring in Wind-Turbine Blade Applications," in *Windpower '98, American Wind Energy Association Meeting and Exhibition*, 1998, no. 1981.
- [187] "Pololu Jrk 12v12 USB Motor Controller with Feedback," *Pololu Corporation*. [Online]. Available: <http://www.pololu.com/catalog/product/1393>. [Accessed: 14-Jan-2013].
- [188] ST Engineering Manual, "Automotive Fully Integrated H-Bridge Motor Driver," 2005.
- [189] "90Watts VEH Series Power Supply Manual," 2011. [Online]. Available: http://www.xppower.com/pdfs/V-Brand_Catalog_2011.pdf. [Accessed: 14-Jan-2013].

- [190] L. M. Surhone, M. T. Timpledon, and S. F. Marseken, Eds., *Serial Port: RS-232, Serial Communication, Parallel Port, Ethernet, IEEE 1394 Interface, Universal Serial Bus*. Betascript Publishing, 2010.
- [191] “MATLAB (R2008b) User Manual,” Natick, Massachusetts, 2008.
- [192] K. J. Astrom and R. Murray, *Feedback systems: An introduction for Scientists and Engineers*. Princeton University Press, 2008.
- [193] D. Xue, Y. Chen, and D. P. Atherton, *Linear Feedback Control*, 1st ed. Society for Industrial Mathematics, 2008.
- [194] G. C. Goodwin, S. F. Graebe, and M. E. Salgado, *Control System Design*. Prentice Hall, 2000.
- [195] E. H. Bristol, “On a new measure of interaction for multivariable process control,” *IEEE Transactions on Automatic Control*, vol. 11, no. 1, pp. 133–134, 1966.
- [196] G. J. Balas and J. C. Doyle, “Collocated Versus Non-collocated Multivariable Control for Flexible Structure,” *American Control Conference*, pp. 1923–1928, 1990.
- [197] D. S. Bernstein and W. M. Haddad, “Nonlinear controllers for positive real systems with arbitrary input nonlinearities,” *IEEE Transactions on Automatic Control*, vol. 39, no. 7, pp. 1513 – 1517, 1994.
- [198] J. T. Wen, “Time Domain and Frequency Domain Conditions for Strict Positive Realness,” *IEEE Transactions on Automatic Control*, vol. 33, pp. 988–992, 1988.
- [199] L. Hitz and B. D. O. Anderson, “Discrete positive-real functions and their application to system stability,” in *the IEE*, 1969, vol. 116, no. I, pp. 153–155.
- [200] M. D. McLaren and G. L. Slater, “Robust multivariable control of large space structures using positivity,” *Journal of Guidance, Control, and Dynamics*, vol. 10, pp. 393–400, 1987.
- [201] R. Lozano-Leal and S. M. Joshi, “On the design of dissipative LQG-type controllers,” in *The 27th IEEE Conference on Decision and Control*, 1988, vol. 2, pp. 1645–1646.
- [202] D. C. Hyland, “Distributed parameter modeling of flexible spacecraft: Where’s the beef?,” *NASA Workshop on Distributed Parameter Modeling and Control of flexible Aerospace Systems, NASA Conference Publication*, vol. 3242, pp. 3–23, 1994.

- [203] B. C. Moore, "On the flexibility offered by state feedback in multivariable systems beyond closed loop eigenvalue assignment," *1975 IEEE Conference on Decision and Control including the 14th Symposium on Adaptive Processes*, vol. 14, pp. 207–214, 1975.
- [204] G. Klein and B. C. Moore, "Eigenvalue-generalized eigenvector assignment with state feedback," *IEEE Transactions on Automatic Control*, vol. 22, no. 1, pp. 140–141, 1977.
- [205] J. Kautsky, N. K. Nichols, and P. Van Dooren, "Robust Pole Assignment in Linear State Feedback," *International Journal of Control*, vol. 41, no. 5, pp. 1129–1155, 1985.
- [206] F. Fallside, *Control Systems Design by Pole-Zero Assignment*, New York: Academic Press, 1977.
- [207] P. G. Maghami and S. Gupta, "Design of Constant Gain Dissipative Controllers for Eigensystem Assignment in Passive Systems," *Journal of Guidance, Control, and Dynamics*, vol. 20, no. 4, pp. 648–657, Jul. 1997.
- [208] G. S. Miminis and C. C. Paige, "An algorithm for pole-assignment of time-invariant multi-input linear systems," *International Journal of Control*, vol. 35, pp. 341–354, 1982.
- [209] G. S. Miminis and C. C. Paige, "A Direct Algorithm for Pole Assignment of Time-invariant Multi-input Linear Systems using State Feedback," *Automatica*, vol. 24, no. 3, pp. 343–356, 1988.
- [210] B. Datta, "An algorithm to assign eigenvalues in a Hessenberg matrix: Single input case," *IEEE Transactions on Automatic Control*, vol. 32, no. 5, pp. 414–417, 1987.
- [211] R. V. Patel and P. Misra, "Numerical Algorithms for Eigenvalue Assignment by State Feedback," *Proceeding of the IEEE*, vol. 72, no. 12, pp. 1755–1764, 1984.
- [212] B. N. Datta, *Numerical methods for linear control systems design and analysis*. New York: Academic Press, 2002.
- [213] M. Balas, "Trends in large space structure control theory: Fondest hopes, wildest dreams," *IEEE Transactions on Automatic Control*, vol. 27, no. 3, pp. 522–535, Jun. 1982.
- [214] S. M. Joshi, *Control of Large Flexible Space Structures*. New York: Springer-Verlag, 1989.
- [215] R. J. Benhabib, R. P. Iwens, and R. L. Jackson, "Stability of large space structure control systems using positivity concepts," *Journal of guidance and control*, vol. 4, pp. 487–494, 1981.

- [216] G. F. Franklin, J. D. Powell, and A. Emami-Naeini, *Feedback Control of Dynamic Systems*, Sixth. Pearson, 2009.
- [217] B. D. O. Anderson and D. G. Luengerger, “Design of Multivariable Feedback Systems,” *Proceeding of the IEE*, vol. 114, pp. 395–399, 1967.
- [218] H. Kojima, Y. Sugimoto, and Y. Furukawa, “Experimental study on dynamics and control of tethered satellite systems with climber,” *Acta Astronautica*, vol. 69, no. 1–2, pp. 96–108, Jul. 2011.
- [219] A. Y. N. Sofla, S. A. Meguid, K. T. Tan, and W. K. Yeo, “Shape morphing of aircraft wing: Status and challenges,” *Materials & Design*, vol. 31, no. 3, pp. 1284–1292, Mar. 2010.
- [220] W. F. Arnold and A. J. Laub, “Generalized Eigenproblem Algorithms and Software for Algebraic Riccati Equations,” in *The IEEE*, 1984, vol. 72, pp. 1746–1754.
- [221] W. Jun and L. Yuping, “A Distributed Coordinated Control Scheme for Morphing Wings with Sampled Communication,” *Chinese Journal of Aeronautics*, vol. 23, no. 3, pp. 364–369, Jun. 2010.
- [222] L. H. Shu, K. Ueda, I. Chiu, and H. Cheong, “Biologically inspired design,” *CIRP Annals - Manufacturing Technology*, vol. 60, no. 2, pp. 673–693, Jan. 2011.
- [223] R. D. Beer, H. J. Chiel, R. D. Quinn, and R. E. Ritzmann, “Biorobotic approaches to the study of motor systems.,” *Current opinion in neurobiology*, vol. 8, no. 6, pp. 777–82, Dec. 1998.
- [224] J. C. Doyle, “Guaranteed margins for LQG regulators,” *IEEE Transactions on Automatic Control*, vol. 23, pp. 756–757, 1978.
- [225] J. C. Doyle and G. Stein, “Robustness with Observers,” *IEEE Transactions on Automatic Control*, vol. 24, pp. 607–611, 1979.
- [226] J. C. Doyle and G. Stein, “Multivariable Feedback Design: Concepts for a Classical/Modern Synthesis,” *IEEE Transactions on Automatic Control*, vol. 26, no. 1, pp. 4–16, 1981.
- [227] M. Athans, “A tutorial on LQG/LTR method,” in *American Control Conference*, 1986, pp. 1289–1296.
- [228] J. S. Freudenberg and D. P. Looze, “Right Half Plane Poles and Zeros and Design Tradeoffs in Feedback Systems,” *IEEE Transactions on Automatic Control*, vol. 30, pp. 555–561, 1985.

- [229] U. S, N. C. H, and W. J. B, *Elementary Structural Analysis*, Fourth. New York: McGraw-Hill, 1991.
- [230] V. Chawla, S. Utku, and B. K. Wada, "Vibration control by limiting the maximum axial forces in space trusses," in *AIAA/ASME/ASCE/AHS/ASC 34th Structures, Structural Dynamics and Material conference*, 1993, vol. 107.
- [231] M. Sener, S. Utku, and B. K. Wada, "Geometry control in prestressed adaptive space trusses," *Smart materials and structures*, vol. 3, pp. 219–225, 1994.
- [232] A. V Ramesh, S. Utku, and B. K. Wada, "Real-time control of geometry and stiffness in adaptive structures," *Computer Methods in Applied Mechanics and Engineering*, vol. 90, no. 1–3, pp. 761–779, 1991.
- [233] L. Gaudiller and S. Bochar, "Adaptive active control of flexible structures subjected to rigid body displacements," *Journal of Sound and Vibration*, vol. 283, pp. 311–339, May 2005.
- [234] L. Gaudiller and J. Der Hagopian, "Active Control of Flexible Structures Using a Minimum Number of Components," *Journal of Sound and Vibration*, vol. 193, no. 3, pp. 713–741, Jun. 1996.
- [235] B. Fallahi, S. Lai, and C. Venkat, "A finite element formulation of a flexible slider crank mechanism using local coordinates," *Journal of Dynamic Systems, Measurement and Control*, vol. 117, no. 3, pp. 329–335, 1995.
- [236] T. Koyama and H. Asada, "Design of an Arm with Double Actuators for High Speed and High Accuracy Manipulation," in *American Control Conference*, 1991, pp. 1435–1437.
- [237] Y. C. Liu and S. M. Yang, "Vibration Control Experiment of a Slewing Flexible Beam," *Journal of Dynamic Systems, Measurement and Control*, vol. 117, pp. 432–435, 1995.
- [238] S. Lahaye, J.-L. Boimond, and L. Hardouin, "Optimal control of (min,+) linear time-varying systems," in *8th International Workshop on Petri Nets and Performance Models (Cat. No.PR00331)*, 1999, pp. 170–178.
- [239] M. Grimble and P. Martin, "Time-Varying Optimal Control of a Non-Linear System," in *42nd IEEE Conference on Decision and Control*, 2003, no. December, pp. 3495–3500.
- [240] A. S. Wroldsen, "Modelling and Control of Tensegrity Structures," Norwegian University of Science and Technology, 2007.
- [241] B. Adam and I. F. C. Smith, "Active tensegrity: A control framework for an adaptive civil-engineering structure," *Computers and Structures*, vol. 86, no. 23–24, pp. 2215–2223, 2008.

- [242] R. Skelton, “Dynamics and control of tensegrity systems,” in *Proceedings of the IUTAM Symposium on Vibration Control of Nonlinear Mechanisms and Structures*, 2005, vol. 32, pp. 309–318.
- [243] F. Lewis, *Optimal Estimation*. John Wiley & Sons, Inc., 1986.
- [244] H. J. Kushner, *Stochastic Stability and Control*. Academic Press, New York, 1967.

Appendix

LINEAR OPTIMAL CONTROL SYSTEMS

A.1 Linear Optimal State-feedback Regulator

Consider the following linear time invariant (LTI) system:

$$\dot{x} = Ax + Bu \quad (\text{A.1})$$

with the controlled variable written in the following form:

$$z = Hx \quad (\text{A.2})$$

Also, consider the following quadratic criterion:

$$\int [z^T R_3 z + u^T R_2 u] dt \quad (\text{A.3})$$

where R_3 and R_2 are positive-definite constant weighting matrices. The first term of (A.3) is equivalent to $\int x^T R_1 x dt$ since (A.2) can be substituted in this term to deduce the following expression:

$$R_1 = H^T R_3 H \quad (\text{A.4})$$

where R_1 is a positive semi-definite matrix. A widely used starting point in the selection of R_1 and R_2 is the Bryson's rule [154]; however, it is convenient to choose R_1 and R_2 as diagonal matrices and these matrices are subsequently modified in the design process to achieve an acceptable trade-off between performance and control effort [216]. The problem of determining an input u^o for which the criterion (A.3) is minimal is known as the time-invariant deterministic linear optimal regulator problem. It should be noted that various versions and extensions of the criterion expressed in (A.3) exist. The optimal input is generated through a linear control law of the following form:

$$u^o = -K^o x \quad (\text{A.5})$$

where K^o is computed as follows:

$$K^o = R_2^{-1} B^T P \quad (\text{A.6})$$

K^o denotes the linear optimal regulator gain while K denotes simply the linear regulator gain; the constant positive semi-definite matrix P , if it exists, is obtained by solving the following algebraic Riccati equation:

$$0 = H^T R_3 H - P B R_2^{-1} B^T P + A^T P + P A \quad (\text{A.7})$$

Moreover, the control law expressed in (A.5) makes the closed-loop system to be asymptotically stable in general [151]. That is, by substituting (A.5) into (A.1), the resulting closed-loop system is asymptotically stable; the closed-loop system can be expressed as follows:

$$\dot{x} = (A - B K^o) x \quad (\text{A.8})$$

In addition, a linear control law $u = -Kx$ (which is not necessarily optimal) can be computed by choosing the linear gain matrix K appropriately (using pole-placement, for instance) so that the poles of the closed-loop system in (A.8) are located on the left-hand side of the complex-plane (and complex poles appear in conjugate pairs) to achieve asymptotic stability with the requirement that the plant (that is, the open-loop system) is completely controllable. Choosing the closed-loop poles far into the left-hand side of the complex plane results in a transient response that dies down arbitrarily fast which requires large input amplitudes to achieve in general. However, if K is computed using (A.6), the finding of the minimum of the criterion in (A.3) takes into account limits on the inputs amplitudes and speed of convergence to steady-state through matrices R_2 and R_3 , respectively.

Furthermore, the time-invariant stochastic linear optimal regulator problem can be expressed in the following terms: For a LTI system described by the following expression:

$$\dot{x} = Ax + Bu + w \quad (\text{A.9a})$$

$$z = Hx \quad (\text{A.9b})$$

where w represents white noise with intensity V , the quadratic criterion (instead of the expression in (A.3)) is written in the following form:

$$E[\int (z^T R_3 z + u^T R_2 u) dt] \quad (\text{A.10})$$

where $E[\cdot]$ denotes the expected value operator. Equation (A.4) still holds for the expression in (A.10); likewise, the optimal input is computed using equations (A.4 – A.7). Also, if (A.5) is the solution for which the criterion in (A.7) is minimum, then the white noise $w(t)$ in Equation (A.9a) is Gaussian. The block diagrams of the time-invariant deterministic and stochastic linear optimal regulators are shown in (a) and (b) of Figure A.1.

A.2 Linear Optimal Observer

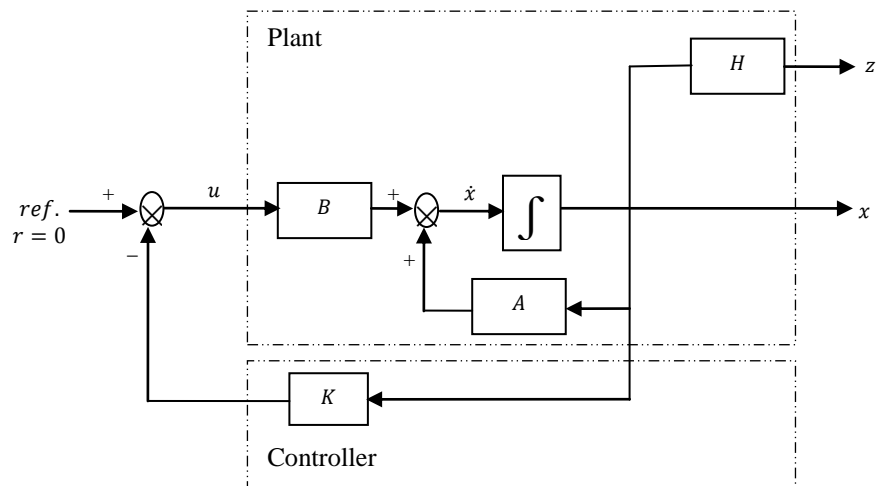
In the discussion of the preceding section, it was assumed that the entire state variables (the complete state vector) can be accurately measured. A more realistic system can be expressed as follows:

$$\dot{x} = Ax + Bu \quad (\text{A.11a})$$

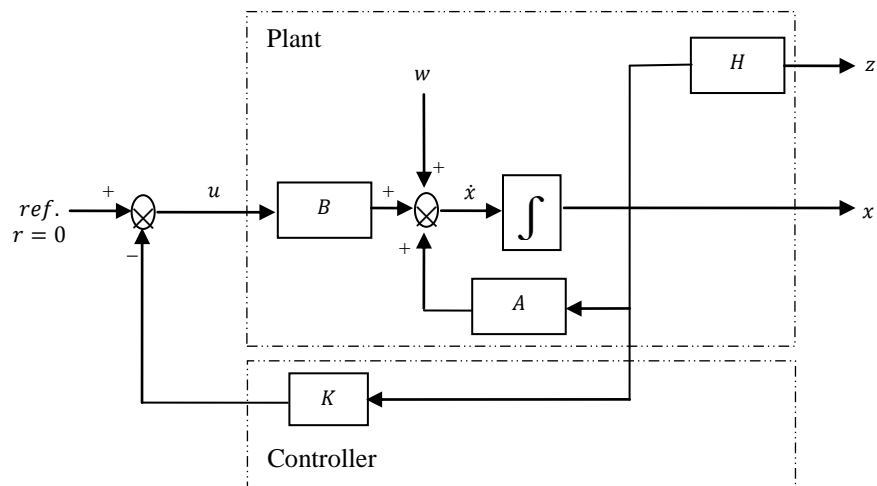
$$y = Cx \quad (\text{A.11b})$$

where y is the observed variable with dimension less than (meaning that only a few number of state variables can be measured) or, at most, equal to that of x . Thus, it would be desirable to obtain or reconstruct, at least, an approximate of the value of x in order to be able to use the linear regulator of the preceding section. Let the reconstructed state be denoted as \hat{x} ; the differential system that obtains \hat{x} so that $x - \hat{x} \rightarrow 0$ as $t \rightarrow \infty$ is called an observer (or estimator). An optimal observer is commonly called the Kalman-Bucy, or simply Kalman, filter or estimator [243]. Let the observer of the LTI system in Equation (A.11) be represented by the following LTI system:

$$\dot{\hat{x}} = F\hat{x} + Gy + Ju \quad (\text{A.12})$$



(a)



(b)

Figure A.1: (a) and (b) are the time-invariant deterministic and stochastic linear optimal regulators, respectively.

The reconstructed error e can be expressed as follows:

$$e = x - \hat{x} \quad (\text{A.13})$$

Thus, subtracting (A.12) from (A.11a), and eliminating y by substituting (A.11b), leads to the following expression:

$$x - \dot{\hat{x}} = (A - GC)x - F\hat{x} + (B - J)u \quad (\text{A.14})$$

Let $G = L$ where L is an arbitrary constant matrix; if $\dot{x} - \dot{\hat{x}} = 0$ (that is, $\dot{x} = \dot{\hat{x}}$), then from (A.14) the following expressions are valid:

$$A - LC = F \quad (\text{A.15a})$$

$$G = L \quad (\text{A.15b})$$

$$B = J \quad (\text{A.15c})$$

Substituting (A.15) in (A.12) leads to the following three equivalent –at least theoretically [216] – expressions of a full-order observer (an observer that reconstructs the complete state vector):

$$\dot{\hat{x}} = A\hat{x} + Bu + L(y - C\hat{x}) \quad (\text{A.16a})$$

$$\dot{\hat{x}} = (A - LC)\hat{x} + Bu + Ly \quad (\text{A.16b})$$

$$\dot{\hat{x}} = (A - LC - BK)\hat{x} + Ly \quad (\text{A.16c})$$

It should be noted that it is possible to find observers of dimension less than that of the system. These are often called reduced-order observer and are particularly useful in situations where the controller to be designed for a system is of much lower dimension than the dimension of the system. More details on the reduced-order observers can be found in [151], for example. Meanwhile, continuing the discussion on the full-order observer, substituting (A.15) in (A.14), and substituting (A.13) in the resulting equation, leads to the following expression:

$$\dot{e} = (A - LC)e \quad (\text{A.17})$$

Thus, if the reconstruction error differential equation of (A.17) is asymptotically stable (that is, $e \rightarrow 0$ and $t \rightarrow \infty$), the observer in (A.16) is also asymptotically stable. As such, observer designs for the LTI system in (A.11) using the observer (A.16) involves determining the value of the constant matrix L such that the observer is asymptotically stable. Moreover, just as in the determination of the constant gain matrix K for the regulator by pole-placement, the determination of the constant gain matrix L for the

observer is also possible using pole-placement with the restriction that the system (A.11) is completely observable. Furthermore, optimal value of the observer gain matrix L can be obtained by finding the minimum of a quadratic criterion. The discussion on the optimization method of finding L follows:

For a LTI system described by the following expressions:

$$\dot{x} = Ax + Bu + w_1 \quad (\text{A.18a})$$

$$y = Cx + w_2 \quad (\text{A.18b})$$

where w_1 and w_2 are the state excitation (disturbance) noise and measurement noise, respectively, assuming that the column vector $[w_1^T \ w_2^T]^T$ can be represented as a white noise with intensity V , then the following expressions are valid:

$$E \left[\begin{pmatrix} w_1(t) \\ w_2(t) \end{pmatrix} \begin{pmatrix} w_1^T(\tau) & w_2^T(\tau) \end{pmatrix} \right] = V(t)\delta(t - \tau) \quad (\text{A.19a})$$

$$V(t) = \begin{bmatrix} V_1(t) & V_{12}(t) \\ V_{12}^T(t) & V_2(t) \end{bmatrix} \quad (\text{A.19b})$$

where $\delta(t)$ is already defined by Equation (4.21). The reconstruction error e is given by Equation (A.13). The mean square reconstruction error can be computed using the following expression:

$$E[e^T W e] \quad (\text{A.20})$$

where W is a symmetric positive definite weighting matrix which describes a measure of the correctness of the state reconstruction by the observer at a given time. Let (A.16) represent the observer for the system in (A.18); the problem of finding L such that the quadratic criterion in (A.20) is minimum is known as the optimal observer problem. Let a positive definite matrix Q represent the variance matrix of e which can be described by the following expression:

$$E[(e - \bar{e})(e - \bar{e})^T] = Q \quad (\text{A.21})$$

where $\bar{e} = E[e]$ represents the mean of e . Assuming that $V_{12} = 0$ (that is, w_1 and w_2 are uncorrelated) and $V_2 > 0$, the solution to the optimal observer problem is obtained using the following expression:

$$L^o = QC^T V_2^{-1} \quad (\text{A.22})$$

characteristic values consist of the characteristic values of $A - BK$ (the regulator poles) and $A - LC$ (the observer poles). This means that asymptotically stable regulator and asymptotically stable observers can be designed separately (by pole-placement or otherwise) and their combination results in an asymptotically stable control systems. This conclusion is known as the separation principle [151]. It should be noted that for a LTI system, controllability and observability are necessary and sufficient conditions for arbitrary assignment of both the regulator and the observer poles (with the restriction that complex poles occur in conjugate pairs).

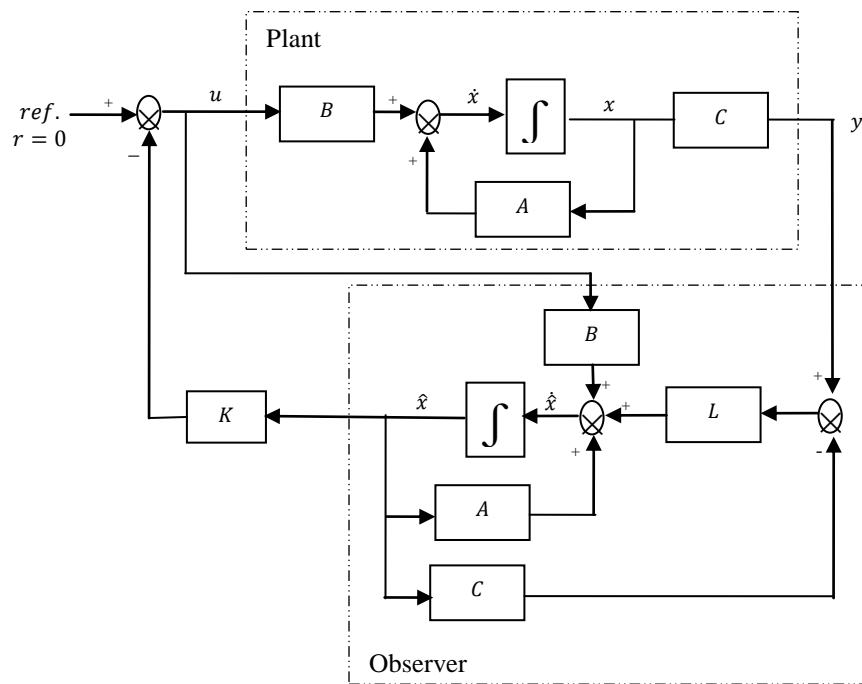


Figure A.3: A structure of a linear output-feedback control system

For the LTI system of Equation (A.18), let the controlled variable be given by Equation (A.9b) for this system; the problem of finding the optimal control law u such that the criterion expressed in (A.10) is minimum is known as the time-invariant stochastic linear optimal output-feedback regulator problem. The solution to this problem (the optimal linear solution) is given as follows:

$$u = -K^o \hat{x} \quad (\text{A.25})$$

where K^o is computed from Equation (A.6) and the reconstructed state \hat{x} is the output of the linear optimal observer (that is, an observer with a linear gain matrix L^o

computed using Equation (A.22)). Moreover, if w_1 and w_2 are Gaussian white noises, the optimal linear solution is the optimal solution [244]. Figure A.4 shows the structure of the optimal linear output-feedback control system for a system with state excitation and measurement noises.

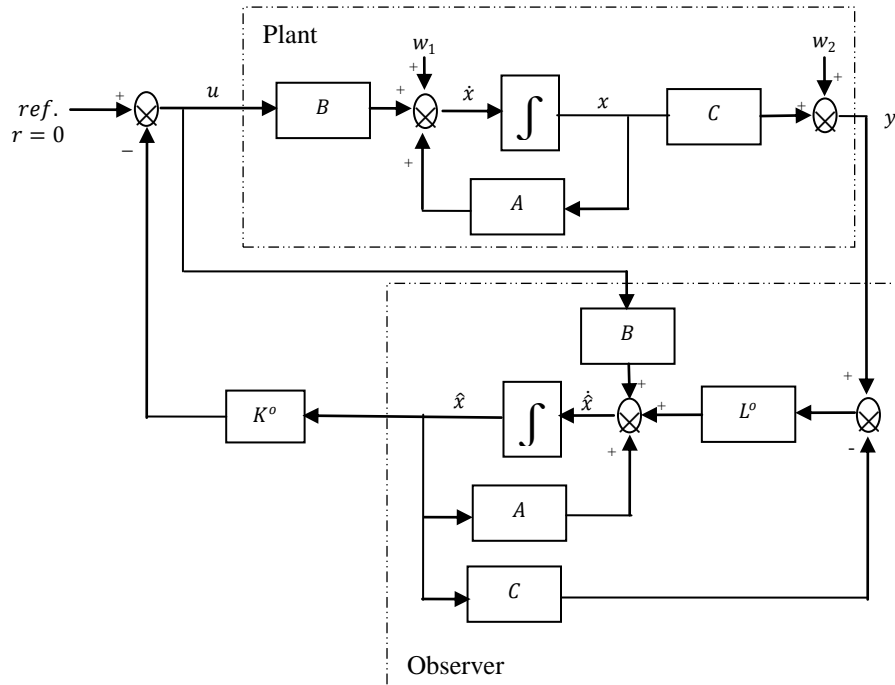


Figure A.4: A structure of the optimal linear feedback control system for a system with state excitation and measurement noises

A.4 Linear Optimal Tracking System and Integral Control

So far, only the control system in which the reference variable is constant, and as such the controller is designed for good disturbance rejection, has been considered. A step further in the design process is to include a command following, or tracking, feature into the controller so that the controlled variable tracks a reference variable that is not necessarily a constant. Accordingly, the regulator problem is a special case of the tracking problem.

Among many possible configurations, the most widely used block diagram of a linear tracking control system is shown in Figure A.5; compared to Figure A.3, extra blocks (matrices) M and \bar{N} are introduced in this figure. Thus, the task of designing a linear tracking control system involves finding the values of matrices M and \bar{N} in

addition to finding the regulator and observer gain matrices. Moreover, the equation of the linear observer for this linear tracking control system is obtained by adding $(M \cdot r)$ to the expression in Equation (A.16); this can be expressed as follows:

$$\dot{\hat{x}} = (A - LC)\hat{x} + Bu + Ly + Mr \quad (\text{A.26})$$

Also, the control law for this case is obtained by adding $(\bar{N} \cdot r)$ to the control law ($u = -K\hat{x}$); this can be written as follows:

$$u = -K\hat{x} + \bar{N}r \quad (\text{A.27})$$

It should be noted that both M and \bar{N} are external signals (as can be seen from equations (A.26) and (A.27)) and, as such, the characteristic values of the closed-loop system are not affected by their introduction into the control system. Thus, the characteristic values of both the linear output-feedback control systems of Figures A.3 and A.5 are the same (of course, it is assumed that the plant matrices A, B, C, D and the regulator and observer gain matrices, K and L respectively, are the same for both control systems). It should be noticed that the configuration of Figure A.3 can be obtained by substituting $r = 0, M = 0$ and $\bar{N} = 1$ in the configuration of Figure A.5 (making Figure A.3 a special form of Figure A.5). Importantly, this indicates that, for the configuration of the linear tracking system of Figure A.5, if M and \bar{N} are known, the design task remains determining the optimal linear output-feedback controller; this can be done using the separation principle, for example, of the preceding section (Section A.3) and doing so using the optimal solutions of the quadratic criteria for computing the optimal regulator and observer gains gives the linear optimal tracking control system for this configuration. However, different possible configurations (that can be defined by the different choices of matrices M and \bar{N}) of a linear tracking system give different responses to command input mainly because (while the closed-loop poles are identical) the zeros of the transfer function are different in general. Consequently, the matrices \bar{N} and M affect the transient response but not the stability of the linear tracking systems. One of the techniques of obtaining matrices M and \bar{N} is given in [216]; this technique is described in the paragraph that follows.

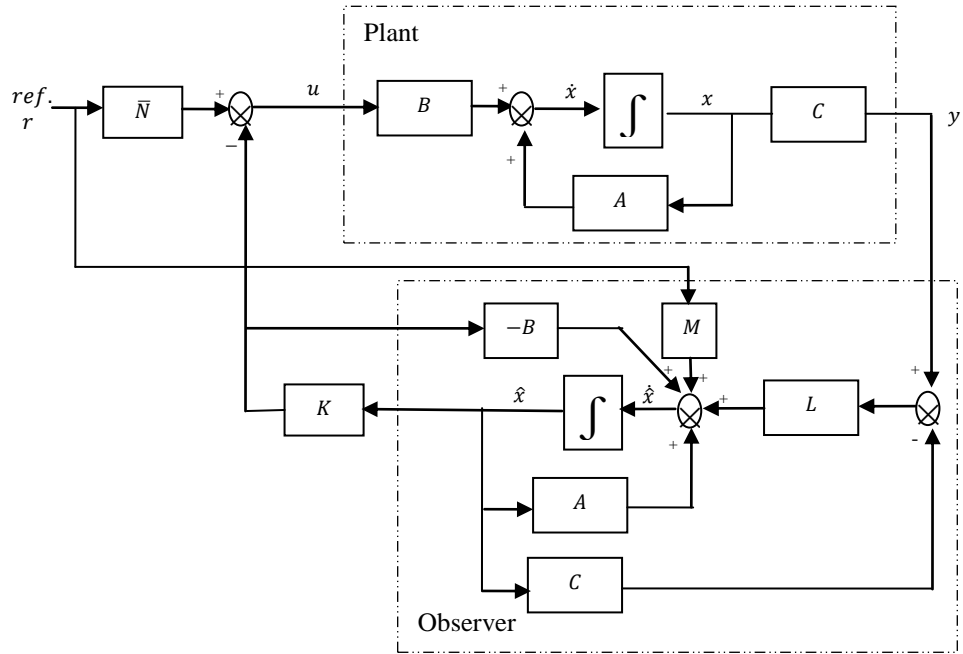


Figure A.5: A block diagram of a linear tracking control system

For a general linear tracking system, the control input can be expressed as follows:

$$u = r - Kx \quad (\text{A.28})$$

At a steady state of zero error, a general system (A, B, C, D) has its differential equation reduced to the following expressions:

$$0 = Ax_{ss} + Bu_{ss} \quad (\text{A.29a})$$

$$y_{ss} = Cx_{ss} + Ju_{ss} \quad (\text{A.29b})$$

where x_{ss} , u_{ss} and y_{ss} are constants denoting the values of the state variable, control input and output variable at steady-states. Thus, at steady-state, the control law can be expressed as follows:

$$u = u_{ss} - K(x - x_{ss}) \quad (\text{A.30})$$

With this equation, no error implies that $x = x_{ss}$ and $u = u_{ss}$. It would be desired that the following expression is true at steady-state:

$$y_{ss} = r_{ss} \quad (\text{A.31})$$

where r_{ss} denote the reference variable at steady-state. Let $x = M \cdot r$ and $u = N \cdot r$; then at steady-state, the expressions for x_{ss} and u_{ss} can be written as follows:

$$x_{ss} = Mr_{ss} \quad (\text{A.32a})$$

$$u_{ss} = Nr_{ss} \quad (\text{A.32b})$$

Substituting (A.32) in (A.29), noting the equation in (A.31) and re-arranging the resulting expression, leads to the following equations:

$$\begin{bmatrix} A & B \\ C & D \end{bmatrix} \begin{bmatrix} M \\ N \end{bmatrix} = \begin{bmatrix} 0 \\ I \end{bmatrix} \quad (\text{A.33a})$$

$$\begin{bmatrix} M \\ N \end{bmatrix} = \left(\begin{bmatrix} A & B \\ C & D \end{bmatrix}^T \begin{bmatrix} A & B \\ C & D \end{bmatrix} \right)^{-1} \begin{bmatrix} A & B \\ C & D \end{bmatrix} \begin{bmatrix} 0 \\ I \end{bmatrix} \quad (\text{A.33b})$$

That is, Equation (A.33a) can be solved for M and N using (A.33b) if it is given that matrices A , B , C and D are known. Moreover, by substituting Equation (A.32) in (A.30), the following expression is obtained:

$$u = -Kx + \bar{N}r \quad (\text{A.34})$$

where $\bar{N} = N + KM$ (the subscript 'ss' has been removed from A.34 to indicate that this is the control law in the general case; the steady-state is a special case of this). The expression in (A.34) is the input required to get a steady-state error of zero to a step-input. Hence, the values of M and \bar{N} obtained using the technique that has just been described can then be used for the linear tracking control system whose block diagram is shown in Figure A.5. However, this control system is not robust to plant parameter changes and therefore will result to non-zero error when the system parameters or reference variables change [216]; as such, the inclusion of integral action (thereby, making the system an Integral Control System) can be used to tackle this problem and obtain a robust tracking system.

Consider the introduction of an integrator in a linear output-feedback control system as shown in Figure A.6. The integral state x_I and its differential equation can be written as follows:

$$x_I = \int \omega dt \quad (\text{A.35a})$$

$$\dot{x}_I = r - Cx \quad (\text{A.35b})$$

where $\omega = r - y$ is the feedback error. Thus, an augmented state equation formed by the plant and the integral state equation can be written as follows:

$$\dot{\underline{x}} = \begin{bmatrix} \dot{x} \\ \dot{x}_I \end{bmatrix} = \begin{bmatrix} A & 0 \\ -C & 0 \end{bmatrix} \begin{bmatrix} x \\ x_I \end{bmatrix} + \begin{bmatrix} B \\ 0 \end{bmatrix} u + \begin{bmatrix} 0 \\ I \end{bmatrix} r \quad (\text{A.36a})$$

$$y = [C \quad 0] \begin{bmatrix} x \\ x_I \end{bmatrix} \quad (\text{A.36b})$$

where $\underline{x} = [x^T \quad x_I^T]^T$ and the control input u is now given by the following expression:

$$u = -\underline{K} \underline{x} \quad (\text{A.37})$$

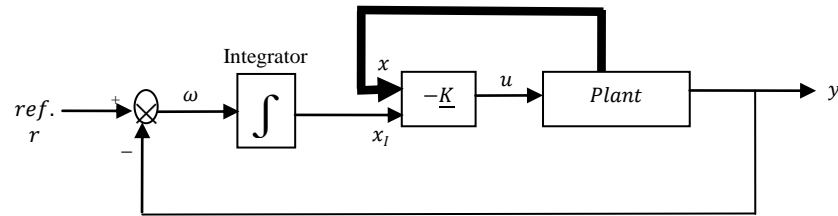


Figure A.6: A block diagram of an Integral Control System

The augmented state equation in (A.36) and the control law in (A.37) can now be expressed in the form of the standard linear optimal regulator problem of Section A.1 using the following state-space model:

$$\dot{\underline{x}} = \underline{A} \underline{x} + \underline{B} u \quad (\text{A.38a})$$

$$y = \underline{C} \underline{x} \quad (\text{A.38b})$$

$$u = -\underline{K} \underline{x} \quad (\text{A.38c})$$

where $\underline{A} = \begin{bmatrix} A & 0 \\ -C & 0 \end{bmatrix}$, $\underline{B} = \begin{bmatrix} B \\ 0 \end{bmatrix}$ and $\underline{C} = [C \quad 0]$; moreover, the following quadratic criterion for determining optimal linear regulator gain for the deterministic and stochastic cases (instead of (A.3) and (A.10), respectively) must now be used:

$$\int (\underline{x}^T \underline{R}_3 \underline{x} + u^T R_2 u) dt \quad (\text{A.39a})$$

$$E \left[\int (\underline{x}^T \underline{R}_3 \underline{x} + u^T R_2 u) dt \right] \quad (\text{A.39b})$$

where $\underline{R}_3 = \begin{bmatrix} R_3 & 0 \\ 0 & R_I \end{bmatrix}$ and R_I is a constant positive definite weighting matrix. Optimal value of \underline{K} can thus be computed as presented in Section A.1 with R_3 replaced with \underline{R}_3 . Also, \underline{K} can be partitioned as $\underline{K} = [K \ : \ K_I]$ so that Equation (A.37) can be written as follows:

$$u = -[K \quad K_I] \begin{bmatrix} x \\ x_I \end{bmatrix} = -Kx - K_I x_I \quad (\text{A.40})$$

It should be noted that the state variable x in (A.40) is to be determined by an observer. Thus, the structure (block diagram) of a linear optimal tracking system with integral action can be obtained using the following steps:

Step 1: Substitute Equation (A.40) into the block diagram of Figure A.6

Step 2: Add the observer defined by Equation (A.26) into the resulting structure (where x is now replaced with the output of the observer \hat{x}). It should be noted that the observer is obtained by substituting (A.27) in (A.26); the observer equation for the block diagram can therefore be written as follows:

$$\dot{\hat{x}} = (A - LC - BK)\hat{x} + Ly + \underline{M}r \quad (\text{A.41})$$

where $\underline{M} = B\bar{N} + M$.

Step 3: Connect the block diagram so that the control law is obtained by adding $(\bar{N} \cdot r)$ to (A.40); this can be expressed as follows:

$$u = -Kx - K_I x_I + \bar{N}r \quad (\text{A.42})$$

The final structure of the optimal linear tracking system with integral control is shown in Figure A.7. The observer gain matrix L in this system is computed either by pole-placement or by finding an optimal solution to a quadratic criterion (minimum of a quadratic cost-function) as discussed in Section A.2.

In summary, \underline{K} and L can be found separately – in accordance with the separation principle – by pole-placement which involves assigning the characteristic values of the regulator system $(\underline{A} - \underline{B}\underline{K})$ and the observer system $(\underline{A} - \underline{L}\underline{C})$, respectively, so that these two systems are asymptotically stable. Optimal \underline{K} and L can be obtained by solving the optimal linear regulator and the optimal linear observer problems,

respectively, using techniques described in Sections A.1-A.3. However, in solving for \underline{K} , the augmented state equation of (A.38) must be used as the state-space model. The regulator gain \underline{K} and the integral gain \underline{K}_I are the left- and right-hand side partitions of \underline{K} , respectively.

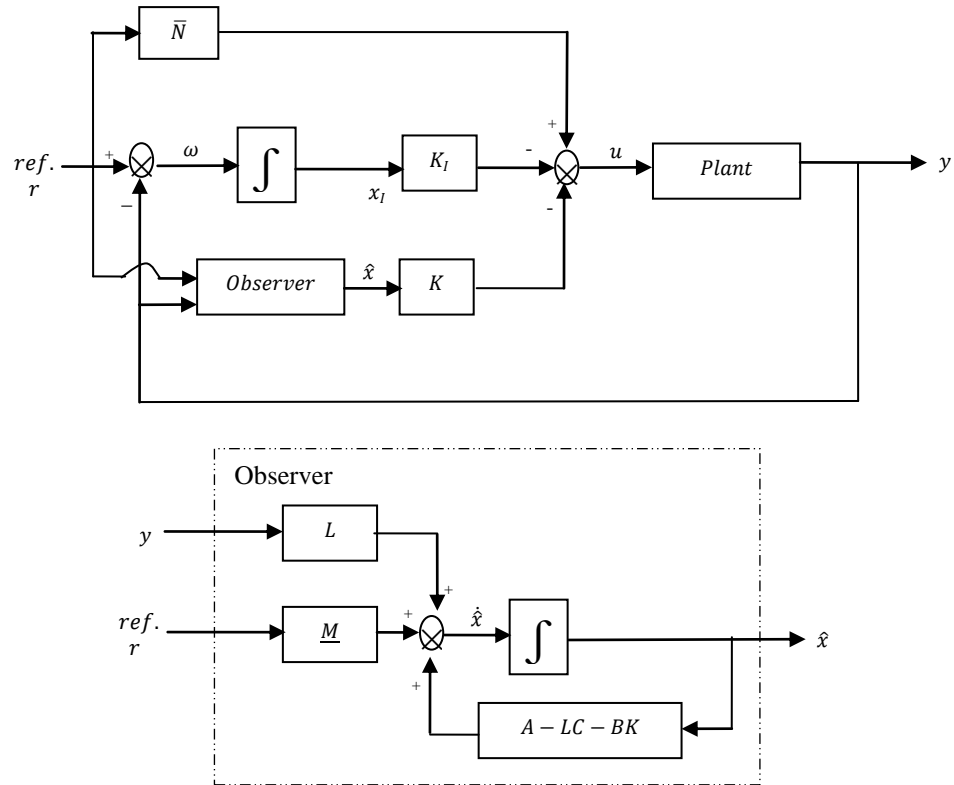


Figure A.7: A structure of the optimal linear tracking system with integral action